



UNIVERSITY OF
BIRMINGHAM

Cytotoxic Effects of Silver Nanoparticles to Embryonic Zebrafish (*Danio Rerio*) Cells: Focussing on the Development of Alternative Models for Nano (Eco)Toxicity Studies

by

Ana Isabel Carrazco Quevedo

A thesis submitted to the University of Birmingham for the degree of

DOCTOR OF PHILOSOPHY

School of Geography, Earth, and Environmental Science

College of Life and Environmental Sciences

University of Birmingham

March 2021

UNIVERSITY OF
BIRMINGHAM

University of Birmingham Research Archive

e-theses repository

This unpublished thesis/dissertation is copyright of the author and/or third parties. The intellectual property rights of the author or third parties in respect of this work are as defined by The Copyright Designs and Patents Act 1988 or as modified by any successor legislation.

Any use made of information contained in this thesis/dissertation must be in accordance with that legislation and must be properly acknowledged. Further distribution or reproduction in any format is prohibited without the permission of the copyright holder.

Covid disruption statement

Due to the significant disruption experienced as a result of the COVID-19 pandemic, including mental health effects and total closure of the University of Birmingham facilities, such as libraries, laboratories, and working spaces (March-September 2020), the research planned for my last year of the PhD (2020) was adjusted and some of the planned experiments could not be completed.

Abstract

This thesis presents an initial evaluation of the utility of adherent embryonic zebrafish fibroblast cells (ZF4) as a potential early-stage aquatic *in vitro* model for nanosafety evaluation, assessing the molecular and toxicological responses activated by exposure to silver nanoparticles (AgNPs) of different sizes and their ionic counterpart (AgNO₃). A range of characterisation methods were implemented to evaluate changes in the physico-chemical properties of AgNPs, such as hydrodynamic size, zeta potential, polydispersity index, dissolution and agglomeration in the different exposure media used, including cell culture media supplemented with 10 % serum (CCM), serum-free media (SFM) and ultra-pure water (UPW). The biological responses of the ZF4 cells were assessed by exposing the cells to three representative AgNP sizes (10, 30 and 100 nm) and three concentrations of the NPs (2.5, 5 and 10 µg/mL) and AgNO₃ (1, 1.5 and 2 µg/mL) determined on the basis of a 24-hour cytotoxicity exposure, representing low, medium, and high (EC₅₀) concentrations, respectively.

Results demonstrated that the exposure medium had a significant impact on the physiochemical characteristics of the Ag NPs, inducing dissolution and / or agglomeration and sedimentation, with CCM having a stabilisation effect due to protein corona formation. The biological responses in ZF4 cells revealed that the AgNP size, exposure concentration, and form (particulate versus ionic) played a key role in mediating toxicity. A NP size and concentration-dependent toxicity was observed, which correlated with the amount of ionic Ag for all the biological assays, demonstrating that the 10 nm AgNPs and

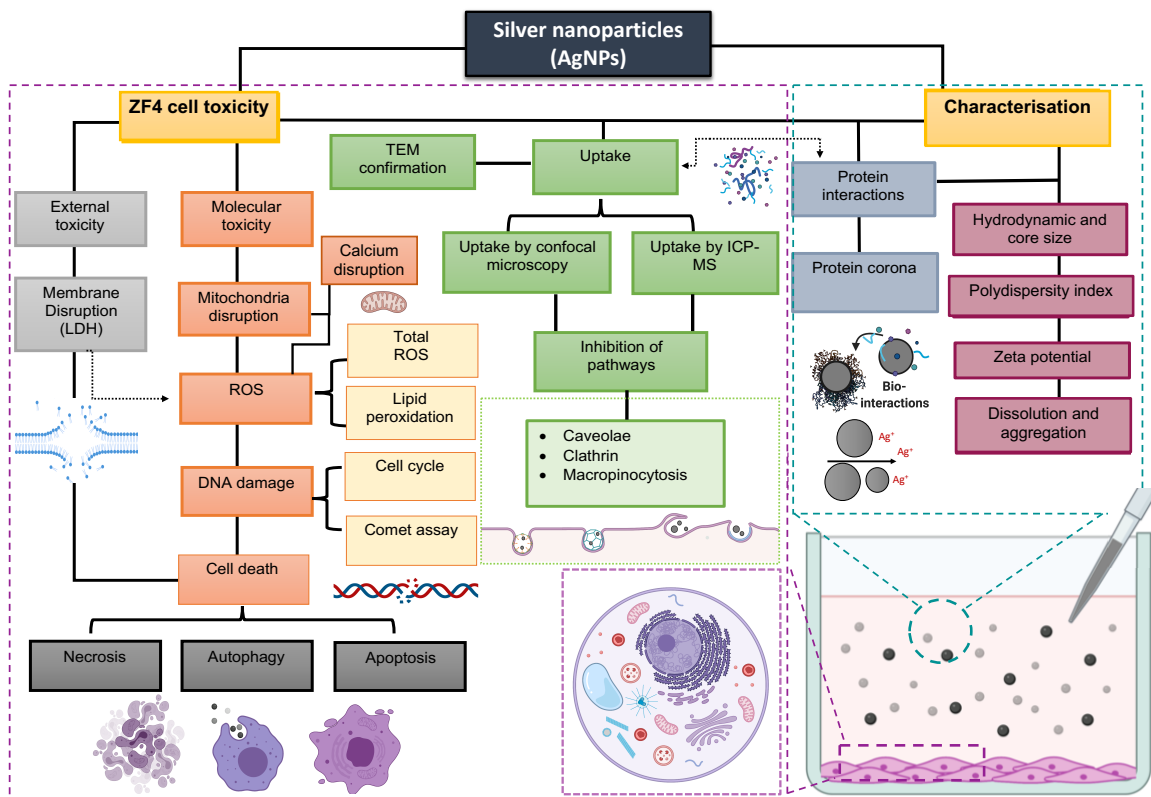
the ionic control induced significant cellular damage, compared to the 30 and 100 nm AgNPs which underwent less dissolution and less uptake on a particle number basis at constant exposure mass. AgNPs were found to disrupt the plasma membrane, leading to leakage of cytoplasmatic enzymes and peroxidation of lipids.

Internalisation of the NPs was found to be mediated by different endocytic processes, such as clathrin and caveolae-mediated endocytosis for the 30 and 100 nm AgNPs, whereas the 10 nm AgNPs were mainly internalised by macropinocytosis and simple diffusion due to their small size. Similarly, the data suggested that the dissolved Ag⁺ ions were able to escape the endocytic vesicles and disrupt intracellular homeostasis by inducing damage to the mitochondrial membrane, lysosomes, and endosomes, which affected biological processes such as autophagy. The disruption of the intracellular contents leads to the generation of Reactive Oxygen Species (ROS), which along with free NPs and ionic silver (Ag⁺) disrupted calcium flux, and induced cell cycle arrest. Deoxyribonucleic acid (DNA) damage was confirmed as DNA strand breaks, the amount of which was strongly related to the cell death mechanism induced. Cell death is the final outcome of cytotoxicity, and can be linked to apoptosis, which is mediated via a mitochondrial pathway as the cell attempts to overcome the damage, as found for the 30 and 100 nm AgNPs, whereas necrosis was activated when the cells suffered irreparable damage such as with the 10 nm and ionic Ag (AgNO₃).

To conclude, fibroblast-like ZF4 cells have great potential to be used as an aquatic early-stage *in vitro* model for nanotoxicity studies, providing insights about the toxicity of AgNPs. The responses to the AgNPs in ZF4 cells were comparable to responses reported for

similar NPs in other fish cell and mammalian models. In addition, our results provide insights about the molecular events triggered as part of a cytotoxic response, potentially contributing to the establishment of Adverse Outcome Pathways (AOP), and in support of efforts towards reduction of animal experimentation.

Graphical abstract



Acknowledgements

I would like to express my deepest appreciation to my supervisors Prof Eugenia Valsami-Jones and Prof Iseult Lynch for being a pillar of support and inspiration throughout my PhD research. I am deeply grateful for all the time, encouragement, and hard work invested in this project; without you, none of this would have been possible.

I would also like to extend my sincere thanks to Prof Eva, for giving me the opportunity of being part of the ACEnano project, which provided me with the funding necessary to accomplish an essential part my research, as well as plenty of opportunities to gain professional experience while writing publications and attending to workshops and conferences. Likewise, I would like to acknowledge Prof Iseult and the NanoCommons project for funding my attendance to workshops and conferences, which also gave me new professional experiences as well as the opportunity to visit incredible places.

I would also like to thank all the people I have had the pleasure to work with at our lab.

First of all, I would like to thank Emily for sharing her invaluable cell culture skills, which were the basis for my research. Laura and Sophie, thank you for your kind assistance with the TEM samples. Also thanks a lot to Grace, Marie, Andy, Hayat, Hassan, Marie, Aline, and especially Clarissa for making the long days at the lab more enjoyable. I also owe a particular thanks to Chris and Norman for the support in running hundreds of ICP-MS samples. Also, a special thanks goes to Nick for his kind assistance with any issues I had

with lab orders, invoices, cleaning rota, etc; your help made things so much easier at the lab.

I am also very grateful to staff members and friends from the Pharmacy school that I had the pleasure to meet. Particularly from the Nanomedicine group, Hanouf, Abdullah, and Rifka; thanks a lot for our breakfast/dinner chats that kept me going through hard times while sharing our lab experiences and concerns with plenty of food. Adriana from the flow cytometer facilities at the Medical school, thanks a lot for your assistance and kind words. Alex from the BALM facilities, for his assistance with the confocal microscope.

A special thanks to my amazing family for constantly supporting and motivating me to keep going during all the years I spent abroad. Thank you very much for your kind words and constant video calls when I needed them the most. Principally, I am deeply indebted to my mom: Mamá, muchas gracias por todo tu apoyo incondicional, monetario y emocional; gracias por siempre motivarme a seguir adelante, nunca rendirme y siempre dar lo mejor de mí. Gracias por ser el mejor ejemplo a seguir. To my sister and my beautiful nieces; thank you for greeting me every December with lots of hugs, enthusiasm, food, and free stress relief massages!

Last but not least, I am deeply grateful to Dr Fabricio Ledezma for being a source of unconditional support in every aspect. Thanks a lot for nurturing my research skills with our long chemical, statistical, and math classes. Thanks a lot for always cheer me up with wise words (and very long chats) when I really need them.

My eternal thanks and appreciation to all the people who supported me throughout my PhD and made this accomplishment possible. THANK YOU!

List of publications

This thesis includes three chapters that were published in peer-reviewed journals. Papers accepted for publication directly from this doctoral research include:

QUEVEDO, A. C., LYNCH I. & VALSAMI-JONES, E. (2021). Silver nanoparticle induced toxicity and cell death mechanisms in embryonic zebrafish cells. *Nanoscale*, 2021. **13**(12): p. 6142-6161.

QUEVEDO, A. C., LYNCH I. & VALSAMI-JONES, E. (2021). Cellular repair mechanisms triggered by exposure to silver nanoparticles and ionic silver in embryonic zebrafish cells. *Environmental Science: Nano*, 8(9): p. 2507-2522.

QUEVEDO, A. C., ELLIS L-J.A., LYNCH I. & VALSAMI-JONES, E. (2021). Mechanisms of Silver Nanoparticle Uptake by Embryonic Zebrafish Cells. *Nanomaterials*, **11**(10): p. 2699.

Papers published/accepted that are not directly related to the research topic, but that were completed during the PhD course include:

BRIFFA S, ELLIS L. J, HARRISON D, **QUEVEDO A. C.**, ADWIBI I, REILLY K, BASHIRU I; TAIWO H. A., HOUSSEIN H. D. & VALSAMI-JONES E. (2021). A review of nanomaterial applications in biomedicine with a specific focus on technologies against coronavirus infections. Manuscript submitted to *Nanoscale Advances*.

DONG F, **QUEVEDO A. C.**, WANG X, VALSAMI-JONES E, & KREFT, J-U. (2021). Experimental evolution of *Pseudomonas putida* under silver ion versus nanoparticle stress. *Environ Microbiol*, Online ahead of print. doi: 10.1111/1462-2920.15854.

QUEVEDO A. C., GUGGENHEIM E, BRIFFA S. M, ADAMS J, LOFTS S, KWAK M, GEOL LEE T, JOHNSTON C, WAGNER S, HOLBROOK R, HACHENBERGER Y, TENTSCHERT J, AND VALSAMI-JONES, E (2020). UV-Vis Spectroscopic Characterization of Nanomaterials in Aqueous Media, *JoVE*, no. 176, pp. e61764.

CARRAZCO-QUEVEDO, A., SALAMANCA, M.J., POYNTER, A, LYNCH, I. & VALSAMI-JONES, E. (2019). Bioaccumulation and toxic effects of nanoparticulate and

ionic silver in *Saccostrea glomerata* (rock oyster). *Ecotoxicology and Environmental Safety* 179: 127-134.

Table of contents

Covid disruption statement.....	I
Abstract.. ..	II
Acknowledgements	V
List of publications.....	VII
Table of contents.....	IX
List of figures	XIV
List of tables	XVII
List of abbreviations	XVIII
Chapter 1: Introduction	
1.1 Nanotechnology as an emerging field.....	1
1.2 Origin of NMs	2
1.3 Engineered or manufactured NMs	2
1.4 Silver Nanoparticles (AgNPs): a widely applied nanomaterial	3
1.5 AgNPs, a risk for the environment?	5
1.6 Behaviour of AgNPs in aqueous environments	8
1.6.1 Oxidation and complexation.....	8
1.6.2 Agglomeration and dissolution.....	9
1.7 AgNPs in experimental media.....	11
1.8 Toxicity of Ag ⁺ and AgNPs in fish	13
1.9 Factors that influence the transport, fate, and toxicity of AgNP	17
1.10 Interactions between AgNPs and biological systems	20
1.10.1 Protein corona.....	20
1.10.2 Cellular internalisation pathways	21
1.11 Cellular and toxicological effects of NPs.....	25
1.11.1 Membrane disruption and adaptative responses	25
1.11.2 Mitochondrial dysfunction	28

1.11.3	Oxidative stress	29
1.11.4	DNA damage and repair mechanisms	30
1.11.4.1	DNA repair mechanisms: cell cycle	32
1.11.5	Cell death mechanisms.....	34
1.11.5.1	Apoptosis	35
1.11.5.2	Autophagy.....	37
1.11.5.3	Necrosis	39
1.11.6	Representative toxicological biological models: Zebrafish.....	40
1.11.7	Alternative testing frameworks and strategies	44
1.11.8	Embryonic zebrafish cells: a potential model for nanotoxicity studies	45
1.12	Thesis hypothesis and objectives of the research	53
Chapter 2: Silver nanoparticle induced toxicity and cell death mechanisms in embryonic zebrafish cells		
2.1	Abstract.....	56
2.2	Introduction	57
2.3	Materials and methods.....	60
2.3.1	Characterisation of AgNPs.....	60
2.3.2	Silver nitrate (AgNO ₃) stock	61
2.3.3	Dissolution of AgNPs in water and CCM	61
2.3.4	Culture of embryonic zebrafish cells (ZF4)	64
2.3.4.1	Culture of cells for flow cytometry	64
2.3.5	Lactate dehydrogenase activity (LDH) assay	65
2.3.6	Autophagy assay	67
2.3.7	Apoptosis versus necrosis assay.....	68
2.3.8	Mitochondrial membrane potential (MMP).....	70
2.3.9	Lipid peroxidation.....	71
2.3.10	Statistical analysis.....	72
2.4	Results	73
2.4.1	Characterisation of AgNPs in ultrapure water and culture media	73

2.4.2	Dissolution of AgNPs in water and CCM	76
2.4.3	Lactate dehydrogenase activity (LDH) assay	79
2.4.4	Autophagy induction	82
2.4.5	Apoptosis and necrosis.....	83
2.4.6	Mitochondrial membrane potential.....	85
2.4.7	Lipid peroxidation.....	89
2.5	Discussion.....	94
2.6	Conclusions	105
2.7	Author Contributions	106
2.7.1	Conflicts of interest	107
2.7.2	Acknowledgements.....	107
Chapter 3: Cellular repair mechanisms triggered by exposure to silver nanoparticles (AgNPs) and ionic silver (AgNO₃) in embryonic zebrafish cells (ZF4)		
3.1	Abstract.....	108
3.1	Introduction	109
3.2	Materials and methods.....	111
3.2.1	AgNPs characterisation	111
3.2.2	Silver nitrate (AgNO ₃) stock.....	112
3.2.3	Culturing of embryonic Zebrafish cells (ZF4).....	112
3.2.4	Toxicity of AgNPs and AgNO ₃	113
3.2.5	Nanoparticle internalisation by ZF4 cells	114
3.2.6	Intracellular calcium flux.....	115
3.2.7	Oxidative stress	116
3.2.8	Cell cycle analysis.....	118
3.2.9	DNA damage determined by Comet assay.....	119
3.2.10	Statistical analysis.....	120
3.3	Results	121
3.3.1	Characterisation of the NPs	121
3.3.2	LDH assay	123

3.3.3	Nanoparticle internalisation.....	126
3.3.4	Intracellular calcium flux.....	132
3.3.5	Oxidative stress	133
3.3.6	Cell cycle arrest	136
3.3.7	DNA damage by comet assay	138
3.4	Discussion.....	142
3.5	Conclusions	150
3.6	Acknowledgements.....	151
Chapter 4: Cellular uptake mechanisms of silver nanoparticles (AgNPs) by embryonic zebrafish cells (ZF4)		
4.1	Abstract.....	152
4.2	Introduction	153
4.3	Methodology	155
4.3.1	Characterisation of AgNPs.....	155
4.3.2	Culture of cells	156
4.3.3	Quantification of total silver in ZF4 cells using ICP-MS	156
4.3.3.1	Exposure of ZF4 cells to AgNPs	156
4.3.3.2	Digestion of the cells for quantification of Ag internalisation.....	157
4.3.4	Uptake pathway inhibition using pharmacological inhibitors.....	157
4.3.4.1	Visualisation of the inhibition of cellular uptake pathways	157
4.3.4.2	Quantification of internalised Ag ⁺ after inhibition of cellular uptake	159
4.3.5	Imaging of intracellular AgNPs using TEM	160
4.3.6	Early endosome induction (EEI)	161
4.3.7	Autophagy response	162
4.3.8	Protein corona isolation and analysis of proteins using PAGE	163
4.3.9	Statistical analysis.....	164
4.4	Results	164
4.4.1	Characterisation of the AgNPs.....	164
4.4.2	Cellular uptake using ICP-MS.....	168

4.4.3	Inhibition of the cellular uptake pathways using confocal microscopy	169
4.4.3.1	Quantification of the uptake of Ag ⁺ following inhibition of the cellular uptake	172
4.4.4	Intracellular localisation of NPs using TEM.....	176
4.4.5	Early endosomes induction (EEI).....	178
4.4.6	Autophagy response	180
4.4.7	Protein corona isolation and analysis of proteins using PAGE and mass spectrometry.....	181
4.5	Discussion.....	187
4.6	Conclusions	193
4.7	Acknowledgements	194
Chapter 5: Discussion, future work, and conclusions		
5.1	Discussion.....	195
5.1.1	Characterisation of the NPs	196
5.1.2	Uptake mechanisms in ZF4 cells	198
5.1.3	Mechanistic insights from protein binding	201
5.1.4	Potential cytotoxicity- Is there a nano effect?	202
5.1.5	Regulatory context.....	207
5.2	Preliminary work towards ZF4 3D cell models.....	211
5.3	Conclusions	213
6.	References.....	215
7.	SI Chapter 2.....	237
8.	SI Chapter 3.....	260
9.	SI Chapter 4.....	284

List of figures

Chapter 1

Figure 1.1. Nanometre (nm) scale of different objects found in nature	2
Figure 1.2. Market share of different nanomaterials and the main uses of silver nanoparticles in Europe from 2016-2020	4
Figure 1.3. Release of AgNPs into aquatic environments, including their possible chemical and biological interactions.	11
Figure 1.4. Chemical and biological interactions of AgNPs in cell culture medium and cells.	13
Figure 1.5. Schematic diagram to illustrate the ion-transport of sodium (Na^+) and chloride (Cl^-) in gill epithelia.	15
Figure 1.6. Mechanism of acute silver toxicity in freshwater fish. Toxicity is related to the blocking of ion transport through membranes in gills of fish.	16
Figure 1.7. DNA damage and ROS formation.	30
Figure 1.8. Cell cycle phases and responses to overcome cellular damage.	34
Figure 1.9. Types of cell death and their key features.	35
Figure 1.10. Zebrafish models, advantages, and disadvantages.	44
Figure 1.11. Traditional testing models vs cellular based models.	45
Figure 1.12. Zebrafish embryonic cells as an alternative toxicological model.	51
Figure 1.13. Summary of the hypothesis, goals, and overall aim of the research.	55

Chapter 2

Figure 2. 1. Flow cytometry quadrant.	70
Figure 2. 2. TEM characterisation of the 3 different AgNPs by TEM.	73
Figure 2. 3. Hydrodynamic diameter of AgNPs by DLS in different test media at the different concentrations.	75

Figure 2. 4. Dissolution of AgNPs in ultrapure water (UPW) and complete culture media (CCM).....	79
Figure 2. 5. Viability of embryonic zebrafish cells (ZF4) treated with AgNPs and AgNO ₃ for 3, 24, 48 and 72 hrs.	81
Figure 2. 6. Autophagy induction in ZF4 cells treated with AgNPs or AgNO ₃ for 24 hours.	83
Figure 2. 7. Populations of ZF4 cells that were viable, apoptotic, and necrotic following treatment with AgNPs or AgNO ₃ for 24 hours.	85
Figure 2. 8. ZF4 cells stained with MitoHealth to assess mitochondrial permeability. ...	87
Figure 2. 9. Mitochondrial membrane permeability of ZF4 cells treated with AgNPs or AgNO ₃ for 24 hours.	89
Figure 2. 10. Lipid peroxidation in ZF4 cells treated with AgNPs or AgNO ₃ for 24 hours.	91
Figure 2. 11. Comparison of all the data presented in Figures above.....	93
Figure 2. 12. The number of particles at the different AgNPs mass concentrations.	98

Chapter 3

Figure 3.1. Serum Free Medium (SFM) and Complete Culture Medium (CCM) at different time points.	122
Figure 3.2. Cytotoxicity of AgNPs and AgNO ₃ to ZF4 cells in Serum Free Medium (SFM).	125
Figure 3.3. Internalisation of AgNPs by ZF4 cells in CCM determined by confocal microscopy.	127
Figure 3.4. Representative confocal images of ZF4 cells treated with AgNPs.....	129
Figure 3.5. Confocal images of ZF4 cells treated with AgNPs for 2 hours.....	130
Figure 3.6. Confocal images of ZF4 cells treated with AgNPs for 24 hours.....	131
Figure 3.7. Intracellular calcium induced by AgNPs and AgNO ₃ in ZF4 cells at 24 hours in CCM.	133
Figure 3.8. Total oxidative stress in ZF4 cells treated with AgNPs and AgNO ₃	135

Figure 3.9. Impact of AgNPs on cell cycle progression of ZF4 cells.	138
Figure 3.10. Comet assay images.....	139
Figure 3.11. DNA damage in ZF4 cells treated with AgNPs and AgNO ₃	141
Figure 3.12. Hypothetical cellular mechanisms of effects induced to ZF4 cells by AgNP exposure.....	149

Chapter 4

Figure 4.1. Characterisation of AgNPs.....	167
Figure 4.2. Intracellular uptake of AgNPs.....	169
Figure 4.3. Inhibition of the cellular uptake pathways.	171
Figure 4.4. Quantification of the inhibition of the cellular uptake pathways.....	175
Figure 4.5. TEM images of cells treated with AgNPs.	177
Figure 4.6. Early endosome induction.....	179
Figure 4.7. Autophagy induction in ZF4 cells as determined by confocal microscopy.	181
Figure 4.8. Coomassie blue staining of PAGE gels for isolated protein corona.....	183
Figure 4.9. Proteins secreted during AgNPs exposure in medium supplemented with 10% FBS.	186

Chapter 5

Figure 5.1. Aims and gaps addressed by the research presented in this thesis.	196
Figure 5.2. Biological responses triggered in ZF4 cells after exposure to AgNPs and ionic Ag.	206
Figure 5.3. Preliminary experimental results to develop 3D models using ZF4 cells. ...	212

List of tables

Table 1.1. Key physicochemical characteristics of AgNPs.....	19
Table 1.2. Endocytic and non-endocytic uptake pathways in cells.	24
Table 1.3. NP exposure to fish cells.....	47
Table 1.4. Literature review of recent NMs-toxicity studies in embryonic zebrafish cells (ZF4).....	52
Table 2.1. Total surface area for AgNPs of different sizes at the different mass concentrations utilised.....	99
Table 4.1. Analysis of the proteins secreted by ZF4 cells in response to the AgNPs and identified in the NP coronas.	184

List of abbreviations

Adenosine triphosphate	ATP
Adverse Outcome Pathways	AOP
Ag	Silver
Ag ⁺	Silver ions
AgNO ³	Silver nitrate
AgNPs	Silver nanoparticles
Allophycocyanin	APC
Aluminium	Al
Atomic force microscope	AFM
Cl	Chlorine
Calcium	Ca ²⁺
Carbon dioxide	CO ₂
Catalase	CAT
Chloride ions	Cl ⁻
Chlorpromazine	CLZ
Cholera toxin beta subunit	CTB
Complete culture medium	CCM
Compound Annual Growth Rate	CAGR
Cyclin-dependent kinases	CDKs
Deoxyribonucleic acid	DNA
Dimethyl sulfoxide	DMSO
Dissolved organic matter	DOM
Double-strand breaks	DSBs
Dynamic Light Scattering	DLS
Early endosome formation	EEF
Early endosomes	EE
Electrostatic double layer	EDL
Embryonic zebrafish cells	ZF4
Fish Embryo Acute Toxicity	FET
Fluorescein isothiocyanate	FITC
Fluorescence-activated cell sorting	FACS
Foetal Bovine Serum	FBS
Genistein	Gen
Glutathione peroxidase	GPx
Glutathione reductase	GR

Gold	Au
Hours post fertilization	hpf
Hydrogen peroxide	H ₂ O ₂
Hydroxyl ions	OH ⁻
Inductively coupled plasma mass spectrometry	ICP-MS
Inner mitochondrial membrane	IMM
Intermembrane space	IMS
Iron	Fe
K ⁺	Potassium ions
Kilodaltons	KDa
Lactate dehydrogenase	LDH
Late endosomes	LE
Liver zebrafish cells	BZL
Low density lipoprotein	LDL
Low density polyethylene	LDPE
Low melting point agarose	LMA
Manganese	Mn
Microscopy	TEM
Mitochondrial membrane	MM
Mitochondrial outer membrane permeabilization	MOMP
Mitochondrial permeability transition pore	MPTP
Na ⁺	Sodium ions
Nanomaterials	NMs
Nanometre	nm
Nanoparticle Tracking Analysis	NTA
Nanoparticles	NPs
Natural organic matter	NOM
Nitric acid	HNO ₃
Normal melting point agarose	NMA
Organisation for Economic Co-operation and Development	OECD
Phosphate-buffered saline	PBS
Plasma membrane	PM
Polyacrylamide gel electrophoresis	PAGE
Polydispersity index	PDI
Polyethylenimine	bPEI
Polyvinylpyrrolidone	PVP
Propidium iodide	PI
Reactive oxygen species	ROS

Red fluorescent protein	RFP
Scanning X-ray microscope	STM
Serum free medium	SFM
Silicon	Si
Silicon oxide	SiO ₂
Silver	Ag
Silver carbonate	Ag ₂ CO ₃
Silver chloride	AgCl
Silver ions	Ag ⁺
Silver nanoparticles	AgNPs
Silver nitrate	AgNO ₃
Silver perchlorate	AgClO ₄
Silver sulphide	Ag ₂ S
Single-strand breaks	SSBs
Sodium dodecyl sulfate	SDS
Superoxide dismutase	SOD
Surface Area	SA
Tetramethylrhodamine	TRITC
Titanium	Ti
Titanium dioxide	TiO ₂
Toll-like receptors	TLRs
Trans-Golgi network	TGN
Transferrin	Tf
Transmission Electron Microscopy	TEM
Tumour necrosis factor	TNF
Ultrapure water	UPW
Ultraviolet	UV
Ultraviolet–visible spectrophotometry	UV-Vis
Unstirred layer	USL
Quantitative structure activity relationships	QSAR
Van der Waals	vdW
Wastewater treatment plants	WWTPs
Wheat germ agglutinin	WGA
Wortmannin	Wort
Zinc	Zn
Zinc oxide	ZnO
Zinc oxide NPs	ZnONPs

Chapter 1: Introduction

1.1 Nanotechnology as an emerging field

The manipulation and design of materials on the nanometre scale is opening a world of innovative possibilities, with hundreds of benefits and substantial impacts on almost all industries and all areas of society in the field of nanotechnology. The prefix 'nano' is derived from the Greek 'nanos' which means 'dwarf'. 'Nano' has become a popular label for science empowered by the special properties occurring in the nanoscale [1, 2]. Nanotechnology is a multidisciplinary science that spans almost all fields of science and technology, such as physics, chemistry, materials sciences, medical sector, automotive industries, and many other engineering, medical, and environmental sciences. Nanotechnology focuses on the design and manufacturing of nanomaterials (NMs) to create consumer products with exceptional and unique physical, chemical, and biological properties by manipulating the material's size with at least one dimension is of 100 nanometre (nm) or less in length scale (Figure 1.1) [2]. NMs are considered innovative products, requiring new legislation and definition for regulatory purposes. The European Commission (2011/696/EU) suggested the definition of NMs as follow: "Nanomaterial means a natural, incidental or manufactured material containing particles, in an unbound state or as an aggregate or agglomerate and where, for 50% or more of the particles in the number size distribution, one or more external dimensions is in the size range 1 nm–100 nm" [3].

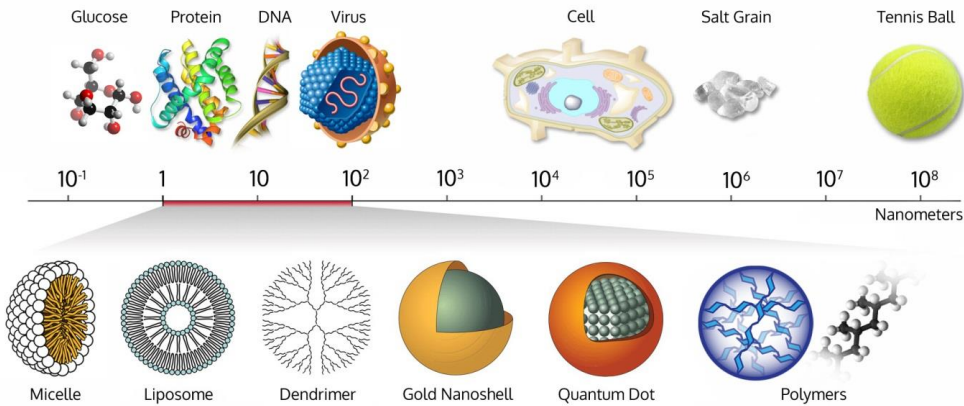


Figure 1.1. Nanometre (nm) scale of different objects found in nature [4].

1.2 Origin of NMs

NMs can arise in three different ways; natural, incidental, and intentionally produced (manufactured or engineered) as described below:

1. Natural NMs include those from naturally occurring environmental processes. For example, through (bio)geochemical or mechanical processes, such as volcanic ash, ocean spray, mineral composites and magnetotactic bacteria [4, 5].
2. Incidental NMs are referred to those produced unintentionally. They result from anthropogenic activity such as industrial processes [6].
3. Manufactured or engineered NMs are conceived, designed, and intentionally produced by humans [6].

1.3 Engineered or manufactured NMs

The field of nanotechnology has achieved many improvements in the synthesis, production, and characterization of NMs since the 1980s [7, 8]. Currently, the market of

manufactured NMs has reached a global value of €20 billion per year, with an estimated increase of 21.1% Compound Annual Growth Rate (CAGR) by 2027 [9]. NMs differ significantly from their bulk form due to their high surface area to volume ratio and possible appearance of quantum effects at the nanoscale range [8]. NMs can be divided into different groups based on their physical forms or shapes (for example carbon can exist as nanotubes, fullerenes, or graphene sheets), or on the basis of their compositions, including for example, the aforementioned carbon family materials, polymeric materials (e.g., dendrimers), metals, including silver (Ag) and copper (Cu), metal oxides, such as titanium (Ti) and titanium dioxide (TiO₂), or can be composed of numerous metals, such as quantum dots; thus providing a wide range of options for any specific application requirements [10-12].

Technological advances have exponentially boosted the profitability of nano-structured materials, leading to a new industrial revolution that offers a basis for numerous applications, opening a broad spectrum of scientific fields due to the ability to manipulate the physiochemical properties of the NMs [8, 13]. For example, by selecting a particular coating on surface of the NMs, the uptake and targeting to a specific tissue or sub-cellular site (e.g., for nanomedicine applications) can be enhanced. Similarly, changing the size and shape (e.g., spheres, cubes, rods, prisms, and stars) of NMs, optimises their properties and allows their incorporation into several consumer goods such as paints, electronics, medical devices [1, 14].

1.4 Silver Nanoparticles (AgNPs): a widely applied nanomaterial

One of the most extensively sub-group of NMs are silver nanoparticles (AgNPs), which represents particles with all three dimensions (width, length and height) less than 100 nm [7]. Silver metallic NPs have become one of the most globally used NMs due to their low cost of fabrication, manufacturing, and storage compared to other noble elements, having an estimated compound CAGR of 13% in 2021 [9, 15]. NMs display unique properties that differ from their bulk material counterpart, which can strongly change their physical, chemical, and biological characteristics due to their surface-to-volume ratio, including high surface area, nano size, molecular weight, high electrical and thermal conductivity, chemical stability, catalytic activity, and optical properties. In addition, metallic NMs can be designed in many forms, including nanospheres, nanocubes, rods, triangular and nanoplates. Their novel properties result in NMs being implemented into many consumer products, such as shampoos, plastics, food packaging, soaps, toothpastes, cosmetics, sunscreens, and anti-odour/anti-microbial textile fabrication such as sports clothing, socks and t-shirts (Figure 1.2) [16, 17].

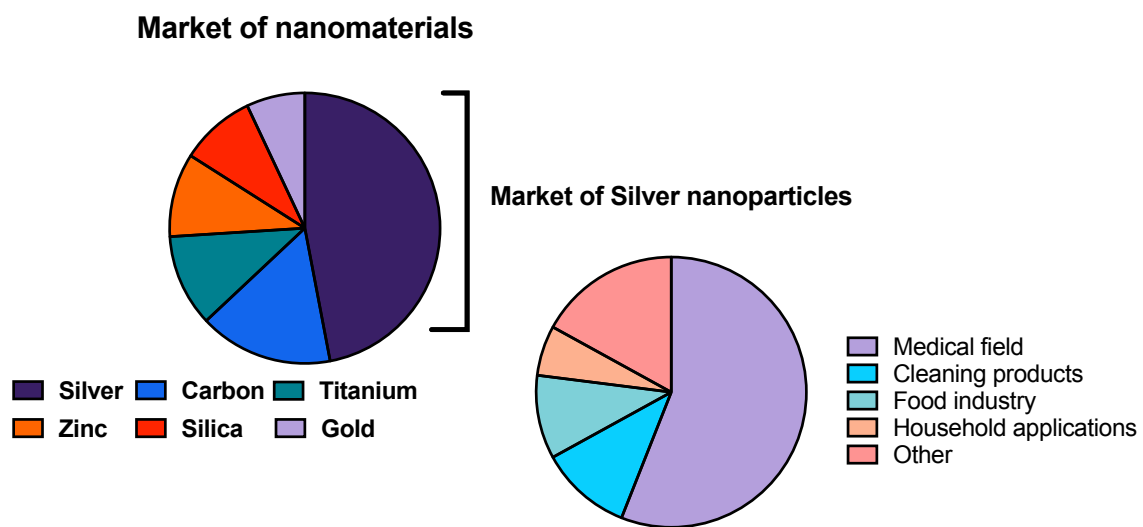


Figure 1.2. Market share of different nanomaterials and the main uses of silver nanoparticles in Europe from 2016-2020 [6, 7, 18].

The incorporation of AgNPs in many medical and other consumer products is strongly related to their antimicrobial effect against bacteria, fungi, and viruses [10, 17, 19]. The antimicrobial mechanism of action of AgNPs has been associated with the binding of silver ions (Ag^+) with the thiol group compounds in the bacteria wall and respiratory system, blocking the energy production, provoking alterations in the cell wall and nuclear damage, and eventually, leading to death [20]. Furthermore, certain interactions with the negative charge of bacterial membranes may induce electrostatic attraction between the bacteria and the AgNPs (due to the presence of carboxyl, phosphate, and amino groups on the cell wall of bacteria). These charge interactions facilitate the AgNPs attachment onto the cell membrane, inducing damage, release of internal contents, inhibition the respiration process, and bacterial death [21, 22].

It is important to note potential differences in the sensitivity of different bacteria to AgNPs. For example, the peptidoglycan cell wall thickness of Gram-positive bacteria (30 nm) has demonstrated to have lower susceptibility to the antibacterial effects of AgNPs, compared to Gram-negative bacteria (3–4 nm) [22-24]. In addition, these antibacterial properties have been recorded since ancient Greece and Rome, describing colloidal silver, as a solution with high effective “medical properties” [10]. Furthermore, silver colloid suspension was extensively used for the treatment of wounds and infections (before the use of antibiotics) in the United States around 1950s [25, 26].

1.5 AgNPs, a risk for the environment?

The incorporation of AgNPs in many day-to-day products provide numerous benefits to society [10, 14]. However, like a double edge sword, AgNPs has given rise to

environmental concerns regarding their release, transformation, and fate in the environment, especially in aquatic ecosystems [12, 14, 27, 28].

The release of AgNPs from consumer products highly depends on the source. For example, AgNPs-based fabrics are more likely to release higher amounts of nano silver in water if exposed to long immersions, different types of detergents, and even to the hardness of water [29, 30]. In this regard, the extensive use of Ag-based products such as detergents, paints, toothpaste, cosmetics, including large manufacturing industries have become a considerable source for AgNPs release into the environment [5, 19, 28]. Once released from consumer products, AgNPs are likely to reach the sewage system, and then wastewater treatment plants (WWTPs) [31, 32]. Although processes in WWTPs are efficient for removal of numerous pollutants, a fraction of certain chemicals, including AgNPs, might not be eliminated. AgNPs present in WWTPs may undergo different processes, such as partitioning, dissolution and release of silver ions (Ag^+), reduction by sulphide to produce an Ag_2S coating on the NPs, and/or still be present in nanoparticulate form, although most likely with a different surface speciation [4, 14, 31, 32]. More than an estimated >94% of silver released into the environment from industrial sites and WWTPs will remain in soils and/or as wastewater sludge [33]. However, a proportion of the silver is able to enter in the aquatic environment, being absorbed by sediments, or remaining as suspended particles and/or as complexed material, where it can be transported downstream to lakes, estuaries or even the sea [33].

The accurate quantification of the concentrations of ionic forms and AgNPs in aquatic environments is difficult and challenging, due to the dynamic behaviour of AgNPs in complex environments, the high production volumes of AgNPs-based products, and

the lack of sensitivity and specificity in methods to differentiate the particle from the ionic metal background in a complex environmental sample [4, 25]. In this regard, the use of models to predict free metal ion concentrations and metal speciation have been widely applied. For example, the Windermere Humic Aqueous model (WHAM), MINEQL and PHREEQC speciation models have shown excellent results in small-scale controlled laboratory environments, predicting free metal ion concentrations and acute metal toxicity for hazard assessments [12, 34].

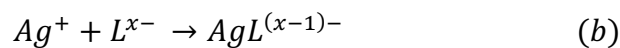
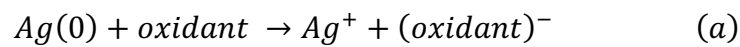
Sophisticated modelling techniques have also used to predicted (ng/L to $\mu\text{g/L}$) concentrations of NPs in the environment, and while these predictions are likely below the acute toxicity thresholds, there are concerns for chronic and sub-lethal effects of AgNPs in aquatic environment, as most of the calculated concentrations could represent insoluble silver forms such as Ag_2S , AgCl , and Ag organic colloids rather than single nanoparticulate forms [4, 25, 35-37]. For example, a study by Syafiuddin et al., (2018) estimated that the release of AgNPs from Malaysian WWTPs can range between 0.13 and 20 mg/L of total Ag [37], while another study by Kaegi et al., (2011) demonstrated that the majority of AgNPs released from WWTP were transformed (>90%) to Ag_2S NPs (within 2 hours of exposure), leading to estimated concentrations of 0.5 mg/L (total Ag) in effluents [38].

Based on these findings, the following sections are focused on the NPs behaviour and effects in aquatic environments, including changes of the physico-chemical characteristics of the NPs in natural and experimental test media.

1.6 Behaviour of AgNPs in aqueous environments

1.6.1 Oxidation and complexation

The behaviour of AgNPs in aqueous solutions will depend on the composition of the water, such as in the case of freshwater (lakes or rivers) or wastewater [39]. Environmental systems are composed of ligands, ranging from simple inorganic and organic ligands such as chloride (Cl⁻), hydroxyl ions (OH⁻), oxalic acid, and tartaric acid to chemically heterogeneous compounds such as humic substances, polysaccharides, hydrous metal oxides, and clays [40]. AgNPs are sensitive to the surrounding environment; consequently, they may undergo chemical and environmental transformations such as aggregation, and/or agglomeration, as well as oxidation from elemental Ag(0) to Ag⁺, with a possible and subsequent binding of Ag⁺ to a ligand [39, 41-43]. This is represented in the general scheme below, where the oxidant can be an oxygen or a reactive oxygen species (a), and L is a ligand forming a complex with Ag⁺ (b) [39, 44].



The oxidation of NMs made from Class b soft metal cations (e.g., Ag, Zn, and Cu) means they can form metal oxides, and due to their strong affinity to bind with electron-dense sulphur atoms, they are highly reactive with sulphur-containing biomacromolecules and other inorganic sulphur present in water, sediments, soils, and air [40, 43]. For example, Ag⁺ in solution can interact with ions and molecules present in aqueous media, including Cl⁻, S₂, organic ligands with thiol groups, and carboxylic acids (e.g., citrate and

lactate) which are widely used in AgNPs coatings [39]. Speciation in natural waters, leads to a large variety of Ag^+ complexes, including free hydrated ions, and complexes with poorly defined natural ligands, as well as Ag^+ adsorbed onto the surface of other suspended particles and colloidal Ag [40].

1.6.2 Agglomeration and dissolution

The colloidal stability of NPs is determined by interparticle and particle surface forces and the nature of media where particles may be found; in combination these properties control phenomena such as agglomeration and dissolution of the NPs [39, 45]. The agglomeration of colloidal particles occurs when the particle surfaces come into contact with each other, allowing a short-range hydrodynamic attraction and leading to their attachment [46]. In aqueous environments, the agglomeration of particles will partly depend on factors mediated by particle–particle collision frequency, Brownian motion and particle number concentration. After collision, NPs may remain as single particles, or form particle–particle, particle–cluster and cluster–cluster agglomerates [47]. Forces such as Van der Waals (vdW) and repulsive electrostatic double layer (EDL), and attractive–repulsive properties of the particles can affect the energy of the collision, and therefore the colloidal stability of the NPs. These forces have been widely described by Derjaguin, Landau, Verwey and Overbeck, and are known as the “DLVO theory”, which is applicable to NPs and to larger colloidal materials, describing the balance between van der Waals attractions and electrostatic repulsions in a liquid medium [47, 48].

In addition, the interaction of the NPs with NOM, which is influenced by the surrounding pH, salinity, and ionic strength, can also affect the colloidal stability, leading

to agglomeration (Figure 1.3). For example, agglomeration in seawater is higher than in freshwater due to high salinity, dissolved organic carbon (DOC), and the pH, which can influence the aggregation based on the surface charge of the involved particles [49, 50]. Similarly, dissolution and sulfidation processes can affect the NP surface properties, toxicity, and persistence, as coating by an insoluble metal- sulphide shell on the particle surface can induce aggregation [43].

Many metal NPs will slowly dissolve (e.g., over several hours or days) by dissolution of metal ions from the surface of the particle. Hence, dissolution of the NPs is considered a critical process that may exhibit different fate, transport characteristics and synergistic toxicity in the environment and within organisms [12, 51, 52]. The dissolution of the NPs is strongly dependent to the presence of oxygen in the environment. For example, in absence of oxygen the dissolution of AgNPs will occur at a slow rate compared to environments with a higher content of oxygen, as dissolved oxygen may turn as a potent silver oxidizing agent (e.g., in aqueous suspensions), increasing the the dissolution rate [39, 53]. For example, the presence of ligands (e.g., chloride, sulphide and organic ligands with thiol groups) can mediate the dissolution rate of AgNPs, leading to increased dissolution by the formation of Ag^+ complexes [39].

The dissolution process occurs at the surface of a particle, and thus less total surface area implies less dissolution. Other variables that influence the dissolution process are redox and pH, both of which influence dissolution rate and as a result fate, and toxicity of NPs [54]. In addition, the solubility and extent of particle dissolution are strongly related to the material, size, shape, and complexes in the surrounding

environment [41, 52]. For example, small particles may present a higher solubility and consequently major dissolution in medium compared to larger NPs sizes [55, 56].

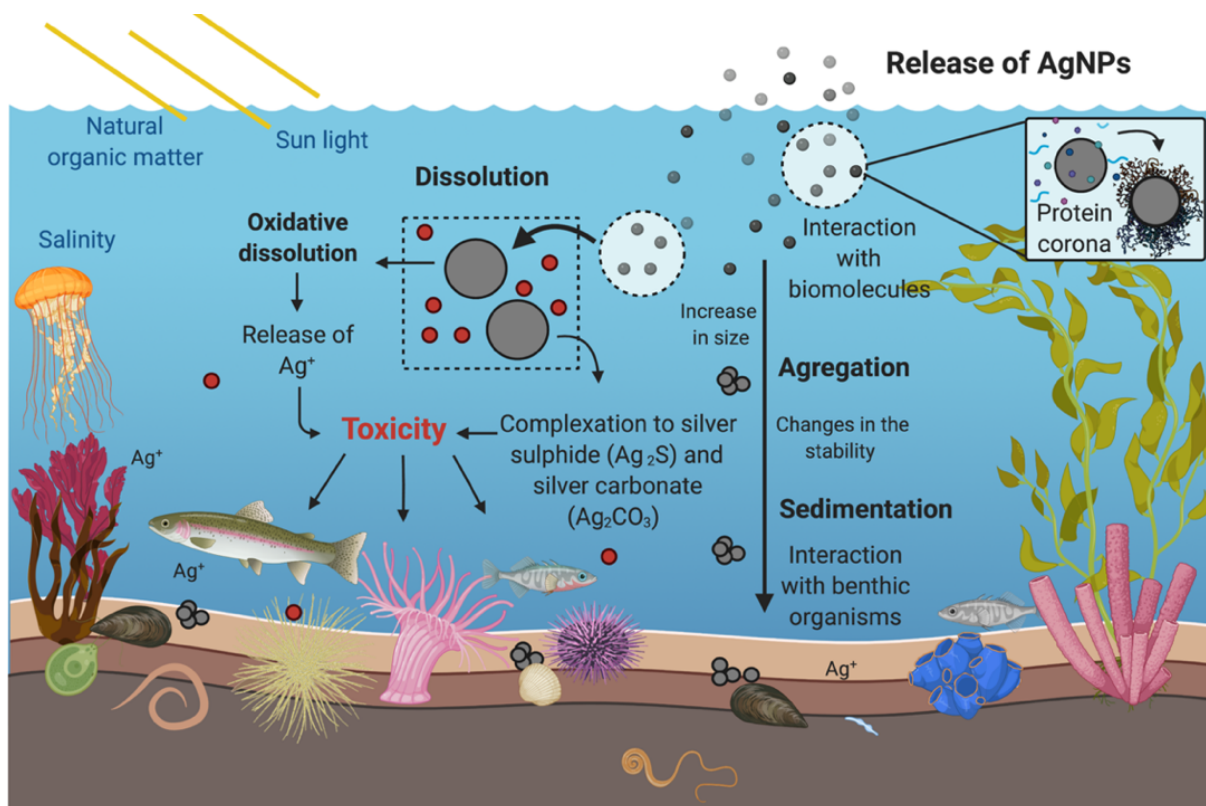


Figure 1.3. Release of AgNPs into aquatic environments, including their possible chemical and biological interactions. Figure created with Biorender Software under licence agreement.

1.7 AgNPs in experimental media

In ecotoxicology, the testing of NPs in liquids and biological solutions has been widely used to perform *in vitro* exposures and administer doses [47, 57]. In this regard, cell culture medium is highly implemented in many cell-based studies, as it supports healthy cell growth [58]. Cell medium contains proteins, ligands, inorganic salts, and other biomolecules that are vital for biological systems [58]. However, compared to natural

waters, cell culture medium contains a defined number of salts, vitamins, pH-buffering substances, foetal bovine serum (FBS), and nutrients. These compounds can affect how NPs move through the medium by diffusion, influencing the sedimentation processes of the NPs, altering their coating through corona formation, and changing their hydrodynamic diameter and density, as a result of physical and chemical transformations of the NPs (Figure 1. 4) [39, 52, 58]. For example, Leibovitz's L-15, one of the most commonly used media to culture fish cells, contains 1.26 mM of Ca^{2+} , 0.14 M of NaCl, 140-200 mM of Cl as well as millimolar concentrations of cysteine and methionine. These compounds present in the cell medium can induce agglomeration, complexation of dissolved Ag^+ to Cl, as well as lower the levels of free Ag^+ , as most of the Ag^+ will be bound to cystine and methionine [39]. In this regard, one of the most important variables in media is the Cl concentration, as the speciation of ionic silver will be dependent on this. For example, high concentrations of Cl can impose the formation of AgCl complexes, spanning both uncharged and negatively charged species [39].

In cell culture medium, the colloidal stability of the NPs and metal ions can also be affected, resulting in agglomeration, dissolution and complexation (refer to section 1.4). The kinetic dissolution and concentration of Ag^+ ions (from AgNPs dissolution) may lead to the likelihood for strong reactions with a wide range of biomacromolecules, inorganic salts, glucose, and serum in the medium, influencing the complete or partial dissolution of NPs [53, 59, 60]. The chemistry of metal ions can also be influenced by factors such as pH, ionic strength, presence of ligands that may complex free ions, and the presence of anions that can complex or form other anionic metal species, such as AgCl_2 , including other forms of Cl, OH^- and other cationic metal species (e.g., H^+ , Ca^{2+} , Mg^{2+} , and Na^+)

[12, 61]. For example, in studies by Yue et al., (2014) and Minghetti and Schirmer, (2016) the behaviour of AgNPs in rainbow trout gill cells was strongly linked to the ionic strength and chloride content of the cell medium, influencing the total silver concentration and silver speciation (mostly AgCl_2 and AgCl_3^{2-}), affecting the percentage of released Ag^+ and toxicity [58, 62].

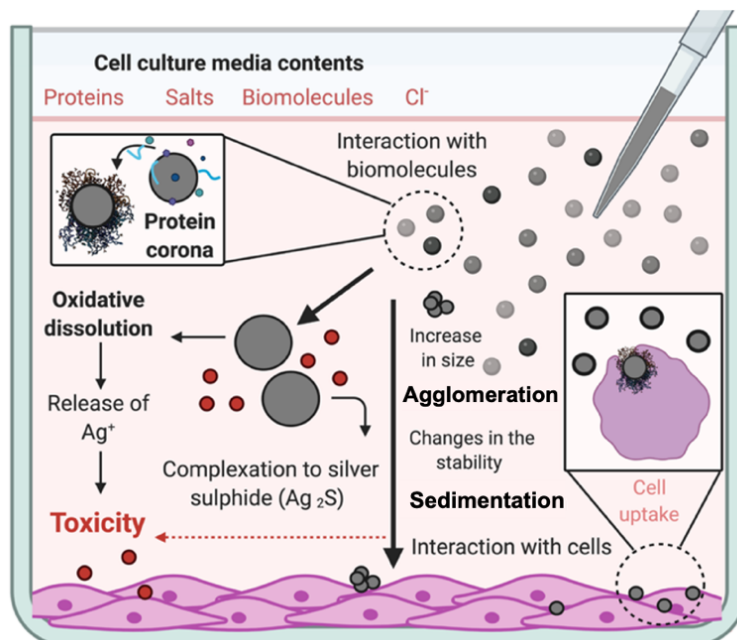


Figure 1.4. Chemical and biological interactions of AgNPs in cell culture medium and cells. Figure created with Biorender Software under licence agreement.

1.8 Toxicity of Ag⁺ and AgNPs in fish

When evaluating the potential interactions of AgNPs and ionic Ag in fish, it is important to consider the mechanisms by which electrolytes (e.g., Na⁺, Cl⁻, and Ca²⁺, toxic metal ions, and organic molecules) are internalised across epithelial cell layers, especially those that have contact with the aqueous environment [63]. For example, in gut mucosa or gill epithelium, the transport of solutes involves the movement of compounds or substances

from the external environment or body fluid into an unstirred layer (USL) formed by water and/or mucus secretions (Figure 1.5) prior to binding to membrane-spanning carrier proteins that enables the exchange of molecules with the layer covering the epithelium, while interacting with ligands in the glycocalyx [64]. Molecules can move across the cell by either diffusion or via cytosolic carries. For example, certain solutes such as Na^+ or glucose can move across the cell membrane by diffusion. On the other hand, transition metals are highly reactive with structural components in the cell, such as haem centres in proteins (which are capable of holding an iron molecule), and therefore these are moved inside the cell by specific carries (e.g., peptides) which allow controlled delivery of relevant molecules into the cells [12, 64].

The forces implicated in this process are often energy-requiring pumps (primary transport) located on the basolateral or serosal membrane, such as ATPase. The outward electrochemical gradient for other ions may depend on the solute (secondary transport). These transport systems move an unequal number of charges across the cell membrane, creating voltage differences and diffusive flux between the cell and the epithelium. This latter movement depends on the permeability of the tight junctions of the cells, whereby the contents of the medium, such as Ca^{2+} and Cl^- , can induce voltage differences via Donnan effects in the mucus layer and within the cells [12, 63, 64].

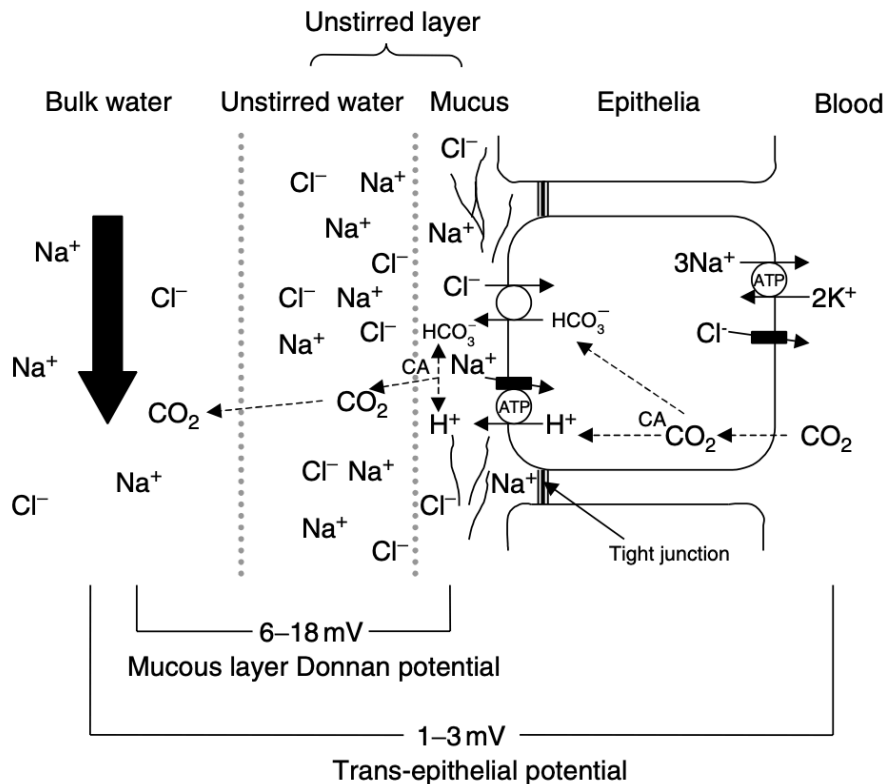


Figure 1.5. Schematic diagram to illustrate the ion-transport of sodium (Na^+) and chloride (Cl^-) in gill epithelia. The figure shows an idealised freshwater-adapted gill epithelium. The abundance of fixed negative charges (muco-proteins) in the unstirred layer may generate a Donnan potential (mucus positively charged with respect to the water) which is a major part of the net transepithelial potential (serosal positive with respect to water). The mucus also contains the protein carbonic anhydrase (CA) which facilitates dissipation of the (H^+) and (HCO_3^-) to CO_2 , thus maintaining the concentration gradients for these counter ions which partly contribute to Na^+ import (secondary transport), whilst the main driving force is derived from the electrogenic sodium pump (see the text for details). The large arrow indicates the direction of water flow. Image and text taken from reference [64].

The primary mechanism of death in fish from Ag^+ exposure has been linked to inhibition of active Na^+ and Cl^- uptake at the gill epithelium due to inhibition of the branchial enzymes involved in ion transport. The principal enzyme affected by silver is Na^+/K^+ ATPase, which is situated on the basolateral membrane of gill cells and is a molecular target for Ag^+ , competing for Na^+ , and inducing disruption of the function and

integrity of the channel. These disturbances can induce (over time) reduced Na^+ levels in the blood plasma, triggering a series of events (Figure 1.6) that will result in increased blood viscosity, arterial blood pressure, and finally cardiovascular collapse [33, 65, 66]. In addition, it has been suggested that Copper (Cu) can also interfere with Na^+ transport across epithelial cells, where Na^+ -sensitive Cu uptake is an artifact of inhibition of Na^+/K^+ -ATPase [67]. Hence, accumulation of Cu^{2+} or Ag^+ in fish gills is linked to interference with Na^+ uptake mechanisms, disrupting the ionic balance and leading to toxicity [68, 69].

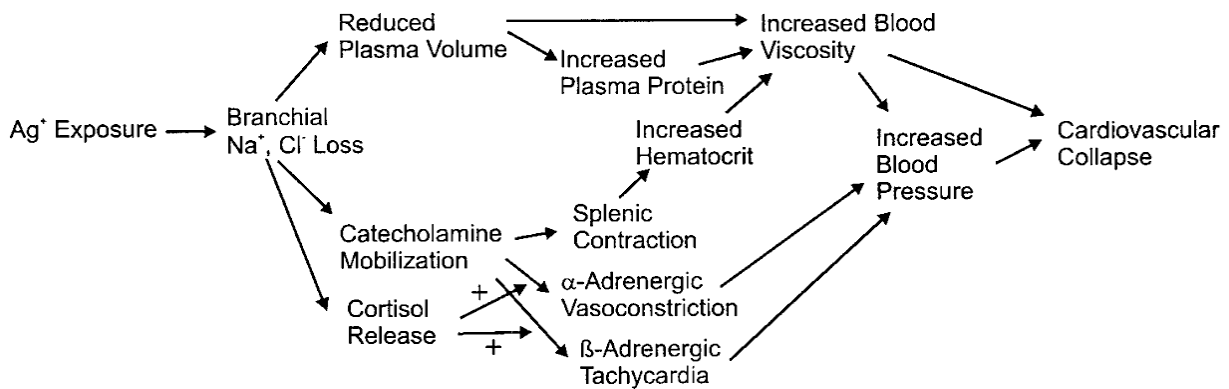


Figure 1.6. Mechanism of acute silver toxicity in freshwater fish. Toxicity is related to the blocking of ion transport through membranes in gills of fish [65].

On the other hand, the mechanisms of metal NPs toxicity in fish species are still largely unknown compared to ionic metals. Hence, the diffusional component for metal NP uptake, which is a function of both particle size and the hydrophobicity of the particle surface, needs to be considered. Besides, toxicological outcomes can be strongly influenced by the biomolecular corona, which influences NPs adhesion onto the plasma membrane (PM) (and subsequent internalisation), induced cellular physiological alterations and triggered biomolecular responses (e.g., oxidative stress, cell death) [62,

70]. The toxicity of metal NPs appears to be lower than equimolar concentrations of the metals in soluble forms; however this may not be the case for all metal NPs, where particle dissolution appeared to explain some but not all of the observed toxicity and mortality in fish [12]. For example, a study by Griffitt et al., (2009) showed that total Ag levels in gills exposed to AgNPs were higher compared to exposure to dissolved Ag, suggesting that the NPs themselves contributed to gill toxicity, not only the dissolved Ag⁺ from the NPs, as most of the soluble metal concentration was removed from the water column after 48 hours [71].

Different studies suggest that the toxicity of metallic NPs (acute lethal concentrations in mg/L) can affect fish gills in a similar way as dissolved metals. For example, through the inactivation Na⁺/K⁺-ATPase activity in the gills, whereas in erythrocytes, the acetylcholinesterase activity respiratory toxicity is affected, including disturbances to tissues and organs like intestine, gills, blood, liver and brain, and oxidative stress [12, 72, 73]. In this regard, a study by Osborne et al., (2015) demonstrated disruption of the Na⁺/K⁺ ion channel and reduction in ATPase activity by AgNPs and AgNO₃ treatments. However, higher toxicity was suggested for the 20 nm AgNPs compared to AgNO₃ and other larger NP sizes (110 nm) in zebrafish [66].

1.9 Factors that influence the transport, fate, and toxicity of AgNP

The behaviour of manufactured NPs in environmental matrices such as natural waters, involves several processes that can mediate their toxicity to biological systems. For example, the stability of the NPs in liquids is modulated by adsorption of NPs onto surfaces, such as the exterior surfaces of organisms, and by abiotic factors, and the

properties of the NPs [47]. In this regard, the unique properties of AgNPs (size, shape, surface area) and chemical composition that differ from their respective soluble metal may produce higher toxicity compared to silver ions, inducing health hazards to aquatic organisms, such as fish, which are inevitably recipients of contaminants released into the aquatic environment [4, 14, 32, 61] (See Table 1.1 for examples).

Table 1.1. Key physicochemical characteristics of AgNPs. The table shows the physicochemical characteristics that have been recognized as key elements in the transport, fate, and toxicity of AgNPs in biological systems.

Factors	NP size and coating	Concentration	Fish species	Outcomes	Reference
Capping agent or stabilizer	10 nm and 50 nm Citrate and polyvinylpyrrolidone (PVP)	82 to 85 mg/L	Japanese medaka (<i>Oryzias latipes</i>).	Significantly different toxicity between the coatings: Citrate-AgNP proved to be most toxic, while PVP and Citrate-AgNP exhibited a lower toxicity.	[74]
Size and shape	20 and 110 nm citrate-coated silver	1 mg/L	Wild-type adult zebrafish	20 nm citrate-AgNPs were more toxic than 110 nm citrate-AgNPs and AgNO ₃ . The toxicity was shown via higher Ag deposition and content in the gills and intestines of zebrafish, as well as disruption of the Na ⁺ /K ⁺ ion channel by a reduction in ATPase activity.	[66]
Surface area	5–25 nm citrate-coated silver	10, 5, 2.5, 1.25, 0.625, and 0.312 mg/L	<i>Oryzias latipes</i> juveniles	The degree of Ag ⁺ dissolution and toxicity were strongly linked to the surface area of the NPs as well as to their shape, when comparing AgNPs versus Ag-nanowires in <i>O. latipes</i> .	[75]
Charge	20 nm PVP coated	10.32 mg/L	Goodeid fish <i>Chapalichthys pardalis</i>	Positively charged AgNPs can adhere to the cell membrane, modifying its permeability and thereby penetrating the cell. Once inside, AgNPs, in the presence H ₂ O ₂ can catalyse the release of Ag ⁺ and act synergistically on thiol groups of proteins, interfering with their function and therefore inducing toxicity.	[76]
Dose and dosimetry	50, 80 and 200 nm PVP coated	50 nm (5.3 µg/cm ² , 2.7 × 10 ¹¹ ENMs/cm ²), 80 nm (5.3 µg/cm ² , 0.55 × 10 ¹¹ ENMs/cm ²) and 200 nm (10.5 µg/cm ² , 0.2 × 10 ¹¹ ENMs/cm ²)	Not applicable	Smaller NPs (50 nm) were most cytotoxic when comparing by mass concentration; however, recalculation of the results from mass to the surface area of NMs (cm ² /cm ²) and number of NMs per cm ² (NMs/cm ²) displayed a different trend, suggesting that the 200 nm size was the most mutagenic and cytotoxic.	[77].

1.10 Interactions between AgNPs and biological systems

1.10.1 Protein corona

As soon as NPs get in contact with a biological fluid, they interact with the proteins and other biomolecules, resulting in formation of a protein coating on the surface of the NPs, known as the “protein corona”, which will define a new biological identity of the particle [78-80]. The corona composition depends on the nature of the biological fluids in which NPs are exposed (such as natural waters, foetal bovine serum and/or human serum), the abundance and type of proteins, the particle type, surface properties and time of incubation; factors that may lead to different interactions with cellular receptors and thus different biological outcomes [78-81]. The relevance of eco-coronas from biomolecules such as metabolites from microorganism activity and/or NOM in natural waters is still emerging [82]. Conversely, the interaction of NPs exposed to mammalian serum or plasma has been widely explored. Protein corona studies in fish are sparse; however, protein coronas from fish or fish cells have been characterized in several fish species, including rainbow trout gill cells [83], zebrafish [84], and plasma of smallmouth bass (*Micropterus dolomieu*) [85], revealing mechanisms of intracellular toxicity (e.g., cellular stress) [82]. For example, Yue et al., (2016), demonstrated that the protein corona can provide insights into the NP processing and storage in cells, including mechanisms of metabolic stress response through the identification of specific stress-response proteins [83].

In cell culture medium, there is a larger number of proteins and ions present compared to the natural organic matter present in natural aquatic systems; hence, the formation of the protein corona in culture medium will contain free (detached) proteins that may

engage with cellular receptors enabling the particles to interact directly with the cell membrane through the protein coating. Corona-coated NPs interaction with cellular receptors can trigger a cascade of responses, influencing NPs uptake and distribution, binding of AgNPs with thiol group-containing proteins, as well as with Na⁺/K⁺-ATPase, which are susceptible to AgNP binding and functional impairment [86].

1.10.2 Cellular internalisation pathways

The internalisation of Ag⁺ in aquatic organisms (e.g., fish) is strongly linked to adsorption and metal-binding functional groups such as carboxylate, phosphate and amino groups, located on the membrane surface, which facilitate elemental internalisation (see section 1.8 for further details) [40, 64]. On the other hand, the uptake of NPs has been associated with endocytic and non-endocytic process. The uptake machinery can be generally divided in different forms of endocytosis. For example, phagocytosis is strongly related to certain cells (phagocytes), whereas pinocytosis is active in most types of cells, and it has been suggested to be responsible for NPs internalisation through endocytosis processes [70, 87-92]. Endocytosis can be generally sub-divided in clathrin and caveolae-mediated endocytosis, micropinocytosis, and clathrin and caveolae independent endocytosis (Table 1.2). In contrast to the well-known endocytosis pathways (phagocytosis and pinocytosis), autophagy is an underestimated process that may also facilitate the internalisation of NPs [93]. It has gained acceptance in recent years due to its physiological significance in engulfing and degrading particles as well as its close relation to other cellular processes, such as cell death [93].

In laboratory exposures *in vitro* (cells attached onto a surface), the internalisation of NPs will be higher compared to *in vivo* exposures due to the closer interaction between the immobilised cells and the NPs in suspension. A similar principle has been described for surface-attached microorganisms, whereby higher uptake rates of different solutes are observed due to decreases in the diffusion boundary layer thickness, and advective flow past their surface [40]. On the other hand, the internalisation of NPs by organisms present in the aquatic environment will be initially mediated by the interaction of the NPs with the external surfaces of the organism. For example, in fish the internalisation of NPs can be mediated via respiratory or dietary intake due to the NPs small size. In this regard, water drunk by the fish will deliver NPs to the gut mucosa, whereas NPs in suspension are part of the water flowing between the secondary lamellae of the gills and thus have easy access to the gill surface layers [94, 95].

NMs are likely to be adsorbed onto the gill surface, then in epithelial cells, NPs can be internalised via endocytosis (Table 1.2). The internalisation of NPs generally begins with the NPs binding to cationic sites on the plasma membrane, followed by the activation of endocytosis and signal transduction processes [96]. Then, the cell membrane produces a membrane-bound vesicle or endosomes (early and late), which is a common sorting station to transport cargo for all endocytic processes [97, 98]. The endocytic mechanisms in fish cells have been explored by just a few studies, mainly in rainbow trout gill cells, suggesting that clathrin-mediated endocytosis caveolae-mediated endocytosis and micropinocytosis pathways are active in fish cells (e.g., RTgill-W1 cells and ZF4 cells), whereas autophagy in fish cells remains misperceived [86, 99-101]. Most NP-uptake studies, in both mammals and fish cells, highlight the role of the physiochemical

properties of the NPs in the activation of different cellular uptake pathways (see Table 1.2 for examples) [97, 98].

Compared to NPs, the internalisation of Ag ions has been widely described via transmembrane transport proteins through the cell membrane. Membrane spanning proteins have ion channels in the middle, which is selective for certain molecules on the basis of charge and pore size including Na⁺, K⁺, Ca²⁺, Cu²⁺, and Cl channels, that can be closed or opened by particular proteins or amino acids on the surface of the channel [64, 102]. For example, in fish, epithelial cells are enriched with Na⁺/K⁺-ATPase or Na⁺ pumps, which establish the electrochemical gradient for Na⁺ uptake, supporting electrochemical properties and Na⁺ export back into blood [64]. Transport proteins have been linked to the efficient passage of Ag⁺ through the cell membrane, as its properties are similar to those of Na⁺ and Cu²⁺ ions [39]. Hence, both Ag⁺ and Cu²⁺ can be taken up via apical Na⁺ channels in rainbow trout fish. Cu²⁺ transporter proteins such as CTR1 have been shown to be strongly inhibited by Ag⁺ resulting in reduced Cu²⁺ uptake, due to high affinity of Ag⁺ for the Cu²⁺ transporter protein. If the affinity of the Ag⁺ ions for the transporter protein is less than that of Cu²⁺, Ag does not inhibit Cu²⁺ transport, but in this case Cu²⁺ is mediated via DMT1 rather than Ctr1 [39, 69, 102].

Table 1.2. Endocytic and non-endocytic uptake pathways in cells.

Pathway	Size of the vesicle	Description of the process	Examples in fish cells
Phagocytosis	>0.5 µm	Phagocytosis is a process where cells (mainly macrophages or dendritic cells) engulf particulate matter such as bacteria, cell debris, or even intact cells to digest them [97, 103, 104].	The uptake of 50 nm polystyrene NPs was related to phagocytosis in embryonic zebrafish cells (ZF4) [101].
Clathrin	60–200 nm	Molecules such as NPs, interact with clathrin-1 protein receptors on the cytomembrane to form endocytic vesicles, such as early endosomes, which are the first endocytic compartment to accept the incoming cargo internalized from the cell membrane, causing the vesicles to wrap and internalise the cargo as clathrin-coated vesicles (CCV) [92, 104, 105].	3–9 nm polyacrylic acid NPs were taken up by Rtgill-W1 cells via clathrin-coated pits [99].
Caveolae	50–60 nm	The binding between receptors on the plasma membrane and NPs induces the formation of the flask-shaped vesicles (endosomes), that detach from the membrane to traffic the cargo within the cell. The process involves the formation of smaller vesicles called caveolae, closely related to the integral membrane proteins (caveolin)[92, 105].	30-100 nm TiO ₂ NPs uptake by RT Liver-W1 cells was mediated via caveolae- endocytosis [100].
Macropinocytosis	>150 nm	Induces the internalisation of nonspecific cargo through the formation of large vesicles with significant amounts of fluid. This pathway starts with external stimulation to induce the activation of the receptor tyrosine kinases, which mediates a signalling cascade to induce the formation of the macropinosomes [105, 106]. In cells, the macropinosomes return to the cell membrane to release their contents to the extracellular space, making this process dependant on the type of cell [106].	The internalisation of 50 nm polystyrene NPs was mainly by clatrin-mediated endocytosis in ZF4 cells [101].
Non endocytic pathway			
Autophagy	140 to 500 nm	Autophagy is a self-degradative process linked to maintenance of primary biological activities during cellular stress (e.g., in the absence of nutrients) by removal of impaired proteins, damaged organelles, and other external molecules. The transport of the intracellular cargo is mediated by double-membrane vesicles called autophagosomes, which mature after fusion with the lysosome, promoting self-degradation of the transported cargo in the autophagosomal compartments by lysosomal acid proteases [93]	100 nm AgNPs and 50 nm CuNPs induced lysosomal autophagy to remove foreign matter and damaged organelles in rainbow trout hepatocytes [107].

1.11 Cellular and toxicological effects of NPs

The toxicological effects of NPs and transition metals in fish will partly depend on the absorption onto a sensitive site on the cell surface, inducing toxicity via membrane disruption. In this regard, the potential for negative outcomes can be related to the activation and/or inactivation of biochemical pathways dependent on specific enzymes and proteins, repair mechanisms and/or cell death [108].

The following section will illustrate principles and provide examples of AgNPs toxicity on eukaryote cells, paying detailed attention to fish and fish cells processes.

1.11.1 Membrane disruption and adaptative responses

The plasma membrane (PM) is the first cellular entity that directly interacts with exogenous NMs, becoming a key point in triggering any possible negative effect in the biological system [109, 110]. For example, in fish cells, cell transmembrane proteins, that regulate the transport of cationic electrolytes across the plasma membrane, including Na^+/K^+ -ATPase, are likely to be disrupted by Ag^+ as mentioned in section 1.6. Here, Ag^+ exposures can induce branchial Na^+ and Cl^- loss, triggering reduced plasma volume, increase blood viscosity, and finally cardiovascular collapse and death (see Figure 1.6 for more examples) [67, 68, 86]. Conversely, the internalisation of NPs is unlikely to occur via ion transporters due to their larger size [40, 61]. During NP interaction with cells, proteins in the cell culture medium are prone to bind with NPs, influencing how the cell recognises the newly protein-coated NPs, as the properties (conformation) and functions of proteins can change compared to unbound proteins [57, 86, 111].

Several intracellular biochemical responses, such as oxidative stress, organelle disruption, and cell death have been strongly linked to the physicochemical properties of the NPs, including differences in toxicity related to their size, charge, and dissolved Ag ion fraction [112-115]. It has been demonstrated that metal NPs and Ag ions are capable of reducing metabolic activity and disrupting plasma membrane and lysosomal integrity, affecting normal cellular function and homeostasis [86, 116]. Disruption of the plasma membrane is strongly linked to the induction of apoptotic cell death, mainly through the activation of death receptors such as TNFR1, Fas, DR5 and DR6 (located on the cell surface), that bind to specific ligands including NF, Fas ligand (FasL) and TRAIL to transmit signals that induce cell death [117].

In fish, another important process that occurs on the membranes is the active transport of ions such as Na^+ , Cl^- , and Ca^{2+} from the gills into their bodies against large electrochemical gradients, which control the permeability of cell membranes to other ions and to water for physiological processes [118, 119]. For example, the uptake of Ca^{2+} is predominantly via the gills and requires a transcellular movement of Ca^{2+} over the apical membrane into the cell. Then, Ca^{2+} that has entered the cell is extruded by energized Ca^{2+} pumps in the basolateral domain of the plasma membrane. For example, in gill cells, the uptake of Ca^{2+} is linked to the Na^+/K^+ -ATPase activity on the basolateral plasma membranes, which can also maintain an inward sodium gradient as the driving force in the extrusion of $\text{Na}^+/\text{Ca}^{2+}$ exchanger [120, 121].

The effects of calcium on the uptake of different transition metals (e.g., Cd, Zn and Co) by fish has been previously reported, suggesting a correlation between divalent metal ions and Ca^{2+} changes due to the ion and water permeability of membranes, the

transmembrane potential of the gills, and competition with transition metals for the same uptake site on the cell membrane [118, 122, 123]. The perturbation of Ca^{2+} by transition metals is linked to their uptake via the Ca^{2+} channel, resulting in interference with the basolateral membrane Ca^{2+} extrusion channel [124]. In addition, it has been demonstrated that the transport and internal regulation of Ca^{2+} in fish may not be affected by Ag ions [125]. However, other authors suggest that Ag, which inhibits Na^+ transport, may share the apical Na^+ uptake pathway in freshwater fish gills, and by analogy with other metals, inhibit Ca^{2+} transport and Ca^{2+} uptake process [126, 127].

The branchial uptake of calcium has specific features that may differ from other organisms; however, disturbances in the Ca^{2+} homeostasis have been related to disruption of the PM, as well as with other cellular physiological and pathological responses in both human and fish cells. For example, organelles such as Golgi apparatus and endoplasmic reticulum (ER) can participate in the regulation, storage, and release of Ca^{2+} in human and fish hepatocytes, where their disruption has been linked to toxicity outcomes [128-130]. For example, polystyrene and silica NPs have been reported to release Ca^{2+} from intracellular stores, where increases in the intracellular levels and cytotoxicity after 24 hours was linked to the type of membrane damage [131].

The disruption of Ca^{2+} can result in damage to the mitochondria and cytoskeleton due to the activation of endonucleases, proteases, and phospholipases, intensifying the cell and mitochondrial membrane damage, leading to the formation of inner membrane pores and mitochondrial permeability [132, 133].

1.11.2 Mitochondrial dysfunction

The mitochondria provide the majority of the energy required for cellular functions and works as a barrier to maintain calcium levels inside the cell. Disruptions in the Ca^{2+} homeostasis may induce outer mitochondrial membrane permeability, affecting the membrane ATPase ion pump as well as the extracellular Ca^{2+} balance, significantly increasing mitochondrial reactive oxygen species (ROS) production due to high concentrations of the Bcl2 family of proteins [133-135].

The overproduction of highly reactive hydroxyl radicals can lead to impairment or defective mitochondrial complexes I and/or III functioning, resulting in increased electron reduction of oxygen to superoxide, and damage to macromolecules inside the mitochondria, such as lipids, proteins, and DNA [136]. In addition, permeability and loss of the MM potential have been associated with the release of apoptogenic proteins from the mitochondria, such as cytochrome *c* oxidase into the cytosol from the IMM triggers the activation of the apoptosome complex via caspase 9, a prolific initiator caspase that targets and activates caspase 3, which are considered to be the point of no return in the apoptotic signalling cascade, provoking cellular death [135, 137, 138]. The role of the mitochondria, and disturbances by Ag^+ exposure, has been widely explored in mammalian and fish cells, highlighting the toxicity of both forms of silver and the accumulation of AgNPs inside the nucleoli and mitochondria with possible long-term effects [113].

1.11.3 Oxidative stress

ROS can be produced in different cellular systems such as on the plasma membrane, in the cytosol, peroxisomes, and the ER [139, 140]. Cellular processes such as protein phosphorylation, activation of transcriptional factors, apoptosis, and cellular differentiation may lead to leakage of electrons from the respiratory chain complexes, triggering a low percentage of oxygen reduction, which results in the formation of superoxide anion radicals that are kept inside the cell at low levels (passive ROS function) to maintain cellular homeostasis [139, 141, 142]. The overproduction of free radicals and oxidants by organisms in response to AgNPs and ionic Ag⁺ exposures is associated to oxidative stress due to impairment of the cell's antioxidant defence system (e.g., superoxide dismutase (SOD), glutathione peroxidase (GPx), and catalase (CAT), affecting the ability of the biological system to remove these reactive products [140]. Induction of ROS in fish cells (ZF4 and ZFL) has been linked to the activation of Nrf2, regulating the cellular defence against oxidative stress and for which correlation has been achieved with classical toxicological endpoints using *in vivo* exposures [143, 144].

The effects of ionic Ag⁺ on the cell antioxidant defence system have been widely documented in fish, demonstrating that disruption of Na⁺, K⁺, and H⁺ homeostasis can lead to oxidative stress. Similar findings have been associated with exposure to AgNPs and their dissolved metal ions [145, 146]. Besides, oxidative stress has been reported to induce damage in the mitochondria and DNA, disturbances in the synthesis of ATP, proteins, lipids, Ca²⁺ imbalance, and cell death via apoptosis [141, 142, 147, 148].

1.11.4 DNA damage and repair mechanisms

DNA is a complex molecular structure composed of two chains that coil around each other to form a double helix with complementary sequences of nucleic bases. The phosphate groups are located on the outside and the base pairs are linked by hydrogen bonding in the interior. The four nucleotides are composed of the bases adenine (A), guanine (G), thymine (T) and cytosine (C) and a sugar-phosphate group [149]. DNA is highly susceptible to structural modifications by different stimuli, which can result in severe aberrations and disadvantageous mutations [150, 151]. For example, positively charged metal ions can interact directly or indirectly with sites characterized by high electron density or negatively charged residues of DNA. Target-sites on DNA for cationic metal ion binding could be the negatively charged phosphates of the backbone of both strands and/or the electron donor atoms of the bases, such as N and O. The predominant mode of metal binding can take place at the N7 and O6 of guanine and N7 and N1 of adenine bases and the N3 of pyrimidines [149, 152].

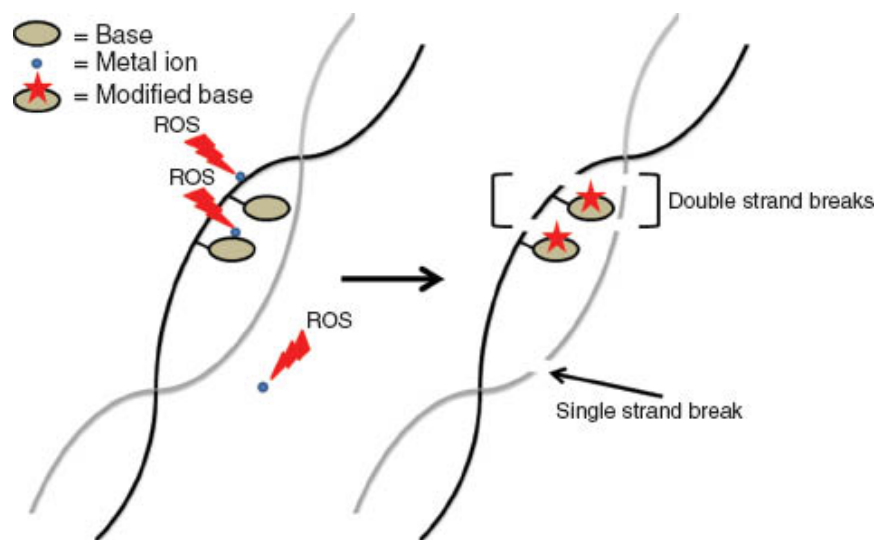


Figure 1.7. DNA damage and ROS formation. The illustration shows ROS formation and oxidative DNA damage from metal ions free in solution and metal ions bound to the phosphate backbone and individual bases [152].

The DNA-metal ion binding can induce the formation of single-strand breaks (SSBs), which arise when one of the two strands of the DNA duplex are damaged. Similarly, double-strand breaks (DSBs) arise when both of the DNA strands are severely damaged, inducing a crucial downstream triggering of apoptosis to prevent replication of the damaged DNA and thus to maintain the genomic stability [153-155]. For example, 8-OH-dG is an accepted, site-specific oxidative DNA damage marker (closely related to DSBs) that is produced by ROS generated from metal ions bound at, or near, the G base. In addition, the toxicity of AgNPs has been linked to the ability of dissolved metal ions to bind to specific DNA sites, inducing SSBs and DSBs [156].

The assessment of DNA breaks in mammalian cells has been extensively described, whereas for fish cells slight modifications have been applied to the most commonly used protocols (e.g., Alkaline comet assay) [157]. For fish, it has been suggested that the formation of DNA lesions can be modulated by seasonal variables in aquatic ecosystems, namely those related to variations in lipid content, biotransformation activity and/or spawning cycles [158]. To exemplify this, a study by George et al., (2014) demonstrated that zebrafish cells and embryos exposed to AgNPs under simulated solar light exposure conditions can induce higher physicochemical transformation of AgNPs leading to oxidative stress-dependent cytotoxicity compared to AgNP treatments under dark conditions [159].

1.11.4.1 DNA repair mechanisms: cell cycle

The DNA damage response pathway involves a variety of intracellular processes following detection of DNA damage; first the cell activates signalling cascades which are active through the different stages of the cell cycle, allowing the cell to first attempt repair the DNA damage, including, protein modifications such as mis-regulation of cyclin-dependent kinases (CDKs), activation of cell cycle checkpoints and cell cycle transcriptional responses to overcome the damage, and where repair is not possible, activation of cell death pathways [150, 160].

Zebrafish, like mammals, have many genes involved in DNA repair, including, base excision repair (BER), incompatibility DNA (MMR), nucleotide excision repair (NER) and direct reversion (DR) different transcripts, [161]. In addition, other important genes have been described in fish exposed to metallic NPs (e.g., AuNPs), including Fanconi anemia group F protein (FANCF), which is an essential component of a nuclear core complex that protects the genome against chromosomal aberrations, mismatch repair protein (Msh6) supporting the proper repair of DNA, and upregulation of genes (gaad and rad 51) that are key for repairing damaged DNA [162]. A study in zebrafish exposed to 0.25 µg/L of 14 nm AuNP-citrate over 20 days demonstrated the activation of FANCF as a response to damage, to help maintain the genetic integrity and cell survival. FANCG and Msh6 have been found expressed in fish after exposure to NPs, suggesting their ability to induce DNA repair proteins that may operate in post-replication repair or have a cell cycle checkpoint function [163, 164].

In general terms, DNA repair mechanisms involve complex process with regulatory proteins such as CDKs, which lead to mitosis and culminate in the division of two daughter cells (see Figure 1.7 for the cellular phases) [160]. Once the DNA damage has been repaired, the DNA damage checkpoint in the cell cycle is deactivated (checkpoint recovery), and finally the cell resumes the cycle progression by leaving the cell cycle arrest phase [150, 153]. However, when the DNA repair mechanisms are unsuccessful due to irreparable DNA damage, such as DSBs, the cell undergoes apoptosis by the activation of pro-apoptotic factors such as the caspase-3 and p53 proteins, culminating in programmed cell death [148, 153, 160]. For example, a study in a Bluegill fry (*Lepomis macrochirus*) cell line (BF-2) and zebrafish embryos demonstrated that exposure to metal NPs such as Ag and TiO₂ can result in a significant increase in the nuclear area leading to cell cycle arrest. In this study, enhanced effects of AgNPs were linked to surface oxidation and physicochemical modification of AgNPs and shedding of Ag⁺, leading to an increased bioavailability of ionic silver [159]. The resulting genomic alterations may be caused by the direct action of AuNP (or Ag⁺ ions) through their binding to DNA or indirectly, through the generation of oxidative stress that can lead to DNA strand breaks, as discussed in section 1.11.4 [164].

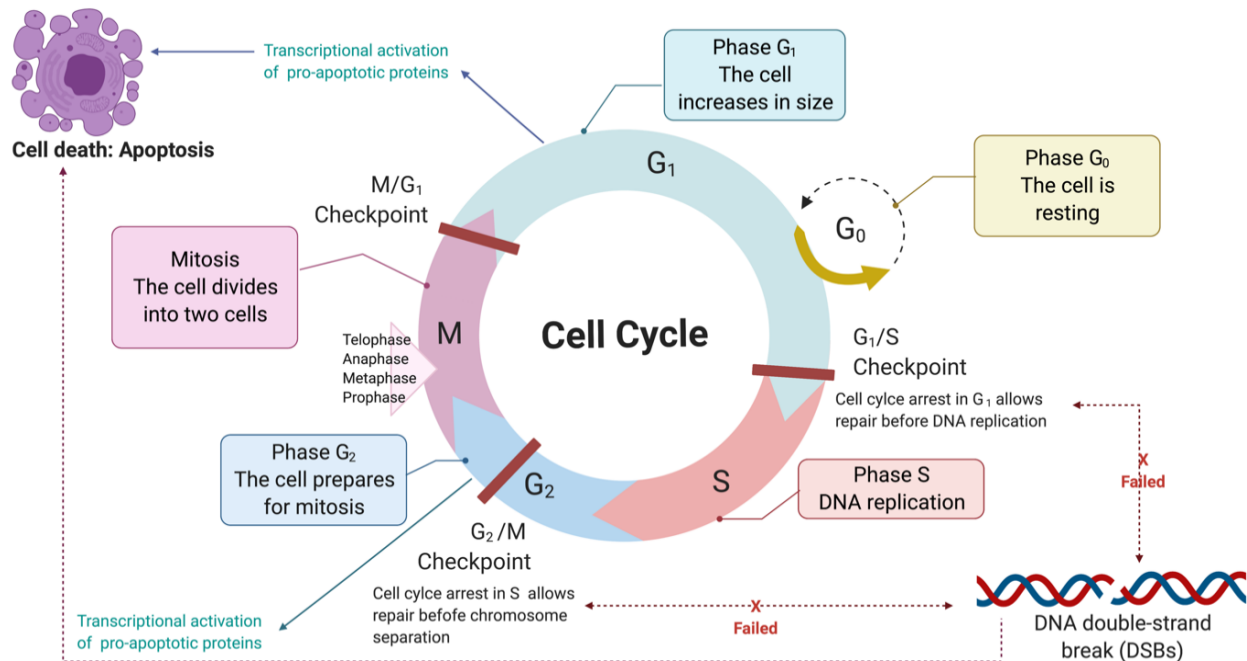


Figure 1.8. Cell cycle phases and responses to overcome cellular damage. Phase G₀, when the cell is resting. This stage can also be induced by cellular starvation; phase G₁, where the cell grows and prepares for DNA replication; phase S, wherein the cell copies all the DNA and begins the synthesis; phase G₂, in which the cell prepares to divide by organizing and condensing all the genetic material, and finally phase M (mitosis), whereby the cell finally divides into two daughter cells [153, 160]. Figure created with Biorender Software under licence agreement.

1.11.5 Cell death mechanisms

Cell death is a critical process that maintains cellular homeostasis by eliminating damaged cells as part of a natural process, such as the replacement of old cells by new ones as following irreparable cellular damage [165, 166]. There are three major types of morphologically distinct cell death, including apoptosis known as type I, autophagic cell death or type II, and necrosis or type III cell death (Figure 1.8). The three cell death mechanisms can result in overlapping and sharing of signalling pathways, which can be triggered in response to specific stimuli [167].

The following section further discusses each mechanism, highlighting the communal signalling pathways with other cellular processes and other cell death types.

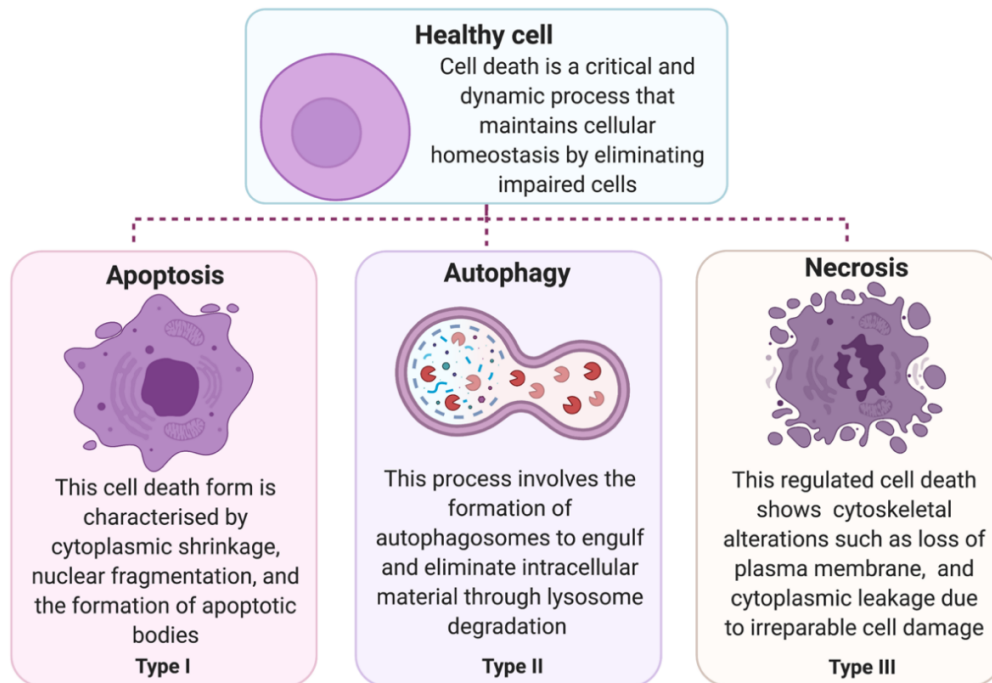


Figure 1.9. Types of cell death and their key features. Figure created with Biorender Software under licence agreement.

1.11.5.1 Apoptosis

Apoptosis, or programmed cell death, is a natural mechanism for physiological cell deletion characterised by cytoplasmic shrinkage, nuclear fragmentation, the formation of apoptotic bodies, and activation of caspase proteases such as caspase-3, caspase-6, and caspase-7 [166, 167]. Apoptosis can be triggered by two major signalling pathways: the mitochondrial or intrinsic pathway and the death receptor or extrinsic pathway [166]. The intrinsic pathway is linked to mitochondrial outer membrane permeabilization (MOMP) and is initiated by pro-apoptotic and anti-apoptotic members of the B-cell

lymphoma 2 (Bcl-2) family, as a result of the leakage of internal mitochondrial apoptogenic factors from the mitochondrial intermembrane space into the cytosol, such as cytochrome c, Smac/DIABLO and Omi, triggering apoptosis [166, 168, 169]. In this regard, the zebrafish genome contains homologs of most mammalian Bcl-2 family members, including mitochondrial permeability transition pore and MOMP responses, which are also part of the apoptotic machinery of fish, like in mammals [117, 170]. Fish stress signalling responses have been related to cytochrome c release and caspase-3 activation, which are also linked to DNA damage, ROS overload, and ER stress [166, 167, 171]. Interestingly, studies in fish have demonstrated that increasing concentrations of NMs can lead to different cytotoxic and clastogenic effects, triggering the induction of different genes being upregulated [164, 172]. For example, a study by Teles, et al., (2019) in zebrafish recorded the induction of apoptosis-related genes, such as perforin 1, a gene encoding for proteins that promote cytolysis and apoptosis of target cells by facilitating the uptake of cytotoxic granzymes, after exposure to low concentrations (0.5 µg/L for 24 hours) of AuNPs. By contrast, for the highest AuNP concentration (50 µg/L, 24 hours), upregulation of genes linked to autophagy and endoplasmic reticulum stress (e.g., HSPC171 and HSC70 proteins), together with a downregulation of apoptosis-related genes (e.g., programmed cell death 7) was observed [164].

On the other hand, the extrinsic pathway begins outside a cell as a response to the extracellular environment. This pathway involves transmembrane receptor-mediated interactions that are driven by plasma membrane receptors. Their activation depends on the binding of the ligands to the surface death receptor of a tumour necrosis factor (TNF)

receptor gene, such as TNFR1, Fas, DR3, DR4, DR5 and DR6, leading to apoptosis, inflammatory responses, and/or necrotic cell death [166, 167].

In fish, core parts of the apoptotic machinery are expressed identically as in mammalian models. For example, apoptosis was mediated by caspase 2, 3, 6, 7, 8, 9, and 10 in rainbow trout, with caspase 6 being highlighted as playing an immunoregulatory role in apoptosis in fish immune responses [170]. However, some differences between fish and mammalian apoptosis pathways have been demonstrated, including the fact that the extrinsic and intrinsic pathways of apoptosis occur despite the lack of a C-terminal region in the Fas-associated protein with a death domain in fish. The importance of apoptosis in fish has been explored, demonstrating that apoptosis may play an important role in different biological process, including in the fish life cycle [170, 171, 173]. For example, a study by Maeno et al., (2000) suggested that cell shrinkage and apoptosis are induced by activation of ionic processes involving K^+ and Cl^- channels [171].

1.11.5.2 Autophagy

Autophagy, like apoptosis, is a cytoprotective and controlled process which involves the formation of autophagosomes to engulf and eliminate intracellular material, such as proteins, damaged organelles, and endogenous substrates (xenophagy) through lysosomes degradation [168, 174, 175]. The induction of autophagy machinery requires the expression of Atg1/Unc-51-like kinase (ULK) complex and vacuolar protein sorting-34 (VPS34/PI3K-C3), which transduce the signals to begin with membrane isolation leading to autophagosome formation. Then, the autophagosome fuses with the lysosome, forming an autolysosome for degradation and recycling of cellular components [176, 177].

As a stress response, autophagy can be described as an attempt by dying cells to overcome cell death by recycling essential cellular components to maintain the functions for cell survival during starvation periods [167, 178]. For example, the effects of starvation on fish tissues and muscle and hepatic enzymes have shown the induction of proteolytic enzyme activities, including breaking down cell components for energy consumption, demonstrating that autophagy under starvation and stress conditions is induced by the PI3KC3 pathway, including post-translational modifications that produced two distinct forms of MAP1-LC3B, which are a cytosolic and a membrane-bound form [179]. In fish cells, autophagy needs to be further explored, especially the role of complementary autophagic routes that involve the direct delivery of cytosolic proteins targeted for degradation to the lysosomes. For example, LAMP2A's role in chaperone-mediated autophagy (CMA), has been described in several fish species, suggesting that CMA appeared much earlier during fish evolution than previously believed, and therefore is potentially also present in embryo cells, highlighting the homology between fish and mammalian species [180].

The role of autophagy in cell death has been recently investigated in mammalian cells, mainly due to their role in many human diseases, including neurodegenerative or infectious diseases, and several cancers, suggesting a potential link between autophagy and cell death due to the activation of apoptosis and necrosis signalling proteins [177, 181]. In fish, autophagy has been mainly described as an important adaptive mechanism for protein degradation that allows them to survive nutritional starvation [179].

The relationship between autophagy and cell death remains unclear; however, autophagic cell death has been related to the autophagic flux and lysosome function by

Bax or Bak activation [182], caspase-8 inhibition, activation of ROS [183], and hyperactivation of autophagy due to excessive consumption of impaired cytoplasmic components [184].

1.11.5.3 Necrosis

Necrosis is characterized by cytoskeletal alterations such as loss of plasma membrane integrity and cytoplasmic leakage, chromatin condensation and DNA degradation, because of irreparable cell damage [165, 166]. Necrosis is also considered as a form of cell death, involving the upregulation of various pro-inflammatory proteins and is activated by a set of signalling pathways (necroptosis) such as TNFR1, Toll-like receptors (TLRs), and caspase inhibitors that are stimulated when other types of programmed cell death have failed to repair damaged cells [165]. The toxic effects of Ag⁺ and AgNPs on fish cells has already been explored, demonstrating that exposures to AgNPs and Ag ions can induce histopathological alterations in gill tissues, including epithelial cell necrosis [185, 186]. Similarly, in embryonic fish cell lines, the NPs-released dissolved ions (Ag⁺) were able to interact with cell membranes, proteins, and DNA, leading to cell death [114].

Necrosis and apoptosis share similar signalling pathways. For example, when a ligand binds to TNFR1, the pro-survival complex I is activated, this complex activates complex II, triggering caspase-8 and resulting in apoptosis, whereas the formation of complex III results in the inhibition of caspase-8 leading to necrosis [187]. For example, hepatocytes of juvenile carps exposed to 50 nm TiO₂ NPs demonstrated a clear interrelation of apoptosis and necrosis, through cytoplasm vacuolation, and formation of necrotic cell bodies and apoptotic-like bodies [188].

Necrosis is also linked to the induction of mitochondrial permeability transition pore (MPTP), which results in ROS and intracellular calcium overload, disruption of the mitochondrial inner membrane integrity and inhibition of ATP production. In addition, it has been demonstrated that AgNPs are able to accumulate in cytoplasm and mitochondria of rainbow trout hepatocytes, inducing swollen mitochondria and dilated endoplasmic reticulum [107].

1.11.6 Representative toxicological biological models:

Zebrafish

In environmental ecotoxicity, fish are the most utilised vertebrate for environmental hazard and risk assessment, representing an indispensable component of integrated toxicity evaluation in the aquatic environment [189, 190]. Zebrafish (*Danio rerio*) has been a popular laboratory non-mammalian model for more than 20 years, especially for its ability to spawn huge amounts of eggs across the whole year, its high fecundity, rapid development, and an extensive literature base [190]. The rapid development and transparent features that embryo, juvenile larvae, and adult stages of zebrafish display during their cell division, fertilization, and final morphogenesis, makes them suitable for microscopic screening for agents that disrupt normal development [191]. Furthermore, zebrafish share around 70% similarity with human genomes, including major developmental and physiological processes, such as the digestive, nervous and cardiovascular systems, features that can potentially mimic the development of human diseases both genetically and phenotypically facilitating development of detailed understanding of the disease processes and therapeutic strategies [191-193].

Fish testing, along with other organisms, such as algae and invertebrates (e.g., *Daphnia magna*) are integral for hazard identification in environmental risk assessments. Their implementation is necessary for the prospective assessment and classification and labelling of chemicals, impact assessment of surface waters and effluents, and persistence, bioaccumulation and toxicity assessment by the Organisation for Economic Co-operation and Development (OECD) [194]. For example, the OECD Test Guideline (TG) 203 involves studies and validation activities performed in different fish species, such as Japanese medaka, fathead minnow, zebrafish, and rainbow trout [195]. Although, these protocols were originally designed for chemicals that were soluble in water and/or could put into the aqueous phase, attention has been given to assessing their suitability for hazard assessment and implementation in the nanotoxicological field [196, 197]. The handling of NMs in regulatory toxicity tests requires careful consideration regarding the exposure, and interpretation of the data when assessing the negative outcomes, paying particular attention to effects related to the shape, size, and surface charge of NMs [61, 197, 198]

The high levels of regulation that characterize the use of mammalian biological models (e.g., rabbits, rats, mice) are also extended to the zebrafish animal welfare, as the testing on whole fish involves the implementation of tight regulatory requirements, including certified training programs and accepted guidelines for zebrafish husbandry, management, and care [199]. In addition, to improve animal welfare and to minimize unnecessary testing and suffering of laboratory animals, the OECD suggests the implementation of threshold approaches and other non-animal alternatives. For example, to optimising data for development of Quantitative Structure Activity Relationships

(QSAR) methods, several specifications regarding the testing concentrations, relevance to demonstrate 0 and/or 100% mortality, guidance on employing a water control when solvents are used, the introduction of estuarine and marine fish species, as well as the recording of the clinical signs of toxicity including individual fish identification are all required. These improvements to the test guidelines have been suggested for the identification of scientifically robust humane endpoints linked to mortality and interpretation of moribundity [200].

In this current regulatory environment and to reduce the ethical issues implicated in the fish acute toxicity testing, the OCED has approved the use of zebrafish embryonic forms as an alternative for the acute fish toxicity [189]. The use of embryo for toxicity assessment has been accepted and regulated under the OECD TG 210: fish, early-life stage toxicity test (with zebrafish) [201]. Toxicity testing on fish embryos is considered as a great step towards the replacement and refinement methods to lessen animal suffering, since zebrafish embryos demand no ethical permission until 120 h postfertilization (hpf) (onset of independent feeding), and the embryos are likely to experience less suffering or pain than older life stages [190, 202]. However, the toxicity testing of zebrafish embryos is also tightly regulated, optimized and standardized by the OECD as a test to assess toxicity of embryonic forms of fish under the Fish Embryo Acute Toxicity test (FET, OECD236) and still requires breeding of fish to continuously generate the embryo for testing, and sacrifice of the fertilized embryo at 120 hpf [203]. The use of FET provides a total and well-defined developmental study at its early life stages at low cost and being less prone to legal and ethical restrictions as this earliest life-stage (up to 120 hpf) is not defined as “sufficiently aware that they will suffer” under the regulatory frameworks

dealing with animal experimentation. However, after 120 hpf, embryo become capable of independent feeding (larvae stage); therefore, a license is required to conduct any regulated procedure as they can experience pain, distress and lasting harm [190].

Another important characteristic of zebrafish embryo and which could represent a disadvantage in their toxicity testing, is their chorion. The OECD acknowledges that the chorion of the embryo, may represent an important barrier to reduce the likelihood of the certain molecules to reach the target site(s), as it physically and chemically protects and isolate the embryo from external environmental conditions until their hatching (48-72 hpf) [203]. It is important to mention that despite the large pore size on the chorion membrane (0.6-0.7 μm), it may still influence the diffusion of molecules into the embryo, as well as reducing the NP transport, subsequent biological activity, and sensitivity to toxicity testing [204-206]. In this regard, removal of the chorion by chemical methods may disrupt the embryo characteristics, inducing major sensitivity to the tested compound, inhibiting the hatching process leading to secondary morphological effects, as well as producing lower survival rate [207, 208]. Although zebrafish testing has many advantages in the toxicological field (Figure 1.9), the frequent use of acute fish testing has given rise to both economic and ethical concerns related to the animal welfare. Thus, there is an urgent need for methods that promote the acquisition of sensitive ecotoxicity data involving non-animal testing alternative strategies to screen the toxicity of chemicals; these tools are also urgently needed as an integral part of environmental hazard identification and risk assessment of the nanotoxicological field [209].

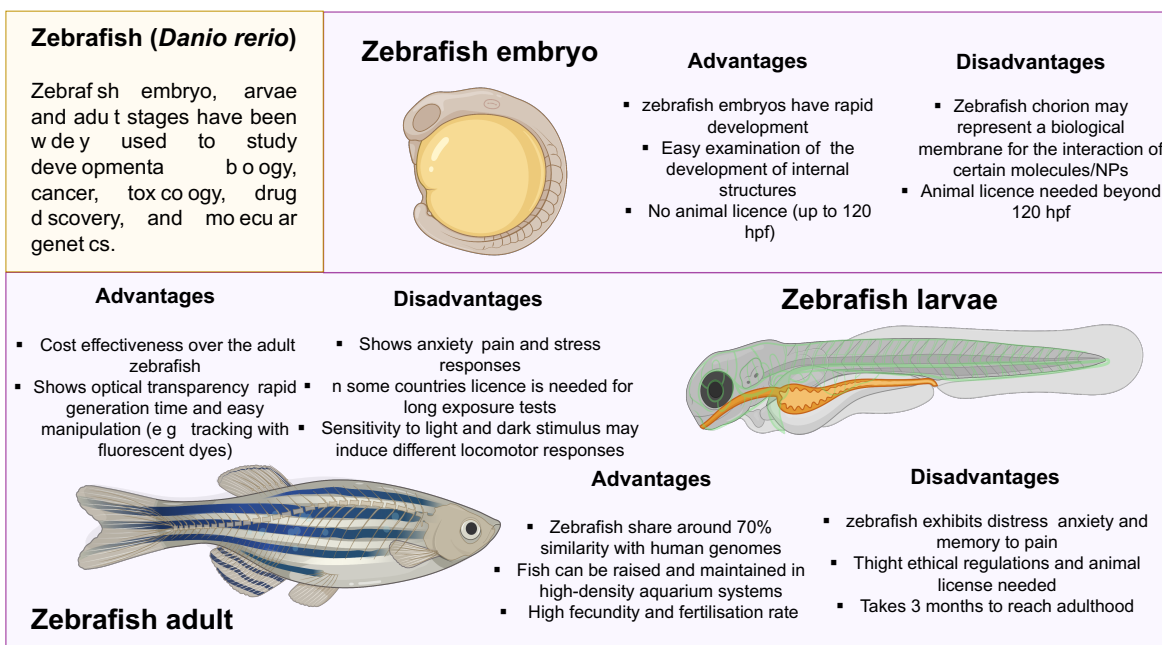


Figure 1.10. Zebrafish models, advantages, and disadvantages. Figure created with Biorender Software under licence agreement.

1.11.7 Alternative testing frameworks and strategies

The application of the 3Rs principles (replacement, refinement, and reduction) of animals in experimentation supports the reduction of animal studies with relative long duration. This is based on a framework focused on alternative and/or more advanced methods to ensure the best animal welfare for future developments in regulatory testing.

Numerous discussions are emerging on the employment of pragmatic approaches in regulatory ecotoxicology. New ethical and legislative frameworks have requested the development of a 21st century scientific approach through the re-evaluation of the use of animal toxicity tests with the utilisation of non-traditional methods to reduce the numbers of animals used in nanosafety assessment. The implementation of the 3Rs requires scientific engagement, design improvement, collaboration, and a responsive

management by the scientific community, in order to achieve a substantial decrease of the numbers of animals used in research (Figure 1.10) [210-212].

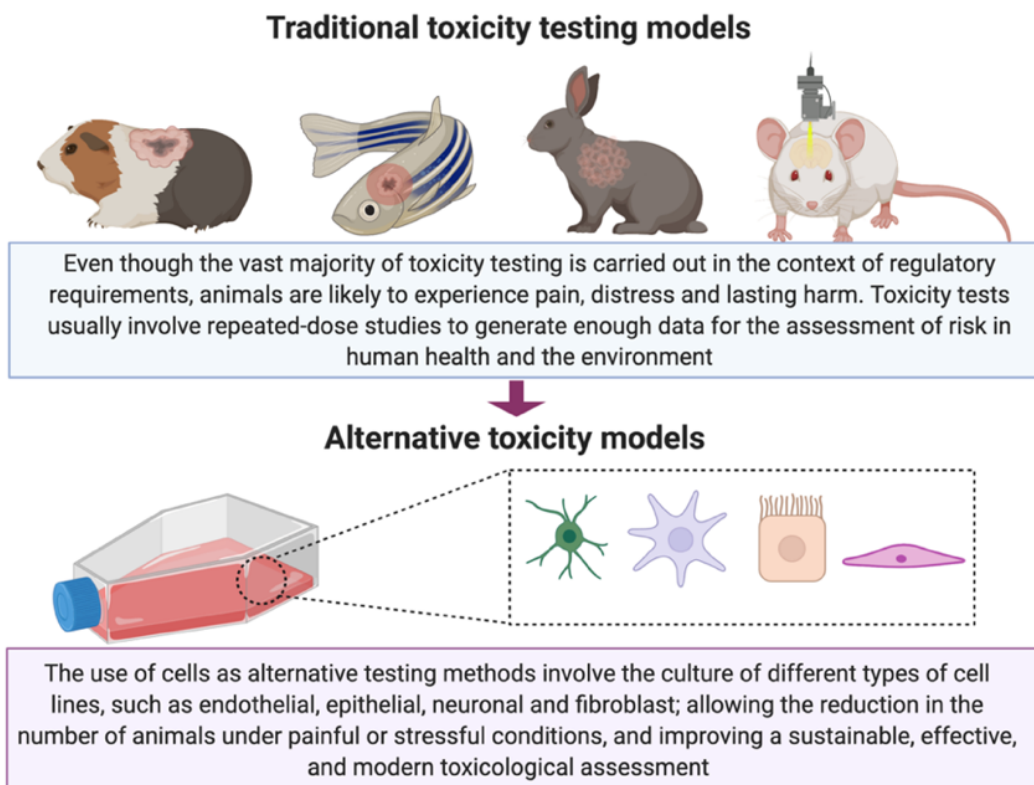


Figure 1.11. Traditional testing models vs cellular based models. Figure created with Biorender Software under licence agreement.

1.11.8 Embryonic zebrafish cells: a potential model for nanotoxicity studies

The establishment and validation of cell culture assays to reduce whole fish tests (when possible) are needed to accomplish a scientific and ethical goal in the ecotoxicological field. For example, the use fish cell cultures as an *in vitro* model have been used to support the 3Rs framework in aquatic toxicology. The first permanent fish cell line was established from the gonads of rainbow trout fish to study viruses [213]; since then, many

other fish cell lines have been recognized from a large variety of tissues and fish models, aiming to represent a wide range of marine and freshwater species [214].

Fish cells offer several scientific, technical, and ethical advantages compared to *in vivo* models. For example, fish cells represent a key level in the biological organisation of adult fish, allowing the detection and understanding of common and unique mechanisms of toxicity in specific stages of development without ethical concerns [215]. In this regard, the origin of the tissue used to establish the cell line may provide insights regarding a specific target and toxic mode action, offering different biological models to compare at the cellular level under the equivalent conditions of toxicant exposure and allowing the prediction of *in vivo* outcomes [86, 216-218]. For example, Rainbow trout gill cells (RTgill-W1) are one of the most common types of fish cell species used for *in vitro* toxicity studies, and indeed are the basis of the recently published (June 2021) OECD Test Guidance 249 on fish cell line acute toxicity [219]. AgNPs along with ionic silver are among the most popular NMs used for eco-toxicity assays due to their widespread use in consumer and medical products (see Section 1.4) followed by TiO₂ NPs. Most of the *in vitro* fish assays are recorded with a short time exposure such as acute toxicity (24 hours, as per the OECD249 test guideline), whereas for *in vivo* studies fish are regularly exposed for up to 96 hours, although mortalities can also be recorded at 24, 48, and 72 hours. Table 1.3 provides examples of studies performed utilising fish cell lines and a range of different NM compositions.

Table 1.3. NP exposure to fish cells. The table shows examples of toxicity evaluation after 24 hours in fish cells using different NMs.

Metal ion and/or NPs	Size (nm)	Concentration	Exposure duration	Fish species	Toxicity outcome	Ref.
AgNPs AgNO ₃	16 nm	8.76 µg/mL 345 µg/mL	24 hours	Hepatoma cell line (<i>Poeciliopsis lucida</i>)	AgNPs produced alterations at the lysosomal and mitochondrial levels. Ag ⁺ ions produced similar cytotoxic effects but at lower concentrations than AgNPs. Both silver forms caused oxidative disruption, but the initial response was delayed in AgNPs until 6h of exposure.	[113]
AgNPs AgNO ₃	20, 40, 100 nm	0.06, 0.25, and 0.5 mg/L	24 hours	Rainbow trout gill cells (<i>Oncorhynchus mykiss</i>)	AgNPs showed size-dependent cytotoxicity, smaller (20 nm) NPs being more toxic than larger (40 and 100 nm) NPs. Ionic Ag ⁺ showed higher cytotoxicity than the NPs including inhibition of Na ⁺ /K ⁺ -ATPase in gill cells.	[220]
AgNPs	19 nm	20 µM	24 hours	Rainbow trout gill cells (<i>Oncorhynchus mykiss</i>)	Release of stress-related proteins. Uptake of AgNPs and dissolution of the NPs (4.8-fold higher) than the initial ionic concentration. Inhibition of the Na ⁺ /K ⁺ -ATPase activity.	[83]
ZnONPs	20 and 50 nm	100 µg/mL	24 hours	Topminnow fish (<i>Poeciliopsis lucida</i>)	ZnO NP aggregates contributed substantially to the cytotoxic effects, including damage to the plasma membrane and DNA alteration.	[221]
AgNPs AgNO ₃	5 nm and 10 nm	1.9 mg/L 2.5 mg/L	24 hours	Rainbow trout hepatocytes (<i>Oncorhynchus mykiss</i>)	Toxicity in a concentration-dependent manner and higher ROS levels. Dissolved organic carbon (DOC) did not alter the particles potency of cytotoxicity or ROS induction capacity.	[116]

TiO ₂	74 nm and 185 nm	100 µg/mL	24 and 72 hours of exposure	Liver and gill cells (<i>Onchorynchus mykiss</i>)	Toxicity was initiated after NP binding to the cell surface (and then endocytosed). Interference with fluorometric assays was recorded.	[222]
AgNPs CuNPs	8 nm	1.5 mg/L 0.15 mg/L	28 days	Rainbow trout hepatocytes (<i>Oncorhynchus mykiss</i>)	Shrunken cells, nuclear necrosis, ROS, and mitochondrial damage were recorded for AgNPs. AgNPs were more toxic to rainbow trout hepatocytes compared to copper NPs.	[107]
AgNPs	18 and 29 nm	400 and 800 µg/L	24, 72, 168 hours	Liver fish cells (<i>Labeo rohita</i>)	AgNPs impacts were size and dose-dependent, inducing ROS, DNA damage and disruption of cellular responses	[223]
AgNPs	12 nm	12.5 and 25 µg/mL	24 hours	Bluegill sunfish cell line (<i>Lepomis macrochirus</i>)	Solar light induced physicochemical transformation of TiO ₂ and Ag NPs and enhanced their toxic potential	[159]
AgNPs AgNO ₃	50 nm	18 µg/mL 2 µg/mL	96 hours	Gill gill cells (<i>Catla catla</i>)	Linear correlations between each <i>in vitro</i> EC ₅₀ and the <i>in vivo</i> LC ₅₀ data were highly significant. DNA damage and nuclear fragmentation (condensation) were recorded for all treatments.	[224]
Copper oxide (Cu ₂ O) NPs	60 nm	8, 20, 40, 60, 80, 160, and 320 µg/mL	3 hours	Fish cells (<i>Carassius auratus</i>)	Dosages of Cu ₂ O NPs greater than 40 µg/mL were toxic to blood cells, inducing membrane damage.	[225]
Cobalt oxide (Co ₃ O ₄) NPs	30 and 50 nm	10 µg/mL	24 hours	Gill cells (<i>Oncorhynchus mykiss</i>)	NPs showed higher toxicity than ions. Concentrations of ions released from the NPs did not reduce cell viability, and minimally impacted ROS levels	[226]

Unlike zebrafish embryos and adult fish, zebrafish cells can be cultured with faster and efficient approach; for example, cells can be easily assessed using quantification techniques. In addition, physiological conditions, such as levels of nutrients, regulation of the matrix, and even cell substrate attachment can be easily controlled in cell culture [227, 228]. In this regard, the use of embryonic zebrafish cells (ZF4) represents a promising *in vitro* model to provide additional insights into the toxicity of NMs, opening up a new means by which to evaluate the toxicological effects and biological responses of NMs in aquatic *in vitro* models [101, 229-232].

The first ZF4 cells were established from 1-day old zebrafish embryos by Driever and Rangini in 1993, representing the earliest stage in the fish organisation, compared to other fish cell lines that were established from adult tissues [229, 233]. In addition, ZF4 cells were the first fibroblast-like zebrafish cell line that was maintained using a conventional medium supplemented with mammalian serum, which is currently a standard condition widely applied in the culture of different fish cells [233-235]. Apart from their easy proliferation using common cell culture media (supplemented with 5–10% mammalian serum), ZF4 cells can resist longer periods without medium removal, as well as showing higher resistance to environmental media with varying osmolarities [236]. ZF4 cells are commonly maintained under 5% carbon dioxide (CO₂), despite the recorded physiological effects on fish (e.g., acid-base regulation) [237]. Besides, the culture of ZF4 cells can be maintained over multiple passages as can cells from other fish and mammalian cell lines [101, 143, 202]. However, to maintain the cell line viable, lower temperatures (22-28 °C) are required to resemble the temperature of the donor habitat [215].

Fish cell models involve major control of the physicochemical and physiological environment, allowing a faster comparison of their relative sensitivity to environmental contaminants, revealing the mechanistic of sensitivity differences at the cellular and molecular level, including their perseveration for large periods [215, 228] (See Table 1.3 for examples). Fish cell lines, such as ZF4 cells are emerging as a valuable, quick, and cost-effective screening tool in the ecotoxicological assessment of NMs. For example, ZF4 cells have recently been reported as a test system for toxicity assessment of nanomaterials and nano-plastics, involving a range of NMs such as polystyrene, copper, silver, and zinc, facilitating a rapid assessment of toxicity, elucidating the NMs behaviour as well as evaluating their cellular interactions in a complex and relevant biological exposure medium (See Table 1.4) [211, 236, 238].

In addition, recent publications have suggested the use of zebrafish cells as a potential model to elucidate nano-toxicity responses [101, 143, 239]. Studies in these cells may potentially support the implementation of the Adverse Outcome Pathways (AOP) regulatory framework, potentially improving the development of more predictive and ethical regulatory toxicology, creating a wider network of scientific data-driven approaches that cover the diversity of biological and exposure contexts, redefining the safety and risk assessment of NMs (Figure 1.11) [240, 241].

Zebrafish cells: an alternative toxicological model

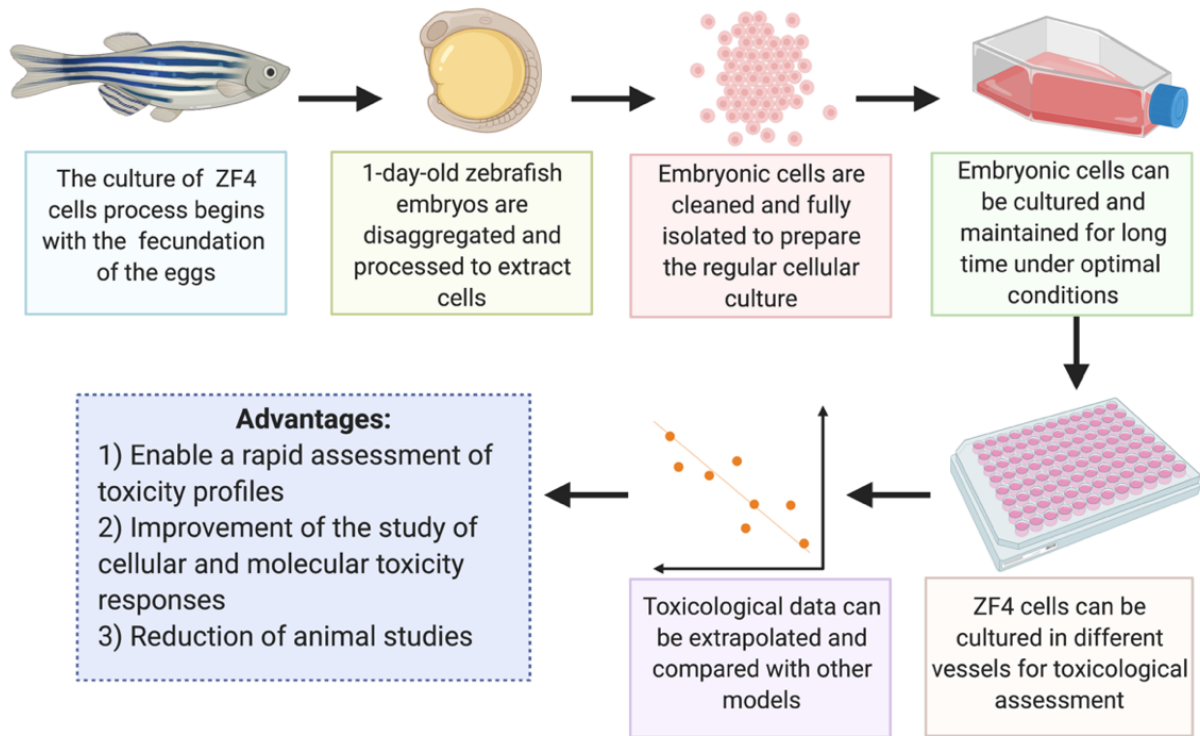


Figure 1.12. Zebrafish embryonic cells as an alternative toxicological model. Figure created with Biorender Software under licence agreement.

Table 1.4. Literature review of recent NMs-toxicity studies in embryonic zebrafish cells (ZF4). The table shows results from an online search for ZF4 cells studies using NMs.

Type of NMs	Size (nm)	Concentration	Exposure duration	Responses in ZF4 cells	Type of publication	Year	Ref.
Polystyrene (PS) NPs	50 nm and 1 μ M	10 mg/L	24 hours	Uptake was related to the size, Toxicity mediated by lysosomal alkalization and oxidative stress.	Scientific paper	2021	[101]
Cu ₂ O	130 nm and 200 nm	500 mg/L	3 hours	High bioaccumulation of Cu and lysosome-mediated exocytosis of the NPs. Induction of Glutathione and ROS mediated toxicity.	Scientific paper	2021	[242]
AgNPs AgNO ₃	53 nm	2 mg/L 1 mg/L	24 hours	Dissolution of NPs and toxicity, mitochondrial specific toxicity, including deformation, impaired respiration of mitochondria and cell death.	Scientific paper	2021	[114]
ZnO-NPs	8 to 20 nm	0.3 to 0.9 μ M	24, 48 and 72 hours	Dissolution of NPs stimulated lysosomal accumulation and ROS production. Lysosomal mediated-uptake and mitochondrial toxicity.	Scientific paper	2021	[243]
Quantum dots (QDs)	6 nm	20 mg/L	24 and 72 hours	QDs induced hypoxia and ROS generation in hepatic cells, which leads to apoptosis, specifically through the TDP-43 pathway.	Scientific paper	2020	[244]
Zinc oxide NPs (ZnO) and Zn ions	70 nm	16.3 μ g/mL 14.8 μ g/mL	24, 48, 72 and 96 hours	ZnO NPs showed less toxicity compared to Zn ions, which demonstrated disruption of the lysosomes, release of intracellular Zn ²⁺ , and cell death.	PhD thesis	2019	[245]

1.12 Thesis hypothesis and objectives of the research

I) Hypothesis

The hypothesis of this study is that exposure of ionic silver (AgNO_3) and different sizes of PVP-capped AgNPs to ZF4 cells may trigger different uptake and mechanistic pathways, leading to discernible differences in toxicity between nano Ag versus ionic Ag, revealing differences in cellular process and cell death mechanisms activated by the different Ag forms (Figure 1.13).

II) Objectives

Overall, the work described in this thesis aimed to investigate and provide an initial assessment of the biological outcomes of AgNPs compared to ionic Ag^+ in ZF4 cells as a potential novel *in vitro* model. In addition, this cell line was carefully selected as an early-stage model for zebrafish, aiming to provide scientific research and knowledge about embryonic zebrafish cells. Other specific objectives in this study were:

1. To investigate the behaviour of PVP-capped AgNPs in different testing environments, such as complete cell culture medium as a relevant biological fluid (supplemented with serum), serum-free medium and ultra-pure water.

A fundamental aspect of this goal is to explore changes in the hydrodynamic size, zeta potential, polydispersity index and dissolution of the three different AgNPs sizes and the role of medium composition in the dissolution.

2. To evaluate the internalisation and uptake pathways of ZF4 cells exposed to AgNPs, including different endocytic mechanisms induced as a response to AgNPs exposure.

This goal is focused on elucidating the internalisation mechanisms of AgNPs in ZF4 cells and investigating the different endocytic mechanisms as a response to AgNPs exposure. This is a pre-requisite for establishing dose-response relationships.

3. To explore the mechanistic responses of ZF4 cells to AgNPs, including the role of the particle size and exposure concentration on their cytotoxicity to ZF4 cells.

For this aim, a series of biological assays are performed to elucidate the dose-response and the relationship between the different molecular mechanisms of cytotoxicity and the exposure form of the Ag.

4. To demonstrate the potential use of commercial fish cells to assess the toxicity mechanisms of different sized PVP-capped AgNPs.

A fundamental part of this aim is the discussion of the biological responses of ZF4 cells compared to other cellular models, presenting an initial assessment of ZF4 cells as a potential in vitro model for NMs (and chemical) toxicity assessment.

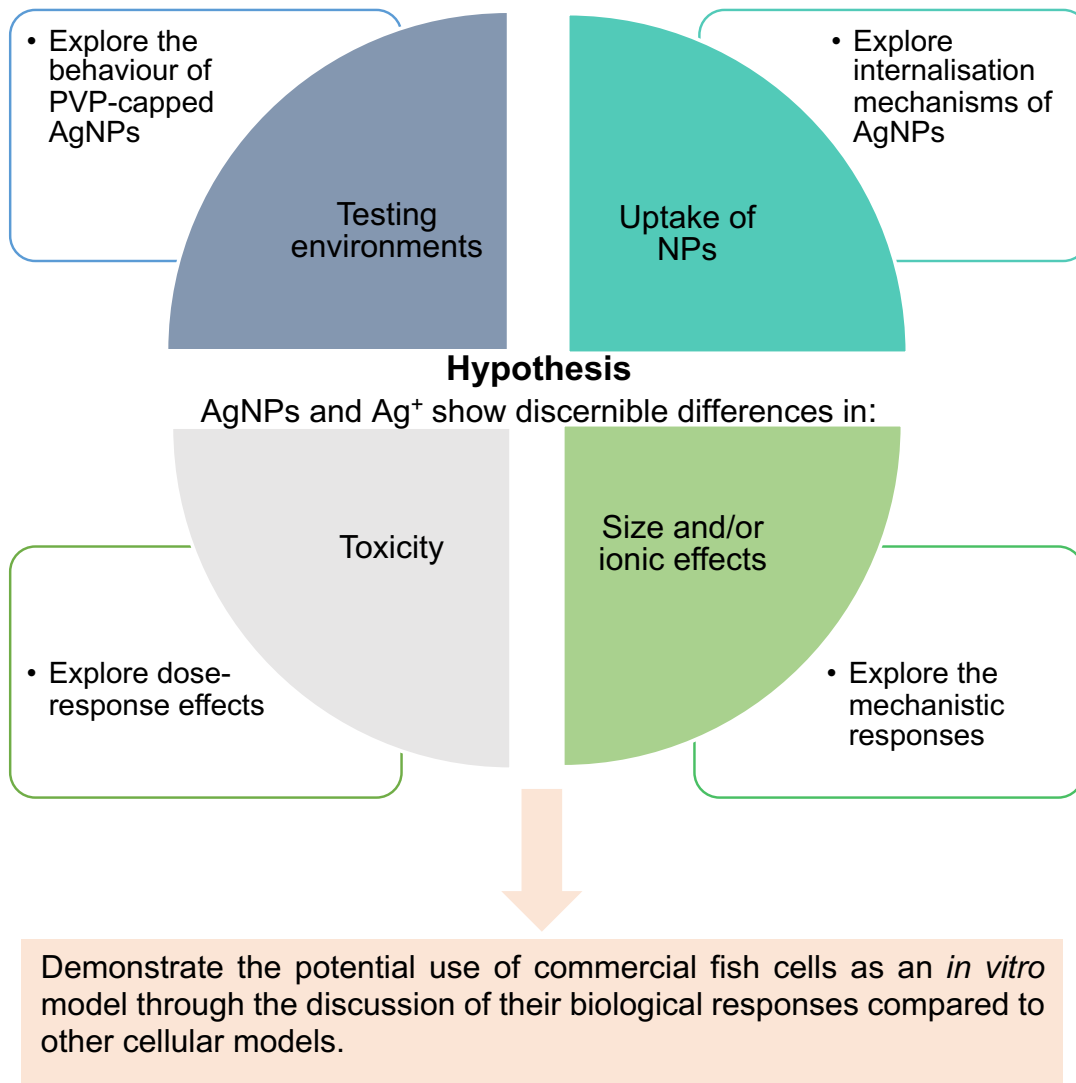


Figure 1.13. Summary of the hypothesis, goals, and overall aim of the research.

Chapter 2

Silver nanoparticle induced toxicity and cell death mechanisms in embryonic zebrafish cells

This chapter has been published in the journal Nanoscale by the Royal Society of Chemistry.

Ana C. Quevedo^a, Iseult Lynch^{a*}, Eugenia Valsami-Jones^a

^a School of Geography, Earth and Environmental Sciences, University of Birmingham, Edgbaston, Birmingham, B15 2TT, UK.

*Corresponding author: 

2.1 Abstract

Cell death is the process that regulates homeostasis and biochemical changes in healthy cells. Silver nanoparticles (AgNPs) act as powerful cell death inducers through the disruption of cellular and signalling functions. In this study, embryonic zebrafish cells (ZF4) were used as a potential early-stage aquatic model to evaluate the molecular and cell death mechanisms implicated in the toxicity of AgNPs and Ag⁺. Here, a low, medium, and high concentration (2.5, 5, and 10 µg/mL) of three different sizes of AgNPs (10, 30 and 100 nm) and ionic Ag⁺ (1, 1.5 and 2 µg/mL) were used to investigate whether the size of the nanomaterial, ionic form, and mass concentration were related to the activation of particular cell death mechanisms and/or induction of different signalling pathways.

Changes in the physicochemical properties of the AgNPs were also assessed in the presence of complex medium (cell culture) and reference testing medium (ultra-pure water). Results demonstrated that AgNPs underwent dissolution, as well as changes in hydrodynamic diameter, zeta potential and polydispersity index in both tested media depending on particle size and concentration. Similarly, exposure dose played a key role in regulating the different cell death modalities (apoptosis, necrosis, autophagy), and the signalling pathways (repair mechanisms) in cells that were activated in the attempt to overcome the induced damage. This study contributes to the 3Rs initiative to replace, reduce and refine animal experimentation through the use of alternative models for NMs assessment.

2.2 Introduction

Nanoparticles (NPs) are materials with overall dimensions in the nanoscale range (1-100 nm). NPs have unique properties, which differ significantly from their bulk form, such as increased strength, chemical reactivity or conductivity, and higher surface area [7, 25, 26]. Silver nanoparticles (AgNPs) are considered one of the most globally used nanomaterials (NMs), being incorporated into hundreds of products including electronics, food packaging, textiles and in a variety of biomedical products, such as wound dressings and medical device coatings, mainly due to their inherent antimicrobial properties [17, 25, 246]. Despite the advantages of AgNPs in society, environmental and toxicological risks are associated with their full life cycle, i.e. their fabrication, handling, usage, disposal, and behaviour in the environment [247]. AgNPs are sensitive to the surrounding environment, which may induce environmental transformations, such as aggregation, oxidation, and

dissolution of the NPs, which also includes the release of ionic forms (Ag^+) and its transformation to other forms such as silver sulphide (Ag_2S) and silver chloride (AgCl) [25, 248-250]. The presence of AgNPs and their environmental products in the aquatic environment may trigger a cascade of cellular events, which could potentially lead to a toxic response [168]. Cellular events play an important role in maintaining the health and regulating the development of organisms; while processes such as programmed cell death and other types of regulated cell activity are key to understanding how cells respond to stress, activate survival pathways or even self-initiate cell death mechanisms to eliminate damaged cells [165]. The mechanisms of cellular response to stress factors and the fate of the damaged cells depends on the nature and duration of the stress as well as the cell physiology [165, 168]. For example, lipid peroxidation is described as a process where free radicals attack lipids containing carbon-carbon double bonds and acts as a powerful cell death regulator [168, 251, 252]. Cell death pathways such as apoptosis, necrosis, and autophagy can also be triggered by different stimuli, with each cell death pathway having different timings and mechanisms of induction [168]. Apoptosis can be initiated by mitochondrial impairment and release of cytochrome *c* into the cytosol, triggering the activation of caspases that lead to the apoptotic pathway [167-169]. Necrosis is activated when other types of programmed cell death have failed to repair damaged cells, leading to the elimination of the impaired cells [165, 166]. On the other hand, autophagy is regulated by engulfing and eliminating intracellular material, such as proteins, damaged organelles, and endogenous substrates (xenophagy) through lysosomal degradation [168, 174, 175].

Assessment of the toxicological responses of aquatic organisms to NMs in the environment is extensively growing as more nano-enabled products are developed, driving a need for faster, higher throughput approaches. The need to reduce our reliance on animal testing driven by policy initiatives such as the 3Rs framework, including *in vitro* approaches using alternative cellular models for toxicological assessment [253]. In this context, the use of fish cell lines has been demonstrated to screen cellular and molecular responses of clinical and environmental relevance, providing high sensitivity in the evaluation of diseases, cellular dysfunctions, and toxicity [214, 254, 255]. Cell lines also contribute to exploration of the sequence of molecular and cellular events leading to adverse biological outcomes in response to exposure to NMs, which is key in the development of adverse outcome pathways (AOP) [256]. Here, cell culture testing supports mechanistic insights that may facilitate NM evaluation of biochemical pathways to improve testing strategies for targeted toxicity assessment [251, 257, 258].

In this study, a set of cellular assays utilising continuous embryonic zebrafish cells (ZF4) are presented. The aim was to explore the effectiveness of this cell line as a means for screening the toxicity of NMs. ZF4 cells are a type of adherent fibroblast cells, established from 1-day old zebrafish (*Danio rerio*) embryos. The characteristics of the AgNPs such as representative size (10, 30 and 100 nm) and coating (PVP) were selected to investigate whether these specific features may be linked to the biological and toxicological effects in cells exposed to nanomaterials. Hence, to provide additional mechanistic insights about the processes underlying the AgNPs size-induced toxicity, as well as the pathways triggered by NPs in fish cell lines, we present a detailed assessment of the cell death and signalling mechanisms activated by embryonic zebrafish cells (ZF4)

in response to exposure to AgNPs and ionic silver, proposing ZF4 cells as a potential and suitable model for mechanistic nanotoxicological studies as an alternative to fish testing.

2.3 Materials and methods

2.3.1 Characterisation of AgNPs

Polyvinylpyrrolidone (PVP) coated silver nanoparticles (AgNPs) with core sizes (provided by the manufacturer) 10 ± 2 nm, 30 ± 2 , and 100 ± 8 nm were purchased from Nanocomposix, USA (BioPure, Silver Nanospheres PVP, 1 mg/mL). In order to understand how the physicochemical characteristics of the AgNPs evolve in a complex medium, the AgNPs were characterised using a range of methods and testing media. Transmission Electron Microscopy (TEM) (JEOL JEM-1400) was used to assess the metal core particle size, and Nanoparticle Tracking Analysis (NTA) (Nanosight, NS300, Malvern Instruments, Ltd.) was used to provide the hydrodynamic diameter. AgNP concentrations for TEM (100 $\mu\text{g/mL}$) and NTA (0.012 $\mu\text{g/mL}$) were assessed in ultrapure water (UPW) only. Based on LDH assays (Section 2.3.5), a low, medium, and high biological concentrations of AgNPs (2.5, 5 and 10 $\mu\text{g/mL}$, respectively) for three representative sizes (10, 30 and 100 nm) were assessed as follows. Dynamic Light Scattering (DLS) (Zetasizer Nano series, Malvern) was used to determine the hydrodynamic diameter, Polydispersity index (PDI) and zeta potential in both UPW and complete culture medium (CCM) after 0 and 24 hours. CCM was prepared with DMEM/F12 (Gibco, 11330) supplemented with 10% Foetal Bovine Serum (FBS) (Gibco, 10270) and 1% penicillin and streptomycin (Gibco,15070). For hydrodynamic diameter

and PDI measurements, 1 mL of the AgNPs suspensions (2.5, 5 and 10 $\mu\text{g/mL}$) was placed in disposable polystyrene cuvettes (Sarstedt, 67.742), whereas for zeta potential measurements 700 μL was placed in a folded capillary cell (Malvern, DTS1070); all the samples were prepared fresh and immediately evaluated using a default standard operational procedure adjusted for silver on the V.8.00 software. Detailed methodologies for the TEM, DLS and NTA sample preparation are included in the supplementary information (SI), with TEM images and size distribution graphs included as Figure S7.2 in the SI.

2.3.2 Silver nitrate (AgNO_3) stock

AgNPs in the environment are likely to undergo dissolution and release Ag^+ , therefore, to evaluate the impact of Ag^+ in the toxicity of the AgNPs to ZF4 cells, different concentrations of ionic Ag were prepared as a control (with equivalent mass of silver in ionic form). First, silver nitrate (AgNO_3 salt, VWR chemicals, USA) was weighed calculating the total amount of Ag^+ , then, the AgNO_3 salt was dissolved in UPW to obtain a final concentration of 1 mg/mL of Ag. The suspension was prepared in a laminar flow cabinet to avoid contamination.

2.3.3 Dissolution of AgNPs in water and CCM

For dissolution experiments in water and CCM, a protocol was optimised to ensure the best recovery of ionic silver [52, 259, 260]. The final protocol is as follows:

For dissolution PVP coated AgNPs with sizes of 10, 30, and 100 nm were dispersed in either UPW or CCM. For this, the equation $c_1V_1=c_2V_2$ (where c is concentration and v is volume) was used to calculate from the NP stock (1000 $\mu\text{g}/\text{mL}$), a final concentration of 10 $\mu\text{g}/\text{mL}$ in a total volume of 20 mL for the experiments. For UPW, the AgNP suspensions (10 $\mu\text{g}/\text{mL}$) were placed in low density polyethylene (LDPE) bottles (Thermofisher, 2003-series) and gently shaken (100 rpm) (Benchmark Incu-shaker H100M) at 28°C. Aliquots of 400 μL were taken after 15 and 30 minutes and then at 1, 1.5, 2, 4, and 8 hours. Each sample was placed into a micro centrifugal tube (3Kda, Amicon® Ultra 0.5 mL, UFC5003, Merck) and centrifugated at 20817 x g for 5 minutes at 20°C (Eppendorf, 5430 R). After centrifugation, the filter was carefully removed and the 300 μL of the bottom liquid (containing the dissolved silver fraction) was placed into 15 mL tubes (Falcon, 352196 Fisher scientific) and diluted with 5 mL of 2% HNO_3 (A509-P500, TraceMetal™, Fisher scientific) and left for 24 hours at 4°C. The next day, samples were analysed by Inductively Coupled Plasma Mass Spectrometry (ICP-MS) (NexION 300x, Perkin Elmer).

For dissolution in CCM, the three different AgNP sizes (10, 30 and 100 nm) were also diluted in 20 mL CCM to a final concentration of 10 $\mu\text{g}/\text{mL}$, placed in new LDPE bottles and treated as described for the UPW samples (see above). The filters were subjected to additional washes by adding 500 μL of UPW into each tube and then centrifugated again at 20817 x g for 30 minutes at 20°C. After centrifugation, 400 μL of the supernatants were recovered and added to the corresponding vial, which contained the 1st centrifugation liquid. This process was performed three times to ensure the maximal recovery of the ionic form of Ag. Finally, the recovered mix of the 4 supernatants

(initial + 3 washes) was diluted with 2% HNO₃ for a total volume of 5 mL, left for 24 hours at 4°C and then analysed by ICP-MS.

For all the experiments (in UPW and CCM), three individual replicates were included for each NP size and time point. A calibration curve of 100, 250, 500, 750 and 1000 ppb of certified silver standard solution (Sigma, 12818) prepared in 2% HNO₃ was used to set the ICP-MS. Rhodium ICP-MS standard (Sigma, 04026) (500 ppb) was used as an internal standard, which compensates for the matrix effects caused by differences in the matrix, as well as plasma effects. The sample uptake rate was 0.3mL/min, nebuliser flow ~ 1 mL/min, auxiliary gas flow 1.2 mL/min and plasma gas flow 18 mL/min. Washes with 2% nitric acid were set between samples to eliminate any carry over.

Dissolution curves were constructed based on the Ag concentrations obtained by ICP-MS (raw data) and plotted using Graphpad software. To calculate the value of free silver ions in percent (%), the obtained concentrations values were divided by the concentration added at the start of the experiment and multiplied by 100% as represented in the following formula [261]:

$$\% \text{ of dissolved silver} = \text{Ag measured at time} / \text{AgNPs initial concentration} * 100$$

The formula calculates the percent (%) of dissolution of the total Ag present in the aliquot at the time of sampling [261]. Finally, from the initial slopes of the raw data, the equation of the curve was derived using an integrated rate law (kinetic order) to calculate the maximum dissolution rate in $\mu\text{g mL}^{-1} \text{h}^{-1}$.

2.3.4 Culture of embryonic zebrafish cells (ZF4)

Embryonic zebrafish (ZF4) cells established from 1-day old zebrafish embryos as described by Driever and Rangini, (1993) [233] were purchased from ATCC (ATCC® CRL-2050™). Cells were cultured as described on the manufacturer's website (<https://www.atcc.org/products/all/CRL-2050.aspx>). Briefly, the vial of cells was thawed and resuspended in a T75 flask with a vented cap (Corning, 430641U), containing 1 mL of the cell suspension and 9 mL of CCM for a total volume of 10 mL, and incubated in a humidified atmosphere of 5% CO₂ at 28 °C. The CCM was prepared using DMEM/F12 (Gibco, 11330) supplemented with 10% Foetal Bovine Serum (FBS) (Gibco, 10270) and 1% penicillin and streptomycin (Gibco, 15070).

After the cells reached 80% confluence (4 days), they were passaged by removing the cell medium, washing with 5 mL of phosphate-buffered saline (PBS) (Thermofisher, D5837), detaching with 1.5 mL of 0.25% Trypsin (Gibco, 15090) for 3 minutes, and finally diluted in a total volume of 10 mL of CCM. Two millilitres of the diluted suspension were seeded on T75 flasks in a final volume of 8 mL, and this procedure was repeated once a week to maintain the cell line in T75 flasks.

2.3.4.1 Culture of cells for flow cytometry

For flow cytometry experiments, cells on T75 flasks were detached as previously described, then 3 mL of the diluted suspension was resuspended and reseeded in T175 vented cap flasks (Corning, 431080) in a total volume of 20 mL of CCM and incubated for

one week. After the cells reached 85-90% confluence (5 days), the medium was removed, cells were washed with 10 mL of PBS, detached with 3 mL of trypsin, diluted in 7 mL of CCM, and re-seeded as required for each experiment (see below).

The cell line was maintained in T175 flasks by reseeding 2 mL of the diluted suspension in a total volume of 20 mL CCM in T175 flasks. Cells were maintained in T175 flasks by splitting once a week as described above for the T75 flask cultures.

2.3.5 Lactate dehydrogenase activity (LDH) assay

Different AgNP concentrations were tested to determine the half maximal effective concentration (EC_{50}) of enzyme inhibition by AgNPs and Ag^+ in ZF4 cells. For this, the cytoplasmic enzyme LDH activity was evaluated. First, ZF4 cells were seeded in 96-well flat bottom plates (Corning, 3917) at a density of 8,000 cells per well and in a total volume of 200 μ L to ensure spacious distribution. Cells were cultured using DMEM/F12 supplemented with 10% FBS, and 1% of penicillin and streptomycin at 28 °C, 5% CO_2 . Twenty-four hours post seeding, cells were treated with 5, 10, 20, 30, 40 and 60 μ g/mL of AgNPs and lower concentrations (0.5, 1, 2, 3, 5, and 8 μ g/mL) of Ag^+ (silver nitrate, $AgNO_3$) (Sigma, 209139) as the ionic counterpart, and incubated for 3, 24, 48, and 72 hours. In addition, a positive control of 10% Dimethyl sulfoxide (DMSO) was included at the respective time points to induce approximately 90% of cell lysis [262, 263].

The selected AgNPs and $AgNO_3$ concentrations were based on cytotoxic studies of cells exposed to ionic Ag [26, 220, 264, 265]. After the incubation time, LDH activity was evaluated via LDH assay (CytoTox 96, Promega Corporation, USA) on intact cells using a modified protocol as described by Ali-Boucetta et al. (2011) [262]. This protocol

was selected due to known interferences from AgNPs when following the manufacturer's protocol which was not designed for NPs. These interferences can be related to the intrinsic properties of the NPs, such as emission/absorption and binding of assay molecules to the particle surface, resulting in inaccurate results [262, 266, 267]. No other analyses were performed to evaluate further interferences of the NPs with the original LDH assay. The modified protocol quantifies LDH by a coupled enzymatic reaction in which LDH catalyses the conversion of lactate to pyruvate via NAD⁺ reduction to NADH. Diaphorase then uses NADH to reduce a tetrazolium salt to a red formazan product, which can be measured at 490 nm [268, 269]. The modified assay assesses the LDH enzyme of the intact cells that survived the treatment, rather than detecting the amount of LDH released into the medium following AgNPs induced cellular death [262]. Briefly, the cell medium was aspirated and replaced with 110 μ L of 0.9% lysis solution (Triton X100, Sigma) prepared on the day of the assay with phenol free medium (Thermofisher, 21041025), and incubated for 45 minutes at 28°C. Lysates were collected, transferred into 1.5 mL Eppendorf tubes and centrifuged at 20073 x g (Eppendorf, 5430R) for 5 minutes; 50 μ L of the cell lysate was transferred into 96 well plates, followed by addition of 50 μ L of reconstituted substrate mix (LDH kit Promega, G1780), covered with foil and incubated at room temperature for 15 minutes. Finally, 50 μ L of stop solution (LDH kit Promega) was added; the absorbance was immediately recorded at 492 nm using a FLUOstar Omega microplate reader (BMG Labtech, Germany). Each treatment was individually prepared in triplicate (n = 3), this procedure was repeated 3 times for a total of 9 samples (n = 9) for each of the different AgNPs sizes (10, 30 and 100 nm) and AgNO₃ treatments. The amount of LDH detected represents the number of cells that survived the

AgNP and ionic Ag treatments. The percentage cell survival was calculated based on the LDH activity using the following equation, as suggested in the published protocol [262].

$$\text{Percentage of survival} = \left(\frac{\text{Abs 490 of treated cells}}{\text{Mean Abs 490 of untreated cells}} \right) * 100$$

2.3.6 Autophagy assay

The autophagy response was evaluated using the methodology provided by the manufacturer of the Cell Meter™ Autophagy Assay Kit (23002), applying slight modifications for flow cytometry samples. Briefly, ZF4 cells were seeded in six-well flat bottom plates (Corning, CLS3736) at a density of 5×10^5 cells in a total volume of 2 mL per well, and 24 hours prior to the study. Cell were seeded using DMEM/F12 supplemented with 10% FBS, and 1% penicillin and streptomycin at 28 °C and 5% CO₂. After 24 hrs, ZF4 cells were exposed to low, medium, and high concentrations of AgNPs and AgNO₃ based on the results of the LDH assay where 10 µg/mL decreased cell viability by 50% for the three AgNPs sizes, whereas for AgNO₃, the EC₅₀ concentration was found to be 2 µg/mL. Hence, cells were treated with 2.5, 5 and 10 µg/mL of each one of the three AgNPs sizes (10, 30 and 100 nm) and 1, 1.5 and 2 µg/mL of AgNO₃ for 24 hrs at 28 °C. Rapamycin (Sigma, 553210; 10 µM), an inhibitor of mTOR that specifically binds to mTOR and activates the autophagy of cells was included to induce autophagy [270]. Furthermore, 100 µM Bafilomycin (Sigma, B1793), which inhibits lysosomal V-ATPase, preventing its acidification and disruption of the autophagic flux, was also incubated with the cells for 24 hours to decrease the autophagy response [271]. Blockage of the apical

uptake of Ag⁺ in cells after Bafilomycin exposures was not evaluated, although it is recommended due to possible Na⁺/H⁺ exchange [272].

After the incubation period, the cell medium was removed from all treatments; cells were washed with warm PBS (28 °C) and detached using 0.25% Trypsin for 3 minutes at 28°C. The medium and cells were centrifuged for 10 minutes at 270 x g at 4°C. The supernatant was removed, and the pellet was labelled using Cell Meter™ Autophagy Assay stock following the supplier protocol for flow cytometry. Briefly, 20 µL of Autophagy Green™ was diluted with 10 mL of Stain Buffer, afterwards the cell pellet was stained with 500 µL and incubated at room temperature for 30 minutes. After staining, cells were washed with PBS and centrifuged at 270 x g at room temperature for 10 minutes. The supernatant was discarded, and the cell pellet was diluted with 500 µL of PBS. Labelled cells were analysed by fluorescence-activated cell sorting (FACS) using a BD LSRFortessa™ X-20 system running the software BD FACSDiva version 8.0.1 (Beckton, Dickinson and Company, New Jersey, NY, USA) with the fluorescein isothiocyanate (FITC) filter, which has a fluorescence excitation/emission of 499/521 nm. The flow cytometer was set up using unstained cells with and without NPs (controls), cells labelled with single stains. Then, cell doublets were selected and excluded from the analysis. At least 10,000 counts were recorded per sample and three individual replicates were performed per treatment. Normalisation of the results was calculated using the following formula:

$$\textit{Autophagy} = \left(\frac{\textit{Treated cells}}{\textit{Mean untreated cells}} \right) * 100$$

2.3.7 Apoptosis versus necrosis assay

Evaluation of the cell death mechanism induced by AgNPs and Ag⁺ in ZF4 cells was performed by Alexa Fluor® 488 Annexin V/Dead Cell Apoptosis Kit (ThermoFisher V13242) following the manufacturer's protocol for flow cytometry samples. First, ZF4 cells were seeded in six-well flat bottom plates as initially described in section 2.3.6. After 24 hrs, cells were treated with 2.5, 5 and 10 µg/mL of the three different AgNPs sizes (10, 30 and 100 nm) and AgNO₃ (1, 1.5 and 2 µg/mL) for 24 hrs at 28 °C. In addition, 10% dimethyl sulfoxide (DMSO, Sigma, D4540) was included as a positive control for necrosis. DMSO can interact with the plasma membrane allowing pore formation, decreasing membrane selectivity and increasing cell permeability [273]. On the other hand, 2.5 µM staurosporine (Sigma, S4400) was included as a positive control for apoptosis, due its role in promoting intracellular stress-induced apoptosis through cytochrome c release and mitochondrial depolarization, which has been widely demonstrated [274-276].

After the incubation period, the cell medium was removed; cells were washed with warm PBS (28 °C) and detached using 0.25% Trypsin for 3 minutes at 28°C. Then, the cell medium and cells were centrifuged for 10 minutes at 270 x g at 4°C. The supernatant was carefully removed, and the pellet was labelled with 5µL Alexa Fluor® 488 annexin V and 1 µL of the propidium iodide (PI) working solution and incubated in the dark at room temperature for 15 minutes. The Annexin V corresponding signal provides a very sensitive method for detecting cellular apoptosis, while PI is used to detect necrotic or late apoptotic cells, characterized by the loss of the integrity of the plasma and nuclear membranes. After the incubation period, samples were diluted with 400 µL of 1X annexin-binding buffer and immediately analysed by FACS using FITC and Texas Red® dye filters with fluorescence Excitation/Emission of 499/521 and 535/617 (nm) respectively. The

flow cytometer was set up based on unstained cells with and without NPs (controls), cells labelled with single stains, and by excluding cell doublets from the analysis. At least 10,000 counts were recorded. Flow cytometry results were analysed using FlowJo software. The percentage of cells in each of the different populations were sorted based on the division of the flow cytometry quadrants by cell death mechanism, the data was plotted in two-dimensional dot plots in which PI is represented versus Annexin V-FICT. These plots (see examples in Figure 2.1) were divided into four regions corresponding to: 1) viable cells which are negative to both probes (PI/FITC -/-; Q4); 2) apoptotic cells which are PI negative and Annexin positive (PI/FITC -/+; Q3); 3) late apoptotic/necrotic cells which are PI and Annexin positive (PI/FITC +/+; Q1); 4) necrotic cells which are PI positive and Annexin negative (PI/FITC +/-; Q2) as shown below:

Q1 Late apoptotic cells	Q2 Necrotic cells
Q4 Viable cells	Q3 Apoptotic cells

Figure 2. 1. Flow cytometry quadrant. The quadrants were used to sort/identify the cell death mechanism in cells.

2.3.8 Mitochondrial membrane potential (MMP)

HCS Mitochondrial Health Kit (H10295) was used to assess changes in the mitochondrial membrane potential, as the reagent accumulates in mitochondria of live cells proportional

to the mitochondrial membrane potential. The manufacturer's protocol can evaluate two cell health parameters, mitotoxicity and cellular toxicity; however, for the purposes of this study only mitotoxicity was evaluated. First ZF4 cells were seeded in 96-well flat bottom plates as described in section 2.3.5. After 24 hrs, cells were treated with 2.5, 5 and 10 µg/mL of one the three different AgNPs sizes (10, 30 and 100 nm) or 1, 1.5 and 2 µg/mL of AgNO₃ for 24 hrs at 28 °C. Hydrogen peroxide (100 µM) was included for 30 minutes as positive control. Then, cells were stained with 50 µL each of MitoHealth stain solution for 30 minutes at 28°C. Afterwards, 100 µL of the counterstain/fixation solution was added and cells were incubated for 15 minutes at room temperature to fix the cells and stain the nucleus with Hoechst 33342 for easier automated image analysis. Next, cells were washed twice with 100 µL PBS, and then 200 µL of PBS was added and the cells were scanned using a Tecan Spark plate reader in time resolved fluorescence mode. Then, the plate reader was set to scan tetramethylrhodamine (TRITC) filter, which has an excitation/emission 557/576 nm. Three independent samples were evaluated per treatment. Intensity results were normalised to percentage and the mitochondrial toxicity was determined by signal decrease (lower values) in the TRITC channel compared to naïve cells. In addition, to ensure the reliability of the assay, cells were visualised under a fluorescent microscope (EVOS® FL Cell Imaging System), and images were taken at 20X objective. Intensity results were normalised as follows:

$$MMP = \left(\frac{\text{Treated cells}}{\text{Mean untreated cells}} \right) * 100$$

2.3.9 Lipid peroxidation

To quantify direct damage and oxidation of lipids, Image-iT® Lipid Peroxidation Kit (C10445) was used by following the supplier's protocol for flow cytometry samples. Briefly, ZF4 cells were seeded in six-well flat bottom plates as described in section 2.3.6. After 24 hrs, cells were treated with 2.5, 5 and 10 µg/mL of one of the three AgNPs sizes (10, 30 and 100 nm) or 1, 1.5 and 2 µg/mL of AgNO₃ for 24hrs at 28 °C. A concentration of cumene hydroperoxide, (100 µM) (Image-iT® Lipid Peroxidation Kit) was also included for 2 hours at 28 °C as a positive control to induce lipid peroxidation. Then, cells were washed with PBS and detached using 0.25% Trypsin for 3 minutes at 28°C. The medium and cells were centrifuged for 10 minutes at 270 x g at 4°C. The supernatant was carefully removed, and the cell pellet was labelled using Cell Image-iT® Lipid Peroxidation Sensor at a final concentration of 10 µM in live cell imaging solution (Thermofisher, A14291DJ) for 30 minutes at 28 °C. After the incubation period, dye intensities were analysed by FACS at separate wavelengths using Ex/Em 499/521 nm for FITC and 535/617 nm for Texas red. The ratio of the fluorescence of Texas red to FITC was automatically calculated by FlowJo Software to determine the extent of lipid peroxidation in cells.

2.3.10 Statistical analysis

Viability results were plotted and analysed using GraphPad prism 8 software (V.8.4.3). Flow cytometry results were analysed using FlowJo software (V.10.0.8, FlowJo, LLC, Ashland, OR, USA). Statistical analyses were performed using GraphPad 8 via a two-way ANOVA followed by a Bonferroni post-hoc multiple comparison for all AgNPs and AgNO₃ treatments against the untreated control (naïve). Comparisons across the dataset were analysed by fitting a repeated measures ANOVA automatically in graphpad.

2.4 Results

2.4.1 Characterisation of AgNPs in ultrapure water and culture media

AgNPs were characterised in UPW, and cell culture medium supplemented with 10% FBS (CCM). Results for the TEM size of the AgNPs were consistent with the size range indicated by the manufacturer, displaying 13 ± 2.4 nm, 34.08 ± 2.88 nm, and 101.6 ± 9.2 nm for the 10, 30 and 100 nm AgNPs sizes, respectively. The hydrodynamic diameter measured by NTA in UPW showed similar values for the 10 and 30 nm sized AgNPs (35.9 ± 11.7 nm and 37.8 ± 7.4 nm respectively), whereas for the 100 nm size was close to the measured core size at 107 ± 10.4 nm (Figure 2.2).

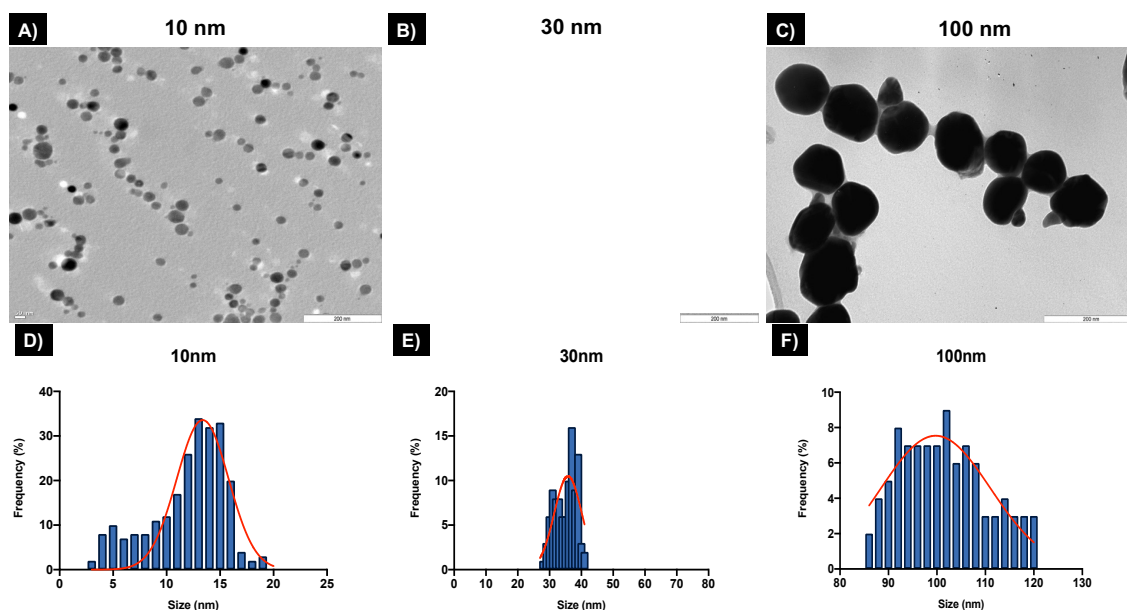


Figure 2. 2. TEM characterisation of the 3 different AgNPs by TEM. The TEM show the AgNPs prepared only in ultrapure water (UPW) at a final concentration of 100 mg/mL. A and D) TEM image and size distribution of the 10 nm AgNPs. B and C) Size and size distribution of the 30 nm AgNPs. C and F) TEM image and results for the 100 nm AgNPs. For size distribution, one sample (n= 1) was analysed, approximately 100 nanoparticles

each were used to calculate a size distribution graph for each of the three particle sizes using GraphPad software. Scale bar is 200 nm.

The characterisation in water and cell media by DLS revealed as expected, different results in terms of the hydrodynamic diameter, showing that the proteins in the cell medium play an important role by increasing the hydrodynamic diameter of all the AgNPs and inducing agglomeration (Figure 2.3). The exposure concentrations (2.5, 5 and 10 $\mu\text{g}/\text{mL}$) also showed to have an effect on the recorded size in UPW, while the sizes in CCM showed similar values for the three concentrations likely as a result of stabilisation of the dispersion through adsorption of proteins to form a corona at the particle surface. The CCM alone showed the presence of a peak around 13 nm after 0 and 24 hours, demonstrating that the size of the protein clusters remained stable for 24 hours. A slight increase in size over the 24 hours was noted in both testing media, except for the 100 nm AgNPs in CCM which decreased slightly in size at the highest concentration (10 mg/mL) after 24 hours. These size fluctuations may be linked to the diffusion coefficient of the NPs in the CCM as well as to protein exchange due to different affinities for the NPs, which play a key role in the hydrodynamic diameter of the AgNPs [277, 278].

The zeta potential results were similar for all AgNPs sizes and concentrations in CCM (-12 to -6 mV); and were largely similar to the values in water whereby the PVP capping stabilises the particles despite their low zeta potential values (all particles were slightly negative with values ranging from -7 to -11 mV). The DLS polydispersity index (PDI) showed noticeable changes in the AgNPs stability in water, displaying fluctuating and higher values after 24 hours (0.3 to 0.4) compared to 0 hours (0.0 to 0.1 which is consistent with highly monodisperse particles). The increase in PDI demonstrates that

AgNPs in water are less stable over the exposure period. At both timepoints, the PDIs in CCM were higher than those in water at both time points but did not change much between 0 and 24 hours, indicating that the corona formation resulted in slight agglomeration initially, but that the dispersion remained stable. The 100 nm size displayed the lowest PDI values (0.01 to 0.07) suggesting that the larger NPs remained monodisperse. A summary of all the results, including TEM images, NTA, and DLS (size, zeta potential, and PDI) can be found in Tables S7.1, S7.2, and S7.3 in the Supplementary Information (SI).

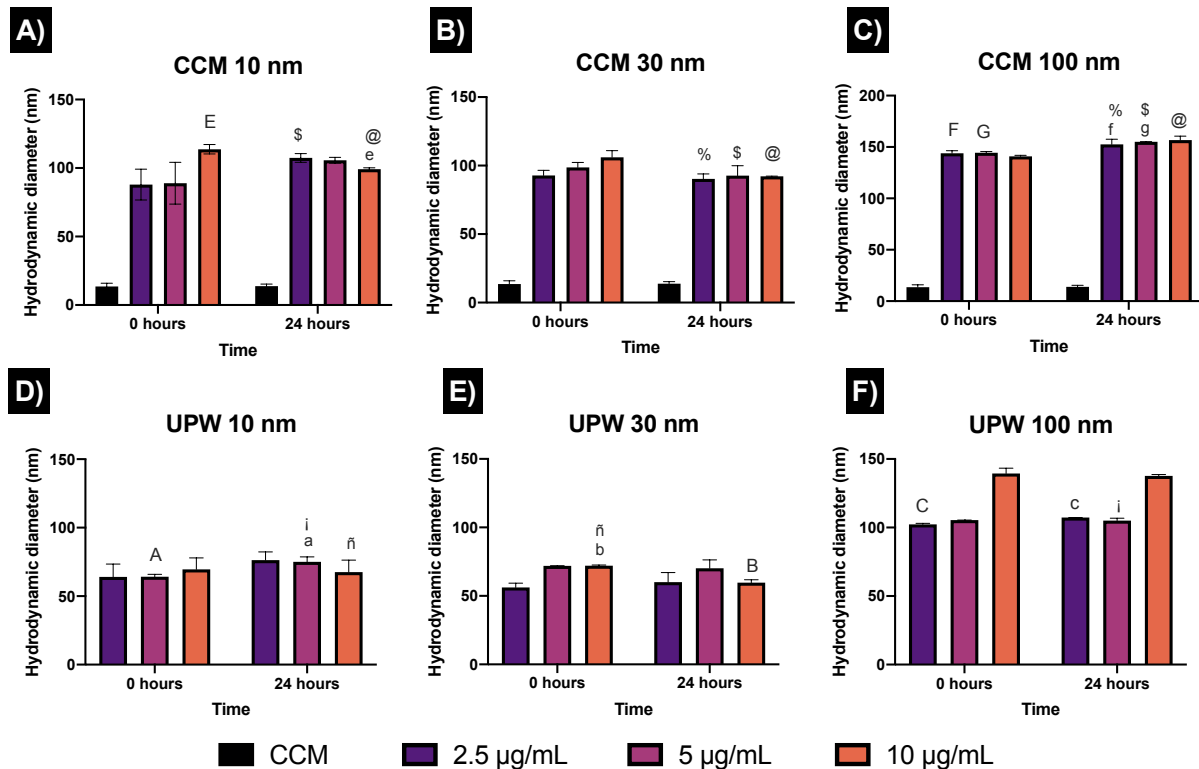


Figure 2.3. Hydrodynamic diameter of AgNPs by DLS in different test media at the different concentrations. A-C) Hydrodynamic diameter in complete culture medium (CCM) of the 10, 30 and 100 nm AgNPs at different concentrations (2.5, 5 and 10 µg/mL) at 0 and 24 hours. B-D) Samples prepared with DMEM/F12 supplemented with 10% foetal bovine serum (FBS). Cell medium alone was also tested to determine the size of the protein clusters present in the medium. D-F) Hydrodynamic diameter of AgNPs in ultrapure water (UPW) The figure shows the mean \pm standard deviation (SD) ($n = 3$) of three independent replicates. The AgNPs concentrations were based on the selected

exposure concentrations for the study ($\mu\text{g}/\text{mL}$). Data with similar letters (upper and lowercase) indicate a statistically significant difference ($p < 0.05$) between time points (0 and 24 hours) for each NP size at the same concentration. Bars with identical symbols denote statistical difference ($p < 0.05$) in the hydrodynamic size between the selected NP sizes.

2.4.2 Dissolution of AgNPs in water and CCM

To further understand changes in the physicochemical properties of the AgNPs in the different media, the dissolution of AgNPs in UPW and CCM was assessed from 15 minutes to 8 hours, as AgNPs in aqueous suspensions reach a steady state dissolution within this time [51, 279]. The released Ag^+ was centrifugally separated and quantified by ICP-MS. Results for the dissolution of AgNPs in water demonstrated different Ag concentrations based on the NP size (10, 30, and 100 nm). The smallest NP size showed higher Ag concentrations compared to the other AgNPs sizes, showing an Ag concentration that exponential increased over time (Figure 2.4). After 15 minutes, the ionic concentration detected was $0.53 \pm 0.01 \mu\text{g}/\text{mL}$ in UPW, this represents dissolution of 5 % of the total Ag present in the aliquot at the time of sampling, and the maximum rate of dissolution during the first few minutes of the experiment was $0.82 \mu\text{g mL}^{-1} \text{h}^{-1}$.

From 30 minutes to 2 hours, the dissolved Ag increased from 0.92 to $1.55 \mu\text{g}/\text{mL}$ (Figure 2.4 A); however, after 2 hours there was a noticeable Ag increase, showing $>2 \mu\text{g}/\text{mL}$ for the last points (4 and 8 hours), with a final dissolved Ag concentration of $2.12 \pm 0.20 \mu\text{g}/\text{mL}$, representing 21% dissolution of the AgNPs and with a maximum dissolution rate of $0.16 \mu\text{g mL}^{-1} \text{h}^{-1}$. The 30 nm size displayed lower dissolved Ag concentrations. At the initial time point, the Ag concentration was recorded as $0.16 \pm 0.18 \mu\text{g}/\text{mL}$, from 30 minutes to 1 hour, the dissolved Ag concentration slowly increased to $0.69 \pm 0.01 \mu\text{g}/\text{mL}$,

representing 6 % dissolution of Ag and a maximum dissolution rate of $0.39 \mu\text{g mL}^{-1} \text{h}^{-1}$. After 4 hours the dissolution of the AgNPs reached equilibrium with $>0.82 \mu\text{g/mL}$ of dissolved silver, which remained constant at the last time points (Figure 2.4B). The biggest size (100 nm) displayed the lowest dissolution; after 15 minutes the recorded Ag concentrations was $0.002 \pm 0.002 \mu\text{g/mL}$, which represents 0.03 % of the total Ag, and a maximum dissolution rate of $0.021 \mu\text{g mL}^{-1} \text{h}^{-1}$. After 1 hour, the dissolution started to reach an apparent equilibrium, with concentrations above $0.020 \mu\text{g/mL}$. Then, after 1.5 hours the Ag concentration value recorded was $0.023 \pm 0.004 \mu\text{g/mL}$, and finally after 8 hours the Ag was $0.025 \pm 0.001 \mu\text{g/mL}$, representing 0.25 % of the initial Ag present, with a maximum dissolution rate of $0.017 \mu\text{g mL}^{-1} \text{h}^{-1}$ (Figure 2.4C).

It is likely that the proteins and other molecules (chloride and phosphate) in the CCM played an important role in modulating the dissolution by interacting with the NPs (e.g., forming a corona) and in the release of ions; additionally, it is possible that the proteins from the serum and possible larger agglomerates were retained in the filters making the release of ions slower and increasing the centrifugation time in the initially designed protocol. Hence, the protocol was modified to ensure the complete recovery of the ions from the centrifugated sample. Results for all AgNPs sizes in CCM displayed noticeable fluctuations and higher standard deviations within replicates, as well as likely a linear dissolution trend in the initial stage of the process. The 10 nm and 30 nm AgNP sizes both underwent partial dissolution, displaying a 10-fold decrease in their dissolution in CCM compared to the results in water. The dissolution for the 10 nm size, started slowly with an initial Ag concentration of $0.10 \pm 0.01 \mu\text{g/mL}$, which represents dissolution of 1 % of the total Ag present; the maximum rate of dissolution during the first 15 minutes of the

experiment was $0.090 \mu\text{g mL}^{-1} \text{h}^{-1}$. After 2 hours, the dissolution reached a steady state, showing concentrations above $0.2 \mu\text{g/mL}$ for the rest of the timepoints.

The 30 nm displayed an initial Ag concentration of $0.096 \pm 0.041 \mu\text{g/mL}$, representing 1% dissolution of the AgNPs and with a maximum dissolution rate of $0.030 \mu\text{g/h}$. However, after 1 and 1.5 hours, the dissolution showed concentrations of 0.132 ± 0.009 and $0.134 \pm 0.01 \mu\text{g/mL}$, respectively. From 2 to 8 hours, the recorded Ag concentrations were slightly lower, with a final concentration of $0.109 \pm 0.012 \mu\text{g/mL}$, which represent 1 % of the initial Ag present and with a maximum dissolution rate of $0.044 \mu\text{g/h}$ (Figure 2.4E). The larger size (100 nm) presented the lowest dissolution compared to the other AgNPs, although dissolution in CCM produced slightly higher values of dissolved ions than those recorded in UPW. The recorded amount of dissolved Ag after 15 minutes was $0.030 \pm 0.011 \mu\text{g/mL}$, representing 0.30 % dissolution and with a maximum rate of $0.103 \mu\text{g mL}^{-1} \text{h}^{-1}$. After 2 hours, the dissolution increased 50%, to $0.062 \pm 0.011 \mu\text{g/mL}$, and finally after 8 hours, the dissolution was recorded as $0.51 \pm 0.29 \mu\text{g/mL}$, with 5 % of Ag released and $0.20 \mu\text{g mL}^{-1} \text{h}^{-1}$ dissolution rate (Figure 2.4F). A summary of the results can be found in Table S7.4 in the SI.

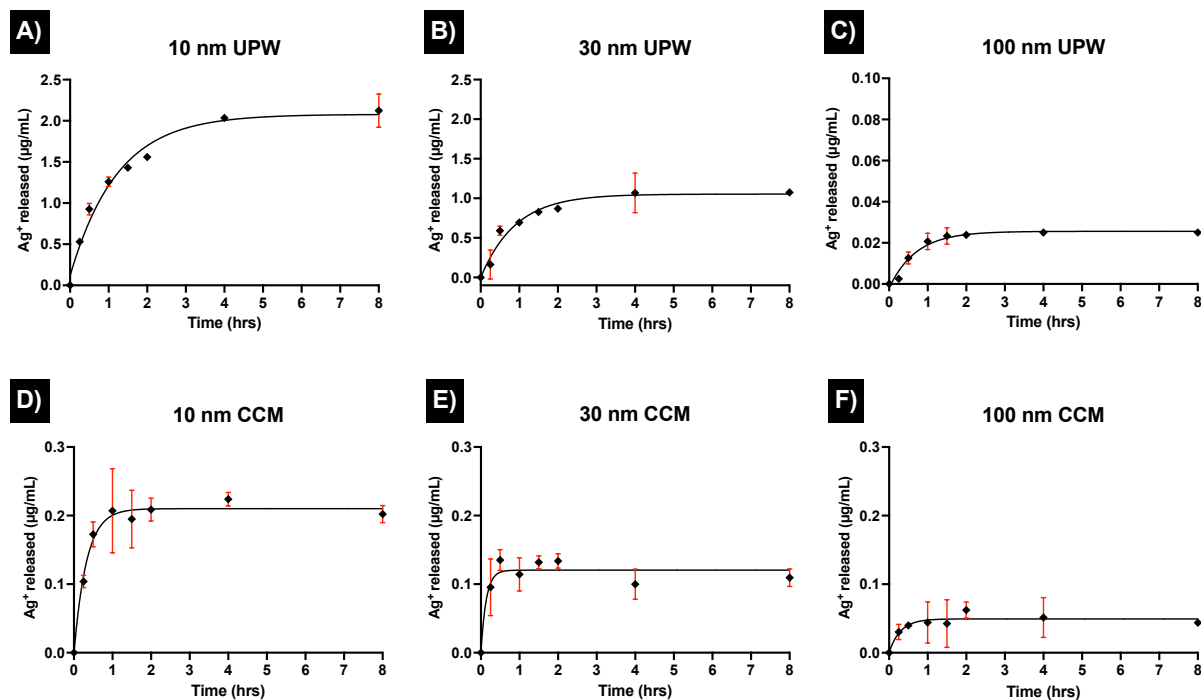


Figure 2. 4. Dissolution of AgNPs in ultrapure water (UPW) and complete culture media (CCM). The figure shows the dissolution of 10 µg/mL of three AgNPs sizes (10, 30 and 100 nm) at different time points and testing media, expressed as Ag⁺ concentration after centrifugation. A-C show the dissolution of 10, 30 and 100 nm at 0.25, 0.5, 1, 1.5, 2, 4 and 8 hours in UPW. Images D-F show the dissolution of the AgNPs in CCM at the previously mentioned sizes and time points. The figure shows the mean ± standard deviation (SD) (n = 3) of three independent replicates. Curves were fitted with GraphPad software using Nonlin fit model. Coefficient of determination (R²) for UPW curves: 10 nm, 0.98, 30 nm, 0.96, 100 nm, 0.96. R² for CCM curves: 10 nm, 0.98, 30 nm, 0.92, 100 nm, 0.90.

2.4.3 Lactate dehydrogenase activity (LDH) assay

The results for 10 nm AgNPs at 3 hours showed no effect on the LDH activity even at the highest concentration (60 µg/mL) (Figure 2.5) compared to the untreated control (naïve). On the other hand, the 30 nm and 100 nm showed a decrease of concentrations higher than 20 µg/mL (84.02 ± 2.86 %) and 30 µg/mL (82.91 µg/mL ± 1.91 %) respectively. After 24 hours, the enzyme activity noticeably decreased for all three sizes, indicating an EC₅₀

of 10 $\mu\text{g/mL}$ (the corresponding values were $50.52 \pm 4.59 \%$, $56.47 \pm 2.31 \%$ and $56.34 \pm 2.56 \%$ for the 10, 30 and 100 nm particles respectively). The LDH enzyme activity in cells exposed to the smaller size (10 nm), suggested that AgNPs are slightly more toxic after 24 hours, compared to the 30 and 100 nm sizes. The ionic counterpart (AgNO_3) showed an evident decline in enzyme activity after 3 hours, with a low concentration of 3 $\mu\text{g/mL}$ resulting in $74.88 \pm 2.23 \%$ cell viability compared to naïve cells ($98.80 \pm 2.06 \%$). After 24 hours, 1 $\mu\text{g/mL}$ AgNO_3 reduced the LDH activity to $82.93 \pm 3.55 \%$, followed by 2 $\mu\text{g/mL}$ with $50.37 \pm 2.36 \%$ and finally at 3 $\mu\text{g/mL}$, the enzymatic activity showed a dramatic decrease with values below 20% (Figure 2.5). This demonstrates that even the slightest increase in the AgNO_3 concentration can have a direct effect on depleting the LDH enzyme activity. Full results can be found in Tables S5, S6 and S7 in SI. Based on these results, a low, medium, and high concentration (2.5, 5, 10 $\mu\text{g/mL}$) for the three AgNPs sizes (10, 30, and 100 nm) and 1, 1.5 and 2 $\mu\text{g/mL}$ for the AgNO_3 (ionic control) were selected in order to evaluate whether the NP size and concentration influences the cytotoxicity and mode of cell death induced in ZF4 cells.

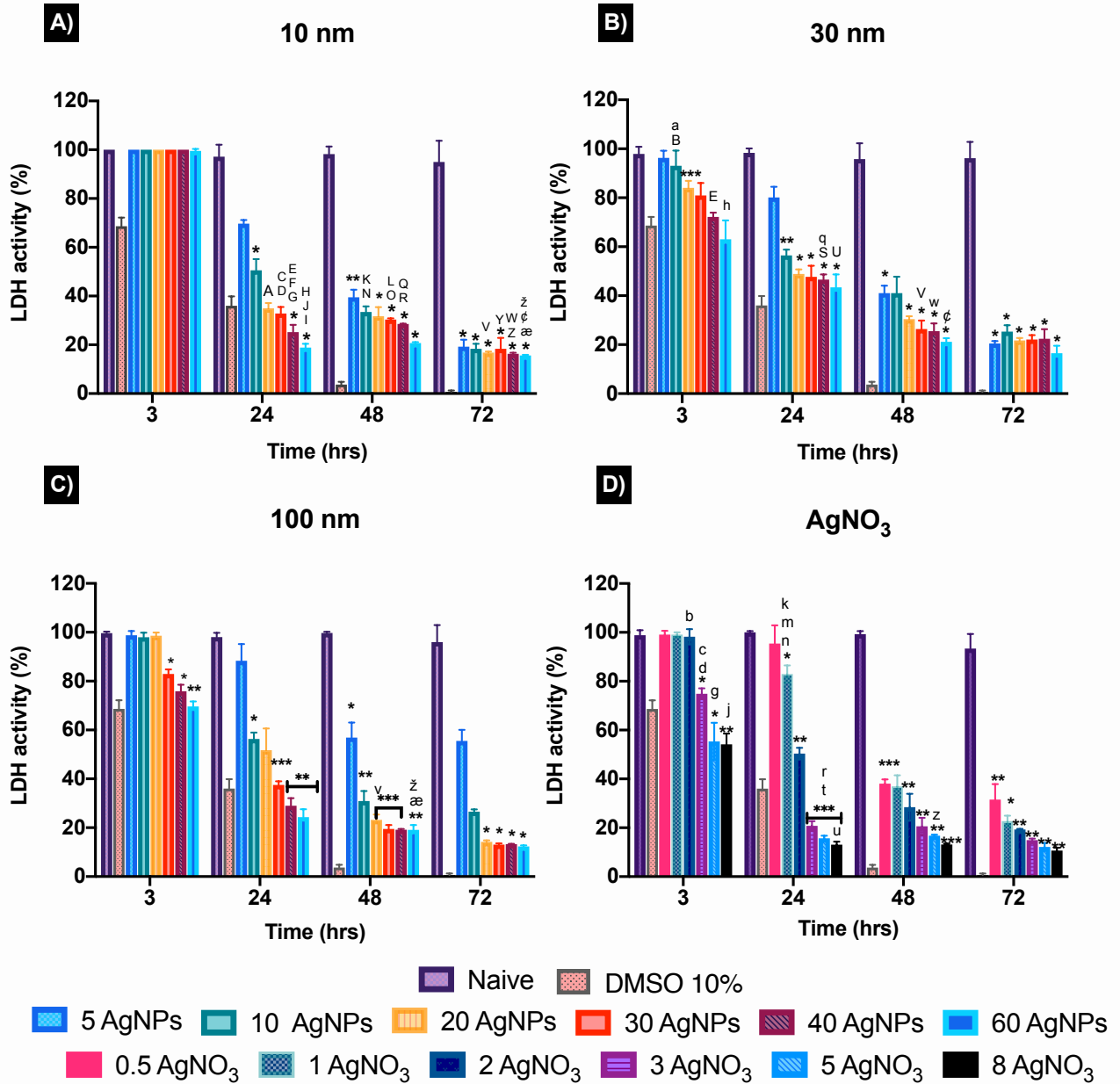


Figure 2.5. Viability of embryonic zebrafish cells (ZF4) treated with AgNPs and AgNO₃ for 3, 24, 48 and 72 hrs. The graphs show the percentage viability of ZF4 cells treated with 5, 10, 20, 30, 40 and 60 µg/mL of three different AgNPs sizes 10 nm (A), 30 nm (B), and 100 nm (C). Similarly, D) shows the viability of cells treated with 0.5, 1, 2, 3, 5, and 8 µg/mL of the ionic control (AgNO₃). A positive control of 10 % DMSO was also added. Graphs represent the mean ± standard deviation (SD) (n = 3) of three individual replicates. Data with asterisks (*) indicate a statistically significant difference of the AgNPs treatments (*p < 0.05, **p < 0.01, and ***p < 0.001) compared with naive cells at each time point. All bars under the brackets are included within the asterisk above. For dose-effect, a multiple comparison analysis between the NP concentrations at each time point was included. Bars with similar letters (upper and lowercase) indicate a statistically

significant difference ($p < 0.05$) between the selected concentrations, sizes, and AgNO_3 at the specific time point.

2.4.4 Autophagy induction

Autophagy results have been normalised from FITC intensities to % against the untreated control (naïve) as shown in the methodology. Figure 2.6 shows the autophagy response in cells after the treatment of AgNPs and AgNO_3 . The analysed results showed only a statistical difference ($p < 0.05$) for the 10 nm AgNPs at 5 $\mu\text{g}/\text{mL}$ (104.88 ± 3.17 %) relative to the naïve. Both 10 and 100 nm AgNPs showed a similar response trend, with autophagy induction at 2.5 $\mu\text{g}/\text{mL}$ (103.12 ± 1.47 and 102.71 ± 3.01 %) for 10 and 100 nm, respectively) and 5 $\mu\text{g}/\text{mL}$ (104.88 ± 3.17 and 101.95 ± 6.70 %) decreasing at the highest concentration (10 $\mu\text{g}/\text{mL}$), suggesting that autophagy process can be affected by cytotoxicity (Figure 2.6A). The 30 nm AgNPs displayed minimal autophagy dose-responses (100.10 ± 0.22 , 103.63 ± 0.69 , and 105.01 ± 0.73 % for the 2.5, 5 and 10 $\mu\text{g}/\text{mL}$ respectively) compared to naïve. The ionic control (Figure 2.6B) indicated inhibition of the autophagy response for all concentrations (1, 1.5 and 2 $\mu\text{g}/\text{mL}$) with 85.90 ± 15.84 , 92.40 ± 9.5 and 97.83 ± 4.41 % respectively, and compared to naïve cells, suggesting that there was no opportunity for the cells to recover. Images to ensure the viability, FlowJo histograms, as well as full values of the normalised results can be found in Tables S7.8 and S7.9 and Figure S7.1 in the SI.

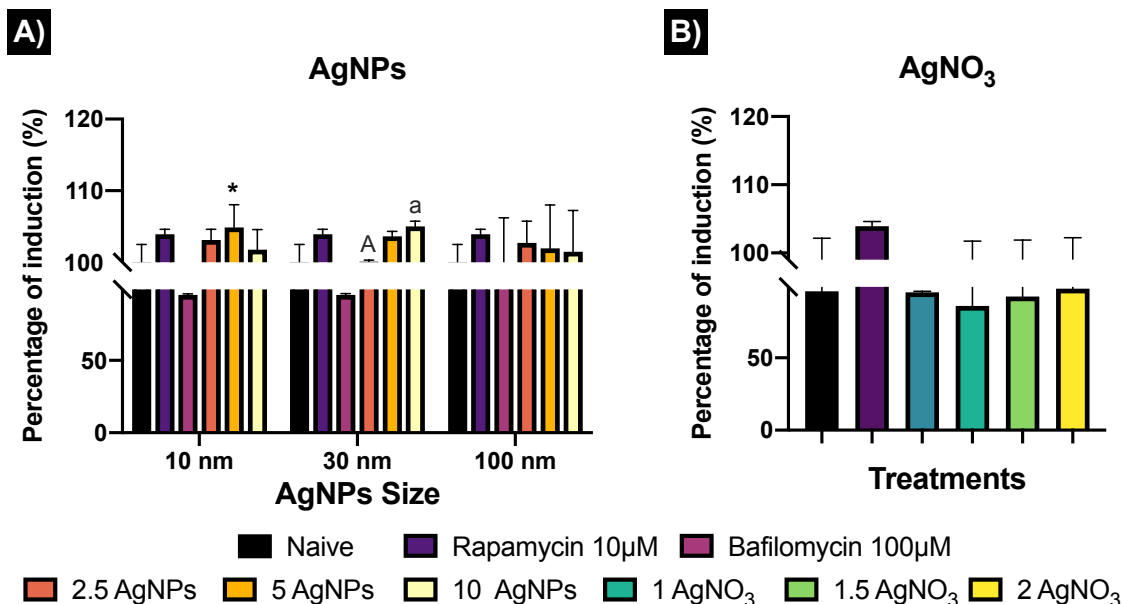


Figure 2. 6. Autophagy induction in ZF4 cells treated with AgNPs or AgNO₃ for 24 hours. Results represent the percentage (%) of autophagy induction against naïve. A) cells treated with 2.5, 5 and 10 µg/mL of AgNPs of three different sizes (10, 30 and 100 nm. B) Cells treated with 1, 1.5 and 2 µg/mL of AgNO₃. 10 µM Rapamycin and 100 µM Bafilomycin were included as controls to induce and decrease autophagy respectively for 2 hours. Data represent the mean of three individual replicates (mean ± standard deviation) (n = 3). Data with asterisks (*) indicate statistically significant difference of AgNPs treatments (p < 0.05) compared to naïve. Data with similar letters (upper and lowercase) represent statistically significant difference (p < 0.05) between the selected concentrations. No statistically significant differences were found between the AgNP sizes and/or AgNO₃.

2.4.5 Apoptosis and necrosis

Cell death plays a vital role regulating homeostasis and this is also reflected in morphological and biochemical changes in cells. AgNPs can disrupt the normal cellular function by inducing abnormal rates of cell death such as apoptosis and necrosis compared to the untreated controls. The results (Figure 2.7) revealed that 10 nm AgNPs induced a major percentage (%) of cell death at all AgNPs concentrations used (2.5, 5,

and 10 $\mu\text{g}/\text{mL}$) by 24 hours with 11.92 ± 4.03 , 17.95 ± 9.58 , and 21.30 ± 1.65 % of the ZF4 cells undergoing apoptosis and 15.77 ± 13.11 , 16.57 ± 12.31 , and 25.46 ± 5.52 % undergoing necrosis, respectively. The 30 and 100 nm sizes showed lower % cell death with a dose-response trend, as expected due to the lower numbers of particles with increasing particle size at constant mass dose [77]. On the other hand, all concentrations of the ionic control (AgNO_3) reduced cell viability and induced apoptosis and necrosis, with 19.81 ± 0.07 , 55.15 ± 0.45 , and 70.54 ± 2.28 necrotic cells at 1, 1.5, and 2 $\mu\text{g}/\text{mL}$ respectively. The untreated control (naïve) showed low percentages of both apoptosis and necrosis and high rates of viability. FlowJo scatter plots and full results can be found as Figure S7.2, as well as in Table S7.10 in the SI.

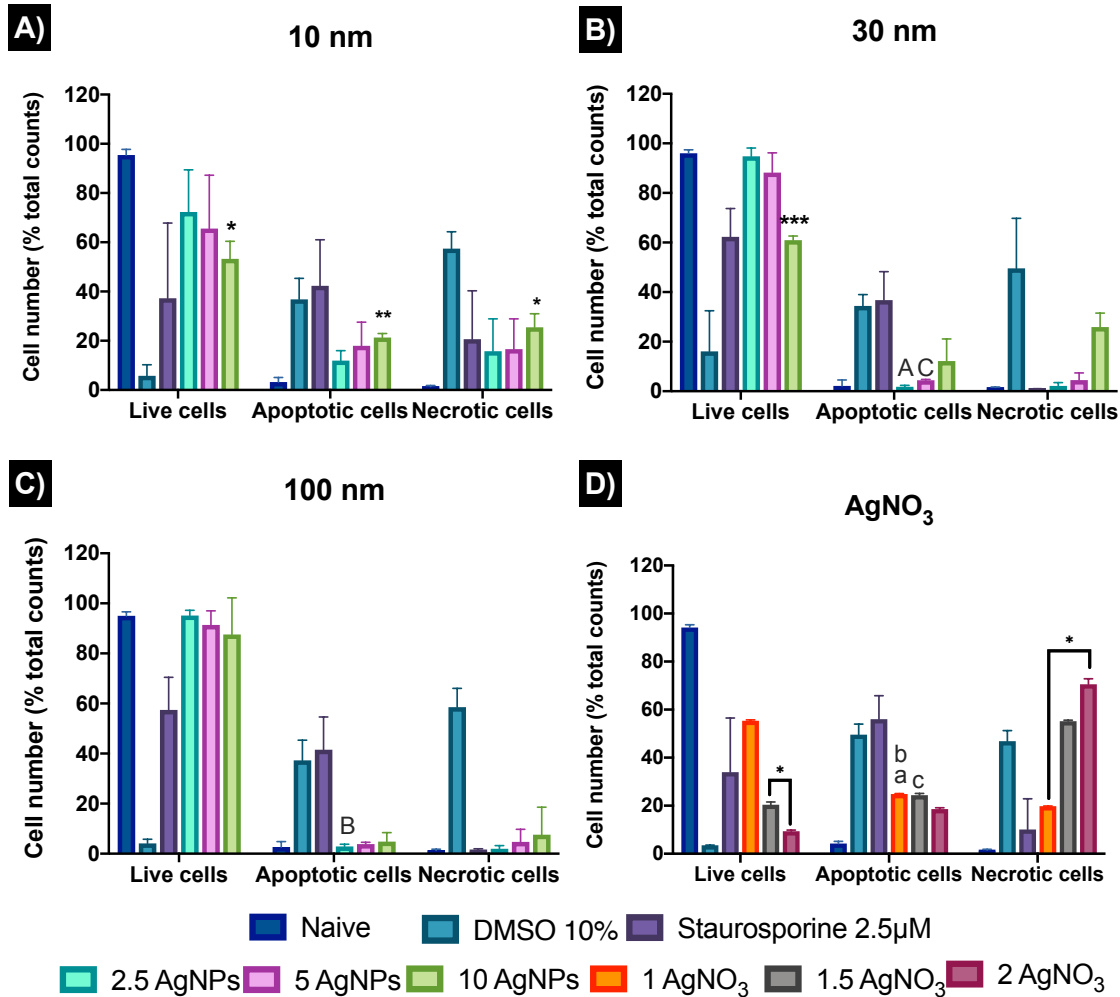


Figure 2. 7. Populations of ZF4 cells that were viable, apoptotic, and necrotic following treatment with AgNPs or AgNO₃ for 24 hours. A), B), C) Cells treated with 2.5, 5 and 10 μg/mL of 10, 30 and 100 nm AgNPs, respectively. D) Cells treated with 1, 1.5 and 2 μg/mL of AgNO₃. 10% Dimethyl sulfoxide (DMSO) and 2.5 μM of staurosporine were included as positive controls for apoptosis and necrosis, respectively. Graphs represent the mean of three individual experiments. The bars show the mean ± standard deviation (SD) (n = 3) of three individual replicates. Data with asterisks (*) indicate statistically significant difference of AgNPs treatments compared to naive (*p < 0.05, **p < 0.01, and ***p < 0.001). All bars under the brackets are included within the asterisk above. Similar letters (upper and lowercase) above the bars denote statistically significant differences (p < 0.05) between the selected treatments.

2.4.6 Mitochondrial membrane potential

To further analyse the role of the mitochondria in the activation of intrinsic cell death mechanisms, MitoHealth staining was used to assess the mitochondrial membrane potential ($\Delta\Psi_m$), rather than cytotoxicity, which can also be evaluated by the assay (DEAD Green™ viability stain). The MitoHealth stain accumulates in the mitochondria of live cells, producing higher fluorescence in healthy cells, proportional to the mitochondrial membrane potential ($\Delta\Psi_m$), hence a decrease in the fluorescence intensity reveals that the mitochondrial membrane has been compromised, leading to mitochondrial dysfunction [280]. In addition, cells were visualised using a fluorescent microscope with representative images shown in Figure 2.8.

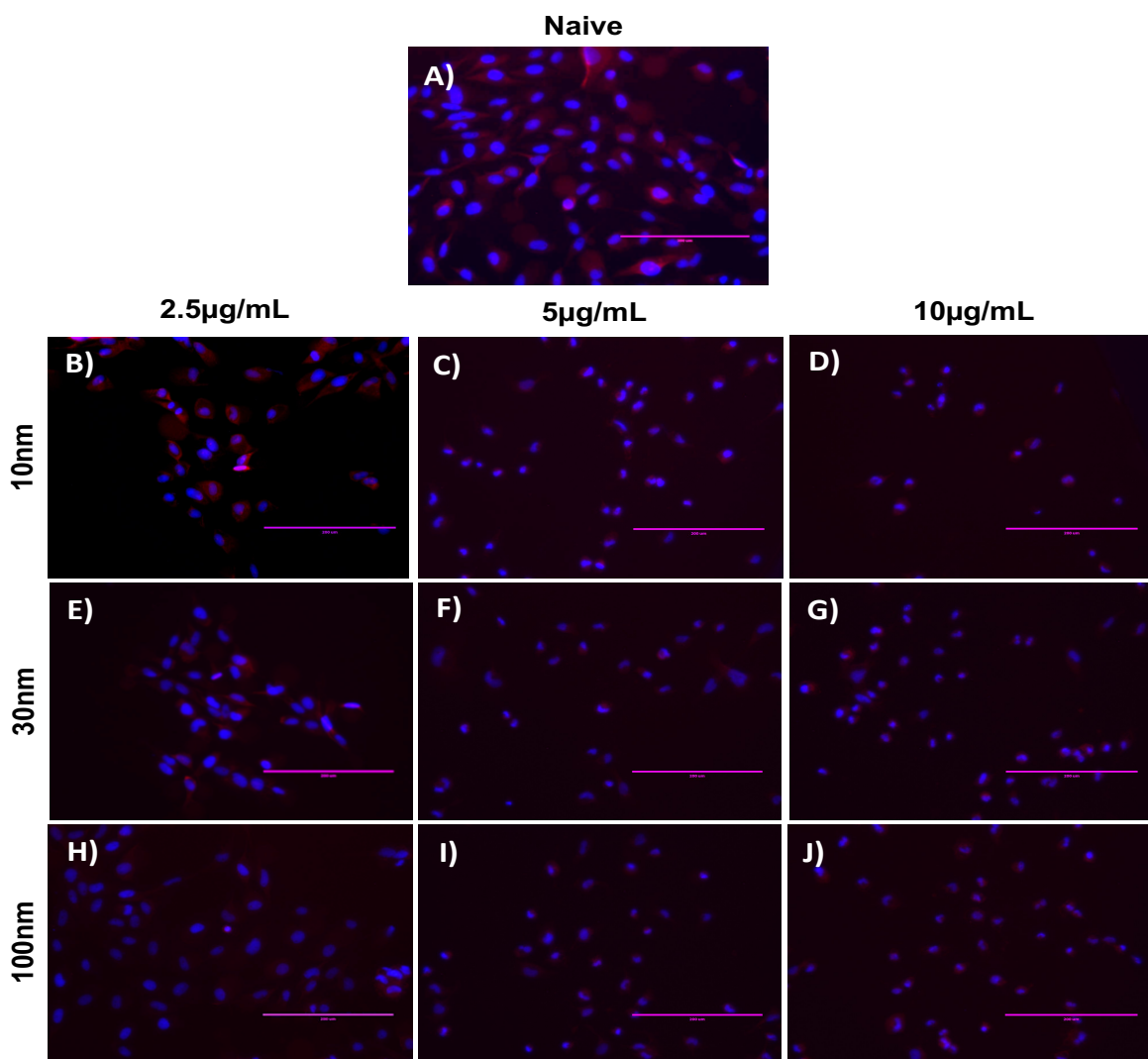


Figure 2. 8. ZF4 cells stained with MitoHealth to assess mitochondrial permeability. Cells were treated with three different AgNPs sizes and 1, 1.5 and 2 $\mu\text{g}/\text{mL}$ of AgNO_3 for 24 hours. A) untreated cells B-D) cell treated with AgNP-concentrations (2.5, 5 and 10 $\mu\text{g}/\text{mL}$) for the 10 nm size. E-G) cell treated with above concentrations for the 30 nm size. H-J Cells treated with 2.5, 5 and 10 $\mu\text{g}/\text{mL}$ of 100 nm AgNPs. Blue staining shows the cell nuclei, bright red staining shows the MitoHealth dye in healthy mitochondria, permeabilization of the mitochondrial membrane shows a reduction in the red dye intensity. Images were taken with a fluorescence microscope using a 20X objective and optical zoom. Scale bar is 200 μm .

The results presented in Figure 2.9 been normalised from fluorescence signal intensity to percentage (%) against naïve, with normalised values shown in Table S7.13 in the SI.

Results for the 10 nm AgNPs displayed the lowest normalised intensity values for mitochondrial membrane potential compared to the other AgNP sizes, with 87.35 ± 5.95 % at 2.5 $\mu\text{g/mL}$, 88.98 ± 4.55 % at 5 $\mu\text{g/mL}$ and 90.54 ± 6.97 % at 10 $\mu\text{g/mL}$ compared to naïve cells with 100 ± 4.03 (healthy membranes taking up fluorescence), suggesting that the low and medium concentrations noticeably disrupt the mitochondrial membrane, whereas the highest concentration (10 $\mu\text{g/mL}$) disrupted the mitochondria less (reduction of just <10% compared to naive). On the other hand, the 30 nm AgNPs displayed the highest membrane disruption values at 2.5 $\mu\text{g/mL}$, showing a low normalized fluorescence intensity, with (85.61 ± 3.5 %), followed by the higher concentration (10 $\mu\text{g/mL}$) with 87.2 ± 6.6 %; whereas the medium concentration (5 $\mu\text{g/mL}$) showed higher normalised intensity values (90.74 ± 4.65 %), which suggests low membrane potential. Similarly, the 100 nm AgNPs induced very limited damage to mitochondrial membrane (as shown in their high normalised intensity values), compared to the 10 and 30 nm AgNPs sizes with 94.7 ± 4.5 , 90.2 ± 2.7 and 87.5 ± 0.3 % for 2.5, 5 and 10 $\mu\text{g/mL}$ respectively. The ionic control displayed a high degree of mitochondrial disruption at the medium (1.5 $\mu\text{g/mL}$) and high (2 $\mu\text{g/mL}$) ionic concentrations (low fluorescence intensity values), with minimal differences between concentrations with 86.94 ± 7.91 and 86.89 ± 3.75 %, respectively. On the other hand, the lowest concentration (1 $\mu\text{g/mL}$), showed low membrane potential values, as demonstrated in its high normalised intensity value (95.22 ± 3.66 %), suggesting that cells were able to cope with a low Ag^+ concentration; however, minimal changes in the ionic Ag concentration induced higher percentages of mitochondrial disruption and therefore higher loss of membrane potential. Full results can be found in Tables S7.11 and S7.12 in the SI.

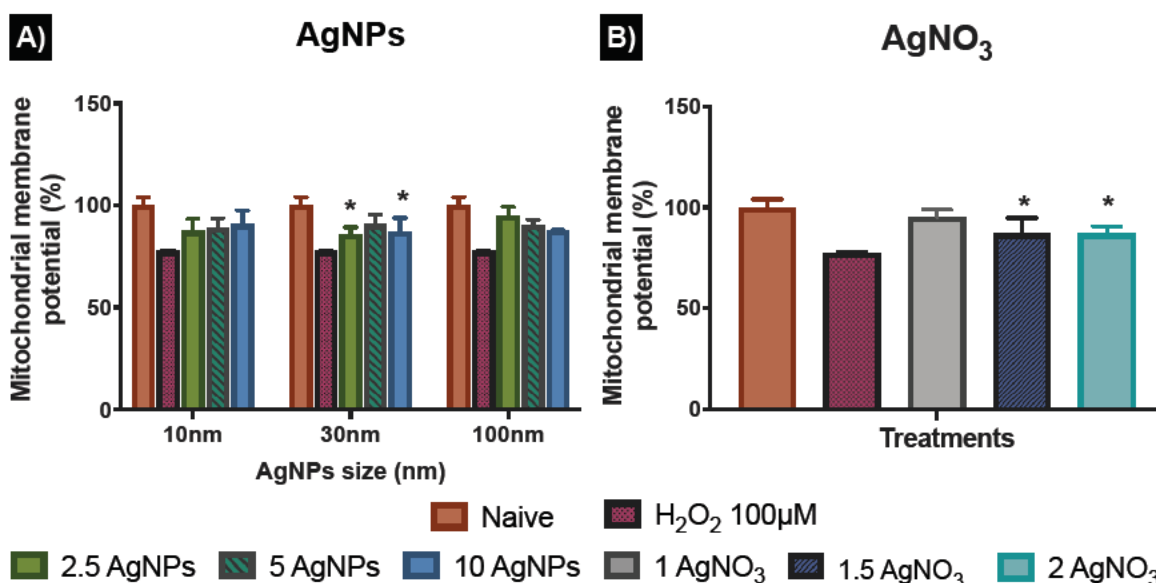


Figure 2.9. Mitochondrial membrane permeability of ZF4 cells treated with AgNPs or AgNO₃ for 24 hours. MitoHealth staining was used to assess the mitochondrial membrane potential by producing higher fluorescence in healthy cells (100 %), whereas a decrease in the fluorescence intensity reveals damage to the mitochondrial membranes. A) Cells treated with 2.5, 5 and 10 µg/mL of AgNPs with three different sizes (10, 30 and 100 nm. B) Cells treated with 1, 1.5 and 2 µg/mL of AgNO₃. Hydrogen peroxide (100 µM) was included for 30 minutes as positive control to induce mitochondrial membrane damage, inducing mitochondrial membrane permeability and low intensity values. Data represent the mean of three individual replicates. The figure shows mean ± standard deviation (SD) (n = 3) of three individual replicates. Data with asterisks (*) indicate statistically significant difference of AgNPs treatments compared to naive (*p < 0.05). No statistically significant differences were found between NP sizes.

2.4.7 Lipid peroxidation

During autophagy, cytoplasmic materials and/or old and damaged organelles are engulfed by autophagosomes and transported to lysosomes for digestion by lysosomal enzymes [281]. Hence, to further analyse the interactions between generation of ROS, autophagy and lysosomes, the cellular degradation of lipids was analysed. Results show the ratio of the fluorescence of Texas red to FITC, which can be described as results with

higher ratio equal to less lipid peroxidation, whereas lower ratio represent major peroxidation rates. The results displayed (Figure 2.10), as expected, a higher ratio of fluorescence (590/520 nm) in the untreated control (0.78 ± 0.21) compared to the positive control (0.678 ± 0.17) and the AgNPs and AgNO₃ treatments. The 10 nm and 30 nm AgNPs displayed a lipid peroxidation concentration-response trend, indicating that at higher AgNP concentrations the cells increase the production of free radical species and consequently show major rates of lipid peroxidation. In addition, the 10 µg/mL concentration for the smallest size (10 nm ANPs) indicated a major induction of lipid peroxidation. The 100 nm results showed an inverse concentration-response, indicating major lipid peroxidation production at the lowest concentration (2.5 µg/mL). The AgNO₃ treatments were even more powerful in inducing lipid peroxidation than the cumene hydroperoxide positive control (0.58 ± 0.38), with 0.38 ± 0.05 , 0.36 ± 0.09 and 0.28 ± 0.09 for 1, 1.5 and 2 µg/mL respectively, demonstrating their high toxicity. Full results showing the ratio of the fluorescence of Texas red to FITC for all treatments can be seen in Table S7.13 and S7.14 in the SI.

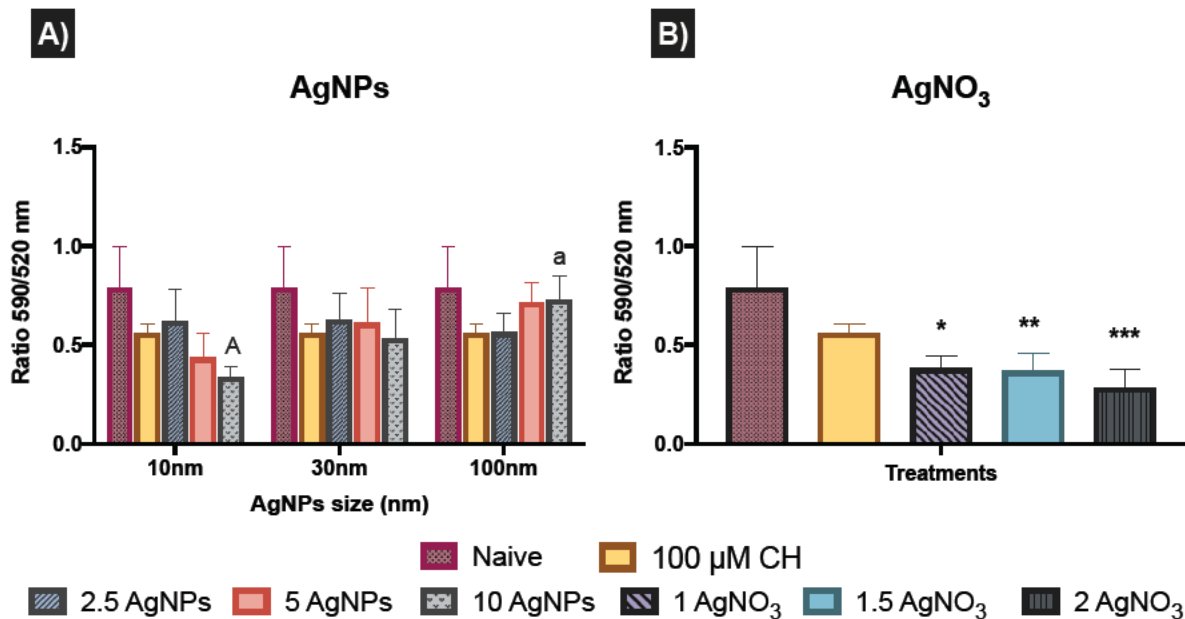


Figure 2. 10. Lipid peroxidation in ZF4 cells treated with AgNPs or AgNO₃ for 24 hours. Results are presented as the ratio of the fluorescence of Texas red to FITC. A) Cells treated with 2.5, 5 and 10 µg/mL of AgNPs of three different sizes (10, 30 and 100 nm). B) Cells treated with 1, 1.5 and 2 µg/mL of AgNO₃. Cumene hydroperoxide (CH) was included (100 µM) for 2 hours as positive control to induce lipid peroxidation. The figure shows mean ± standard deviation (SD) (n = 3) of three individual replicates. Data with asterisks (*) indicate a statistically significant difference (*p < 0.05, **p < 0.01, and ***p < 0.001) of AgNPs and AgNO₃ treatments compared to the untreated control. Similar letters (upper and lowercase) above the bars denote statistically significant difference (p < 0.05) between the selected NP sizes.

To gain further insights into how the cell mechanisms (apoptosis, necrosis, autophagy, mitochondrial membrane potential, and lipid peroxidation) are activated based on cellular responses to the different AgNP treatments and the AgNO₃ controls, all the analysed mechanisms were normalised to percentages and transformed to ratios against their untreated control (naïve). Normalised results were plotted using Graphpad to represent the molecular process the cells undergo as shown in Figure 2.11, which presents the relative strength of the contributions, with the caveat that the % of cells undergoing each

process are very different. Since we know there are baseline levels of these events in normal cells as part of homeostasis, a representation of the untreated ratio of the relative weightings of these 5 processes is also included for comparison.

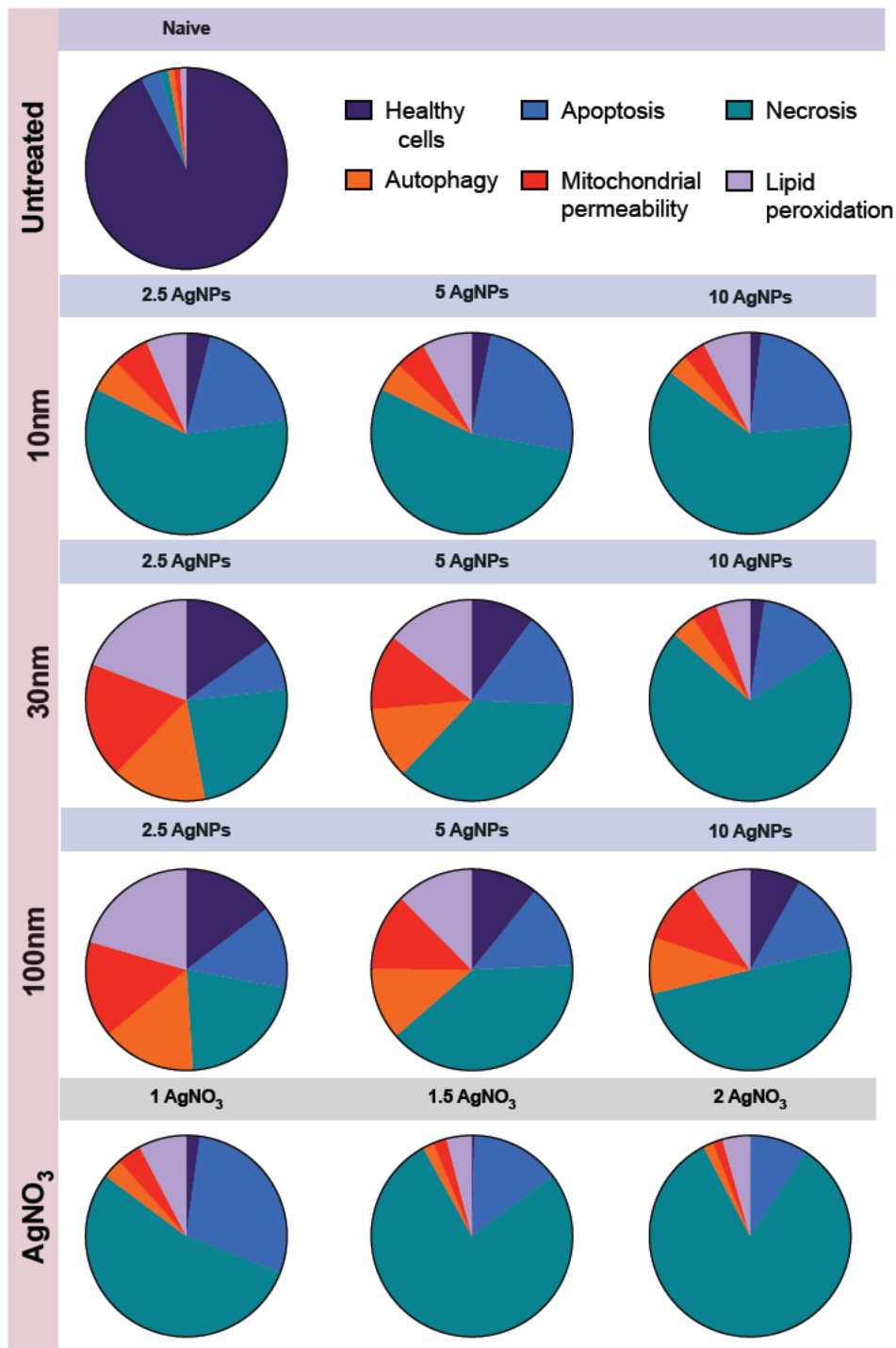


Figure 2. 11. Comparison of all the data presented in Figures above. Results for all the analysed cellular mechanisms for the AgNPs sizes (10, 30 and 100) and AgNO₃ concentrations were normalized to percentage and then to ratio against their respective untreated control. The figure presents the relative strength of the contributions of the cellular mechanisms assessed. AgNPs and AgNO₃ concentrations are presented in µg/mL.

2.5 Discussion

Environmental exposure to NPs is inevitable as they have become part of our daily life, resulting in potential toxicity to biological systems. Therefore, assessment of the interactions between the NPs and the surrounding environment are key to further understanding toxicity outcomes in the biological system [57]. The aquatic environment contains natural organic matter (NOM), which includes a complex matrix of peptides, proteins, and polysaccharides. The medium components can strongly interact with silver in aqueous solution, influencing the physicochemical properties of the AgNPs and consequently affecting their fate, bioavailability, and toxicity [45, 58, 282]. For this reason, characterisation of the AgNPs was performed in simplified media (ultrapure water, UPW) and complex media (complete culture medium containing 10% proteins) in order to correlate the behaviour of the NPs in relevant biological fluids with their impacts [58, 283, 284].

The size distribution assessed by DLS in water versus cell media revealed that the FBS had a direct impact on the physicochemical characteristics of the AgNPs (Table 1-4 SI). The size of the three AgNPs increased in CCM, leading to similar hydrodynamic diameter for 10 and 30 nm AgNPs after 24 hours. The smaller the particle size the higher their tendency to agglomerate in order to reduce their surface area [58, 81, 285]; similarly, large proteins may be able to bind more than one particle or bridge between smaller particles leading to some apparent agglomeration in CCM [278, 286]. In addition, the charge of the NPs can also be affected by the surrounding environment. For example, the zeta potential in CCM became less negative than in water (around -11 mV) due to

charge neutralization, shielding and bridging interactions of serum proteins; a process that can also occur in freshwater systems due to the high ionic strength and NOM concentrations [287, 288].

Particle dissolution is a dynamic process that may occur in aqueous environments, involving the migration of molecules from the NP surface to the bulk solution by crossing a diffusion layer that is heavily populated with a range of molecules and ions with different affinities for silver [289]. The dissolution experiments demonstrated that dissolution of the NPs is strongly affected by the size of the NPs and the surrounding medium composition, as demonstrated by other authors, especially in the presence of sulphides, organic matter and proteins [58-60, 249]. Similarly, other authors demonstrated that chloride ions (Cl^-) can strongly influence AgNP precipitation and chemical transformation to AgCl, as well as mediating their cell viability and toxicity [58-60, 249, 290]. Furthermore, it is important to mention that the results for dissolution of AgNPs in UPW is far from realistic conditions in a biological environment; however, this simplified testing system can provide insights about how the complex environment may affect the physicochemical characteristics of the NPs. The 10 nm AgNPs in UPW presented around 20% dissolution, followed by the 30 nm with 10% and lastly the 100 nm just 0.25%. On the other hand, dissolution of the 10 and 30 nm AgNPs in CCM decreased 10-fold, with 2 and 1 % respectively. Interestingly, the 100 nm showed a slightly higher percentage of dissolution in CCM (0.05 %) than in water. This can be related to the dynamics of the dissolution process, which is strongly influenced by the solute concentration, surrounding environment, and the NP's characteristics, such as surface area, morphology, surface energy, and size [289]. For example, the presence of biomolecules can either enhance or inhibit the dissolution of

the NPs, as the binding of the organic compounds to silver ions alters the equilibrium of the NPs and thus the dissolution kinetics [291-293]. Moreover, a strong relationship between the size of the NPs and their % dissolution has been observed previously [55, 56, 221, 294]. For example, George et al. (2012), demonstrated that the release of Ag ions was higher for 10 nm Ag nanospheres compared to bigger sizes (20 and 40 nm), going from 290 to 850 ppb of dissolved Ag species in zebrafish medium [294]. Other studies have shown similar particle size-dependent dissolution results, speciation of the NPs, as well as interactions between the NPs and the biomolecules in complex environments [55, 56, 58, 62]. Furthermore, AgNPs may have released silver ions (Ag^+) and other ion-ligand complexes (Ag speciation) in CCM, affecting the total detected Ag concentration and toxicity [52, 62, 249].

Although the results for dissolution in complex medium (8 hours) were 10-fold lower, there is still a fraction of dissolved silver that may interact with the biological systems, posing a risk to the aquatic species. Toxicity of AgNPs resulting from release of ionic silver has been previously described in aquatic organisms, e.g. rainbow trout (*Oncorhynchus mykiss*) cells [58, 290, 292, 294, 295], while long-lasting effects of AgNPs in zebrafish (*Danio rerio*) embryo were also confirmed [59, 60, 249]. Aquatic organisms may encounter multiple Ag-forms in nature, as environmental Ag concentrations may represent both particle and ionic forms, which may be mainly derived from wastewater treatment plants. For example, a study by Syafiuddin et al., (2018) estimated AgNPs concentrations between 0.13 to 20 $\mu\text{g}/\text{mL}$ in Malaysia's wastewater treatments plants, with potential to increase up to 70-fold due to the high production volumes of AgNPs-based products [36, 37]. On the other hand, it was particularly challenging to assess the

dissolution of the AgNPs in CCM with the protocol used in water, mainly due to the blockage of the centrifugal filters, which may be related to the proteins in the cell media, agglomeration of the NPs, and/or complexation of released Ag to form ionic species such as AgCl [115]. Therefore, other procedures to assess the dissolution of the AgNPs in complex media (e.g., dialysis) are recommended for further investigation.

The content of silver in cells was not measured in this study, hence the intracellular concentration of AgNPs which induces most of the toxicity outcomes in this study is still unknown; however, this will be discussed in later chapters. Despite these limitations, different biological effects were observed in ZF4 cells exposed to the three AgNPs (10, 30 and 100 nm) used in all the biological assays. The 10 nm AgNPs displayed concentration-dependent cell death and overall, a higher induction of cellular stress mechanisms, compared to the medium and large NPs. These results agree with other authors such as [296], who demonstrated that the smaller the particle size, the greater the biological effects when comparing the particles at constant mass concentration [296, 297]. Even though mass concentrations were used in this study, it is important to consider that each AgNP has very different particle number concentrations. To further explore this, calculations to estimate the number of particles for each particle size and concentration (Figure 2.12). Calculations were performed as described by Huk et al. (2014) and Book et al. [77, 297] (see SI for the specific steps), where the number of particles for each size was obtained from the manufacturer's technical specifications available here: <https://nanocomposix.com/products/biopure-silver-nanospheres-pvp?variant=15906691874905#target>

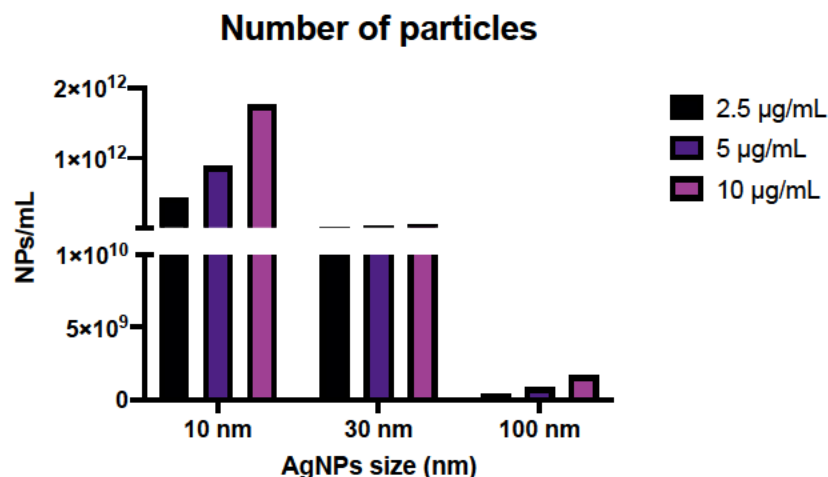


Figure 2. 12. The number of particles at the different AgNPs mass concentrations. The mass concentrations used in this study (2.5, 5, and 10 µg/mL) were re-calculated to show the number of particles per mL. The graph also illustrates the estimated number of NPs that would reduce cell viability by 50% after 24 hours.

Based on these estimations, the toxicity of the smaller AgNPs perhaps can also be related to the fact that there are 1000 times more particles at the highest 10 nm concentration (1.76E+12 NPs/mL) than for the equivalent mass dose (10 µg/mL) of 100 nm AgNPs (1.67E+09 NPs/mL). Therefore, normalising results by particle number may lead to different interpretation of the outcomes, whereby the larger particles could be considered as the most toxic on a particle number basis. This is related to the fact the 100 nm requires a smaller number of particles to decrease the cell viability to 50% (EC₅₀), inducing equivalent cell damage as the smaller AgNPs sizes (10 and 30 nm) when comparing at a mass concentration of 10 µg/mL; this is important to consider when evaluating toxicity of NMs of different sizes. Calculations to obtain the particle number concentration, including full normalised data to particles number can be found in section 7.2.8 of the SI and Table S7.15 in the SI.

Particle uptake is another aspect to consider in NP toxicity [52, 298, 299]. It is conceivable that the toxicity of the 10 nm AgNPs can be linked to the fact that smaller particles can be internalised by the cells more easily and in larger numbers (at constant mass there will be significantly more 10 nm particles than 100 nm NPs as shown in Table 11 in SI), as suggested by other studies [100, 300]. Moreover, another property that shows variation by orders of magnitude is the particle surface area, as small NPs have a larger surface area (SA) compared to the larger AgNPs at constant mass [297]. To verify this, a series of calculations based on the hydrodynamic diameter after 24 hours were performed to obtain the total SA for the NPs at the different mass concentrations (2.5, 5 and 10 µg/mL) [297, 301]. Estimation of the SA demonstrated that the smaller NPs have almost double the SA at 10 µg/mL ($6.22 \times 10^5 \text{ m}^2/\text{g}$) of the 100 nm ($3.67 \times 10^5 \text{ m}^2/\text{g}$), whereas the 30 nm remains in the middle of both sizes with a total SA of ($5.78 \times 10^5 \text{ m}^2/\text{g}$) (Table 2.1). Calculations steps can be found in section 7.2.9 of the SI.

Table 2.1. Total surface area for AgNPs of different sizes at the different mass concentrations utilised. The total surface area was calculated for the three different sizes and mass concentration used in the study. The calculated values are in m^2/g .

AgNPs Size	AgNPs concentration		
	2.5 µg/mL	5 µg/mL	10 µg/mL
10 nm	1.34E-05	2.72E-05	5.78E-05
30 nm	1.59E-05	3.11E-05	6.22E-05
100 nm	9.41E-06	1.85E-05	3.67E-05

Small NPs typically undergo faster dissolution (as demonstrated here in the dissolution studies in Figure 2. 4) increasing their potential toxicity compared to the larger particles [296, 299]. Autophagy can be related to the AgNPs concentration and influences the

induced cell death mechanisms. For example, we found that autophagy was only induced in the presence of NPs, in contrast to the ionic control (AgNO_3) where a decrease in the autophagy levels were apparent. Based on this, autophagy can be linked to cell viability, as AgNO_3 at all concentrations displayed major induction of necrotic cell death, compared to the low AgNPs concentrations. The highest AgNPs concentrations also showed a decrease in the autophagy levels, resulting from the increased necrotic cell death, except for the 30 nm size that showed a clear increase in autophagy with increased AgNP concentration. This suggests that the ZF4 cells are deal with low concentrations of AgNPs by activation of cell death modalities such as apoptosis and autophagy as an attempt to overcome the NP toxicity. However, at high AgNPs concentrations, the cells induce necrosis as they cannot overcome the irreversible damage, as suggested by other authors [267, 302]. The complex relationship between NPs, autophagy, and lysosomal dysfunction has been suggested by several studies [178, 303-305]. Lysosome membrane permeabilization is a key feature of autophagy, which may lead to mitochondrial damage, generation of oxidative stress products and then apoptosis, while massive lysosome permeabilization will lead to cytosolic acidification and necrosis [305-307] [267, 302].

The complex relationship between NPs, autophagy, and lysosomal dysfunction has been suggested by several studies [178, 303-305]. Lysosome membrane permeabilization is a key feature of autophagy, which may lead to mitochondrial damage, generating oxidative stress products and then apoptosis, while massive lysosome permeabilization will lead to cytosolic acidification and necrosis [305-307]. Our results agree with these findings, as NPs and ionic Ag could have induced lysosomal dysfunction, leading to the observed mitochondrial dysfunction, lipid peroxidation and consequent

reduction in the autophagy activity, as previously suggested. In addition, Ag^+ may have a key role in the autophagy pathway, as all the AgNO_3 concentrations indicated a decrease in the autophagy levels in an inverse dose-response manner in terms of the levels of lipid peroxidation. Equally, the highest concentrations of the AgNPs showed a drop in the autophagy levels and high levels of lipid peroxidation, except by the 100 nm size that showed an inverse lipid peroxidation-response trend, as well as low mitochondrial membrane potential. These results may suggest that lysosomal dysfunction and reduced autophagy activity are closely interrelated, when lysosomes are being disrupted, the autophagy response cannot be activated as suggested by other authors [178, 303, 305]. Results observed for the 100 nm AgNPs suggest that larger NPs induce peroxidation and autophagy responses at low concentrations, while higher concentrations reduce autophagy levels with lower lipid peroxidation rates, compared to the lowest AgNPs concentration. Some studies suggest that induction of autophagy is coupled with mitochondrial degradation and apoptosis, as autophagy can lead to, or even activate, apoptosis by triggering the activation or inhibition of caspases and/or endogenous apoptosis inhibitors [174, 296, 308]. Interestingly, the results for autophagy and mitochondrial membrane permeabilization share similar fractional values (Figure 2.11); this suggests that perhaps autophagy is degrading the mitochondria, a process known as mitophagy, suggested by several authors as a way to eliminate damaged mitochondria that have low membrane potential, thus increasing the autophagy response and damage of the mitochondrial function [174, 308]. Furthermore, it is conceivable that the size of the NPs may influence mitochondrial permeabilization and apoptotic cell death via the mitochondrial pathway, as our results showed an increase in the mitochondrial

permeability and apoptosis for medium and large size NPs (30 and 100 nm); similar results published by Zhao et al., (2019), revealed that 270 nm TiO₂ NPs induced mitochondrial fragmentation and ROS in HT22 cells [309]; while Yang et al., (2019), demonstrated that 60 nm silica NPs induced dose-dependent disruption in the mitochondria of hepatoma HepG2 cells, suggesting that NPs may be internalised by the endocytic pathway [296]. Similarly, another study of AgNPs and ionic Ag induced oxidative stress and disturbances to the lysosomes and mitochondria of fish hepatoma cell line PLHC-1 [113].

The cellular interaction with intracellular and extracellular NPs might lead to the destabilization of the lysosomal membranes, as well as the release of hydrolase and protease enzymes into the cytosol, triggering the apoptotic machinery and other signalling pathways, such as mitochondrial dysfunction and ROS [296, 309, 310]. In addition, the induction of oxidative stress may produce large amounts of hydrogen peroxide that will react with the ferruginous materials in the cell, inducing autophagy, mitochondrial ROS, and the degradation of membrane phospholipids by the activation of phospholipase A2 [305, 310]. Based on the summary of our results (Figure 2.11), AgNPs concentrations between 2.5 µg/mL and 5 µg/mL induced high levels of apoptosis and mitochondrial permeability for 30 and 100 nm AgNPs. The 10 nm AgNPs showed lower levels of mitochondrial permeability but higher lipid peroxidation. The data suggest that after AgNP internalization the ZF4 cells triggered lipid peroxidation products and induced apoptosis, perhaps through the mitochondrial and lysosomal dysfunction pathways [178].

The AgNPs concentrations between 2.5 µg/mL and 5 µg/mL induced major rates of apoptosis and mitochondrial permeability for 30 and 100 nm AgNPs, compared to the

smaller 10 nm AgNPs, that indicated lower rates of mitochondria permeability but higher lipid peroxidation values, suggesting that the cells were able to cope with low concentrations of medium size AgNPs, after their internalization, triggering lipid peroxidation products and inducing apoptosis, perhaps through the mitochondrial and lysosomal dysfunction pathways [178]. The results obtained in this study agree with similar findings from *in vivo* and *in vitro* studies. For example, Kim et al., (2013) demonstrated that smaller AgNPs (20 nm) were more toxic than larger NPs (110 nm) on zebrafish embryos at a concentration of 10 mg/L [265]. Similarly, Lee et al. (2018) showed a size dependent toxicity of AgNPs (30-72 nm) on zebrafish embryo, showing that under conditions where the NPs dissolved toxicity was observed with Ag⁺ ions penetrating the chorionic pores, while there was limited toxicity if the NPs agglomerated as they did not come into contact with the zebrafish embryo [249]. The chorion thus serves as a protective barrier reducing the likelihood of molecules to reach the target site(s) in the embryo [203], especially limiting access of NPs due to their size and agglomeration tendencies. In addition, a study by Bilberg et al., 2012, demonstrated that the acute toxicity of AgNPs and Ag ions was different in zebrafish adults, showing an LC₅₀ at 89 µg/L for the NPs; besides, in this study the Ag ions behaved differently than the NPs, showing major effects at lower concentrations (LC₅₀ 28 µg/L) [264].

Certainly, the literature provides a wide range of studies involving the use of zebrafish as a toxicological model [264, 265, 311, 312]. However, most of these studies require an ethical licence and do not consider differences in toxicity during early developmental stages [311]. It has been shown that fish are nociceptive and able to experience pain in an analogous manner as in mammals. Thus, the development of

alternatives to screen the toxicity of xenobiotics is urgently needed [313]. The use of zebrafish cell lines can provide opportunities for the development of new alternatives toxicity models, mainly due to their advantages, such as low cost and maintenance of transient cell populations. Unlike zebrafish embryos and whole fish, zebrafish cells can be cultured with faster and efficient approach, without specialised equipment for their culture and time-consuming maintenance [227]. Furthermore, fish cell lines have been demonstrated to proliferate in serum-free medium conditions [292], as well as providing sensibility and good agreement correlation between *in vivo* and *in vitro* exposures in many toxicological assays [159, 214, 255, 314]. For example, studies by Bury et al., (2014) and Tannerberger et al., (2013) showed a significant correlation in the responses of rainbow trout fish gills (*in vivo*) and fish gill cells (*in vitro*) to exposure to pharmaceutical and chemical compounds, demonstrating less than 5-fold difference in the responses and similar modes of action in both biological systems [255, 314]. Another study by Fent et al., (2012) demonstrated that cell cultures can be used as reliable predictors of potential *in vivo* outcomes, showing that hepatocellular carcinoma (PLHC-1) fish cell line positively correlated with the induction of cytochrome P4501A as in topminnow fish (*Poeciliopsis lucida*) [214]. Similarly, an interrelated dose-dependent toxicity was demonstrated in fish cells (BF2) and zebrafish embryos treated with 12.5 and 25 µg/mL of AgNPs, under dark and simulated light exposure conditions [159]. These studies suggest that embryonic zebrafish cells (ZF4) can be further explored as a sensitive early stage ecotoxicological model, as compared to other commercially available cell lines, such as gill and liver cells that were stabilised from zebrafish adults, ZF4 cells was established from 1-day-old zebrafish embryos, enabling their use as an additional endpoint in the study of acute

toxicity fish test, and contributing to a tiered approach [315]. The biological responses of ZF4 cells induced during the exposure of NPs, can also contribute to fill the gaps between molecular initiating events and adverse outcomes for NMs as part of an Adverse Outcome Pathways (AOPs) framework; as well as providing faster screening of nanotoxicity, with results that can be further correlated with *in vivo* exposures and computerized modelling risk assessment extrapolation approaches [256, 313]. Furthermore, the use of continuous ZF4 cells line can also offer a longer term chronic exposures, providing opportunities for adhering to the 3Rs principles towards the refinement, reduction, and replacement of animal-based toxicity tests [212]. Certainly, the evaluated molecular responses in ZF4 cells will need further investigation; however, the identified biochemical pathways uncovered a field that can be further explored with promising results, as the molecular mechanisms explored in this study can also be found in mammal cell-based models, embryonic and fish stages, facilitating their interpretation and resulting in a 21st century approach for nanotoxicological assessments.

2.6 Conclusions

Toxicological risks arise from the likelihood of AgNPs ending up in the environment, along with their environmental transformations and fate in complex environments, such as dissolution and toxicity. Our results demonstrated that AgNPs underwent dissolution, as well as changes in hydrodynamic diameter, zeta potential and polydispersity index in CCM and water, depending on particle size and concentration. Moreover, results displayed clear differences in the ZF4 responses to the different sizes and doses of AgNPs, including distinct separation of the AgNP versus ionic Ag cellular responses as

well as the close interrelation between all the evaluated processes, which was displayed in the activation or inactivation of different pathways after the exposure of NPs. AgNPs were able to affect the cellular membranes inducing lipid peroxidation, whereas internalised NPs affected autophagy process, leading to release of NPs into the cytosol, inducing dysfunction of lysosomes and permeabilization of the mitochondrial membrane, increasing the production of ROS and triggering cell death as the cell failed to repair the damage. Furthermore, the tested concentrations along with detected dissolved Ag fraction, could potentially represent environmental relevant levels, displaying a possible scenario that aquatic organism may encounter due to extensive commercialization of AgNPs-based products. Furthermore, our study showed the potential use of embryonic zebrafish cells (ZF4) to assess the nanotoxicity of AgNPs as an early-stage model, aiming to the development of ZF4 cells as a new potential aquatic model to further understand the cellular and molecular toxicity response as part of an Adverse outcome pathway (AOP) framework and supporting the 3Rs initiative. Certainly, further research that includes protein expression analyses is needed to identify the flexibility and limitations of ZF4 cells as an aquatic model. However, the evaluated cellular events provide insights of the cell death mechanisms and stress responses of AgNPs, revealing results that may further be linked to organism level to support the development of safer nanomaterials.

2.7 Author Contributions

ACQ designed and performed the experiments, analysed the data, and drafted the manuscript; IL and EVJ conceived the experiments, analysed the data, revised and approved the manuscript.

2.7.1 Conflicts of interest

There are no conflicts to declare.

2.7.2 Acknowledgements

ACQ would like to thank The National Council for Science and Technology (CONACyT) in Mexico for funding her PhD studies. ACQ, IL and EVJ acknowledge support from the European Union Horizon 2020 Programme (H2020) project ACEnano (grant agreement No 720952). Consumables costs for the project were supported by FP7 project EcofriendlyNano (IL, grant agreement No 631612) and H2020 project NanoFASE (grant agreement No 646002).

Chapter 3: Cellular repair mechanisms triggered by exposure to silver nanoparticles (AgNPs) and ionic silver (AgNO₃) in embryonic zebrafish cells (ZF4)

This chapter has been published in Environmental Science: Nano

Ana C. Quevedo^a, Iseult Lynch^{a*}, Eugenia Valsami-Jones^a

^a School of Geography, Earth and Environmental Sciences, University of Birmingham, Edgbaston, Birmingham, B15 2TT, UK.

*Corresponding author: 

3.1 Abstract

The potential environmental risks of silver nanoparticles (AgNPs) are linked to their dynamic and complex behaviour in aquatic ecosystems. In the context of assessing their negative impacts, advanced toxicological studies are necessary to elucidate cellular responses after nanoparticle (NP) exposure. As part of our ongoing efforts to confirm the utility of continuous embryonic zebrafish cells (ZF4) to evaluate molecular mechanisms of cytotoxicity and cellular repair mechanisms triggered after exposure to AgNPs (10 nm, 30 nm and 100 nm) and ionic Ag (as AgNO₃). Results demonstrated the crucial role of the adsorbed protein corona in reducing AgNP cytotoxicity and the time dependent AgNP internalisation. At 2 hours, the NPs were likely to be attached to the cell membranes as part of the first NP-cell encounter, whereas after 24 hours AgNPs were found in lysosomes and in close proximity to the nucleus. The cytotoxicity of PVP-coated AgNPs

was size-related, as smaller (10 nm) AgNPs and ionic silver displayed major induction of all evaluated responses compared to the 30 nm and 100 nm AgNPs. All treatments demonstrated overgeneration of reactive oxygen species (ROS) and disruption of the Ca^{2+} balance. Cells were able to activate defence mechanisms in response to the induced damage, such as cell cycle arrest which prevented cells reaching the S phase, thereby providing time to repair DNA damage. The smaller AgNPs and the ionic control triggered disruption in the cell cycle, high percentages of DNA breaks, and cell death, while exposure to the 100 nm AgNPs led to activation of G1 and G2 phases, suggesting that ZF4 cells may overcome the damage. In addition, the study aims to provide insights about the mode of action of the AgNPs in cells, supporting the establishment of Adverse Outcome Pathways (AOP) and the 3Rs framework for the reduction of animal experimentation.

3.1 Introduction

Silver nanoparticles (AgNPs) are one of the most commonly used nanomaterials in consumer products, primarily due to their antimicrobial properties that have been widely implemented in a diverse range of consumer products, such as soaps, pastes, textiles, and other health sector goods [25]. As the AgNPs market increases so too have environmental concerns about the potential risks linked to the release of AgNPs into ecosystems. Silver-based products are likely to result in the release of dissolved silver, along with other forms of particulate silver (e.g. transformation products), becoming highly toxic to prokaryotes and many marine and freshwater organisms [25].

The physicochemical characteristics (e.g., size, surface, and charge) of nanoparticles (NPs) may influence their cellular internalisation, determining uptake pathways, and potential disruptions of the cellular equilibrium, finally triggering stress-related responses [316]. This redox imbalance within cells often results in increased intracellular reactive oxygen species (ROS), which can be generated in multiple organelles [140, 316]. Intracellular ROS can act as messengers or mediators in many cellular signalling processes, potentially influencing cellular life and death mechanisms. For example, calcium can regulate several physiological processes, acting as a second intracellular messenger [317, 318]. This process is regulated by the presence of ion channels, pumps and carriers, cell domains and organelles transmitting Ca^{2+} mediated signals, including the mitochondria and endoplasmic reticulum (ER) [319, 320].

ROS overload has been associated with intracellular disruption, affecting DNA proteins, lipids, and other macromolecules [321]. For example, DNA interaction with NPs may result in DNA breaks, which exacerbate ROS production and induce a crucial downstream of defence biological responses to maintain the genomic stability [322]. In response to DNA disruption, the cell triggers repair mechanisms such as cell cycle checkpoints, DNA repair regulators, and cell death mechanisms to reduce the probability of mutation [156, 322].

Fish cells, as mammalian cells, can be cultured with optimised cell culture medium, which is normally supplemented with a certain serum percentage (heat-inactivated or not) that will depend on the cell line requirements as well as the type of experiment planned [323]. The supplemented cell medium can strongly interact with AgNPs during biological exposures, providing further insights into the behaviour of the AgNPs in relevant biological

fluids [58, 62]. For example, the addition of serum results in binding of proteins and other biomolecules onto the surface of the NPs (corona formation), inducing changes in their stability (e.g., dissolution agglomeration). The acquired biomolecule corona provides a new identity to the NPs enabling them to engage with cellular receptors, influencing adhesion, uptake, transport, and cytotoxicity [324, 325].

To explore the utility of commercial embryonic zebrafish cells (ZF4) as an emerging *in vitro* aquatic model for nanotoxicity, we present a set of cellular assays exploring the induction of cellular defence mechanisms and cytotoxic outcomes in response to PVP-capped AgNPs are presented. For this, different sizes (10, 30 and 100 nm) and concentrations in comparison to an ionic silver (Ag^+) control were incubated for 24 hours. Furthermore, the aim of this study is to evaluate the effectiveness of this fibroblast adherent cell line as a potential early-stage toxicological screening tool. The mechanistic insights generated from the analysis of the molecular and cellular events activated in the presence of NPs may contribute to different frameworks (e.g., AOPs, 3Rs), supporting the development of safer NMs.

3.2 Materials and methods

3.2.1 AgNPs characterisation

Polyvinylpyrrolidone (PVP) coated silver nanoparticles (AgNPs) with sizes 10, 30, and 100 nm were purchased from Nanocomposix, USA, (BioPure, Silver Nanospheres PVP, 1 mg/mL). The characterisation of the three representative sizes was performed in either DMEM/F12 (Gibco, 11330) Serum Free Medium (SFM) or Complete Culture Medium

(CCM). The CCM was prepared by supplementing DMEM/F12 with 10% Foetal Bovine Serum (FBS) (Gibco, 10270).

A sample (1 mL) containing one of the AgNPs at a final concentration of 10 µg/mL was placed in a disposable polystyrene cuvette (Sarstedt, 67.742), then the hydrodynamic size, zeta potential, and polydispersity were immediately assessed by dynamic light scattering (DLS) (Zetasizer Nano series, Malvern). For zeta potential analysis, 700 µL was prepared freshly and placed in a folded capillary cell (Malvern, DTS1070) for analysis. All samples were prepared freshly and measured directly followed by incubation for 24 hours at 28°C after which the size and zeta potential were re-evaluated to assess the stability of the NPs in the exposure medium.

3.2.2 Silver nitrate (AgNO₃) stock

To further understand the toxicity of the ionic Ag in ZF4 cells, a stock suspension of 1 mg/mL of Ag (with equivalent mass of silver in ionic form) was prepared. The methodology for the preparation of the AgNO₃ stock solution under sterile conditions is described in section 2.3.2 of Chapter 2.

3.2.3 Culturing of embryonic Zebrafish cells (ZF4)

Cells were cultured and maintained in T75 flasks as described in section 2.3.4 of Chapter 2.

3.2.4 Toxicity of AgNPs and AgNO₃

To select exposure concentrations for the AgNPs and AgNO₃ treatments, the effective concentration at which 50% of the cell viability is reduced (EC₅₀) was evaluated by Lactate dehydrogenase activity (LDH) assay. First, ZF4 cells were treated with increasing concentrations of either AgNPs (5, 10, 20, 30, 40 and 60 µg/mL) or AgNO₃ (Sigma, 209139) (0.5, 1, 2, 3, 5, and 8 µg/mL) and incubated for 3, 24, 48, and 72 hours in CCM. To understand the role of the proteins adsorbed to the AgNPs (the NP-corona) in modulating the toxicity of AgNPs and silver ions, serum-free treatments (DMEM/F12) were tested in parallel. Both CCM and serum-free medium (SFM) treatments were prepared freshly on the day the assay was performed, using concentrations (0.25, 0.5, 1, 1.5, 2 and 2.5 µg/mL) of the three AgNP sizes and AgNO₃ concentrations of 0.5, 1, 2, 3, 5, and 8 µg/mL; however, due to the higher toxicity of the NPs in the absence of serum recorded by other authors [292, 323], the treatments were incubated for shorter periods of time, i.e., for 3, 6, 12, and 24 hours. After the incubation times for treatments in CCM and SFM, the cell viability was analysed using the LDH assay (CytoTox 96, Promega Corporation, USA) using a modified protocol (Ali-Boucetta et al. 2011) to measure the LDH content of the live cells instead of LDH released in the media from dying cells after AgNPs exposure [262]. The methodology is described on cancer cells in the original publication by Ali-Boucetta et al. (2011) and in a previous ZF4 cell publication by Quevedo et al. (2020) (refer to section, 2.3.5 in Chapter 2). Twenty-four hours post seeding, cells were treated with AgNPs or AgNO₃ in either CCM (10% FBS) for 3, 24, 48 and 72 hours or SFM for 3, 6, 12, and 24 hours. After each incubation period, the cell medium was removed, cells were lysed and centrifugated. Then, reconstituted substrate mix (LDH kit,

Promega) was added to cells followed by incubation and analysis using a plate reader at 492 nm (Tecan, Spark). All experiments were performed in triplicate (n = 3), for the three AgNPs sizes (10, 30 and 100 nm) and AgNO₃ in CCM and SFM. Results were calculated based on the percentage of cell survival using the following formula:

$$\text{Percentage of survival} = \left(\frac{\text{Abs 490 of treated cells}}{\text{Mean Abs 490 of untreated cells}} \right) * 100$$

3.2.5 Nanoparticle internalisation by ZF4 cells

In order to assess the uptake of AgNPs, cells were seeded in uncoated 24 well plates (13 mm) glass bottom dishes (MatTek, P24G013F) at a density of 100,000 cells in a total volume of 1 mL of CCM and incubated at 28 °C and 5% CO₂. Twenty-four hours post-seeding, the cell medium was replaced with treatments prepared in CCM with final concentrations of 2.5, 5 and 10 µg/mL of 10, 30 or 100 nm AgNPs for either 2 or 24 hours. After the desired incubation period, cells were carefully washed thrice with warm PBS, then the nucleus and lysosomes were marked with 500 µL of a staining solution consisting of warm CCM mixed with 1µL/mL Hoechst 33342 (Thermofisher, 62249) and 1 µL/mL LysoTracker™ Deep Red (Thermofisher, L12492) for 45 minutes at 28 °C. The staining solution was removed, and cells were washed twice with warm PBS. Then, cells were fixed for 20 minutes with 500 µL of 4% Paraformaldehyde (Thermofisher, 43368) diluted in PBS. Finally, the cell membrane was stained with 500 µL of Alexa 488 wheat germ agglutinin (WGA) conjugate solution (Thermofisher, W11261) at a final concentration of 5 µg/mL and incubated for 15 minutes in the dark at room temperature. After the staining period, cells were carefully washed with PBS and then examined by confocal microscopy.

Hoechst staining (excitation/emission 350/461 nm) was used for nucleus identification and was visualised using the blue laser; for lysosomes (647/668 nm) the red filter was used, and for the cell membrane (495/519 nm) the green filter was used. Images were taken with a NIKON A1R 808 series microscope using a 60X objective lens for all channels, including a reflectance filter (488 nm) for the AgNPs (reflectance mode) and optical zoom. The NP reflectance intensity of each cell was isolated by manually drawing a region of interest (ROI) in the acquired image using FIJI open-source image processing tool (V.2.00-RC69) and following the outline of the cells based on the cell membrane staining with Alexa 488 (green). Then, the intracellular background fluorescence of the selected area (determined from an adjacent area without cells) was recorded and subtracted from the initial NP reflectance intensity. A similar method was followed to calculate the total intensity of fluorescence per NP (visible intracellular accumulations of NPs) as described in the literature [91, 238, 326]. See SI for an example of the manual analysis of the AgNP reflectance intensity, as per Figure S8.1.

3.2.6 Intracellular calcium flux

Calcium (Ca^{2+}) plays a key role in diverse cellular signalling functions, providing information about cellular activity and disturbances. To evaluate the intracellular calcium, flux a Screen Quest™ Fluo-8 Calcium Assay Kit was used (AAT Bioquest, 36307). Once inside the cell, the fluorescent dye results in enhanced fluorescent intensity when activated upon binding to calcium [327]. First, cells were seeded in 96-well flat bottom plates as described in section 2.3.5. Twenty-four hours post-seeding, cells were treated with 2.5, 5 or 10 $\mu\text{g}/\text{mL}$ of 10, 30 or 100 nm AgNPs or 1, 1.5 and 2 $\mu\text{g}/\text{mL}$ of AgNO_3

prepared in CCM for 24 hrs at 28 °C. A positive control of 20% Dimethyl sulfoxide (Sigma, D4540), prepared in SFM, was also included for 30 minutes. After the incubation time, the cell medium was carefully removed and cells were stained with 100 µL of the Fluo-8 NW dye working solution, which was prepared by following the manufacturer protocol. Briefly, 10 µL of Fluo-8 NW DMSO working stock were added into 10 mL of 1X assay buffer. The 1X buffer was prepared by mixing 9 mL of Hanks' buffer with 20 mM Hepes buffer into 10X Pluronic® F127 Plus (1 mL). After the working solution was loaded into the plate, the cells were placed in the dark and incubated for 30 minutes at 28°C, then for 30 minutes at room temperature. Immediately, the calcium flux was assessed using a multimode microplate reader (Tecan Spark) in time resolved fluorescence mode. The plate reader was set to monitor the excitation/emission at 490/525 nm.

All experiments were performed in triplicate (n = 3), for the three AgNPs sizes (10, 30 and 100 nm) and AgNO₃. Results were normalised by subtracting the average of the untreated control to obtain base-line corrected values according to the supplier's protocol as follows:

$$\textit{Corrected intensity} = \textit{Intensity treatment} - \textit{Mean naive}$$

3.2.7 Oxidative stress

Many cellular and biochemical alterations are associated with excessive ROS production, especially in cellular organs where the oxygen consumption is high. Hence, to further understand the cytotoxicity of AgNPs and ionic Ag, the total intracellular ROS production was analysed via flow cytometry Total ROS Assay Kit (Thermofisher, 88593074) following

the manufacturer protocol. Cells were seeded and cultured as described in section 2.3.4.1 of Chapter 2, for flow cytometry experiments. After 24 hrs, the medium was replaced with 2.5, 5 and 10 µg/mL of 10, 30 and 100 nm AgNPs and 1, 1.5 and 2 µg/mL AgNO₃, treatments were prepared in CCM and incubated for 24 hrs at 28 °C. 100 µM of Menadione and 5 mM of N-acetyl-L-cysteine (NAC) were prepared in CCM and included as positive controls to induce and inhibit ROS production, respectively. Controls were added one hour before the end of the incubation period. After the incubation period the cell medium was removed, cells were washed with warm PBS and detached using 0.25% trypsin for 3 minutes at 28°C. The medium and cells were centrifuged for 10 minutes at 270 x g at 4°C. The supernatant was removed, and the pellet was labelled using CellROX® Deep Red (Thermofisher, C10422). For this, the cell pellet was resuspended (500 µL) and incubated in CellROX® Reagent for 30 minutes at 28°C; after the incubation, the stained cells were centrifuged at 270 x g at 28°C and finally the pellet was diluted with 500 µL of warm PBS. Afterwards, cells were analysed by FACS using the Allophycocyanin (APC) filter with excitation of 644 nm and emission of 665 nm. The flow cytometer electronic compensation was set up based on unstained cells (control) and cells labelled with the single stain, then, cell doublets were excluded from the analysis as previously described. At least 10,000 counts were analysed per sample and three individual replicates were performed per treatment. Results were analysed using FlowJo V10 software (V.10.0.8, FlowJo, LLC, Ashland, OR, USA). Intensities were normalised to percentage (%) against naïve as follows:

$$\% \text{ Total ROS} = \frac{\text{Intensity treatment}}{\text{Mean naive}} * 100$$

3.2.8 Cell cycle analysis

The cell cycle involves a signalling cascade to divide a cell into two daughter cells; to explore potential disruptions of the cell cycle from exposure to AgNPs and ionic Ag, FxCycle™ PI/RNase Staining Solution (Thermofisher, F10797) flow cytometry was used. Cells were seeded and cultured as described in section 2.3.4.1 of Chapter 2, for flow cytometry experiments. After 24 hrs, treatments prepared in CCM were added at 2.5, 5 or 10 µg/mL of AgNPs (10, 30 and 100 nm) or 1, 1.5 and 2 µg/mL of AgNO₃, and incubated for 24 hrs at 28 °C. 3 µM topotecan (Sigma, T2706) and 10 µM etoposide (Sigma, E1383) were also incubated for 24 hours as positive controls to induce cell cycle arrest in phases S and G₂, respectively. After 24 hours, the cell medium of all treatments was removed, cells were washed with PBS and detached using 0.25% Trypsin for 3 minutes at 28°C. The cell medium and cells were centrifuged for 10 minutes at 270 x g at 4°C. Then, the supernatant was discarded, and the cell pellet was carefully fixed with 3 mL of cold ethanol absolute (Sigma, 34852). After fixation, the cells were centrifuged, and the supernatant fixation was carefully removed. Finally, the cell pellet was stained using 500 µL of red fluorescent Propidium iodide (PI) stain (FxCycle™ PI/Rnase staining) and incubated at room temperature for 30 minutes. Stained cells were analysed by FACS using the PI (Texas red) filter, with an excitation / emission of 535 / 617 nm. The flow cytometer electronic compensation was set as previously described in Chapter 2, which was based on healthy stained and unstained cells and cell doublets were eliminated from the analysis for better results. At least 10,000 counts were analysed per sample and three

replicates were included for all the samples. Flow cytometry results were analysed by FlowJo V10 software using the cell cycle tool.

3.2.9 DNA damage determined by Comet assay

Cells were seeded in 12-well flat bottom plates (Costar, 3737) at a density of 200,000 cells in 1 mL of CCM and incubated at 28 °C and 5% CO₂. After 24 hrs, cells were treated with 2.5, 5 and 10 µg/mL of 10, 30 and 100 nm AgNPs and 1, 1.5 and 2 µg/mL of AgNO₃ for 24hrs at 28 °C. A concentration of 200 µM hydrogen peroxide (H₂O₂) as a positive control prepared in CCM was also included for 30 minutes to induce DNA damage [328]. After the incubation period, the cell medium was removed; cells were washed with PBS and detached using 0.25% trypsin for 3 minutes at 28°C. Then, the medium and cells were centrifuged for 3 minutes at 956 x g at 22°C. After centrifugation, the supernatant was carefully removed, and the cell pellet was resuspended in 100 µL of PBS. Then 20 µL of the diluted cell suspension were mixed with warm (28 °C) 0.7% low melting point agarose (LMA) (Gibco, V384A), then 100 µL of the suspension were added onto a slide pre-coated with 1% normal melting point agarose (NMA) (Promega, V384A) and covered immediately with a glass coverslip (24 x 60 mm); slides were set to cool over ice for 20 minutes at 4°C (see section 1 of the SI for detailed description of the preparation of the buffers and slides). The coverslip was gently removed and another layer of 90 µl LMA was added, another coverslip was added, and the slide was set to cool for 20 minutes at 4°C. After the cold incubation, the coverslips were carefully removed, and the slides were placed into a lysis solution at 4°C overnight. Afterwards, the slides were placed onto an electrophoresis chamber with cold electrophoretic buffer for 20 minutes; after the

unwinding step, electrophoresis was conducted for 20 minutes at 20 V/cm – 300 mA at 4°C. Then, the slides were transferred onto a rack and covered with 2 mL of neutralizing buffer for 5 minutes. The slides were fixed in -20°C ethanol for 5 minutes and set to dry on a flat surface for 24 hours. Finally, the slides were stained with SYBR™ Gold nucleic acid (Thermofisher, S11494) using a 1:1000 dilution of stock solution prepared in UPW. Samples were incubated in the dark for 24 hours at 4°C and then visualised using a fluorescent microscope with the blue laser. Tail intensity (% TI) of 50 Comets was recorded using Comet Assay IV digital software (Perceptive Instruments, Wiltshire, UK). Three replicates were performed for each treatment, equating to 150 Comets per sample to calculate the mean and standard deviation. Images were also taken when recording the TI of the Comets. Results were analysed using Comet Assay IV macro <https://www.instem.com/solutions/genetic-toxicology/comet-assay.php>. A full description of the buffers and details about the sample preparation can be found in section 8.1.1 in the SI.

3.2.10 Statistical analysis

All the results were plotted and analysed using GraphPad prism 8 software (V.8.4.3). Statistical analyses were performed in GraphPad using one-way or two-way ANOVA followed by a Bonferroni post-hoc comparison for all AgNPs and AgNO₃ treatments against the untreated control (naïve).

3.3 Results

3.3.1 Characterisation of the NPs

The AgNPs were characterised in CCM and SFM, displaying noticeable differences in the hydrodynamic sizes after 0 and 24 hours. The sizes of the 10, 30 and 100 nm AgNPs in SFM at 0 hours were recorded as 47.86 ± 0.01 nm, 94.82 ± 0.01 nm and 135.9 ± 0.05 nm; however, after 24 hours, substantial differences were displayed, with $617.21 \pm 0.690 \pm 0.1$, and 540.93 ± 0.03 for the 10, 30 and 100 nm AgNPs, respectively (Figure 3.1). The increase in size after 24 hours in SFM can be linked with the PDI results, as after 24 hours the PDIs recorded were around 1, suggesting high agglomeration and/or sedimentation of the NPs, compared to the fresh samples (0 hours) which showed PDIs between 0.03 and 0.23 for the three AgNPs sizes. On the contrary, the AgNPs sizes in CCM were broadly constant, with only small differences between 0 and 24 hours, which suggests rapid formation of a protein corona as well as some level of agglomeration upon dispersion. Interestingly, the 10 and 30 nm particles displayed similar sizes in CCM at 94.49 ± 0.03 and 95.20 ± 2.85 nm respectively at 0 hours, and 105.66 ± 0.3 and 102.65 ± 0.02 respectively at 24 hours, whereas the 100 nm AgNPs increased from 160.63 ± 0.52 nm (T0) to 175.06 ± 0.5 nm (24 hours). The zeta potential data suggests that the NPs had limited interaction with the medium compounds in SFM as both time points displayed similar results (-6 to -7 mV). On the other hand, the zeta potentials in CCM became slightly more negative (-10 to -12), displaying similar results at 0 and 24 hours (Figure 3.1 D). These results suggest that the small and medium sized AgNPs were more likely to increase in size upon dispersion compared to the larger NPs. Moreover, the

addition of serum had a strong effect on the physiochemical characteristics of the NPs, which can be related to the absorption of proteins onto the NPs, as well as enhancing the colloidal stability through steric mechanisms. Full characterisation results can be found in the supplementary information (SI) as Table S8.1. Further characterisation of the NPs using different concentrations and testing media is broadly described in a previous publication by Quevedo et al., 2021.

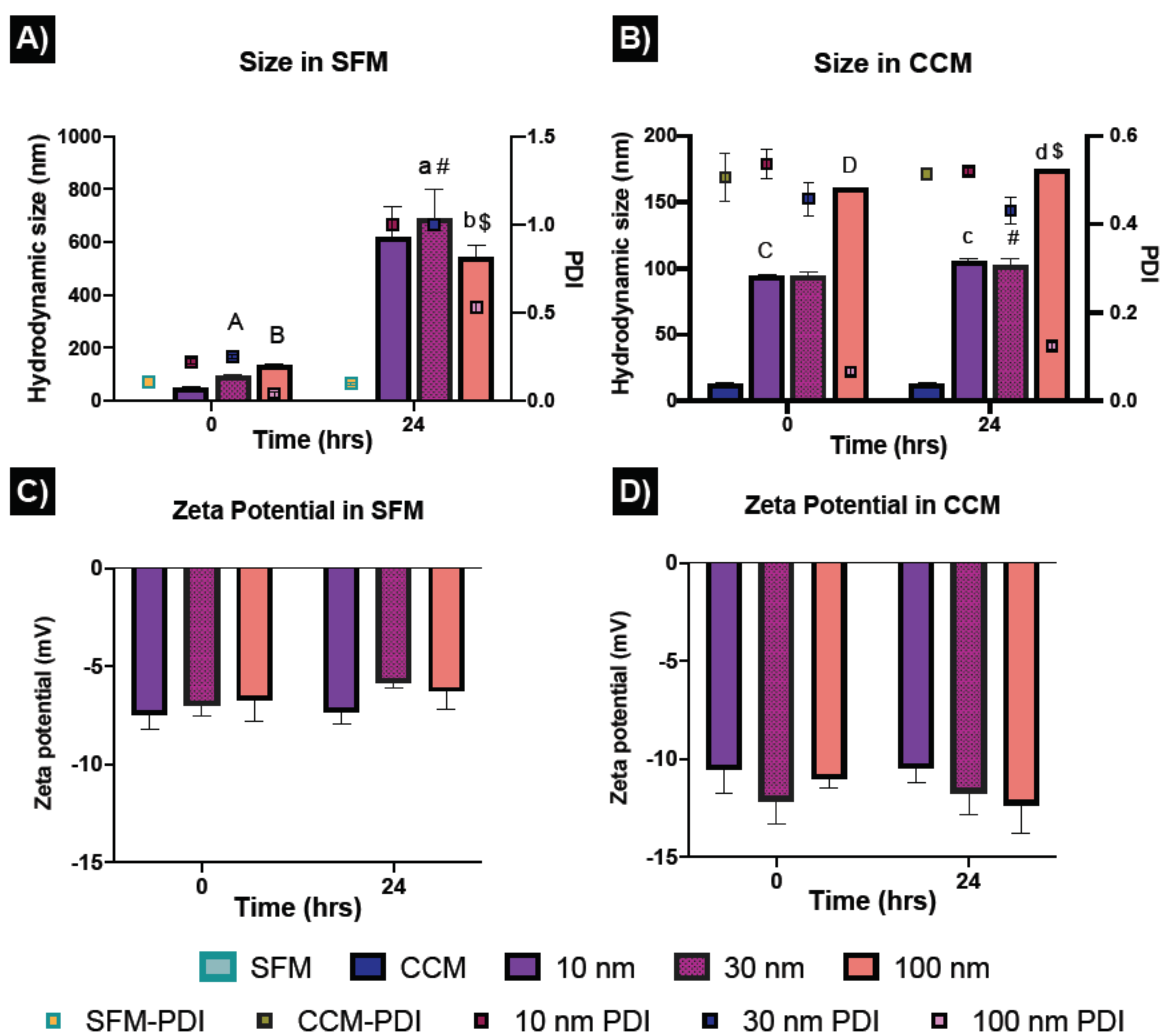


Figure 3.1. Serum Free Medium (SFM) and Complete Culture Medium (CCM) at different time points. Three representative AgNP sizes (10, 30 and 100 nm) were prepared in CCM and SFM at a concentration of 10 $\mu\text{g}/\text{mL}$ and incubated for 0 and 24 hours at 28. $^{\circ}\text{C}$. Figures A and C show the hydrodynamic size (nm) and polydispersity Index (PDI) of the AgNPs in SFM and CCM respectively. C and D show the zeta potential

in SFM and CCM after 0 hours and 24 hours incubation. Results represent the average of three replicates and their standard deviation. The SFM and CCM were characterised also to determine the size of the protein clusters. Data with similar letters (upper and lowercase) indicate a statistically significant difference ($p < 0.05$) between the selected concentrations and time points (0 and 24 hours). Equivalent symbols across the figures represent statistically significant differences ($p < 0.05$) in the hydrodynamic size of the NPs between SFM and CCM treatments.

3.3.2 LDH assay

To evaluate direct NP-cell interactions and the role of the acquired protein corona in mitigating the toxicity of AgNPs and silver ions, treatments prepared in SFM and CCM were compared. Representative low, medium, and high concentrations were selected based on the LDH enzymatic activity and decreased the cell viability to 50% (EC_{50}) after 24 hours in treatments prepared in CCM (see Chapter 2 for details). The recorded EC_{50} for the AgNPs was around 10 $\mu\text{g/mL}$, whereas for AgNO_3 it was 2 $\mu\text{g/mL}$. Hence, concentrations of 2.5, 5 and 10 $\mu\text{g/mL}$ for the AgNPs and 1, 1.5 and 2 $\mu\text{g/mL}$ of ionic Ag were used for subsequent experiments under normal cell culture conditions (10% FBS). A summary of the recorded cell viabilities (%) after 24 hours in CCM can be found as Table S8.2 in the SI. For more information about other tested concentrations, exposure time points and the full methodology used for treatments prepared in CCM, see Chapter 2.

To understand the cytotoxic effects of the AgNPs and its ionic counterpart under serum free conditions, the EC_{50} in ZF4 cells was also determined by LDH enzymatic activity. The AgNP concentrations in SFM were equal to those in the CCM treatments; however, due to the high toxicity recorded (reduction in cell viability %) after 24 hours

(<10 % viability) results are displayed only up to 24 hours of incubation (Figure 3.2). The SFM treatments thus demonstrated higher toxicity compared to the treatments prepared in CCM due to the mediating effects of the corona formed in CCM. The DMEM/F12 medium (SFM) registered a low protein content ($17 \pm 0.22 \mu\text{g/mL}$) compared to the CCM which was supplemented with 10% FBS leading to a protein content of $244 \pm 03.98 \mu\text{g/mL}$. Hence, lower concentrations were selected for the toxicity experiments in SFM due to the massive membrane damage induced by the bare AgNPs. The 10 nm AgNPs in SFM showed a 50% decrease in the cell viability at $2 \mu\text{g/mL}$ after just 6 hours (Figure 3.2A). After 24 hours exposure to the 10 nm AgNPs cell death reached $49.24 \pm 1.52 \%$ at $1 \mu\text{g/mL}$, indicating that as expected the AgNPs in SFM exhibit higher toxicity compared to the treatments in CCM where cell viability was about 50% even with exposure to $10 \mu\text{g/mL}$. For the 30 nm and 100 nm (Figure 3.2 B and C), the toxicity was lower, decreasing the cell population to around 60-70% from 3 to 12 hours at the highest concentration ($2.5 \mu\text{g/mL}$) in SFM. However, after 24 hours, the EC_{50} determined by LDH activity in cells was $1.5 \mu\text{g/mL}$ for both sizes, with 51.19 ± 5.80 and $53.87 \pm 0.42 \%$ cell viability respectively in SFM. On the other hand, the results for the ionic control in SFM (Figure 3.2 D) showed a noticeable decrease (40-50%) in the cell viability after 3 hours at $2 \mu\text{g/mL}$ which by 24 hours had decreased below 70%, with viability percentages ranging from 11-38% for the remaining AgNO_3 concentrations. Thus, the silver ions also displayed higher toxicity in SFM treatments compared to the AgNO_3 treatments in 10% FBS, further demonstrating the important role of proteins in reducing the cytotoxicity of both AgNPs and their ionic counterpart. Therefore, all subsequent treatments were prepared in CCM

to avoid cell distress due to the lack of nutrients as well as to mimic the *in vivo* environment. Full SFM results are presented in Table S8.2 in the SI.

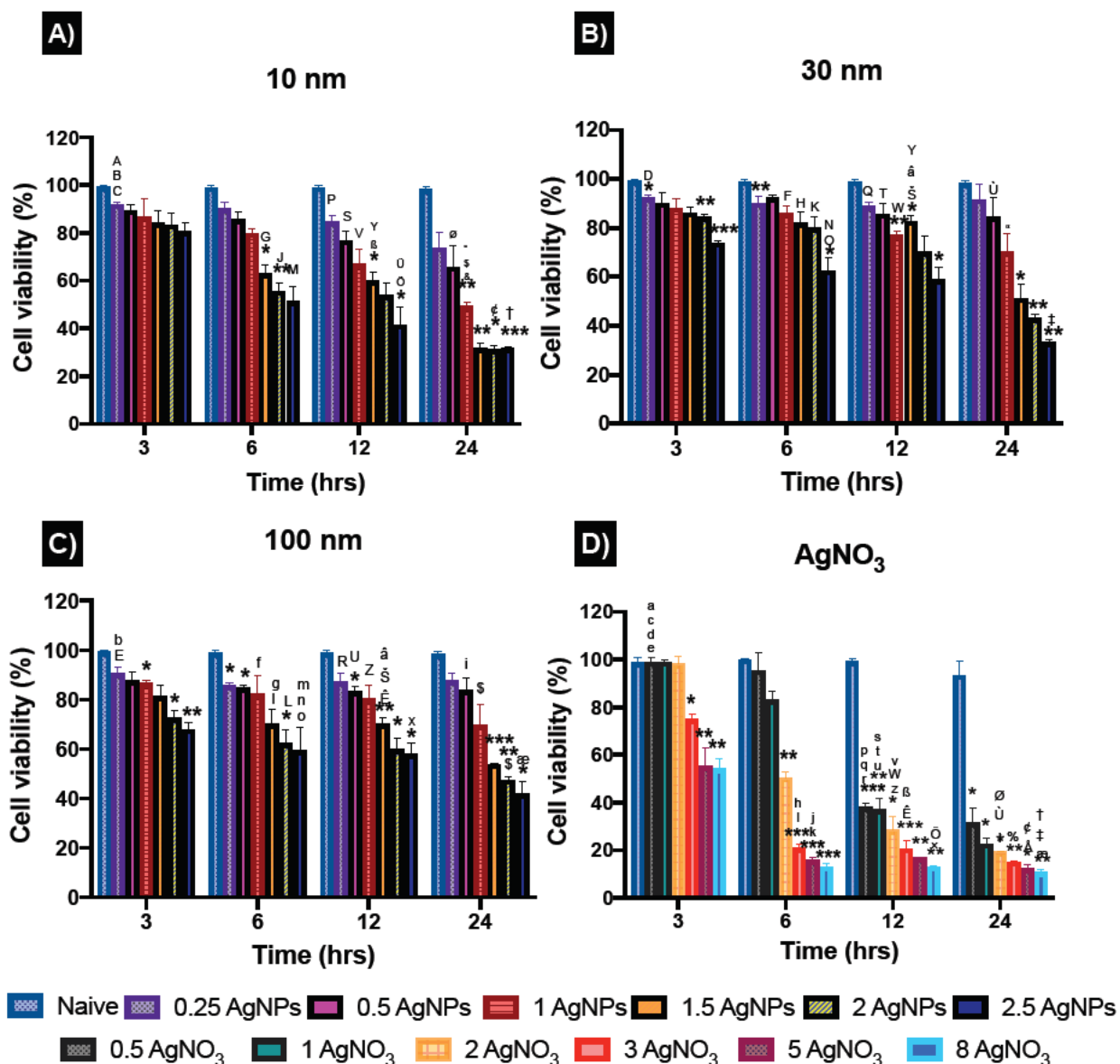


Figure 3.2. Cytotoxicity of AgNPs and AgNO₃ to ZF4 cells in Serum Free Medium (SFM). Cells were treated with AgNPs and AgNO₃ prepared in SFM for 3, 6, 12 and 48 hrs. The graphs show the percentage viability of ZF4 cells treated with 0.25, 0.5, 1, 1.5, 2 and 2.5 $\mu\text{g}/\text{mL}$ of AgNPs for 10 nm A), 30 nm B), and C) 100 nm. D) Viability of cells treated with 0.5, 1, 2, 3, 5, and 8 $\mu\text{g}/\text{mL}$ of AgNO₃. Graphs represent the average of three individual replicates and their standard deviation. Data with asterisks (*) indicate statistically differences between AgNPs treatments compared with the naïve control at each time point (* $p < 0.05$, ** $p < 0.01$, and *** $p < 0.001$). Bars with similar letters (upper

and lowercase) and identical symbols indicate a statistically significant difference ($p < 0.05$) between the selected concentrations, sizes, and AgNO_3 at the specific time point.

3.3.3 Nanoparticle internalisation

Confocal microscopy results were calculated as reflectance per NP (total intensity of fluorescence per NP spot), and to further understand the entry of the NPs into the cells, an estimation of the number of intracellular NPs accumulated per unit area was calculated (NPs/Cell). Intensities were compared with that of the background of the images (black area without NPs) and statistically significant differences between the AgNPs (* $p < 0.05$, ** $p < 0.01$, and *** $p < 0.001$) and the background were found. After 2 hours all the NPs followed an inverse concentration-intensity trend, with higher intensity values at the lowest AgNPs concentration (2.5 $\mu\text{g/mL}$, ** $p < 0.01$) and lower intensity values at the highest AgNPs concentration (10 $\mu\text{g/mL}$) (Figure 3.3 A and Table S8.4 in the SI). The smallest AgNP size (10 nm) presented the highest levels of fluorescent intensity (A.U) of the three AgNP, likely as a result of the higher particle number at constant mass. The 30 nm AgNPs displayed a similar concentration-intensity trend, with intensity values below those of the 10 nm AgNPs, but higher than the 100 nm particles which presented the lowest intensity values for the three AgNP sizes. These results might be related to the NP attachment to the cell surface as well as the NPs internalisation, and the number of particles/mL, which may also influence the uptake of the NPs. After 24 hours, a reduction in the fluorescence intensity for all NPs sizes and concentrations was recorded compared to the initial 2 hours exposure (Figure 3.3B), which is consistent with the data in Figure

3.3A and B where the reflectance decreases between 2 and 24 hours was greatest for the 10 nm particles.

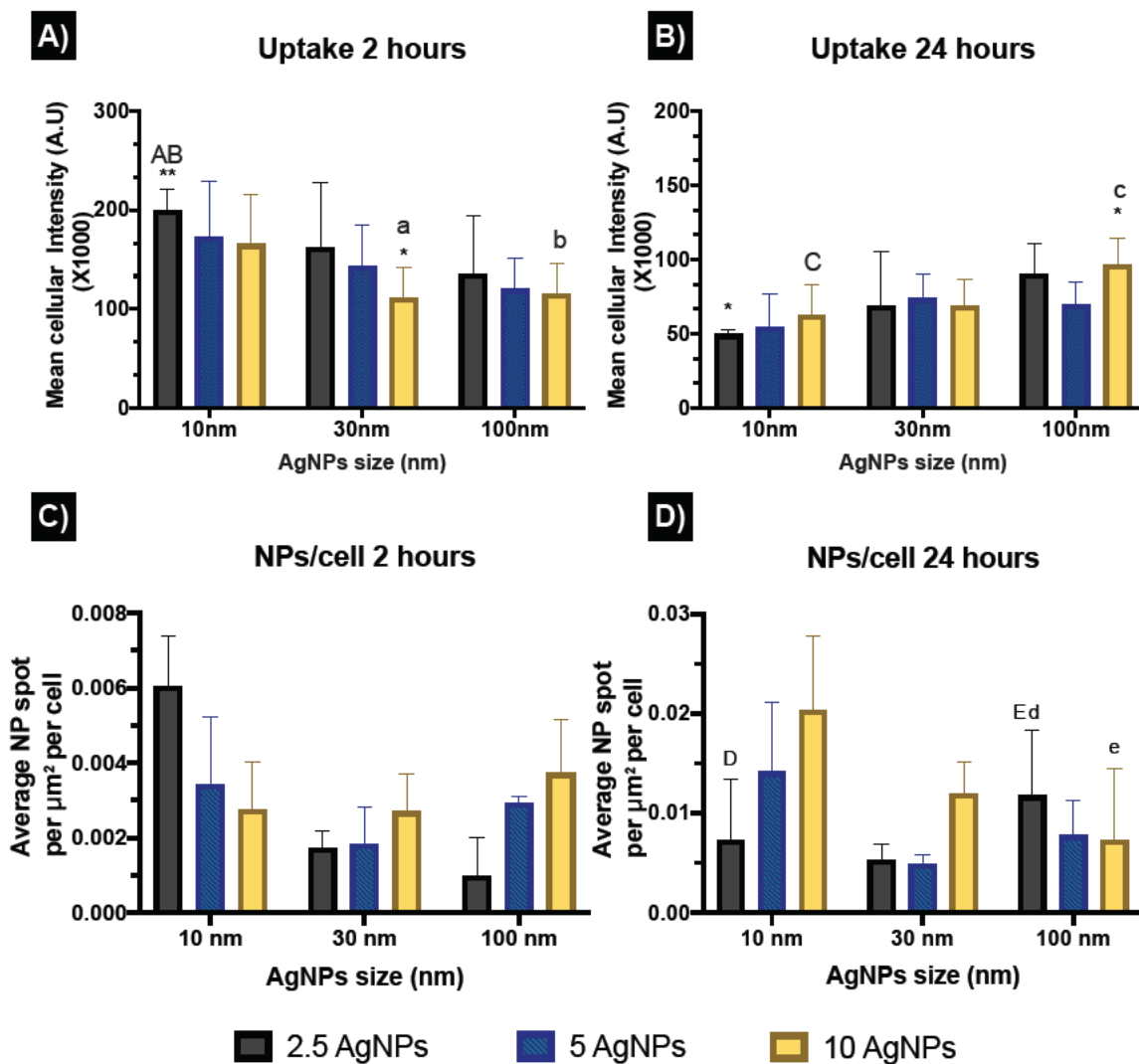


Figure 3.3. Internalisation of AgNPs by ZF4 cells in CCM determined by confocal microscopy. Data is presented as the mean intensity (A.U.) \times 1000 measured after 2 and 24 hours. Samples were treated with 2.5, 5 and 10 $\mu\text{g}/\text{mL}$ of 10, 30 and 100 nm AgNPs. A-B) Uptake of AgNPs of different sizes and concentrations after 2 or 24 h. Results represent the mean cellular intensities of three individual samples, for a total of 12 cells per AgNP concentration and size. C-D) Number of intracellular NPs accumulated per unit area (of cells) at 2 or 24 hours. Results represent the average of three individual samples per AgNP concentration and size (mean \pm SD). Data with asterisks (*) indicate statistically significant differences between AgNPs intensities (* $p < 0.05$, ** $p < 0.01$, and *** $p < 0.001$) and the background. Multiple comparison analysis was performed and

similar letters (upper and lowercase) above the bars denote statistically significant differences ($p < 0.05$) between the selected NP sizes and concentrations.

Estimation of the number of NPs/cells revealed a lower number of NPs at 2 hours, with an overall mean of 0.003 NPs/cell, whereas after 24 hours there was an increase in the number of NPs/cells to 0.01 NPs/cell (Figure 3.3 C and D and Table S8.6 in the SI). The 10 nm size displayed the highest values for both exposure times, which may be related to the larger number of NPs/mL with smaller sized particles at a constant mass concentration. The 100 nm AgNPs showed higher numbers of NPs/cell compared to the 30 nm particles, which showed the lowest intracellular NP accumulation values. The results may suggest that after 2 hours most of the NPs were attached to the cell membrane making their visualisation complex, whereas after 24 hours, the NPs may have undergone agglomeration in the cell lysosomes facilitating their visualisation, but also influencing their intensity by reflecting more (for larger apparent sizes) as shown in the uptake after 24 hours (Figure 3.4B). Confocal images support the fact that AgNPs might be interacting with the cell membranes at shorter exposure times, as the images for 24 hours showed internalisation of the NPs and their accumulation in lysosomes which cluster in close proximity to the blue-stained nuclei (Figure 3.4). Confocal microscopy was only performed on samples containing NPs, as it necessary to have particle mass to reflect the light and thus the ionic control could not be analysed by this method. Additional images are shown in Figures 3.5 and 3.6. A multiple comparison analysis revealed statistically significant differences between the AgNPs concentrations and sizes,

demonstrating an enhanced dose-effect between the three NP sizes. Full results can be found in Tables S8.3, S8.4, S8.5, and S8.6 in the SI.

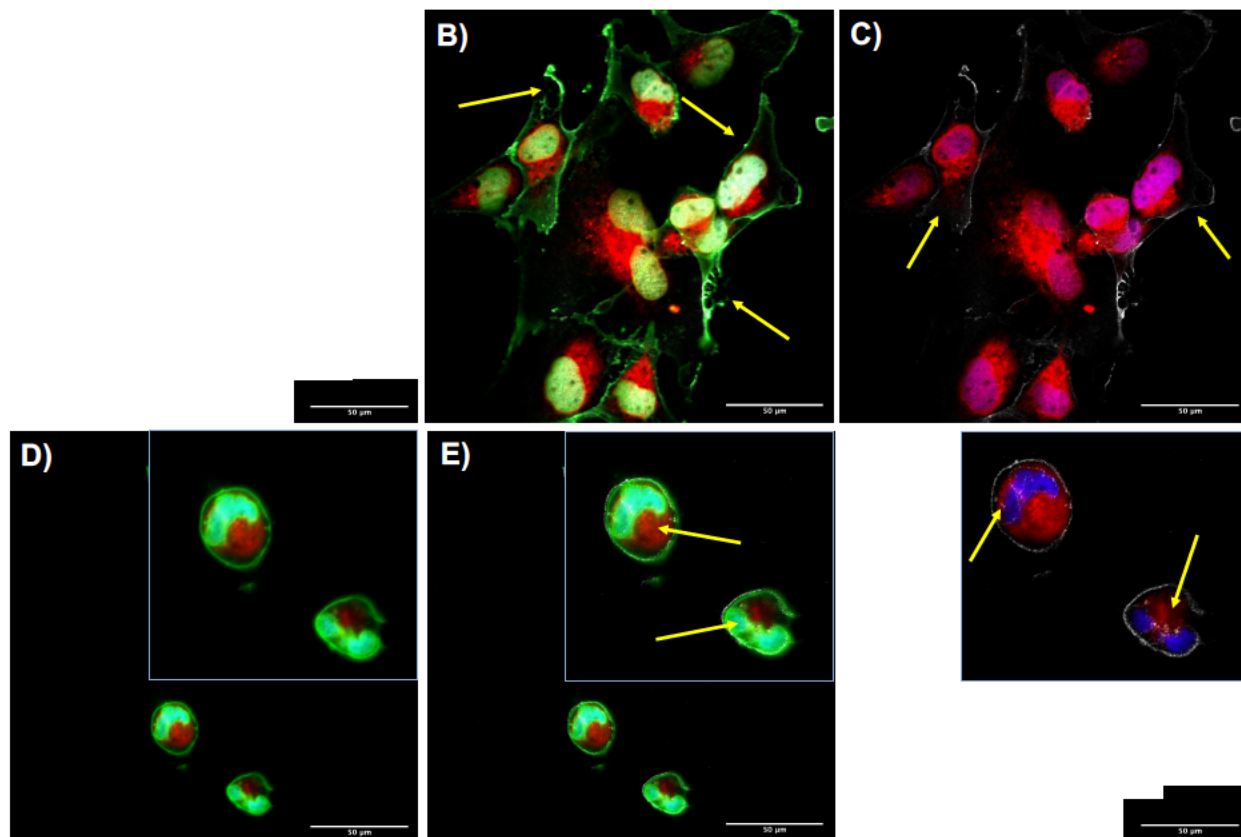


Figure 3.4. Representative confocal images of ZF4 cells treated with AgNPs. Cells were treated with 10 $\mu\text{g}/\text{mL}$ of 10 nm AgNPs for 2 and 24 hours, then stained with Hoechst (blue) for the nucleus, LysoTracker deep red (red) for lysosomes, and Alexa 488 (green) for the cell membrane. Due to visual interference between the NP reflectance and the dye used to stain the cell membrane (B and E), the green channel was removed to visualize the NPs for images C and F. Figures A-C shows cells treated with 10 $\mu\text{g}/\text{mL}$ of 10 nm AgNPs for 2 hours. A) Overlay of the nucleus, lysosomes and cell membrane staining. B) Cell overlay with the NPs channel (reflectance). C) Blue and red staining overlaid with the NPs (reflectance) channel. The Yellow arrows show AgNPs attached onto the cell membrane with no noticeable NP internalisation. Figures D-F show cells treated with 10 $\mu\text{g}/\text{mL}$ of 10 nm AgNPs for 24 hours with a close up of a few cells for better visualisation (yellow box). D) Overlay of blue, red and green dyes. E) Overlay of all three cellular stains and the NPs reflectance. F) Overlay of the red and blue staining and the NPs channel. Yellow arrows pointing to the white dots (NPs) show the internalisation of the NPs and their proximity to the nucleus and their localisation in lysosomes. The scale bar for all the images is 50 μm . Images were taken with a NIKON A1R 808 series microscope using a 60X objective and optical zoom.

3.3.3.1 Remaining confocal images

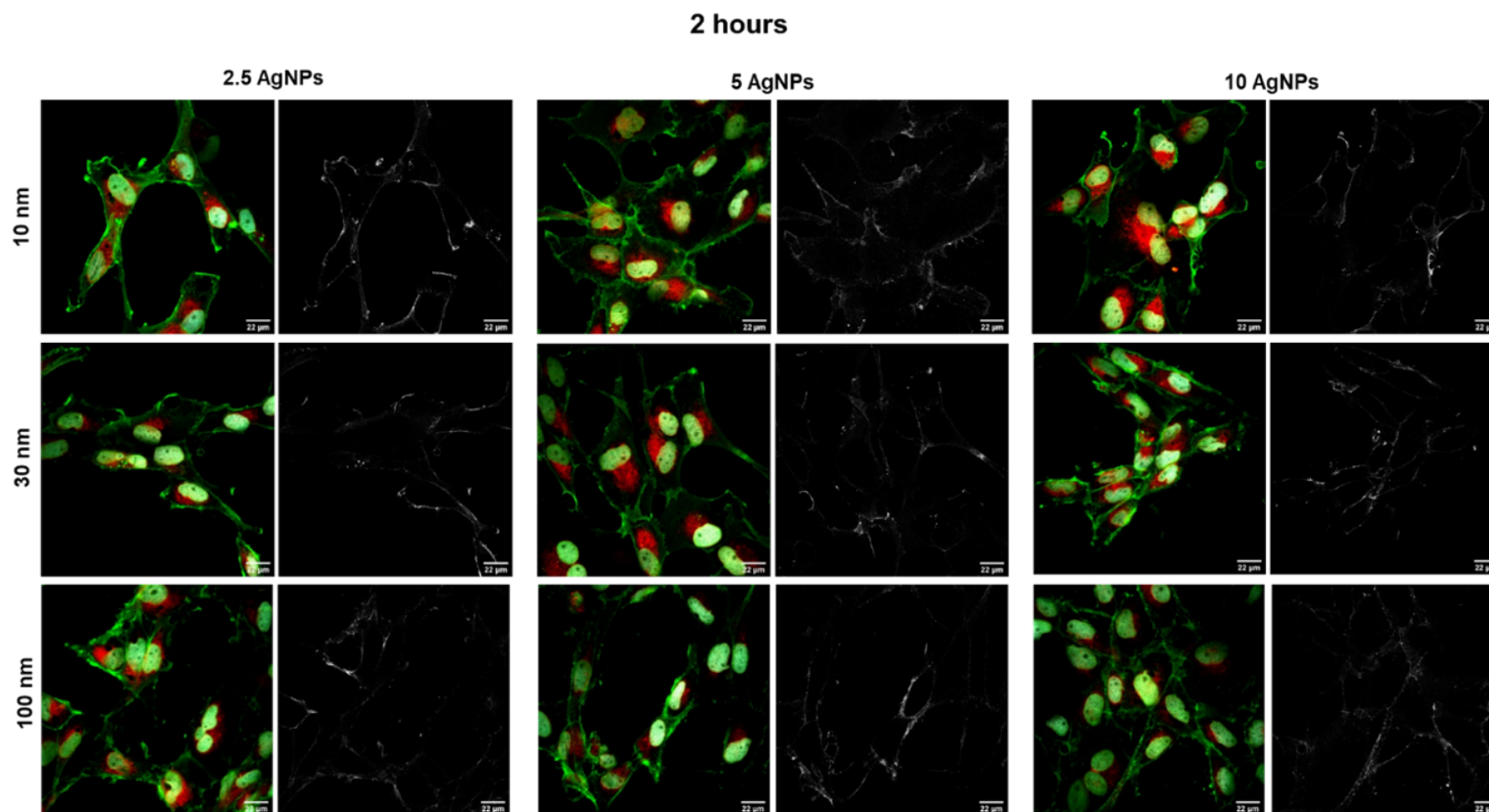


Figure 3.5. Confocal images of ZF4 cells treated with AgNPs for 2 hours. All the images show the composite image which includes the cellular dyes used for organelle identification. Green dye stains the cell membrane. Blue/light green represents the nucleus and red the lysosomes. The images next to the composite (right panels) shows the reflectance channel (NPs) acquired from the same images. The AgNP concentration in $\mu\text{g/mL}$ used for the treatments is shown above the images, while the AgNP size is shown on the left. Images were taken using a 60x objective and optical zoom. The scale bar is 22 μM .

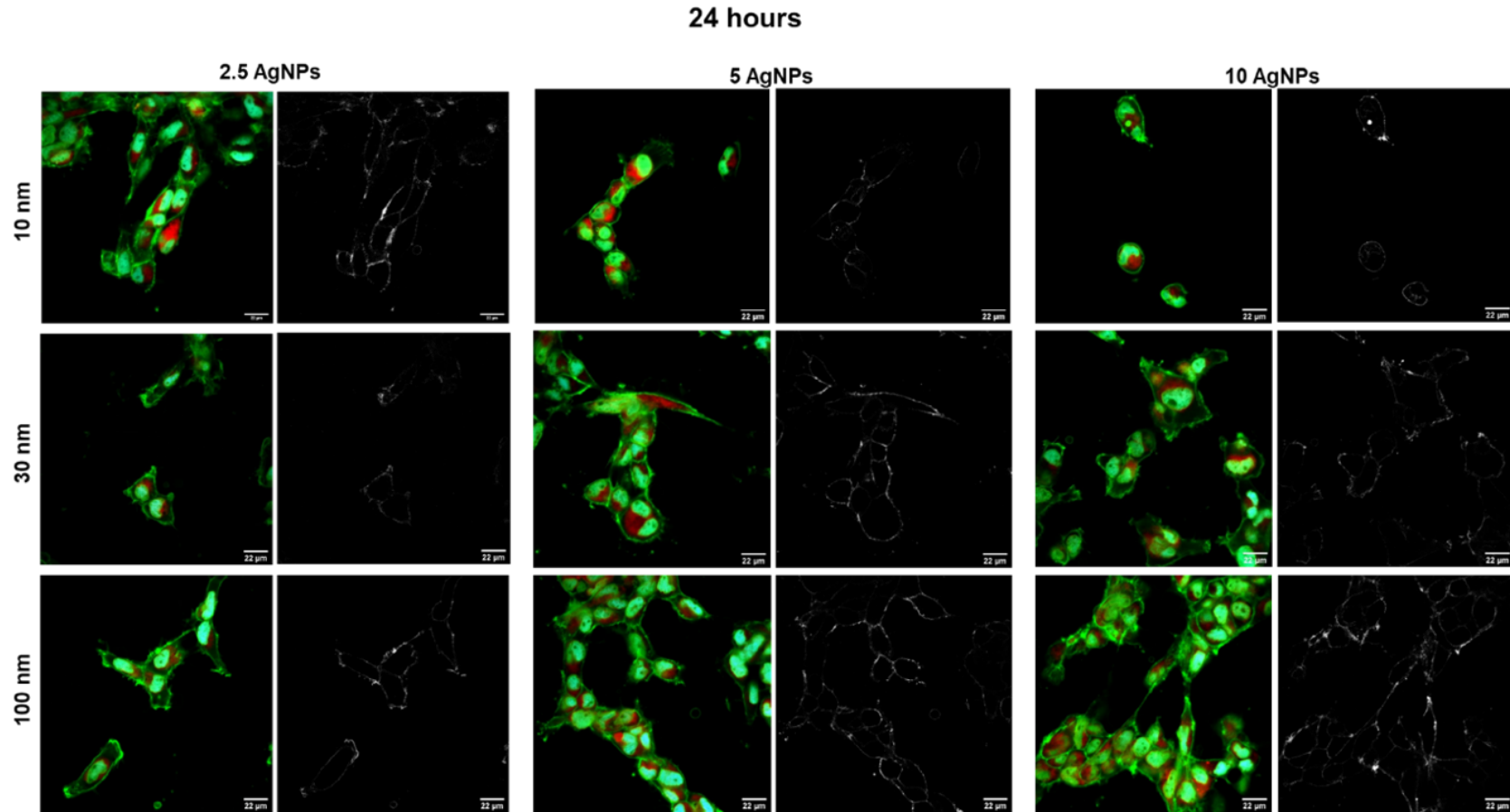


Figure 3.6. Confocal images of ZF4 cells treated with AgNPs for 24 hours. All images show the composite image which includes the cellular dyes used for organelle identification. Green dye stains the cell membrane. Blue/light green indicates the nucleus and red represents the lysosomes. The images next to the composite (right panel) show the reflectance channel (NPs) acquired for the same images. The AgNP concentration in $\mu\text{g/mL}$ used for the treatments is shown above the images, while the the AgNP size is indicated on the left. Images were taken using a 60x objective. and optical zoom. The scale bar is 22 μm .

3.3.4 Intracellular calcium flux

Intracellular calcium (Ca^{2+}) contributes to the maintenance of cellular homeostasis and leads to the transport of Ca^{2+} across cell membranes; thus, in order to understand the impact of AgNPs on this regulated cellular function, the intracellular calcium mobilization was assessed through a negatively charged fluorescent dye (Fluo-8 NW) that stays inside healthy cells, and whose fluorescence is greatly enhanced upon binding to cytosolic Ca^{2+} . The positive control, DMSO, demonstrated the highest intracellular Ca^{2+} mobilisation (363.81 ± 32.91 AU) relative to the naive cells (Figure 3.5). Results for the 10 nm AgNPs displayed the highest intensity at 2.5 $\mu\text{g}/\text{mL}$ (308.3 ± 120.12 AU), followed by 5 $\mu\text{g}/\text{mL}$ (179 ± 43.58 AU) and lastly 10 $\mu\text{g}/\text{mL}$ (119.3 ± 13.86 AU), all of which showed significant differences ($*p < 0.05$) compared to the naive. Conversely, the 30 nm AgNPs showed an inverse concentration trend, with the highest intensity (195.6 ± 20.27 AU) ($*p < 0.05$, compared to naive) at 10 $\mu\text{g}/\text{mL}$, followed by the medium concentration with 134.3 ± 62.18 AU, and lastly the 2.5 $\mu\text{g}/\text{mL}$, which showed the lowest recorded intensity 48.33 ± 20.25 AU). The 100 nm AgNPs displayed high intensity values at 2.5 and 10 $\mu\text{g}/\text{mL}$, with 123.6 ± 4.16 AU with $*p < 0.01$ (compared to naïve), and 187.66 ± 94.78 AU, respectively, whereas the 5 $\mu\text{g}/\text{mL}$ showed a decrease in the intensity to 48.33 ± 37.52 AU. Interestingly, the ionic control displayed statistically significantly different values compared to naïve, at 1 $\mu\text{g}/\text{mL}$ 91.67 ± 5.03 AU ($***p < 0.001$), whereas the 1.5 ($**p < 0.01$) and 2 $\mu\text{g}/\text{mL}$ ($*p < 0.05$) displayed inhibition of the calcium response as shown by

the negative intensity values. Full results can be found in Tables S8.7, S8.8 and S8.9 in the SI.

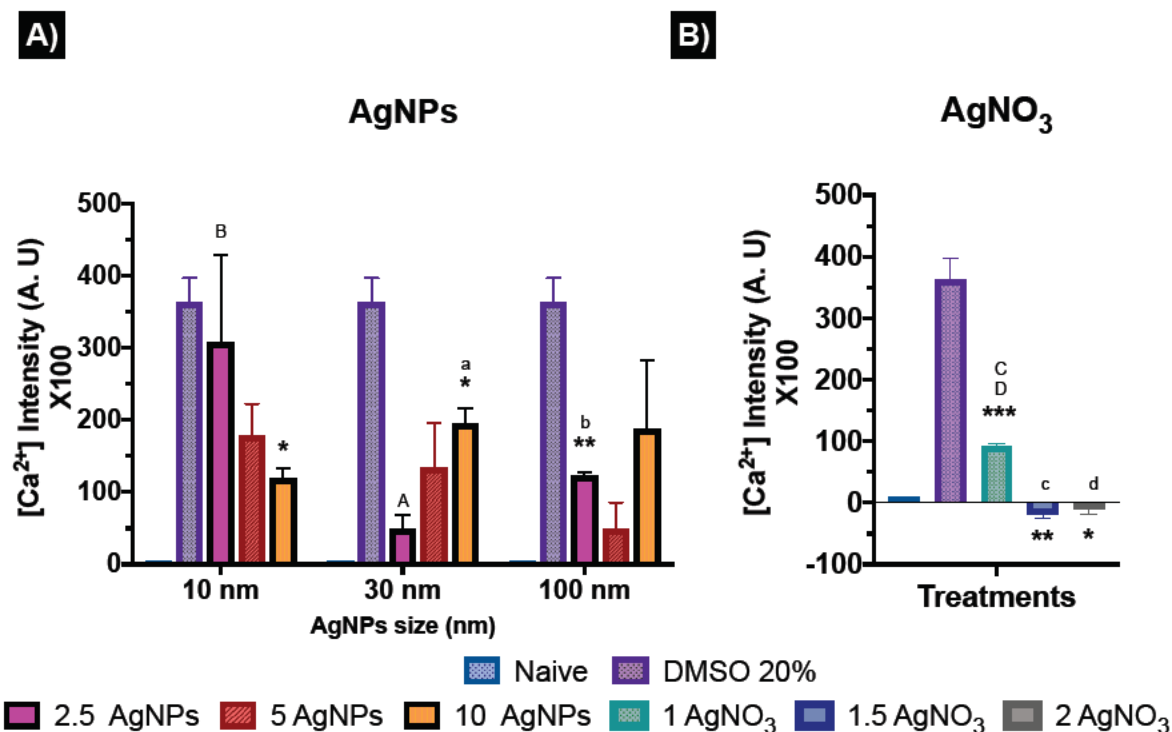


Figure 3.7. Intracellular calcium induced by AgNPs and AgNO₃ in ZF4 cells at 24 hours in CCM. Cells were treated with 2.5, 5 and 10 µg/mL of 10, 30 and 100 nm AgNP and 1, 1.5 and 2 µg/mL of AgNO₃ as ionic control for 24 hours. A positive control of 20% DMSO was also included for 30 minutes to ensure the reliability of the assay. The obtained intensities were normalised by subtracting the mean of the naïve cells from all treatments. Results represent the mean ± standard deviation (SD) of three individual replicates. Data with asterisks (*) indicate a statistically significant difference of AgNPs treatments (*p < 0.05, and ***p < 0.001) compared to the naïve cells. Similar letters (upper and lowercase) above the bars denote statistically significant differences (p < 0.05) between the selected NP sizes and concentrations.

3.3.5 Oxidative stress

Reactive oxygen species (ROS) are highly chemically reactive oxygen-containing molecules that can be generated at low levels as a natural product of oxygen metabolism; however, overload of ROS occurs as response a to cellular disruption and stress. All the NP concentrations tested induced an increase in ROS, except the 2.5 µg/mL concentration for the 10 nm AgNP, which did not display any statistically significant difference compared to naïve, but which did show a dose effect when compared to the other tested AgNP concentrations (Figure 3.8). The 10 nm AgNPs exhibited a dose-dependent increase in ROS- induction, from 106.2 ± 32.11 % at 2.5 µg/mL to 217.2 ± 16.85 % at 10 µg/mL compared to the naïve control (100 ± 18.95 %). The 30 nm AgNPs showed major ROS production at 2.5 µg/mL (136.1 ± 4.77 %) and 10 µg/mL (173.7 ± 8.0 %) with a decrease at 5 µg/mL (121.9 ± 7.9 %), suggesting that cells may have tried (unsuccessfully) to overcome the damage (Figure 3.6). The 100 nm AgNPs also presented ROS induction, however, the lowest concentration displayed the highest ROS production as shown in Figure 3.8.

On the other hand, the AgNO₃ showed a concentration-dependent ROS response, with values similar to those recorded for the 10 nm AgNPs, suggesting a close link between the small NPs, which likely have the highest dissolution, and the ionic complexes. Overall, the results showed that 10 nm AgNPs induced major ROS production at high concentrations, whereas the 30 and 100 nm AgNPs induced ROS at low (2.5 µg/mL) and high concentrations (10 µg/mL). The FlowJo extracted histograms and a table containing a summary of the normalised results can be found as Tables S8.10, S8.11, S8.12, and Figure S8.4 in the SI.

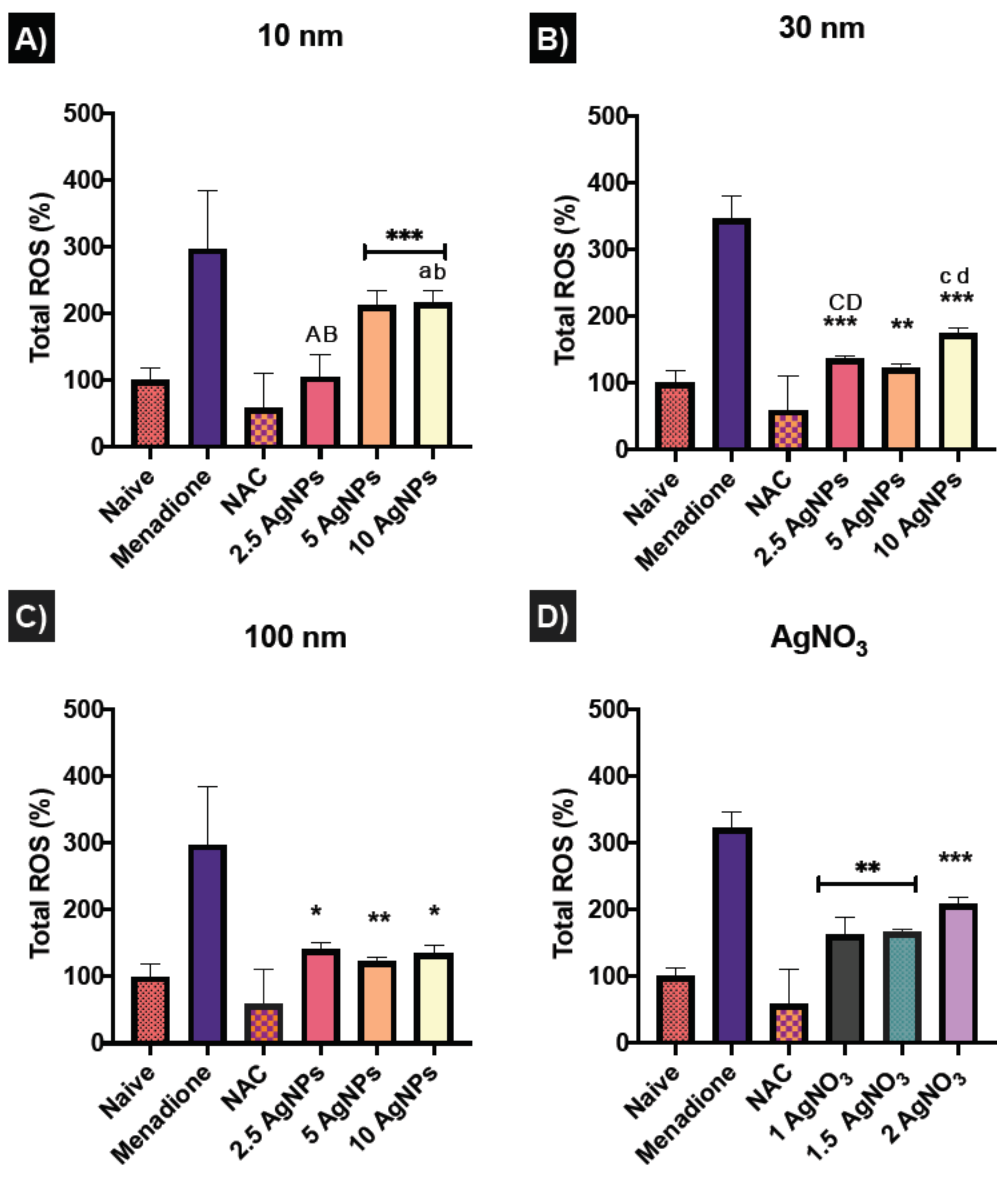


Figure 3.8. Total oxidative stress in ZF4 cells treated with AgNPs and AgNO₃. Graphs show the normalised values of the recorded Allophycocyanin (APC) filter mean intensities. Results were normalised against the naïve cells. A), B), and C) Oxidative stress induced by AgNPs of different sizes after 24 hours. D) ROS production following AgNO₃ exposure for 24 hours. Menadione (100 µM) and N-acetyl-L-cysteine (NAC) 5 mM were included for 1 hour as controls to induce and reduce ROS production, respectively. Data with asterisks (*) indicate statistically significant differences between AgNPs treatments (*p < 0.05, **p < 0.01, and ***p < 0.001) and the naïve cells. All bars under the line are included within the asterisk above. Data with similar letters (upper and lowercase) above the bars denote statistically significant differences (p < 0.05) between the selected concentrations.

3.3.6 Cell cycle arrest

The cell cycle involves a series of events that lead to cell division and replication. An arrest in the cell cycle implies a stopping point in the cycle, where duplication and division are no longer available, since arrest is a process used to facilitate DNA repair before cell proliferation. This is represented by an accumulation (increase in the percentages) of cells in a specific cell cycle phase, indicating that cells were arrested/delayed in that phase [329]. Results for the 10 nm AgNPs showed a reduced percentage (%) of cells in each of the G1, S and G2 phases, except by the lowest AgNP concentration (2.5 µg/mL) which showed a slight increase in the % cells in G2 (11.30 ± 0.3 % compared to 10.03 ± 1.6 % of the naïve cells) (Figure 3.9). The 30 nm AgNPs showed a larger number of cells in phase G1 for the 5 and 10 µg/mL concentrations (67.70 ± 2.78 and 65.06 ± 4.6 %, respectively) compared to naïve, whereas the lowest concentration displayed a decrease in the number of cells in this phase. Similarly, phase S displayed a lower number of cells for the three concentrations, showing at 5 µg/mL a statistically significant difference (* $p < 0.05$) with 67.70 ± 2.78 %, compared to naïve with 65.46 ± 2.2 %. Conversely, phase G2 showed a slight increase in the number of cells in this phase for all the AgNP concentrations, with 12.36 ± 3.15 , 13.18 ± 1.37 , and 12.53 ± 0.37 % for the 2.5, 5 and 10 µg/mL concentrations, respectively, and compared to 10.03 ± 1.6 % of the naïve cells. No statistically significant differences were found for these treatments compared to naïve cells. On the other hand, the 100 nm AgNPs displayed a slight increase in the % of cells at phase G1 at 10 µg/mL, with 65.73 ± 2.45 % compared to 65.46 ± 2.20 % of naïve cells in G1. Phase S showed a lower number of cells (%) in this phase when compared to

naïve. On the contrary, all the AgNP concentrations showed higher % of cells at phase G2, with 11.02 ± 4.18 , 12.46 ± 2.15 and 10.95 ± 1.97 % for 2.5, 5 and 10 $\mu\text{g/mL}$, compared to naïve with 10.03 ± 1.60 %.

Interestingly, all the AgNP concentrations for all three sizes (10, 30 and 100 nm) showed a decrease in phase S of the cell cycle compared to controls, suggesting that cells are not entering this phase (of DNA synthesis), remaining in the other phases of the cell cycle [329]. On the other hand, the 1.5 and 2 $\mu\text{g/mL}$ concentrations of the ionic control (AgNO_3) showed the highest percentages of cells in phase G1 with 68.35 ± 1.06 and 71.0 ± 2.40 % respectively, compared to the naïve and AgNPs treatments. As was the case with the 10 nm AgNPs, the ionic treatments displayed a reduction in the percentage of cells entering into phase G2 at the medium (7.87 ± 0.92) and high concentrations (6.75 ± 0.78), whereas the lowest concentrations (1 $\mu\text{g/mL}$) showed an increase in the % of cells at this phase, with 11.76 ± 0.94 %. A summary of the results, including the percentages obtained for each phase and histograms, can be found in SI as Section 8.2.7, Figure S8.5 and Tables S8.13 and S8.4.

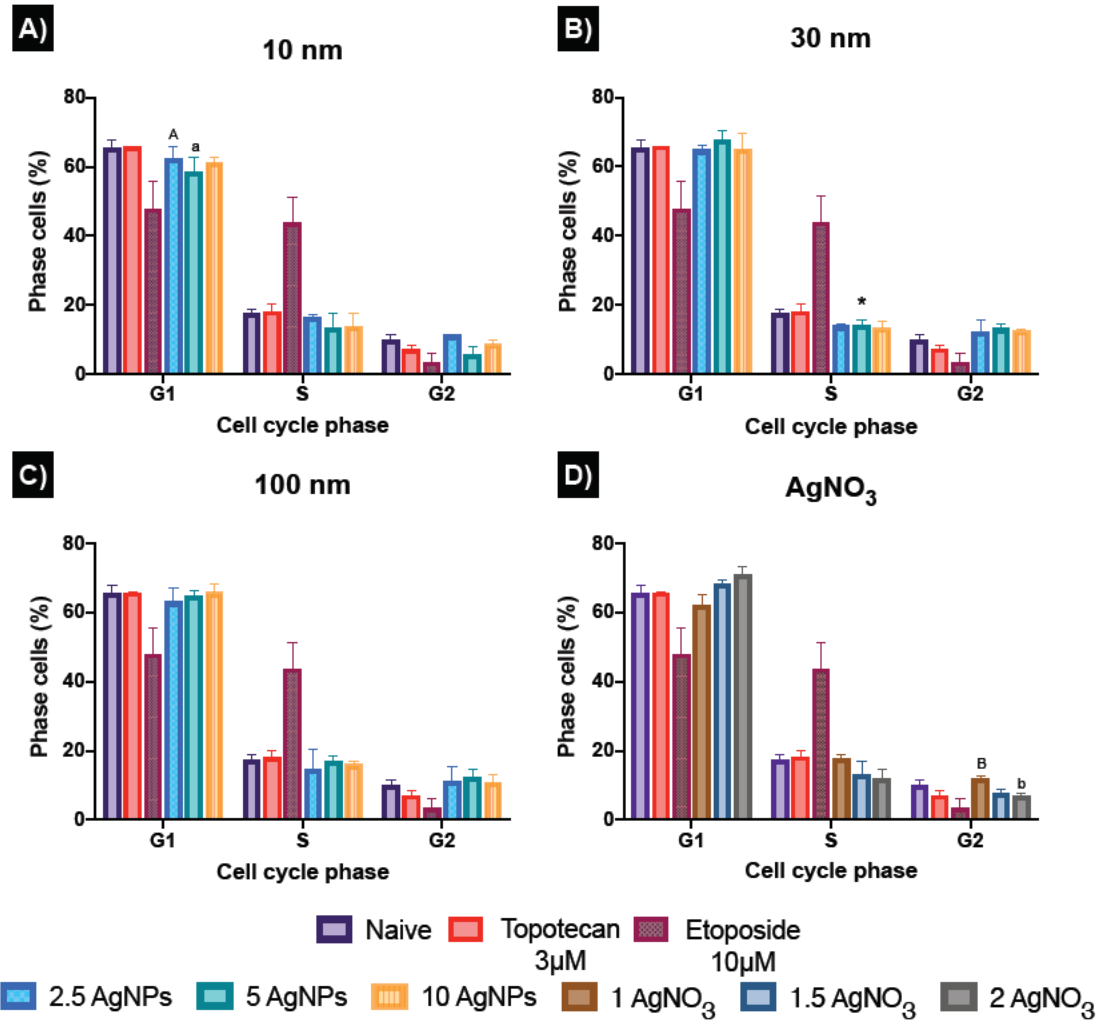


Figure 3.9. Impact of AgNPs on cell cycle progression of ZF4 cells. Cells were treated with either 2.5, 5, and 10 µg/mL of three different AgNPs sizes (10, 30 and 100 nm) or 1, 1.5 and 2 µg/mL of AgNO₃ for 24 hours in CCM. A-D) Percentage (%) of cells in each of the cell cycle phases after the exposure to AgNPs or AgNO₃. Figures represent the mean intensity of propidium iodide versus the number of cells counted (10,000). Concentrations of topotecan (3 µM) and etoposide (10 µM) were included as positive controls for S phase and G2/S phases, respectively. Data with asterisks (*) indicate statistically significant differences between AgNPs treatments and naïve for each phase (*p < 0.05) and the naïve cells. Similar letters (upper and lowercase) above the bars denote statistically significant difference (p < 0.05) between the selected concentrations.

3.3.7 DNA damage by comet assay

Single-cell gel electrophoresis or alkaline Comet assay was used to detect single DNA strand breaks in ZF4 cells exposed to AgNPs and its ionic counterpart (AgNO_3) (Figure 3.10).

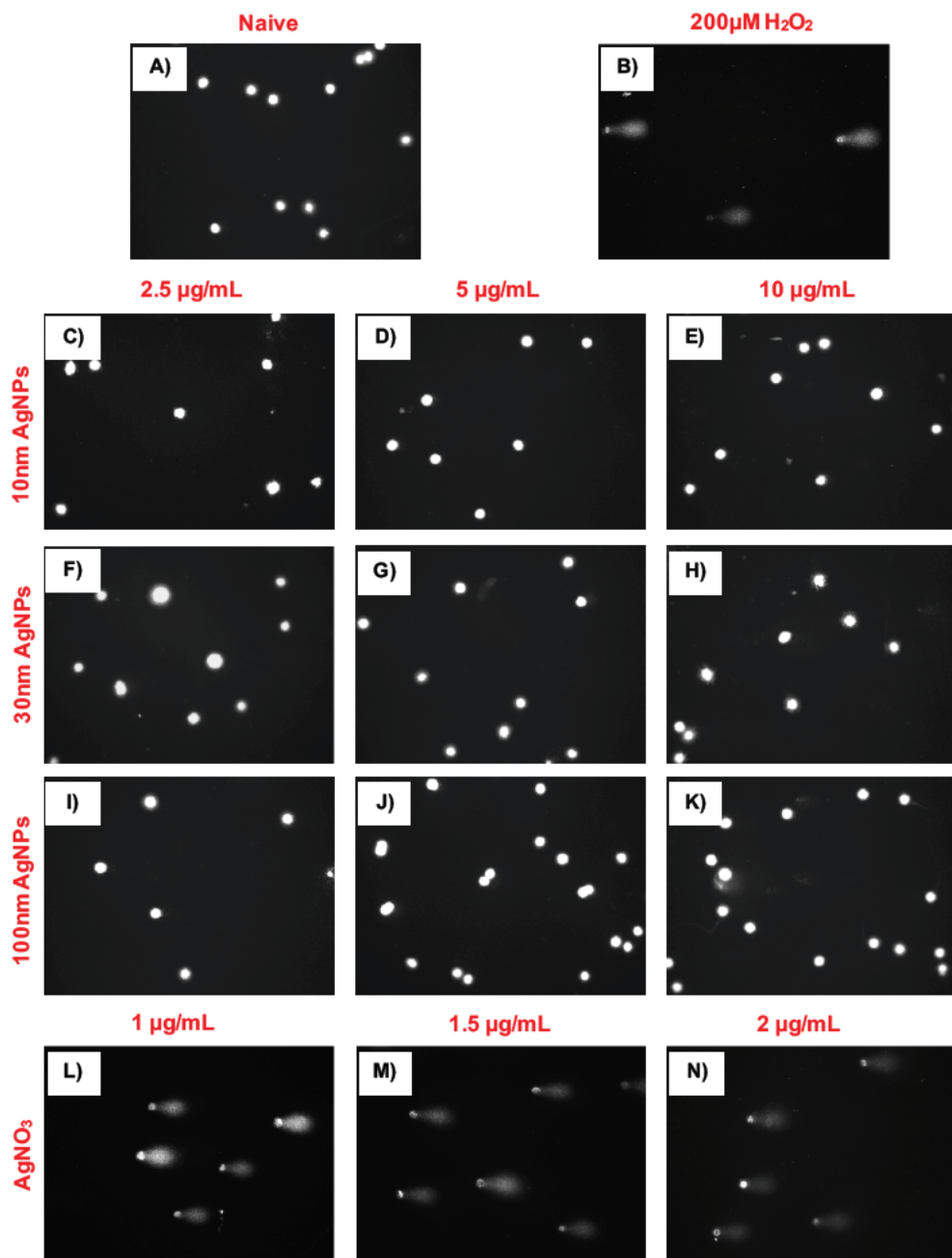


Figure 3.10. Comet assay images. The mass concentrations used are shown above the images while the details of the treatment (AgNP size or ionic control) are shown on the left. The images represent one of the three replicates for each treatment. A) represents untreated cells. B) Positive control. Cells were treated with 200 μM of H_2O_2 for 30 minutes.

C-E) cells treated with 10 nm AgNPs at the different concentrations (2.5, 5 and 10 $\mu\text{g}/\text{mL}$). F-H) Cells treated with 30 nm AgNPs at 2.5, 5 and 10 $\mu\text{g}/\text{mL}$. I-K) Cells treated with 100 nm AgNPs at 2.5, 5 and 10 $\mu\text{g}/\text{mL}$. L-N) Cells were treated with 1, 1.5 and 2 $\mu\text{g}/\text{mL}$ of AgNO_3 . All AgNPs and AgNO_3 treatments were incubated for 24 hours. A concentration of 200 μM hydrogen peroxide (H_2O_2) was included as positive control for 30 minutes to induce DNA damage [328].

The results showed increased DNA strand breaks for all AgNP concentrations and sizes.

The recorded tail percentages (%) following exposure to 2.5, 5, 10 $\mu\text{g}/\text{mL}$ were 7.5 ± 2.61 , 8.70 ± 4.52 , and 11.45 ± 3.53 % for 10 nm AgNPs and 8.32 ± 6.03 , 8.88 ± 9.69 , and 10.45 ± 5.02 % for 30 nm AgNPs (Figure 3.11). Both NP sizes (10 and 30 nm) showed a statistically significant difference at the highest concentration (10 $\mu\text{g}/\text{mL}$). The 100 nm AgNPs displayed the lowest percentages of DNA breaks at the three AgNP concentrations, which suggests that the smaller NPs may interact more easily with the DNA; whereas for the 100 nm AgNPs internalisation and contact with DNA may be less likely. The positive control showed the highest percentage of DNA strand breaks compared to the AgNPs treatments and naïve, displaying almost identical values for the medium and high concentrations, with 79.48 ± 2.67 % for 1 $\mu\text{g}/\text{mL}$, 82.67 ± 1.46 % for 1.5 $\mu\text{g}/\text{mL}$ and 82.90 ± 0.91 % 2 $\mu\text{g}/\text{mL}$. Interestingly, the ionic control displayed slightly higher % strand breaks than the positive control (H_2O_2), with 46.81 ± 6.02 %.

The AgNO_3 treatments also showed a significant difference at all the concentrations compared to the naïve cells ($***p < 0.001$). Overall, all the comets in the acquired images reveal tail differences between the AgNP treatments versus its ionic counterpart (AgNO_3), which showed massive percentages of DNA breaks compared the nanoparticulate form. A full summary of the results can be found in the Tables S8.15 and S8.16 in the SI.

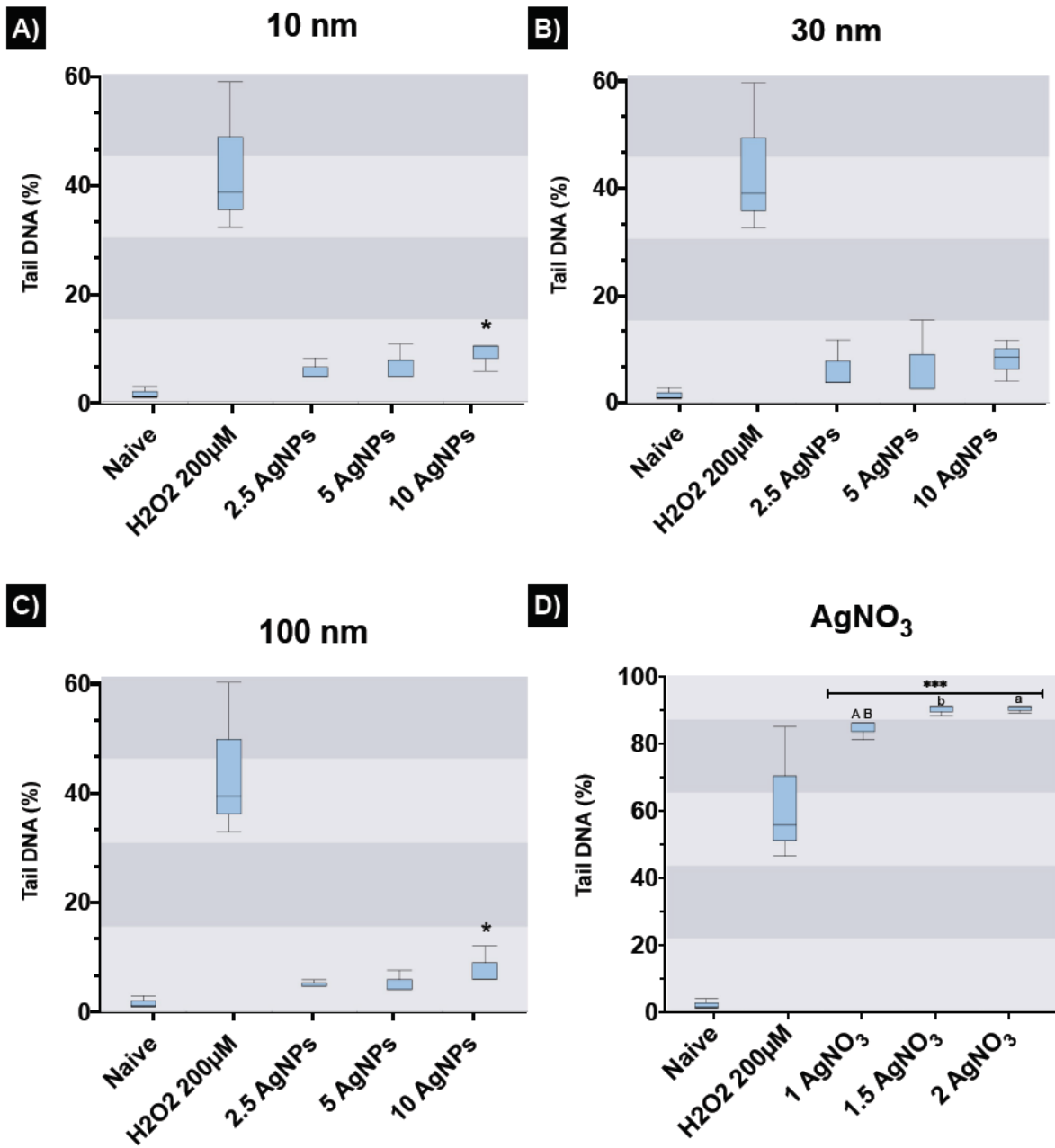


Figure 3.11. DNA damage in ZF4 cells treated with AgNPs and AgNO₃. The mean DNA strand break percentages (%) obtained by analysing the DNA tail intensity (%) were determined using the Comet assay. Three individual replicates were prepared and 150 comets in total were scored per treatment. Comets were analysed using IV comet macro software. Data with asterisks (*) indicate a statistically significant difference of AgNPs treatments (* $p < 0.05$ and *** $p < 0.001$) compared with the naïve cells. All bars under the line are included within the asterisk above. Similar letters (upper and lowercase) above the boxes represent statistically significant difference ($p < 0.05$) between the selected concentrations.

3.4 Discussion

AgNPs are strongly influenced by the surrounding environment. Hence, the interactions between NPs and constituents of the cell medium provide insights about the behaviour of the NPs in relevant biological fluids or complex environments [57]. It is known that the presence of proteins and salts and in cell medium can either reduce or enhance the toxicity of NPs as well as inducing alterations in the physiochemical characteristics of the NPs, such as changes in the size, shape and surface area [58-60, 290]. In this regard, the characterisation in CCM and SFM by DLS demonstrated that the serum had a stabilizing effect on the NPs, as the hydrodynamic size did not change over 24 hours, compared to the AgNPs in SFM, which revealed major agglomeration after 24 hours. Moreover, the zeta potential in CCM treatments remained similar at both time points suggesting that corona formation around the PVP-capped AgNPs in CCM provided additional stability, with corona formation also evidenced by the slight increase in size as a result of the binding of serum proteins onto the surface of the NPs [330-332]. The hydrodynamic size in CCM was expected to increase most for the smaller particle size (10 nm) as the small particle size means that larger proteins may bind more than one particle leading to some agglomeration. Also, for the larger particle, a diameter increase of just a few nm as a result of protein binding, which is less discernable by DLS than the increase in size of the smaller NPs [278]. On the other hand, AgNPs in SFM revealed strong agglomeration and/or sedimentation after 24 hours, with sizes between 500 to 600 nm, presumably due to the high concentration of ionic salts in the medium despite the PVP capping which should provide steric stabilisation [323]. Similar NP behaviour in SFM has been previously demonstrated by other authors [62, 292, 323, 333]. For example, a

study by Yue et al., (2014) determined that citrate AgNPs in SFM exposed to rainbow trout cells presented a noticeable increase in size going from an initial size of 40-100 nm to 1000–1750 nm after 24 hours; although the particles here were electrostatically stabilised only [62].

The dynamic interplay between the intrinsic properties of the NPs and the components of the physiological environment is closely related to cellular responses to the NPs *in vitro* systems [57]. In this study all the experiments were performed in CCM; however, to further understand the effect of serum on the toxicity the NPs, an additional cytotoxic assay in SFM was included. Results demonstrated that AgNPs treatments in CCM (10% FBS) produced a minor cytotoxic effect on cells compared to the serum-free treatments, which revealed higher toxicity at earlier exposure times, as suggested by other authors in mammalian and fish cell models [290, 323, 333-335]. A similar trend was also recorded for all the Ag⁺ concentrations.

In fish, the effect of AgNPs on Na⁺/K⁺-ATPase activity in gills has been attributed to the dissolution of silver ions from the particles, and/or to the presence of silver ions at the surface of the AgNP [68, 127]. In addition, the interaction of AgNPs and Ag⁺ with proteins can alter the protein conformation, inducing unexpected toxicity. This is related to the likelihood of both AgNPs and Ag⁺ to be complexed with thiol groups and to induce protein misfolding, as thiol groups may act as linkers to immobilize AgNPs on electrodes via Ag-S bonds [336, 337]. In this regard, the cytotoxicity of AgNPs in CCM compared to SFM treatments may be influenced by the binding between NPs and ionic silver with the proteins present in the medium, including the likelihood of Ag to undergo chemical transformations in complex environments. For example, in fish, constituents of the

medium (e.g., organic matter, ions, proteins) can strongly complex Ag^+ , causing a decline in silver bioavailability, and leading to changes in silver accumulation and toxicity over time [68, 127]. On the other hand, the absence of biomolecules (from serum) in the SFM treatments may result in higher cellular damage due to the strong adhesion of the bare NPs to the cell membrane, potentially forming a corona from biomolecules pulled out from the cell membrane, such as cytosolic proteins (from the cytoskeleton) and other cell membrane proteins [338, 339].

The cellular uptake and biodistribution of NPs are strongly influenced by proteins in the biological suspension, affecting their fate, bioavailability, and potential toxicity [45, 58, 282, 340]. Results for NP internalisation by confocal microscopy showed a major NP intensity during the first 2 hours, however, this might be due to NP adhesion to the cell membrane and not cellular uptake. It has been previously reported by Abdelkhalik et al. (2018) that the cellular adhesion of polystyrene NPs occurred after 10 minutes of exposure, whereas internalisation was confirmed after 24 hours in a much slower rate [341]. The confocal images agree with these findings; after 2 hours, the AgNPs were mainly associated with the cell membranes, while after 24 hours of exposure, the AgNPs were found located centrally and close to the lysosomes in the cells (Figure 3.4). In addition, NPs/cell calculations demonstrated a major number of visible intracellular NPs after 24 hours, especially for the 10 nm particles, which can be related to the larger number of NPs/mL at constant mass. In addition to the number of NPs/cells, the estimation of the total SA of the NPs' in our previous study at the different mass concentrations (2.5, 5 and 10 $\mu\text{g}/\text{mL}$) confirms that the smaller NPs have the largest SA

(e.g., $6.22 \times 10^{05} \text{ m}^2/\text{g}$ at $10 \text{ }\mu\text{g}/\text{mL}$) followed by the 30 nm which ($5.78 \times 10^{05} \text{ m}^2/\text{g}$ at $10 \text{ }\mu\text{g}/\text{mL}$) and lastly the 100 nm NPs ($3.67 \times 10^{05} \text{ m}^2/\text{g}$ at $10 \text{ }\mu\text{g}/\text{mL}$) [342].

Results for the uptake of NPs (based on reflected intensity) at both exposure times (2 and 24 hours) showed inverse tendencies, with the highest intensity values at 2 hours ($10 \text{ nm} > 30 \text{ nm} > 100 \text{ nm}$), whereas after 24 hours, there was a notable decrease in the intensity of NPs, and the overall intensity was in the order $100 \text{ nm} > 30 \text{ nm} > 10 \text{ nm}$. These results may suggest that cells might be able to cope with NPs at short exposure times, as most of the NPs were located surrounding the cell membrane (Figure 3.4); after 24 hours, other factors may be influencing the intensity of the NPs such as dissolution (mainly for smaller NPs as 10 nm), which may decrease intensity levels and agglomeration (higher intensity for larger NP sizes) [343]. Furthermore, cells may inactivate pre-existing uptake routes due to saturation of the uptake pathways (after long exposure periods), related to the massive energy input needed to activate other cellular processes, such as stress mechanisms [344].

The internalisation of the NPs can be achieved by different membrane interactions and uptake processes, such as receptor-ligand mediated active process, as well as non-specific routes such as passive fluid encapsulation. The likelihood of AgNPs (10, 30 and 100 nm) entering cells through either direct membrane-bound interactions and/or fluid phase encapsulation (through clathrin-coated pits) was calculated based upon the properties of the vesicles and the NPs (e.g., size) as described by other authors [91, 238]. See Table S8.14 in the SI for the calculation steps. Results for the highest AgNP concentrations ($10 \text{ }\mu\text{g}/\text{mL}$) suggest that the 10 and 100 nm sizes were more likely to enter the cells via fluid phase (clathrin-coated), whereas for the 30 nm AgNPs, the calculations

showed a clear likelihood for the NPs to enter the cell via membrane proteins/receptors, showing a larger number of NPs at the cell surface and in the lumen which may enter the cells by binding to the inner membrane vesicle rather than through the fluid phase (see results in SI Section 8.2.10 as Table S8.18). However, further studies are necessary to confirm this hypothesis.

Interestingly, the exposure concentrations, size, and form (particulate or dissolved) of the AgNPs were linked to the induction of different biological outcomes. It has been suggested that smaller particle sizes may present a higher biological effect compared to larger particles at constant mass concentration due to the higher number of smaller particles [296, 297]. ZF4 cellular exposure to AgNPs and AgNO₃ resulted in an overgeneration of ROS, especially with the smaller sized AgNPs at all concentrations, supporting the likelihood of higher toxicity of the smaller size, which can be more easily internalised, inducing major intracellular disruption as well as producing a higher release of ion Ag inside the cells. The release of ions from NPs has been linked to a number of cytotoxic responses, becoming a threat to aquatic organism as suggested in other fish cell studies [58, 112, 290, 292, 294, 295]. The overgeneration of ROS by NPs exposure has been strongly related to disruption of other signalling related process. For example, intracellular silver can be oxidized to Ag–O– and finally stabilizes as Ag–S–, which is most likely bounds to proteins. The high affinity of Ag to –SH groups will also affect the antioxidant defence of the cells as Ag will most likely also bind to GSH, leading to oxidative stress and mitochondria-mediated intrinsic apoptosis, DNA damage, impairment of the cell cycle and eventually cell death [113, 337, 345, 346]. In this regard, a study by Bermejo-Nogales et al., (2016) in hepatoma fish (*Poeciliopsis lucida*) cells

demonstrated that AgNPs and Ag⁺ were able to induce oxidative stress via mitochondrial membrane potential disruption, eventually leading to cell death [113].

In addition, elevation of intrinsic Ca²⁺ content by metallic ions has been demonstrated to alter the antioxidant system in mammalian and fish cells. For example, elevated cytosolic Ca²⁺ may lead to excessive Ca²⁺ uptake by mitochondria, affecting the Ca²⁺ influx, stimulating the activation of dehydrogenases (and thus the up regulation of aerobic metabolism), and finally lead to apoptotic or necrotic cell death [319, 320]. Results for the intracellular Ca²⁺ mobilisation in the ZF4 cells tested herein demonstrated that the Ca²⁺ flux was increased by exposure to AgNPs. This perhaps can be related to the inhibition of Na⁺-K⁺-ATPase activity by Ag⁺ ions (released from the AgNPs following internalisation). Inhibition of this enzyme has been demonstrated as a major route of toxicity in fish, blocking the Na⁺ uptake and inducing reversal of the Na/Ca exchanger on the cell membrane, finally leading to increased intracellular Ca²⁺ and toxicity [65-67].

On the other hand, the Ca²⁺ response in the ZF4 cells to the ionic counterpart showed a decrease in the intracellular Ca²⁺, as indicated by the apparently negative values at the highest AgNO₃ concentrations. This perhaps can be related to a possible inhibition of Ca²⁺ uptake channel, decreasing the Ca²⁺ levels, as well as Ca²⁺ depletion by ROS scavenger products [347, 348]. However, further studies are necessary to evaluate the role of the Ca²⁺ and related channels in ZF4 cells.

The interaction between AgNPs and ZF4 cells can result in DNA damage and impairment of the cell cycle [349-351]. In addition, Ag ions are likely to bind to natural bases (cytosine-cytosine [C:C] mismatch), forming a C-Ag-C base pair, and stabilizing the duplex DNA containing the C:C mismatched base pair [352]. DNA break (determined

via Comet assay) results demonstrated a strong association between the % DNA strand breaks and the AgNPs size and concentration; here again the smaller AgNPs (10 nm) and the ionic control at all concentrations induced the highest % DNA strand breaks. These results are related to the fact that all AgNPs sizes and concentrations tested induced disruption in the cell cycle, preventing cells from reaching the S phase in which DNA replication occurs as suggested by other authors [329, 353]. The cell cycle results for the 10 nm AgNPs may suggest that the cells were not able to proliferate and continue with mitosis, instead relying on cell death as a means to overcome the DNA damage [354]. On the other hand, the 30 and 100 nm AgNP sizes clearly displayed an increase in the % cells accumulating in the G1 and G2 phases, which relates to cell proliferation, suggesting the induction of cell cycle arrest at these phases, providing time for the cell to repair the DNA damage and carry on with the processes for cell division [156, 322]. The DNA damage results can also be related to the likelihood of AgNPs interacting directly with proteins involved in the cell cycle via binding to thiol groups, affecting proteins from the cell cycle regulation pathway and therefore inducing DNA damage and toxicity [355]. Furthermore, the activation of the pro-apoptotic proteins (e.g., Bax family), which regulates cell cycle checkpoints, DNA repair, and cell death to maintain genomic stability cannot be excluded in fish cells [156]. For example, GADD45 is a protein that has been shown to interact and inhibit the kinase activity of the Cdk1/cyclinB1 complex after exposure to NPs, demonstrating a key role in the activation of G2/M phase [356]. However, further studies are necessary to explore the role of these pro-apoptotic proteins in the activation of apoptosis in ZF4 cells.

Overall, the evaluated cellular mechanisms triggered in response to NP-mediated toxicity elucidates the dynamic interplay between pathways and molecular responses activated to deal with the generation of oxidative stress and calcium disturbances, genetic damage, inhibition of cell division and induction of cell death, as suggested in the schematic illustration showing the dynamic interplay of the mechanisms evaluated in this study (Figure 3.12).

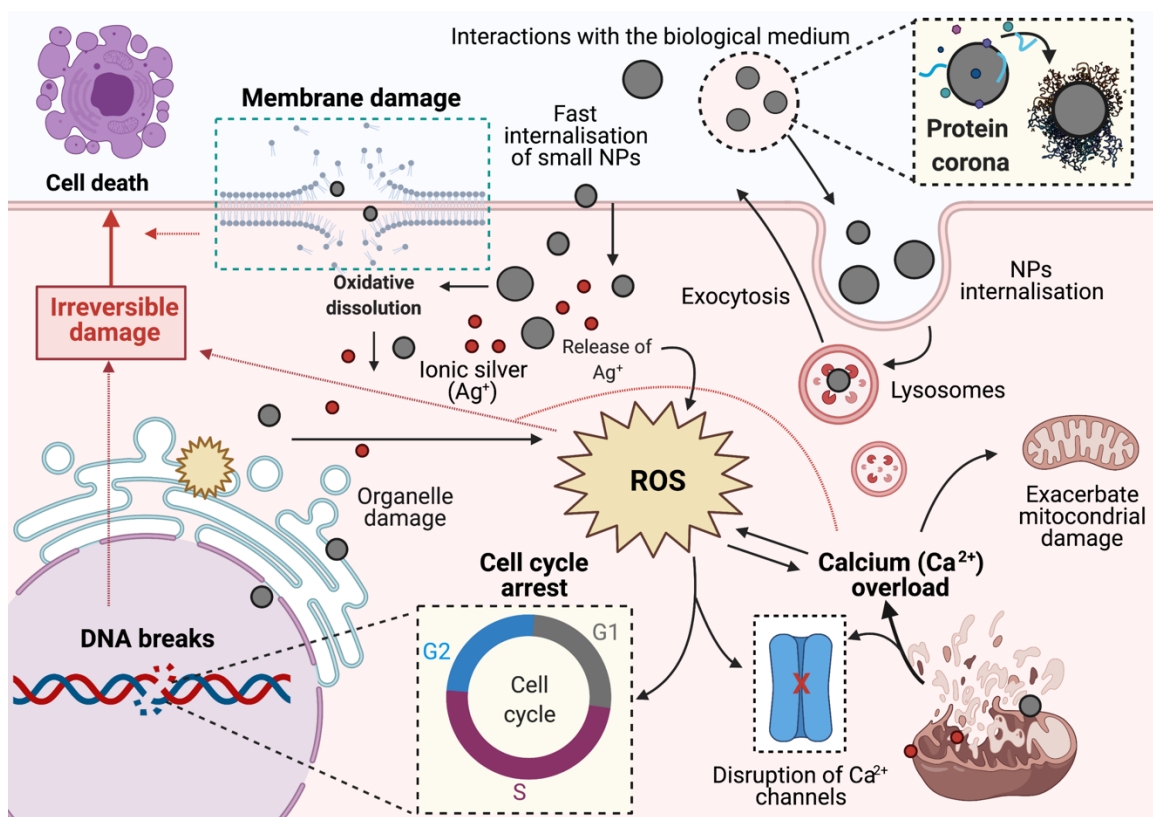


Figure 3.12. Hypothetical cellular mechanisms of effects induced to ZF4 cells by AgNP exposure. The figure illustrates the dynamic interplay of the evaluated mechanisms after exposure to AgNPs and ionic Ag^+ , including NP internalisation, membrane damage, Reactive Oxygen Species (ROS) formation, DNA strand breaks, calcium flux mobilization, and cell cycle arrest. Image created with BioRender software.

3.5 Conclusions

This study demonstrates the potential use of ZF4 cells as an emerging aquatic model to potentially assess toxicity and molecular mechanisms related to exposure to NPs. The interactions between AgNPs and the biological fluids revealed that NPs' physicochemical changes, colloidal stability, and cytotoxicity are closely related to the surrounding environment. Results indicate that 10 nm AgNPs are likely to be easily translocated into the cells, due to their small size and enormous specific surface area, which enables fast dissolution of the NPs and release of ions in the lysosomes, leading to loss of reflectance signal (in the confocal assays), as well as enhancing their Ag⁺ related toxicity and triggering cell death. Results for the uptake of the NPs by confocal microscopy, showed that internalisation of the NPs occurred at longer exposure times (24 hours), while at shorter exposure periods (2 hours) the NPs were mainly associated with the cellular membrane.

The internalisation of the NPs triggered the activation of defence mechanisms to deal with induced NP-toxicity. These responses were strongly linked to the concentration and size of the AgNPs and form (Ag ions), including binding with proteins, disruption of calcium flux by Ag⁺, overgeneration of ROS, cell cycle impairment, and DNA damage. These data, while confirming much of what is already known about AgNP toxicity, are an important addition to the literature as they indicate that ZF4 cells, which as a continuous adherent zebrafish embryo cell line, behave similarly to other fish and mammalian cells, representing a model for high throughput screening to assess nanotoxicity in fish species.

3.6 Acknowledgements

ACQ, IL and EVJ acknowledge support from the European Union Horizon 2020 Programme (H2020) projects as stated in section 2.7.2 “Acknowledgements” in Chapter 2. ACQ would like to thank Dr. Nikolas J Hodges for his kind assistance with the Comet assay technique.

Chapter 4: Cellular uptake mechanisms of silver nanoparticles (AgNPs) by embryonic zebrafish cells (ZF4)

This chapter has now been published in the journal Nanomaterials by MDPI.

Ana C. Quevedo^a, Laura-Jayne A. Ellis,^a Iseult Lynch^{a*}, Eugenia Valsami-Jones^a

^a School of Geography, Earth and Environmental Sciences, University of Birmingham, Edgbaston, Birmingham, B15 2TT, UK.

*Corresponding author: 

4.1 Abstract

Evaluation of the uptake pathways in cells during exposure to nanoparticles (NPs) is key for risk assessment and development of safer nanomaterials, as the internalisation and fate of NPs is linked to their toxicity and mode of action. Here, we determined the uptake mechanisms involved in the internalisation of 10, 30, and 100 nm AgNPs by embryonic zebrafish cells (ZF4). Characterisation of the NPs in Ultrapure Water (UPW) and Complete Culture Media (CCM) supplemented with 10% serum proteins, revealed that the medium influenced the NPs physicochemical characteristics such as size, charge, and biomolecule absorption. Uptake results demonstrated a NP size and time-dependent uptake, showing the highest total silver uptake for the smallest (10 nm) AgNPs size, with $0.80 \pm 0.57 \mu\text{g/mL}$ at the lowest exposure concentration (2.5 $\mu\text{g/mL}$) after 2 hours.

Conversely, after 24 hours, the highest concentration (10 µg/mL) for the 10 nm and 100 nm AgNPs, revealed the highest cellular load at 5 µg/mL for both sizes. Inhibition of the caveolae, clathrin and macropinocytosis endocytic pathways by pharmaceutical inhibitors (genistein, chlorpromazine, and wortmannin respectively) revealed that uptake was mainly via macropinocytosis for the 10 nm size and caveolae-mediated pathway for the 30 and 100 nm AgNPs. The induction of autophagy was also strongly related to the NP size, showing the highest percentage of induction for the 10 nm ($204.8 \pm 48.2\%$) compared to naive cells, suggesting that autophagy can be activated along with endocytosis to deal with exposure to NPs. TEM imaging suggests the potential uptake of NPs and distribution across the cytoplasm inside intracellular vesicles. An increase in the Early Endosome Induction (EEI) was observed for the three AgNP sizes at 2 hours, whereas after 24 hours, a decrease in the EEI was recorded.

4.2 Introduction

Silver nanoparticles (AgNPs) are broadly used nanomaterials in the biomedical and industrial fields, being incorporated into many daily life products, paints and textiles, due to their highly effective antimicrobial properties [14, 25]. The NPs physicochemical characteristics such as small size and large surface area provide numerous advantages in hundreds of nano-based products; however, negative effects also arise from these unique characteristics, demanding proper toxicological assessment of the possible negative outcomes linked to their release into the environment, in conjunction with an in depth understanding of their biological behaviour and effects following cellular exposure and internalisation [98, 339].

The behaviour of AgNPs in complex environments such as body fluids (gastric) or cellular media, is strongly influenced by the chemical composition of the medium, like pH, presence of salts, ions, and biomolecules. These compounds may induce a set of transformations in the physico-chemical properties of the NPs (e.g. dissolution, agglomeration, complexation), which may result in different toxicity outcomes [357]. For example, dissolution of the NPs, where the Ag^+ release is fostered by molecular oxygen available in the medium but hindered by the presence of chloride and sulphide that passivate the NP surface through the formation of AgCl or Ag_2S , respectively [39, 357]. In this regard, metallic ions such as silver ions (Ag^+) can enter the cells by hijacking systems on the cell membranes, including ion channels or other transporters (e.g., Na^+ , K , Ca^{2+} , Cu^{2+} , Cl channels and CTR1 and DMT1 [64, 102]. On the other hand, metal NPs seem to bypass such mechanisms and enter the cell via endocytosis [83, 86]. Endocytosis broadly involves different uptake processes, such as caveolae and clathrin mediated uptake and macropinocytosis [104, 105]. Non-endocytic process such as autophagy have gained relevance due to its physiological significance in engulfing, transporting, re-using, and degrading cellular components [93].

The use of pharmaceutical inhibitors to assess the endocytic pathways involved in the internalisation of NPs has been widely accepted in the scientific community and applied in a variety of cellular models [8,12-14]. The effectiveness of the pharmacological inhibitors is determined through assessment of the reduction of uptake of a chemical or transport molecules (e.g., cholera toxin, transferrin, dextran etc.) known to be internalized through that specific endocytic pathway, demonstrating their effectiveness by blocking the desired pathway [8].

In the present study, we aimed to assess the presence of the endocytic mechanisms involved in the uptake of different AgNP sizes (10, 30, and 100 nm) and concentrations (2.5, 5 and 10 $\mu\text{g}/\text{mL}$), using pharmacological inhibitors in embryonic zebrafish cells (ZF4). The goal was to provide insights about the internalisation of NPs in ZF4 cells, including the relationship between NP-uptake, formation of early endosomes, and autophagy. Finally, we aimed to demonstrate the utility of the ZF4 adherent continuous cell line for assessment of nanotoxicity, supporting the cellular based models and exploring uptake and the associated signalling pathways as potential molecular initiating events.

4.3 Methodology

4.3.1 Characterisation of AgNPs

Polyvinylpyrrolidone (PVP) coated silver nanoparticles (AgNPs) with sizes of 10, 30, and 100 nm were purchased from Nanocompositix, USA. The characterisation of AgNPs was performed in different testing media, such as simple water matrix (Ultrapure Water, UPW) and Complete Culture Media (CCM). The preparation of the CCM was described in Chapters 2 and 3. Similarly, the protocols used for characterisation of the NPs by DLS, including hydrodynamic diameter, PDI and zeta potential were described in Chapter 2, section 2.3.1 and in Chapter 3, section 3.3.1.

Ultraviolet visible light (UV-Vis) spectrophotometry was used to determine the optical spectra of the AgNPs (Abs_{max}) and to provide a complementary measure of particle size. Both techniques were applied in UPW and CCM, with AgNP dispersions prepared at a final concentration of 10 $\mu\text{g}/\text{mL}$ and incubated at 28°C for 0 and 24 hours. Then, 1

mL of the sample was placed in 3 mL disposable cuvettes (Sarstedt, 67742). All the samples were prepared fresh and immediately evaluated.

4.3.2 Culture of cells

Embryonic zebrafish (ZF4) cells were cultured as described in Chapters 2 and 3.

4.3.3 Quantification of total silver in ZF4 cells using ICP-MS

4.3.3.1 Exposure of ZF4 cells to AgNPs

Inductively Coupled Plasma Mass Spectrometry (ICP-MS) was implemented to assess the total silver uptake in ZF4 cells after exposure to AgNPs. For this, different methodologies were tested to standardise the protocol to ensure the maximum detection of ionic silver from AgNPs [259, 358, 359]. The final protocol was established as follow. First, ZF4 cells were seeded in six-well flat bottom plates (Corning, CLS3736) at a density of 5×10^5 cells per well in a total volume of 2 mL, using CCM. At 24 hours post-seeding ZF4 cells were treated to a low, medium, and high concentration (2.5, 5 and $\mu\text{g/mL}$) of the three representative AgNPs sizes (10, 30 and 100 nm); then, cells were incubated for 24 hours at 5% CO_2 and 28 °C. The tested AgNP concentrations were selected based on the Lactate dehydrogenase (LDH) assay used to quantify the LDH activity of ZF4 cells after AgNPs exposure. The methodology and results for this protocol, have been described in Chapter 2, section 2.4.3.

4.3.3.2 Digestion of the cells for quantification of Ag internalisation

After the treatment with AgNPs for 24 hours, the cell medium was removed and 3 mL of aqua regia was added. The aqua regia was prepared with 37% hydrochloric acid (H/1200/PB17, Fisher Scientific) and 70% nitric acid (A509-P500, TraceMetal™, Fisher scientific) in a ratio of 3:1. Cells attached to the six well plates were carefully washed with 500 µL of warm PBS (28°C) twice to ensure the removal of non-intracellular AgNPs. Cells were detached using 0.25% trypsin for 3 minutes at 28°C. Then, 3mL of aqua regia (prepared as previously described) was added per well, then cells were resuspended, and the mix was transferred to an individual clean glass vial. The glass vials were properly closed and placed in an oven overnight at 70°C. The next day, the acid digested samples were diluted with ultra-pure water to reach a 2% HNO₃ concentration. Then, the diluted samples were filtered with 22 µm syringe filters (E4780-1226, StarLab) to ensure the removal of any possible traces of cell debris and/or blocking of the ICP-MS tubes. Finally, the filtered samples were analysed using ICP-MS (NexION 300x, Perkin Elmer). The ICP-MS was calibrated as described in Chapter 2, section 2.3.3. Results are expressed as the mean of three independent replicates (n = 3) for each AgNP size and concentration. As described in Chapter 2, a preliminary experiment demonstrated a recovery of >95% Ag compared to the initial Ag concentration after centrifugation; therefore, efficiency calculations were not added to the results.

4.3.4 Uptake pathway inhibition using pharmacological inhibitors

4.3.4.1 Visualisation of the inhibition of cellular uptake pathways

When using inhibitors for endocytosis pathways, it is essential to confirm that the desired uptake pathway was effectively inhibited by the respective chemical inhibitors. To test the inhibition of desired cellular uptake ZF4 cells were seeded in 24 well MatTek 13 mm glass bottom dishes (MatTek, P24G013F) at a density of 100,000 cells/mL in CCM for a total volume of 1 mL and incubated at 28 °C and 5% CO₂. Twenty-four hours post-seeding, cells were pre-incubated with different concentrations of chemical inhibitors based on literature review [88, 92, 105], selecting the following as the final concentrations, which successfully inhibited the desired uptake pathway: 100 µg/mL of genistein (G6649, Sigma) for 20 minutes at 28 °C to inhibit the caveolae pathway, 10 µg/mL of chlorpromazine (C8138, Sigma) for 30 minutes at 28 °C to inhibit the clathrin mediated pathway, and 10 µg/mL of wortmannin (W1628, Sigma) for 10 minutes at room temperature for the macropinocytosis pathway.

All the inhibitors were prepared at the desired concentration in CCM in total volume of 500 µL per well. After the incubation period with the chemical inhibitors, the cell medium was removed and cells were carefully washed twice with 500 µL of warm PBS, then the respective markers (known to selectively enter cells via a specific pathway) were added for 2 hours at 28 °C (in a total volume of 500 µL) as positive controls to confirm that the inhibition was successful. The final concentrations for the transport molecules (controls) were as follows: 1 µg/mL of Cholera toxin subunit b (C1655, Sigma) for genistein treatments and to assess the caveolae pathway, 500 µg/mL of Transferrin Conjugate Alexa Fluor™ 488 (T13342, ThermoFisher) for chlorpromazine treatments and clathrin mediated pathway, and 500 µg/mL of dextran-Rhodamine B (D1824, ThermoFisher) for wortmannin treatments. After the incubation time, the cell medium was removed, and cells

were washed twice with warm PBS. Then, cells were fixed for 20 minutes with 500 μ L of 4% paraformaldehyde (16% Thermofisher, 43368) diluted in PBS and then examined by confocal microscopy using a NIKON A1R 808 series microscope. Images were recorded with a 60X objective and employing optical zoom. For, the red filter was used for dextran-rhodamine B, which has an Excitation/Emission of 647/668 nm, the green filter was used for cholera toxin subunit b and transferrin conjugate Alexa Fluor both with an Ext/Em of 495/519 nm. Images were processed by using FIJI open-source image processing tool (V.2.00-RC69). Results represent three individual replicates ($n = 3$) for each inhibitor. The percentage of inhibition was calculated using the intensity of the markers without treatment (untreated cells) versus intensity after treatment (inhibited cells) with the pharmaceutical inhibitors, as shown in the following formula:

$$\% \text{ of inhibition} = \frac{\text{Intensity of inhibited cells}}{\text{Mean intensity untreated cells}} * 100$$

4.3.4.2 Quantification of internalised Ag⁺ after inhibition of cellular uptake

Once the inhibition of the uptake pathways and the relevant concentrations of the pharmacological inhibitors were confirmed by confocal microscopy (to ensure the reliability of the assay); ZF4 cells were seeded in six-well flat bottom plates section 4.3.1. After 24 hrs, cells were incubated with 100 μ g/mL of genistein for 20 minutes at 28 $^{\circ}$ C, 20 μ g/mL of chlorpromazine for 30 minutes at 28 $^{\circ}$ C, and 10 μ g/mL of wortmannin for 10 minutes at room temperature. Inhibitors were prepared in CCM for a total volume of 2 mL per well. After incubation with the chemical inhibitors, the cell medium was discarded, and

cells were washed twice with 500 μL of warm PBS (28 $^{\circ}\text{C}$). Then, cells were treated with 2.5, 5 and 10 $\mu\text{g}/\text{mL}$ of AgNPs for 10, 30 and 100 nm sizes for 2 hrs at 28 $^{\circ}\text{C}$ in a final volume of 2 mL per well. After the AgNPs incubation period, the cell medium was removed. Cells attached to the six well plates were carefully washed with 500 μL of warm PBS twice and detached using 0.25% trypsin for 3 minutes at 28 $^{\circ}\text{C}$. Then, 3 mL of aqua regia (as described in section 4.3.3.2) were added and the mix was transferred to a clean glass vial for digestion. Then, samples were acid digested, diluted, and analysed using ICP-MS as described in section 2.3.3 of Chapter 2. Three individual replicates ($n = 3$) were analysed for each NP size, concentration, and chemical inhibitor used. Results were multiplied by the corresponding dilution factor and then the following formula was implemented to normalise all the data to percentage (%), considering naive (untreated cells) as 100%.

$$\text{Total Ag after inhibition} = \frac{\text{Result for each treatment}}{\text{Mean untreated cells}} * 100$$

4.3.5 Imaging of intracellular AgNPs using TEM

To gain further insights about the uptake of AgNPs by ZF4 cells, TEM analysis of the highest AgNPs concentration (10 $\mu\text{g}/\text{mL}$) was implemented. The protocol described by Ellis et al., (2020) was modified and adapted to ZF4 cells [360]. Briefly, ZF4 cells were seeded in six-well flat bottom plates as described in section 4.3.3.1. After 24 hrs, cells were treated with 10 $\mu\text{g}/\text{mL}$ of AgNPs for the 10, 30 and 100 nm sizes for 24 hrs at 28 $^{\circ}\text{C}$. After the AgNPs incubation period, the cell medium was removed, and cells were washed with 1 mL of warm PBS and then detached using 0.25% trypsin for 3 minutes at 28 $^{\circ}\text{C}$ in

a total volume of 2 mL. The detached cells were centrifuged for 10 minutes at 270 x g at 20 °C. Then, the supernatant was carefully removed, and the cell pellet was diluted with 2.5% glutaraldehyde in a 0.1M PBS provided by the Centre for Electron Microscopy at the University of Birmingham (UK), followed by 10 minutes of centrifugation at 270 x g at 20 °C (Eppendorf, 5430R). Finally, cells were dehydrated in ethanol and embedded in epoxy resin before sectioning using an ultramicrotome to cut 0.1 µm sections with a diamond knife. Sections were collected onto 300 mesh copper (Cu) grids on carbon film (Agar scientific UK, AGS160-3) and images were visualized using JEOL 1200EX 80kV and JEOL 1400EX 80kV microscopes.

4.3.6 Early endosome induction (EEI)

To further understand the endocytosis process, the induction of EE was evaluated by labelling early endosomes with red fluorescent protein (RFP) using cellLight™ Early Endosomes-RFP BacMam 2.0 (C10587) and following the supplier protocol. Briefly, ZF4 cells were seeded in 96-well flat bottom plates (Corning, 3917) in a total number of 8000 cells per well and in a final volume of 200 µL of CCM. Cells were left to attach overnight at 28 °C with 5% CO₂. The next day, AgNP treatments of 2.5, 5 and 10 µg/mL for different AgNP sizes (10, 30 and 100) were mixed with 2 µL of BacMam 2.0 reagent in a final volume of 200 µL per well. Then, the cell medium was gently aspirated, and cells were treated with the AgNPs mixed with the cell light dye and incubated for 24 hours at 28 °C with 5% CO₂. After the desired incubation time, the intensity of the red fluorescent protein of three individual replicates (n = 3) was measured by fluorescent microplate reader

(Tecan, Spark) using an Excitation and Emission of 555 / 584 nm respectively. The following calculation was used to normalise the results to percentage (%).

$$\text{Percentage of induction (\%)} = \frac{\text{Intensity treatment}}{\text{Mean intensity untreated cells}} * 100$$

4.3.7 Autophagy response

To evaluate the autophagy response in the uptake of AgNPs in ZF4, a modified protocol for autophagy evaluation by flow cytometry was adapted for confocal microscopy [342]. Briefly, ZF4 cells were seeded in uncoated 24 well MatTek 13 mm glass bottom dishes as described in section 4.3.4.1. Twenty-four hours post-seeding, cells were treated with 2.5, 5 and 10 µg/mL of 10, 30 and 100 nm AgNPs for 24 hours. After the incubation period, the cell medium was removed, and 500 µL of CCM mixed with nucleus and lysosome staining was added to the cells and incubated at 28°C for 30 minutes. The organelle labelling solution was prepared in warm CCM containing 1µL/mL of Hoechst 33342 (Thermofisher, 62249) and 1 µL/mL of LysoTracker™ Deep Red (Thermofisher, L12492). After the incubation period, the medium containing the first dyes were removed, and cells were washed twice with warm PBS. Then, cells were stained using Cell Meter™ Autophagy Assay Kit (23002). First, a stock solution was prepared with 20µL of Autophagy Green™ diluted in 10 mL of Stain Buffer. Then, 500 µL of the staining solution was added to cells and incubated at room temperature for 30 minutes (in the dark). Then, the autophagy staining medium was removed, and cells were washed with warm PBS once. Immediately a fixation was performed with 500 µL of 4% paraformaldehyde (16%

Thermofisher, 43368) diluted in PBS. Finally, cells were examined by confocal microscopy using a NIKON A1R 808 series microscope. Images were recorded with a 60X objective and employing optical zoom for all channels. For nucleus identification, the blue laser was used, with an excitation and emission of 350/461 nm, the red filter was used for the lysosomes (647/668 nm), and for autophagy response the green filter (495/519 nm). The intensity of three individual cells per replicate (n = 3) were analysed by FIJI open-source image processing tool (V.2.00-RC69). The following calculation was used to normalise the intensity results to percentage (%).

$$\text{Percentage of induction (\%)} = \frac{\text{Intensity treatment}}{\text{Mean intensity untreated cells}} * 100$$

4.3.8 Protein corona isolation and analysis of proteins using PAGE

To further understand the implications of the NP-protein in ZF4 cells, the protein corona was isolated by following a protocol by Docter et al., (2014) [361]. Briefly, cells were seeded in six-well plates as described in section 4.3.1. After 24 hrs, cells were treated with 2.5, 5 and 10 µg/mL of AgNPs of sizes 10, 30 and 100 nm for either 2 or 24 hours. After the exposure time, the cell medium was removed, placed in 2 mL Eppendorf tubes, and centrifuged at 20817 x g for 20 minutes at 4°C. Then, the supernatant was discarded, and the AgNP pellet was washed with 1 mL of PBS. The washing step was repeated three times. The pellet was eluted with 100 µL of SDS 4x Laemmli sample buffer (Sigma, S3401) and incubated at 95°C for 5 minutes. The eluted corona was gently transferred into a fresh tube and stored at -20°C for future analysis.

The isolated proteins were run on a 12.5% polyacrylamide gel electrophoresis (PAGE) at 170 V for 1.5 hours, then the gel was carefully washed with 10 mL of water and stained with 25% Coomassie blue staining at 37°C overnight. Afterwards, the gel was destained for 24 hours with a solution prepared with 10% acetic acid, 50% methanol and 40% UPW (with shaking and at least three solvent changes). Images were recorded by Gel Doc™ EZ Imager - Bio-Rad, using the white tray and selecting the protein analysis by Coomassie blue option in the software. Bands confirming the presence of proteins for the highest AgNP concentration (10 mg/mL) and sizes (10, 30 and 100 nm) were cut and sent for protein/peptide identification at the Advanced Mass Spectrometry Facility in the School of Biosciences at the University of Birmingham.

4.3.9 Statistical analysis

Results were plotted and statistically analysed using GraphPad V8.1 software by either one or two-way ANOVA followed by a Bonferroni post-hoc multiple comparison for all AgNPs and AgNO₃ treatments against the untreated control (naive).

4.4 Results

4.4.1 Characterisation of the AgNPs

The characterisation of the AgNPs in a simple testing media such as UPW and in a more complex and relevant environment such as CCM, are key to understand their impact on biological systems. The core size was evaluated by TEM in UPW; results demonstrated that the core was very close to one stated by the manufacturer, with recorded sizes of 13

± 2.4 for the 10 nm, 34 ± 2.8 for the 30 nm and 101.6 ± 9.2 for the 100 nm as discussed in Chapters 2 and 3. New analysis for the hydrodynamic diameter in UPW using DLS revealed that all three AgNPs sizes remained stable between 0 and 24 hours, showing a small increase of $< 2\%$ between time points, whereas the 100 nm presented a higher decrease ($<3\%$) compared after 24 hours. The polydispersity index (PDI) presented no changes for the 10 and 30 nm at the different time points, whereas the 100 nm displayed a small decrease in the PDI after 24 hours (from 0.06 to 0.03). The zeta potential in water displayed similar values between time points for the 10 and 30 nm, with less than 2% of variation. On the other hand, the 100 nm AgNPs displayed a noticeable decrease in zeta potential after 24 hours, with a final value of -23.46 ± 0.56 mV despite the particle stabilisation being steric in nature as result of the PVP coatings (Figure 4.1C).

The hydrodynamic diameter of the AgNPs after 24 hours in CCM was higher than in water, as expected, due to the presence of proteins and other biomolecules, which influence the dynamic behaviour of AgNPs in complex environments. The 10 and 30 nm sizes increased approximately 50% after 24 hours (Figure 4.1B), compared to their initial size. On the contrary, the 100 nm AgNPs showed a low hydrodynamic size, reaching 182.06 ± 4.25 nm after 24 hrs. The values for the zeta potential in CCM showed noticeable changes compared to the values in water (became less negative) due to the presence of FBS in the cell culture medium. This can be related to the shielding effect due to charge neutralization, and bridging interactions with the serum proteins. For example, the zeta potential values in CCM ranged between -7 to -12 mV at 0 and 24 hours, compared to values in water, which ranged from -17 to -57 mV at both time points (Figure 4.1D).

The absorption spectra (Abs_{max}) assessed by UV-VIS also displayed different values between the tested media. Samples in UPW displayed higher absorption efficiency as the absorption dominates the UV-VIS spectra, displaying only one peak for each measurement, whereas the samples in CCM showed two peaks and scattered photon flux due to the presence of proteins and other biomolecules in the cell medium (Figure S9.1 in the SI). The 10 and 30 nm NPs had high Abs_{max} at both timepoints, whereas the 100 nm absorbed less light with <1%. The samples prepared in CCM revealed different values for each AgNP size due to the protein background. The 10 nm presented almost a 50% decrease from the initial recorded size after 24 hours. The 30 nm size showed almost equal values for both time points (around 1.0 Abs_{max}) indicating very limited evolution of the sample beyond the initial interaction with the FBS. The absorbance of the 100 nm AgNPs displayed an increased value compared to the initial timepoint, reaching $1.195 \pm 0.00 Abs_{max}$ after 24 hours, reflecting light from internal interfaces and creating a scattering component. A summary of all the results, including UV-Vis images be found in Table S9.1, S9.2 and Figure S9.1 and in the supplementary information (SI).

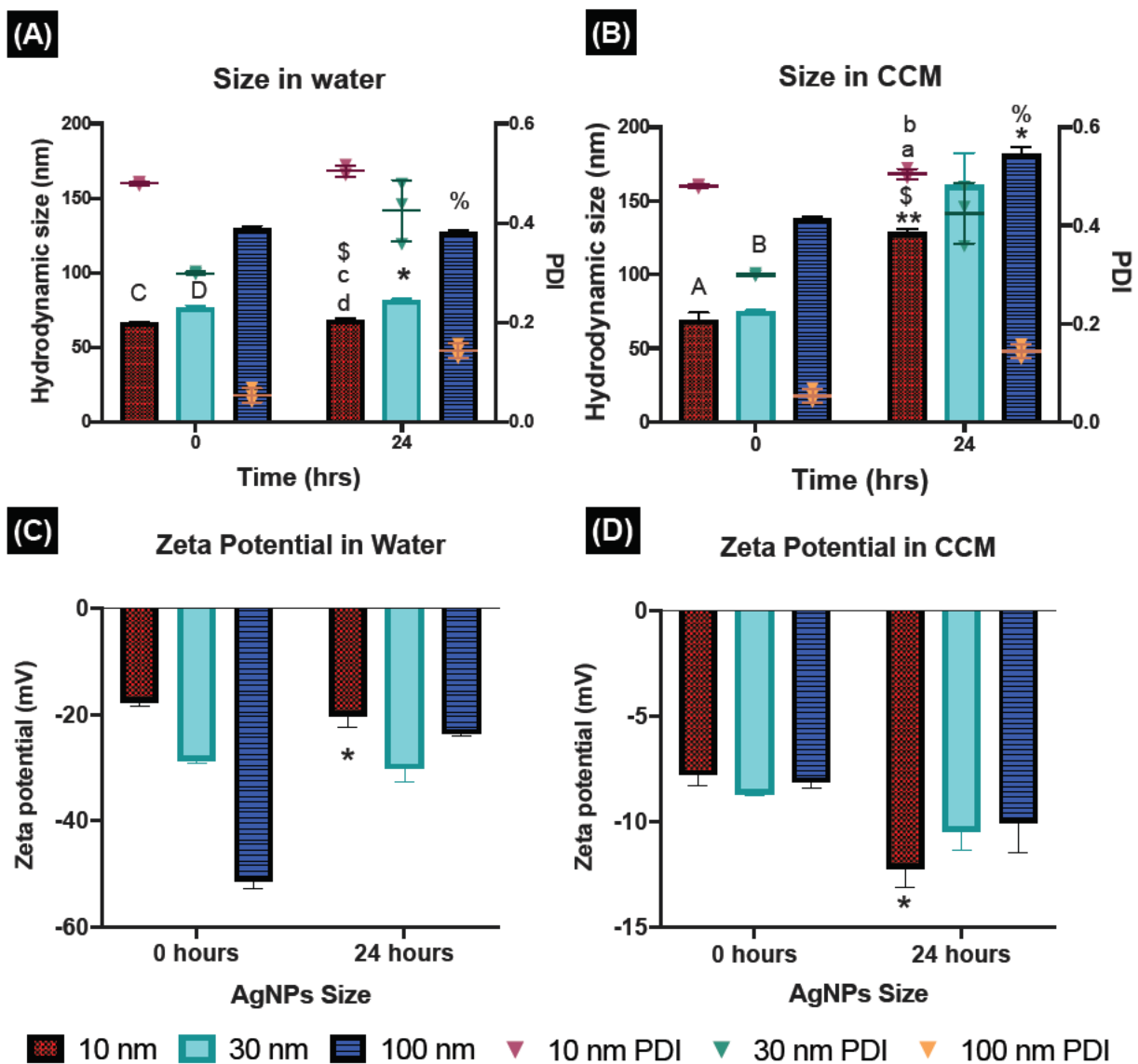


Figure 4.1. Characterisation of AgNPs. The characterisation of the AgNPs was performed following 0 and 24 hours of incubation in water and CCM by DLS. A and C show the hydrodynamic size and Zeta potential in water. B and D show the hydrodynamic size and Zeta potential in CCM. A-B left axis show the PDI recorded for each AgNP. Data with asterisks (*) indicate statistically significant differences ($*p < 0.05$ and $**p < 0.01$) between timepoints (0 and 24 hours) for the selected NP size. Similar letters (upper and lowercase letters) above the bars represent statistically significant difference ($p < 0.05$) between the selected sizes for the same testing fluid. Identical symbols denote statistically significant difference ($p < 0.05$) between water and CCM for the same NP size.

4.4.2 Cellular uptake using ICP-MS

The total metal (Ag) concentration in the ZF4 cells was evaluated using ICP-MS. Results demonstrated lower total Ag concentrations ($\mu\text{g/mL}$) in cells at 2 hours and compared to at 24 hours, which showed an almost 50% increase for most treatments (Figure 4.2). Results for the 10 nm size at 2 hours displayed slightly higher $\mu\text{g/mL}$ concentrations compared to the other NP sizes at this time point, showing an inverse-concentration trend, with $0.80 \pm 0.57 \mu\text{g/mL}$ for 2.5 $\mu\text{g/mL}$ and $0.25 \pm 0.09 \mu\text{g/mL}$ for the highest AgNPs concentration (10 $\mu\text{g/mL}$). The 30 and 100 nm showed similar concentrations ($0.03 \pm 0.01 \mu\text{g/mL}$) at 10 $\mu\text{g/mL}$, whereas at 2.5 $\mu\text{g/mL}$, the 100 nm display slightly higher results, with $0.07 \pm 0.02 \mu\text{g/mL}$, compared to $0.05 \pm 0.06 \mu\text{g/mL}$ for the 30 nm size at the lowest concentration (Figure 4.2A).

On the other hand, results for the total Ag accumulation were time-dependant, showing higher Ag concentrations after 24 hours, including statistically significant differences ($*p < 0.05$ and $***p < 0.001$) for almost all concentrations compared to naive (untreated cells) ($0.003 \pm 0.006 \mu\text{g/mL}$) as well as concentration effects between sizes (Figure 4.2B). The 10 and 100 nm sizes showed similar results for the medium and high concentrations, whereas for the 10 $\mu\text{g/mL}$, results were 5.05 ± 2.20 and $5.13 \pm 0.75 \mu\text{g/mL}$. The lowest AgNP concentration (2.5 $\mu\text{g/mL}$) showed higher uptake results for the 100 nm ($1.42 \pm 0.12 \mu\text{g/mL}$), whereas the 10 nm displayed an approximate 60% decrease ($0.86 \pm 0.14 \mu\text{g/mL}$) compared to the 100 nm. Conversely, the 30 nm size displayed the lowest concentrations compared to the other NP sizes at 24 hours, with an increasing concentration trend, with 0.54 ± 0.15 for the 2.5 $\mu\text{g/mL}$ and $2.60 \pm 0.20 \mu\text{g/mL}$ for the

highest AgNP concentration (10 µg/mL). Full results and complementary data can be found in Tables S9.3 and S9.4 in the SI.

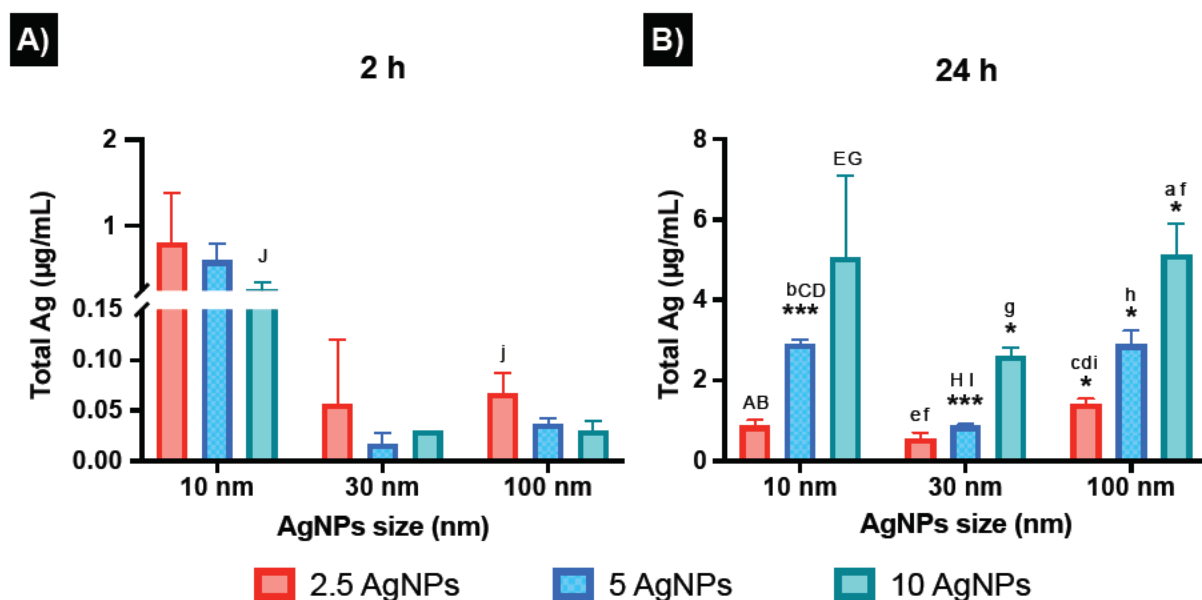


Figure 4.2. Intracellular uptake of AgNPs. Cells were treated with 2.5, 5 and 10 µg/mL of three different AgNP sizes (10, 30 and 100 nm) for 2 and/or 24 hours. Results were obtained by analysing the digested samples using ICP-MS. Data represents three independent samples and the standard deviation (mean ± SD). Results are expressed in µg/mL. Data with asterisks (*) indicate a statistically significant difference (* $p < 0.05$ and *** $p < 0.001$) between cells treated with AgNPs compared to naive cells (non-treated cells) for each point and concentration. Naive is not included in the figures. Data with similar letters (upper and lowercase letters) represent statistically significant difference ($p < 0.05$) between the selected concentrations and NM sizes.

4.4.3 Inhibition of the cellular uptake pathways using confocal microscopy

Different pharmacological inhibitors were used to block the three main endocytic pathways, including: genistein, which is an inhibitor of the tyrosine kinases involved in caveolae-mediated endocytosis, chlorpromazine, which inhibits clathrin disassembly and

its receptor from the cell membrane during clathrin-mediated endocytosis, and wortmannin which inhibits membrane phospholipids such as phosphoinositide-3-kinase (PI3K) which are closely interrelated with the activation of macropinocytosis [92, 106]. The effectiveness of the pharmacological inhibitors to block the desired pathway was tested along a positive control, including transferrin (Tf), which enter cells through clathrin-dependent endocytosis, cholera toxin beta subunit (CTB) linked to caveolae dependent endocytosis, and dextran, a probe for the macropinocytosis pathway [92, 105, 106, 248]. Additionally, to understand the cytotoxic effects of inhibitors on cells, the cell viability of the tested inhibitors at the selected concentrations was evaluated by the LDH assay. The methodology used for the LDH assay has been described in Chapter 2, section 2.3.5.

Confocal microscopy demonstrated that the uptake of 1 $\mu\text{g}/\text{mL}$ of cholera toxin B (Figure 4.3A) was successfully inhibited after treatment with (100 $\mu\text{g}/\text{mL}$) genistein for 20 minutes (inhibition of the caveolae pathway) (Figure 4.3B). Genistein treatments presented visible morphological effects, (e.g., cells became rounded compared to the flat and elongated morphology present in the untreated controls); however, the evaluated cytotoxicity showed a cell viability of $87.56 \pm 4.67\%$ after 20 minutes, compared to the control with 100% of viability (Figure 4.3G). Results for chlorpromazine (10 $\mu\text{g}/\text{mL}$) displayed less cytotoxicity with $91.41 \pm 2.31\%$ of viability after 30 minutes of incubation. Inhibition was confirmed via the reduced uptake of the transferrin (500 $\mu\text{g}/\text{mL}$), as shown in Figures 4.3C-D. On the other hand, wortmannin results displayed higher reduction of cell viability with $82.04 \pm 9.01\%$ after 10 minutes of incubation, however the concentration of 10 $\mu\text{g}/\text{mL}$ proved to be the lowest that can be used to achieve an inhibitory effect of

the macropinocytosis pathway, as shown in Figure 4.3F where some small amount of uptake was still observed and compared to the control (dextran) (Figures 4.3E and F). Most of the inhibitors displayed a reduction in cell viability near 20%, proving that the selected concentrations were suitable to induce around 80% of inhibition for all the tested inhibitors (Figure 4.3H) and for the specific endocytic pathway, without inducing severe cytotoxic effects, as suggested by other studies using a variety of human, mouse, and fish cell lines [88, 92, 99, 362]. Full results can be found in Tables S9.5 and S9.6 in the SI.

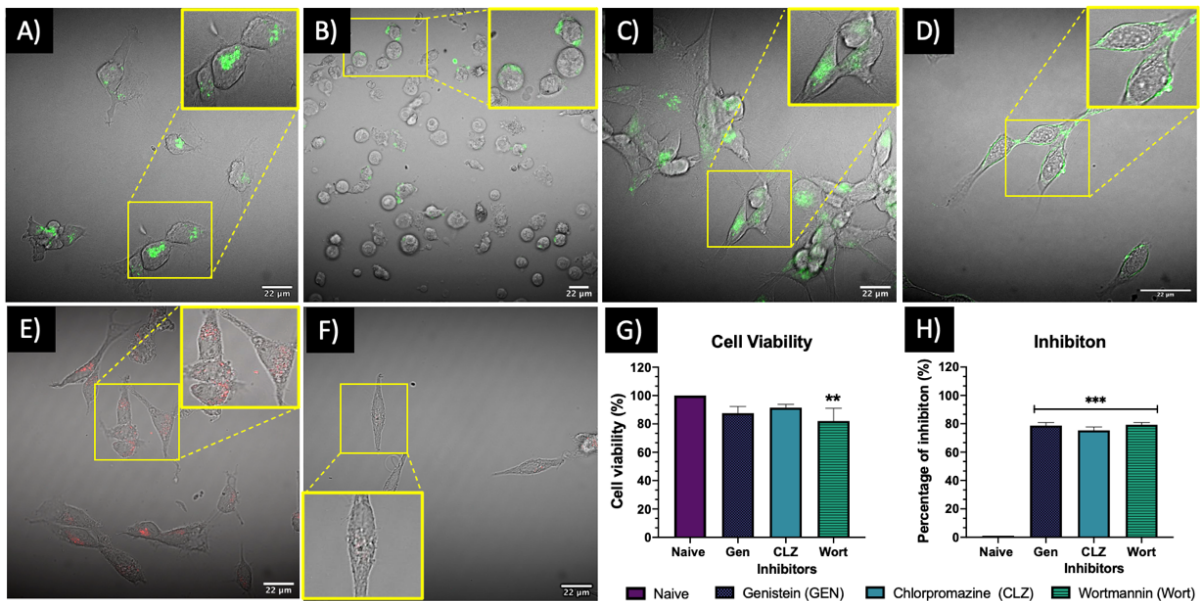


Figure 4.3. Inhibition of the cellular uptake pathways. (A) Uptake of Cholera toxin b (control); (B) Almost complete reduced Cholera toxin b uptake following inhibition of for the caveolae pathway with Genistein at 100 $\mu\text{g}/\text{mL}$ for 20 minutes. (C) Uptake of transferrin (control); (D) Partial reduction of transferrin uptake by the clathrin mediated pathway after treatment with 10 $\mu\text{g}/\text{mL}$ of chlorpromazine for 30 minutes. (E) Uptake of dextran (control); (F) Almost complete reduction in uptake of dextran by macropinocytosis and phagocytosis pathways after treatment with 10 $\mu\text{g}/\text{mL}$ of wortmannin for 10 minutes. All the controls were incubated for 2 hours prior to the addition of the chemical inhibitor. (G) Cell viability (%) by LDH after treatment with the selected inhibitor concentrations and incubation period. (H) The percentage of inhibition calculated for the inhibitor images against their control. Three individual replicates (mean \pm SD) were performed for all the experimental conditions and analysis. Images were taken with 60X objective lens and

employing optical zoom using NIKON A1R 808 microscope. Data with asterisks (*) indicate a statistically significant difference (**p < 0.01, and ***p < 0.001) compared to the naive cells.

4.4.3.1 Quantification of the total Ag⁺ in cells following inhibition of uptake pathways

Once the inhibitory concentrations of the drugs proved to be effective inhibiting the desired pathway, the internalisation of total Ag was quantified using ICP-MS. The total Ag uptake following exposure to the AgNPs was measured only at 2 hours as blocking one uptake pathway can result in activation of other endocytic mechanisms, which may lead to misleading results [88, 92]. Results for the levels of inhibition in the uptake of AgNPs are presented as a percentage (%) with respect to the uptake obtained by ICP-MS and in normal cells exposed to AgNPs under the same conditions and without any inhibitor treatment (Figure 4.4).

Normalised results show different patterns across the different treatment with the inhibitors, AgNPs sizes, and concentrations used. The 10 nm size showed a clear AgNPs uptake-inhibition response for all the chemical treatments and uptake pathways assessed. Results treatments for CLZ treatments showed no significant differences (*p < 0.05, **p < 0.01, and ***p < 0.001) for the low and medium concentrations (2.5, and 5 µg/mL) compared to untreated cells (100%), both with a percentage uptake around >93%; however, the 10 µg/mL showed a significant difference (*p < 0.05) with a low percentage uptake of 39.54 ± 4.67%. Genistein treatments displayed significant differences (*p < 0.05, **p < 0.01) compared to the uptake of the control; in particular, the medium and high AgNP (5 and 10 µg/mL) concentrations showed a reduction in

uptake of the 10 nm AgNPs with 30.71 ± 5.13 % and 6.74 ± 1.12 % uptake respectively relative to the non-inhibited exposures (100%). Similarly, the wortmannin treatments displayed a reduction of uptake at the lowest concentration (54.48 ± 19.20 %), followed by a statistically significant decrease ($*p < 0.05$) at the medium and high concentrations, compared to the uninhibited control. The 30 nm AgNPs showed an inverse trend for CLZ treatments, with a greater inhibition response at the lowest AgNP (2.5 mg/mL) concentration (77.38 ± 17.57) followed by 86.53 ± 8.32 for the 5 $\mu\text{g/mL}$ and no inhibition at all for the 10 $\mu\text{g/mL}$ (100%), suggesting that clathrin mediated pathway is not preferred pathway by ZF4 cells at medium AgNP sizes. Genistein treatments showed significant differences for all the AgNP concentrations ($*p < 0.05$, $**p < 0.01$, and $***p < 0.001$) compared to naive cells, with similar percentages of inhibition for the high and medium AgNPs concentrations (30%), but with a noticeable decrease at the lowest concentration (2.5 $\mu\text{g/mL}$) with 17.90 ± 4.03 %. On the other hand, wortmannin treatments showed a different pattern for the 30 nm AgNPs, with a clear increasing concentration-inhibition response and uptake reduced to 63.16 ± 16.47 % relative to the untreated control at the lowest AgNP concentration and to 33.67 ± 3.60 % for the 10 $\mu\text{g/mL}$. Treatments for the 100 nm size with CLZ displayed higher Ag uptake for the 10 $\mu\text{g/mL}$, compared to the other concentrations. Genistein treatments resulted in statistically significant differences at the low and high concentrations for 100 nm AgNPs compared to the naive ($**p < 0.01$), suggesting that the caveolae pathway is one of the major routes of internalisation for this NP size (100 nm). Results for wortmannin showed an inverse concentration-inhibition response trend, showing the lowest inhibition at 10 $\mu\text{g/mL}$ (33.31 ± 4.00), followed by

51.70 \pm 23.88 % of uptake for the 5 μ g/mL, and finally 63.26 \pm 16.55% at 2.5 μ g/mL relative to the naive cells uptake.

Overall, results suggest that the accumulation of total Ag in cells from AgNPs is dominated by macropinocytosis and caveolae pathway. The 30 nm size showed mainly inhibition in the genistein treatments, suggesting that the caveolae pathway is responsible for the uptake at this size. The 100 nm size similarly showed caveolae pathway activation, followed by clathrin mediated and macropinocytosis pathway. A summary of the results can be found in Tables S9.7, S9.8, and S9.9 in the SI.

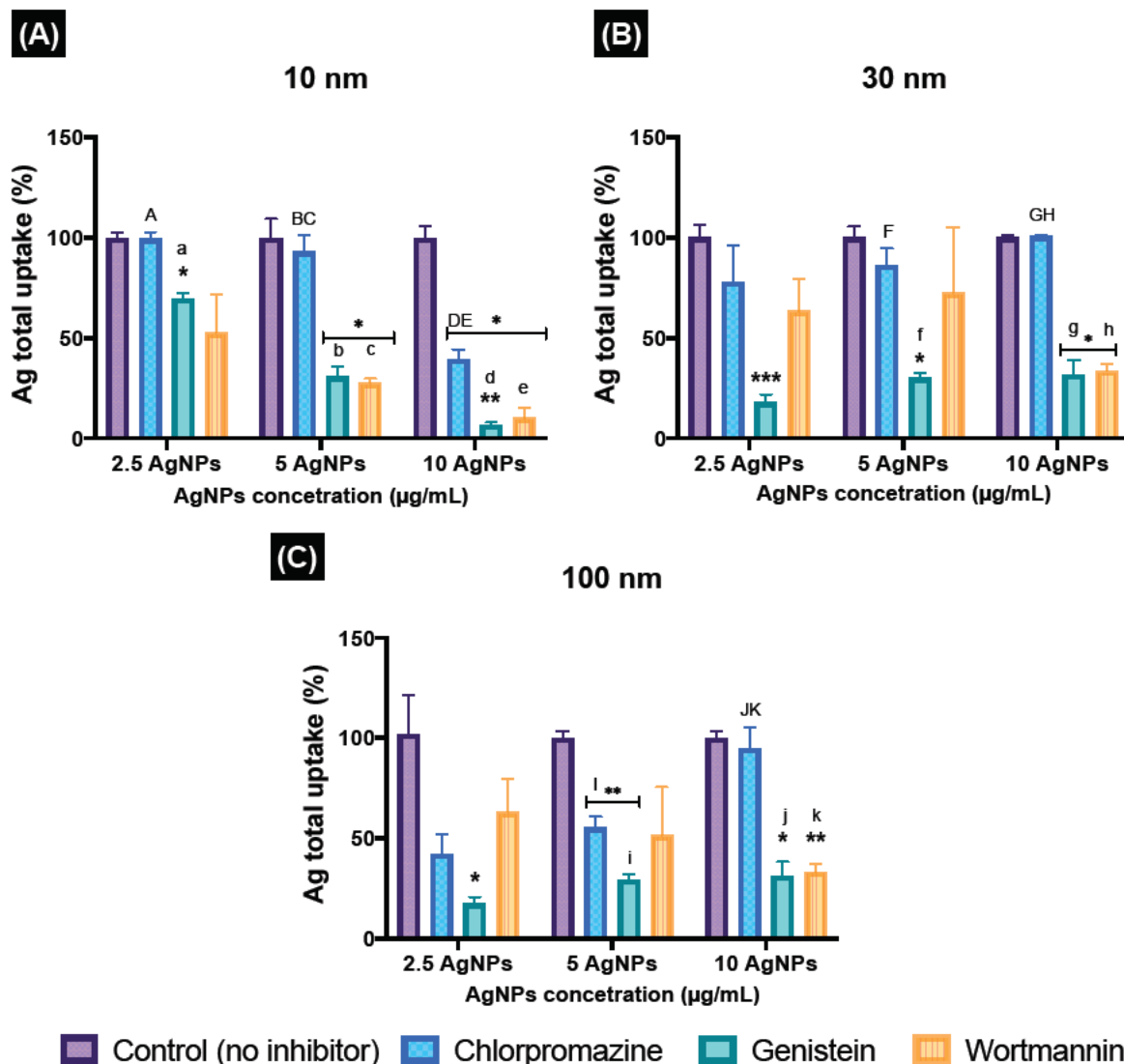


Figure 4.4. Quantification of the inhibition of the cellular uptake pathways. ZF4 cells were treated with either 100 µg/mL of Genistein for 20 minutes, 10 µg/mL of Chlorpromazine for 30 minutes or 10 µg/mL of Wortmannin for 10 minutes. After the treatment with the chemical inhibitor cells were treated with 2.5, 5 and 10 µg/mL of different AgNP sizes (10, 30 and 100 nm) for 2 hours. ICP-MS results for total Ag were normalised to percentage (%) against their untreated control (no inhibitor) for each concentration and size. Results represent the mean of three individual replicates and their standard deviation. Data with asterisks (*) indicate a statistically significant difference from the inhibitors' treatments (* $p < 0.05$, ** $p < 0.01$, and *** $p < 0.001$) compared to naive cells (non-inhibition) at each time point. All bars under the brackets are included within the asterisk above. Similar letters (upper and lowercase letters) above the bars represent statistically significant differences ($p < 0.05$) between the selected concentrations.

4.4.4 Intracellular localisation of NPs using TEM

Analysis of the images revealed the localisation of particles (of an unknown composition but assumed to be AgNPs) inside of intracellular vesicles. The composition can only be assumed as the elemental composition of materials was not analysed. Images from cells treated with small and medium NPs revealed the possible presence of particles located in the cytoplasm and in close proximity to the nucleus (see magnifications in Figure 4.5 A and D). Images (for the 10 nm) showed “NPs” inside intracellular vesicles, with signs of density loss potentially, perhaps due to dissolution (if AgNPs), which made assessment of their diameter challenging (Figure 4.5C). Assuming that the particles in the images are AgNPs, the diameter of the intracellular NPs was calculated as 5.50 ± 3.56 nm, compared to the core size of the NPs determined by TEM (13 ± 2.4 nm), resulting in a size reduction of 57.62% (Figure 4.5 A-C) (see section 9.1.4 in the SI for calculation steps). The diameter of the vesicles with encapsulated unknown NPs, displayed a size of 717.46 ± 78.57 nm (mean \pm SD of 3 different vesicles). In addition, TEM images revealed a possible caveolae pathway as shown in the yellow box in Figure 4.5B. Cells treated with 30 nm (Figure 4.5E) showed the presence of particles around the cell, perhaps as part of their subcellular trafficking in the cell (purple arrows). The larger magnification in Figure 4.5D reveals that particles inside a vesicle and very close to the nucleus (N). The diameter of the intracellular vesicles for cells treated with the 30 nm size was calculated as 697.86 ± 53.76 nm. Analysis of the size of the particles inside the vesicles revealed a size of 26.37 ± 4.55 nm and a percentage size reduction of 19.04% compared to the original TEM size of 34 ± 2.8 nm. TEM images for cells treated with the 100 nm size also showed signs of NP internalisation inside vesicles (Figure 4.5G-I). Figures 4.3 G and H showed a large

number of NPs outside the cellular membrane (blue arrow). Inside the cellular matrix, encapsulated in endosomes a large cluster of NPs is visible with signs of fragmentation if AgNPs (Figure 4.5I). The size of the intracellular NPs in the vesicles was calculated as 96.78 ± 8.36 , with the lowest percentage of reduction (4.16 %), compared to the initial size of 101 ± 9.2 nm and other sizes. Results for the calculated intracellular NP sizes can be found in Table S9.10 in the SI.

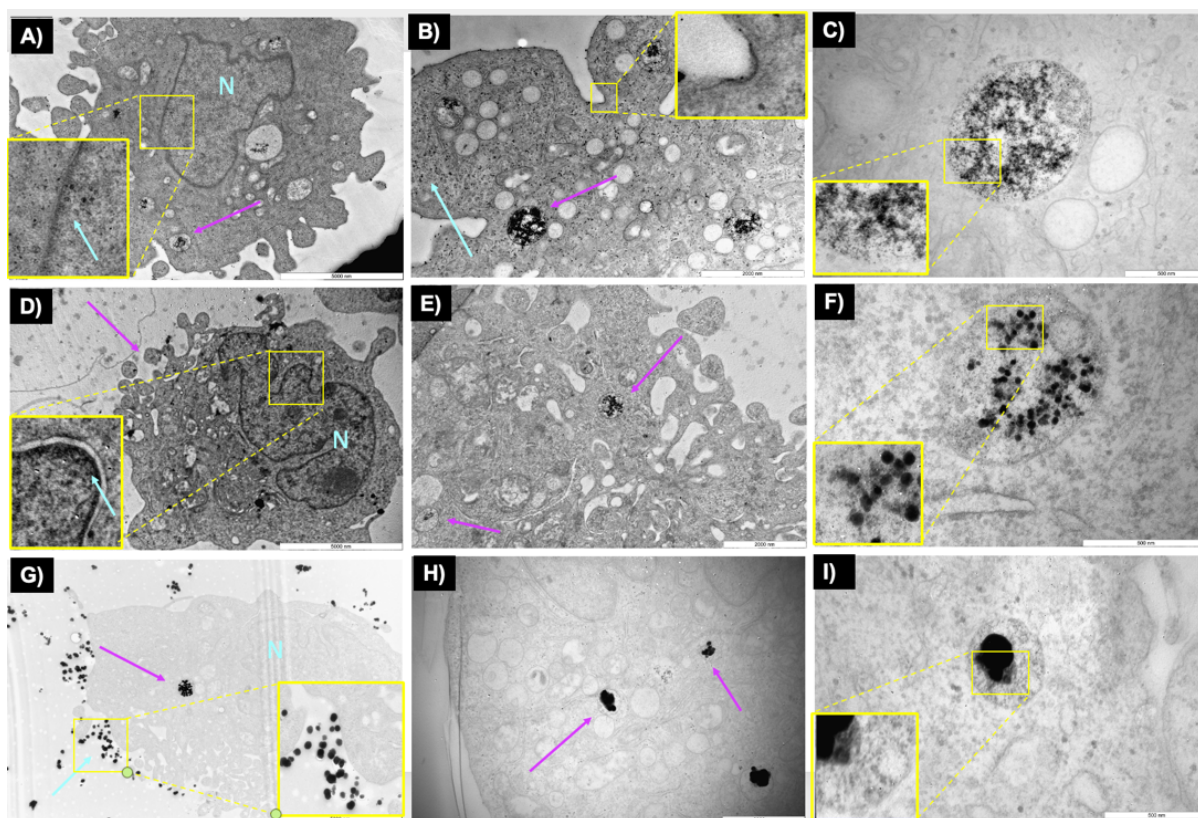


Figure 4.5. TEM images of cells treated with AgNPs. Cells were treated with $10 \mu\text{g/mL}$ of 10, 30 and 100 nm AgNPs for 24 hours. The images show the intracellular fate of particles of an unknown composition, as the elemental composition of materials was not identified. Assuming that the particles are AgNPs, the figures A-C show the uptake of 10 nm. The yellow square in Fig B shows an enlargement of the cell's uptake mechanism. D-F the uptake of 30 nm and G-F the uptake of 100 nm. The scale bars correspond to 5000, 2000, and 500 nm from left to right. Purple arrows indicate the formation of vesicles in the cells, blue arrows indicate NPs in the zoomed figures (yellow squares) and N means nucleus.

4.4.5 Early endosomes induction (EEI)

To gain further insights about the internalisation of the AgNPs in ZF4 cells, the EE induction (EEI) was evaluated by labelling the EE with red fluorescent protein for 2 and 24 hours of incubation. For this, intensity values were normalised and plotted as percentage (%) of EE induction with respect to naïve. Normalised results displayed higher percentages (%) of induction at all concentrations and sizes after 2 hours (>30 %), whereas after 24 hours, results showed a dramatic decrease in the percentage of EEI for all NP sizes and concentrations. The 10 nm size at 2 hours, displayed higher values (%) at 2.5 and 10 µg/mL (128.62 ± 11.76 and 131.7 ± 8.35 %, respectively) compared to the medium concentration (5 µg/mL), which displayed a small drop in the recorded intensity, and consequently reflected as a lower EEI percentage (125.1 ± 3.36 %). Statistically significant differences (* $p < 0.05$) were found for the low and medium concentrations (5 and 10 µg/mL) compared to the untreated control (naive).

After 24 hours, the 10 nm size showed the lowest recorded values (%) at the low and medium concentrations, with 111.13 ± 7.91 % for 2.5 µg/mL and 107.18 ± 2.22 % for 5 µg/mL, whereas the 10 µg/mL showed a slightly higher value with 114.00 ± 4.91 %. On the other hand, the 30 nm size displayed a concentration-dependant trend after 2 hours. Results for 2.5 and 5 µg/mL exposures showed values between 128 to 130%, whereas the 10 µg/mL displayed the highest recorded value (135.61 ± 13.06 %) for all the NP sizes and concentrations. After 24 hours, there was a small decrease in the percentage of EEI for the high and medium concentrations (compared to 2 hours), with values ranging between 114 and 118%. On the other hand, the lowest concentration (2.5 µg/mL)

displayed a similar value (131.7 ± 114.7) to that recorded at 2 hours. An increased percentage of EEI was recorded for the 100 nm size at shorter exposure times (2 hours) and showed an inverse concentration trend with values between 130-133% and statistically significant differences ($*p < 0.05$) against naive for the highest concentration (130.84 ± 5.75). On the contrary, after 24 hours, values were similar with around 118-119% for the low, medium, and high concentrations, showing statistical differences ($*p < 0.05$) at 5 and 10 $\mu\text{g}/\text{mL}$ compared to naive.

Overall, the results demonstrated that the EEI is closely linked to the size of the NPs, as results demonstrated higher EEI percentages for the larger size (100 nm), compared to the other AgNP sizes (10 and 30 nm) at both time points. Exposure time was also demonstrated to play a key role in the EEI, as results displayed a higher percentage of EEI during the first two hours, compared 24 hours, for all the NP sizes. Full results can be found in Tables S9.11 and S9.12 in the SI.

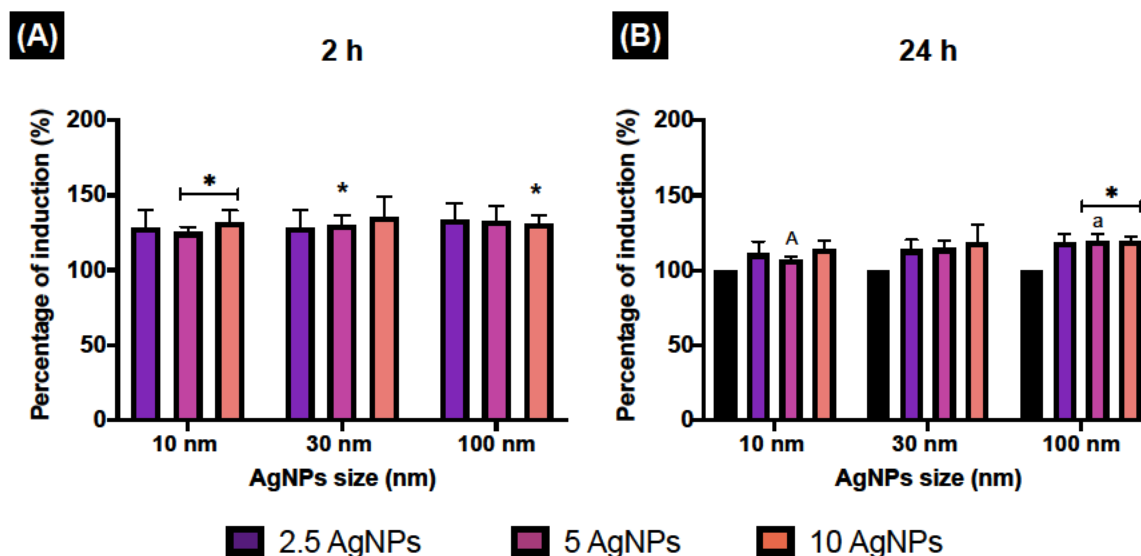


Figure 4.6. Early endosome induction. The percentage of EE induction (EEI) in ZF4 cells treated with 2.5, 5, and 10 $\mu\text{g}/\text{mL}$ of three different AgNP sizes (10, 30 and 100 nm) after 2 and 24 hours. The intensity results were normalised to percentage (%). Data represent the mean and standard deviation of 3 individual replicates. Data with asterisks

(*) indicate a statistically significant difference (* $p < 0.05$) between the treatment compared to the untreated control (naive) at the specific timepoint. Data with similar upper and lowercase letters above the bars indicate statistically significant differences ($p < 0.05$) between the selected NP sizes and concentrations.

4.4.6 Autophagy response

To further investigate the induction of autophagy in ZF4 cells during the exposure of AgNPs, autophagosomes were labelled and assessed. The intensity was normalised to percent (%) relative to the untreated (naive) cells as described in section 2.6. Results displayed the highest percentages (%) for the smallest NP (10 nm), compared to the other NPs sizes (Figure 4.7). Here, the low and high concentrations showed values above 200 %, whereas the medium concentration (5 $\mu\text{g/mL}$) displayed 187.62 ± 41.27 %. A statistically significant difference ($p < 0.05$) for the 2.5 $\mu\text{g/mL}$ against naive cells was found for this size. Similarly, a multiple comparison between the NPs sizes and concentrations showed a statistically significant difference ($p < 0.05$) between the 10 and 30 nm AgNPs for the lowest concentration (2.5 $\mu\text{g/mL}$). The 30 nm AgNPs showed the highest percentages at the lowest AgNP concentration (144.19 ± 22.49 %) compared to the medium and high concentrations, which displayed similar results, with 113.60 ± 5.41 and $114.73 \pm 14.24\%$, respectively.

On the other hand, the 100 nm AgNPs presented the lowest recorded percentage of autophagy for the three NP sizes. The results showed a similar trend as the 30 nm AgNPs, with high percentages at the lowest concentration ($110.15 \pm 4.56\%$), compared to the medium and high concentrations, with 108.15 ± 10.99 % for 5 $\mu\text{g/mL}$ and $104.55 \pm 3.64\%$

for the 10 µg/mL. Normalised results and the remaining confocal images can be found in Table S9.14, S9.15 and S9.16, including autophagy figures as Figure S9.2 in the SI.

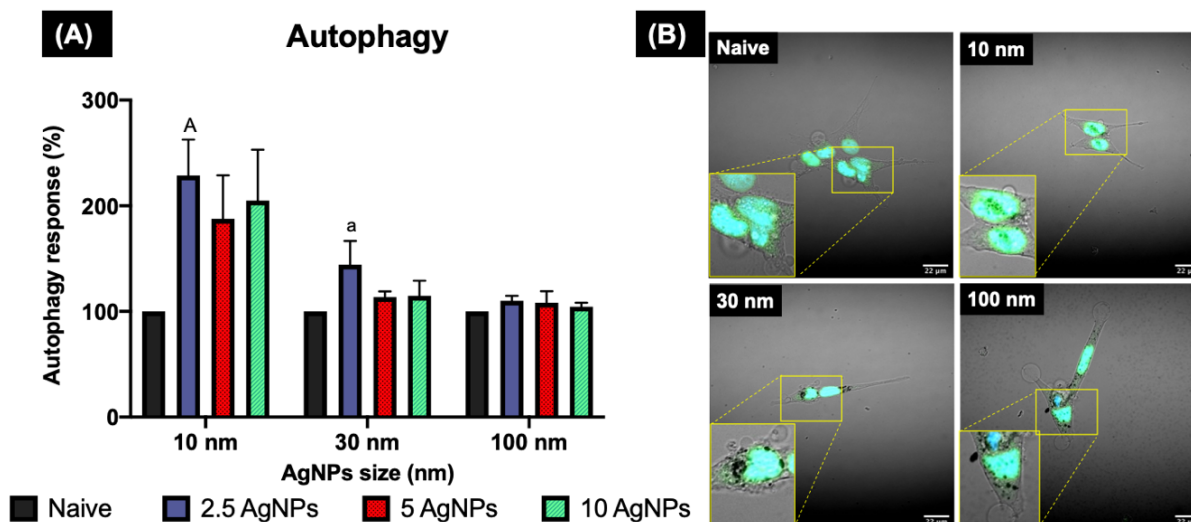


Figure 4.7. Autophagy induction in ZF4 cells as determined by confocal microscopy. ZF4 Cells were treated with 2.5, 5 and 10 µg/mL AgNPs of three different sizes (10, 30 and 100 nm) for 24 hours. Images of the cells with the nucleus (blue) and autophagosome staining (green) were taken at 60X with a NIKON A1R 808 series microscope. A close-up of the labelled cells is marked with yellow lines. The intensity of the labelled autophagosomes in ZF4 cells was recorded by FIJI and normalised to percentage (%) against naive cells. A) Results of three individual replicates are expressed as mean and standard deviation (mean ± SD). A statistical comparison between all treatments was performed. B) Cells treated with 10 µg/mL of different AgNPs sizes and the control. Images for the remaining AgNP concentrations and sizes can be found in the SI. Data with asterisks (*) indicate a statistically significant difference (*p < 0.05) between the treatment compared to the untreated control (naive). Data with similar upper and lowercase letters above the bars indicate statistically significant differences (p < 0.05) between the selected NP sizes.

4.4.7 Protein corona isolation and analysis of proteins using PAGE and mass spectrometry

The isolation of the protein corona from AgNPs after exposure to different mass concentrations and timepoints, revealed that the corona formation can be strongly

mediated by these factors. Bands in the gels were highly visible for treatments with the smaller NPs (10 nm) after 24 hours of exposure compared to 2 hours in CCM. For example, after 2 hours, gel bands for all three AgNP sizes and concentrations were similar, showing a single line between 72-57 kDa (Figure 4.8A), whereas after 24 hours the 10 nm AgNPs at the highest treatment concentration displayed a larger number of proteins across the entire molecular weight range (Figure 4.8B). This suggests that the NP size can influence the composition of their coronas, perhaps due to the secretion of certain (e.g., stress-related) proteins by the cells, increasing the availability of proteins in the cell medium, and driving a dynamic exchange behaviour of the NP-protein binding process.

Accessions from the zebrafish proteome database (Uniprot) (obtained using mass spectrometry) were searched in the Zebrafish Information Network (ZFIN) database of genetic and genomic data for the zebrafish (*Danio rerio*) as a model organism (<https://zfin.org>). Results revealed the presence of different proteins involved in, or upstream of, development and regulation of zebrafish, including proteins located in the cell membrane, cytoplasm, and nucleus (Table 4.1) [363].

To further understand the role of the secreted proteins, an initial experiment to record changes in the protein concentrations in the ZF4 cell medium during AgNP exposure was performed by recovering particles that had not yet been internalised. The results demonstrated that the total protein concentration (in suspension) increased over time for all the NP sizes and concentrations, with approximately a 5-10% increase of the total protein concentration in the medium after 24 hours, compared to the untreated control, which maintained a constant protein concentration after 24 hours (Figure 4.9).

However, further studies are necessary to confirm the mechanistic process behind these findings. The protocol for this initial experiment and results for all concentrations and timepoints can be found in section 9.1.8 in the SI and as Table S9.17.

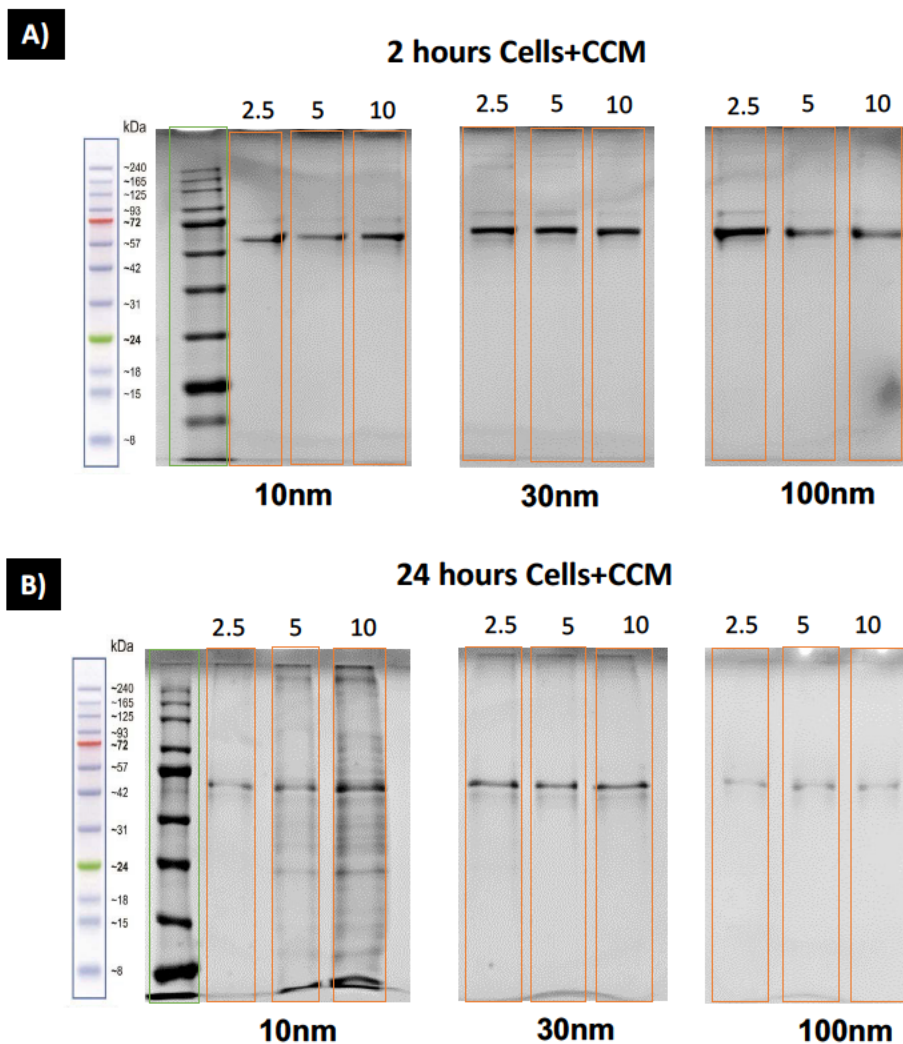


Figure 4.8. Coomassie blue staining of PAGE gels for isolated protein corona. ZF4 cells were treated with different concentrations of AgNPs (2.5, 5 and 10 $\mu\text{g/mL}$) and sizes (10, 30 and 100 nm) for 2 or 24 hours. The lanes outlined in green represent the protein ladder and the orange lanes correspond to the samples. The numbers above the bands show the AgNPs concentrations used in $\mu\text{g/mL}$. A) AgNPs treatments prepared in CCM (DMEM-F12 supplemented with 10% Foetal Bovine Serum) and incubated with ZF4 cells for 2 hours. B) AgNPs treatments prepared in CCM and incubated with ZF4 cells for 24 hours, indicating the evolution of the corona as the ZF4 cells condition the medium.

Table 4.1. Analysis of the proteins secreted by ZF4 cells in response to the AgNPs and identified in the NP coronas. Proteins identified by mass spectrometry on the 10, 30 and 100 nm AgNPs following exposure to zf4 cells for 24 hours. Results represent the summary of the proteins found in the isolated protein coronas following a search in the zebrafish proteome database (uniprot) and ZFIN [363].

Accession	MW [KDa]	Name	Description
F1QGZ6	76.8	Maternal embryonic leucine zipper kinase	Predicted to enable calcium ion binding activity; non-membrane spanning protein tyrosine kinase activity; and protein serine/threonine kinase activity. Involved in hemopoiesis. Acts upstream of or within erythrocyte development and regulation of heart contraction. Predicted to be located in cell cortex. It is expressed in several structures, including digestive system; immature eye; nervous system; pleuroperitoneal region; and proliferative region. Orthologous to human MELK (maternal embryonic complementary kinase).
Q90416	48.7	Retinoic acid receptor RXR-gamma-A	Enables nuclear receptor activity. Involved in positive regulation of transcription by RNA polymerase II. Predicted to be located in the nucleus. Predicted to be part of RNA polymerase II transcription regulator complex. Is expressed in several structures, including mesoderm; neural rod; pharyngeal arch; retina; and tail bud. Human ortholog(s) of this gene implicated in lung non-small cell carcinoma. Orthologous to human RXRG (retinoid X receptor gamma).
P79725	27.4	swelling dependent chloride channel, ICln	Acts upstream of or within axon extension. Predicted to be located in cytoplasm; nucleus; and plasma membrane. Predicted to be part of lysosomal complex. Predicted to be active in cytosol. Orthologous to human CLNS1A (chloride nucleotide-sensitive channel 1A).
Q6K197	51.1	p65 transcription factor	Enables DNA-binding transcription factor activity, RNA polymerase II-specific. Acts upstream of or within anterior/posterior axis specification; mesoderm development; and regulation of apoptotic process. Located in nucleus. Is expressed in intestine and male organism. Human ortholog(s) of this gene implicated in ductal carcinoma in situ; lung non-small cell carcinoma; lymphoma; and renal cell carcinoma. Orthologous to human RELA (RELA proto-oncogene, NF-kB subunit).
Q1XA84	34.5	Ataxin-3 (Fragment)	Predicted to enable thiol-dependent deubiquitinase. Predicted to be involved in protein deubiquitination. Predicted to act upstream of or within proteolysis. Predicted to be active in nucleus. Human ortholog(s) of this gene implicated in Machado-Joseph disease. Orthologous to human ATXN3 (ataxin 3).

P50541	27.6	Max-interacting protein 1	Predicted to enable DNA-binding transcription factor activity, RNA polymerase II-specific and RNA polymerase II cis-regulatory region sequence-specific DNA binding activity. Predicted to be involved in regulation of transcription by RNA polymerase II. Predicted to be located in nucleus. Is expressed in several structures, including axial chorda mesoderm; median fin fold; nervous system; neural tube; and periderm. Human ortholog(s) of this gene implicated in neurofibrosarcoma and prostate cancer. Orthologous to human MXI1 (MAX interactor 1, dimerization protein).
---------------	------	---------------------------	--

Complete Culture Medium (CCM)

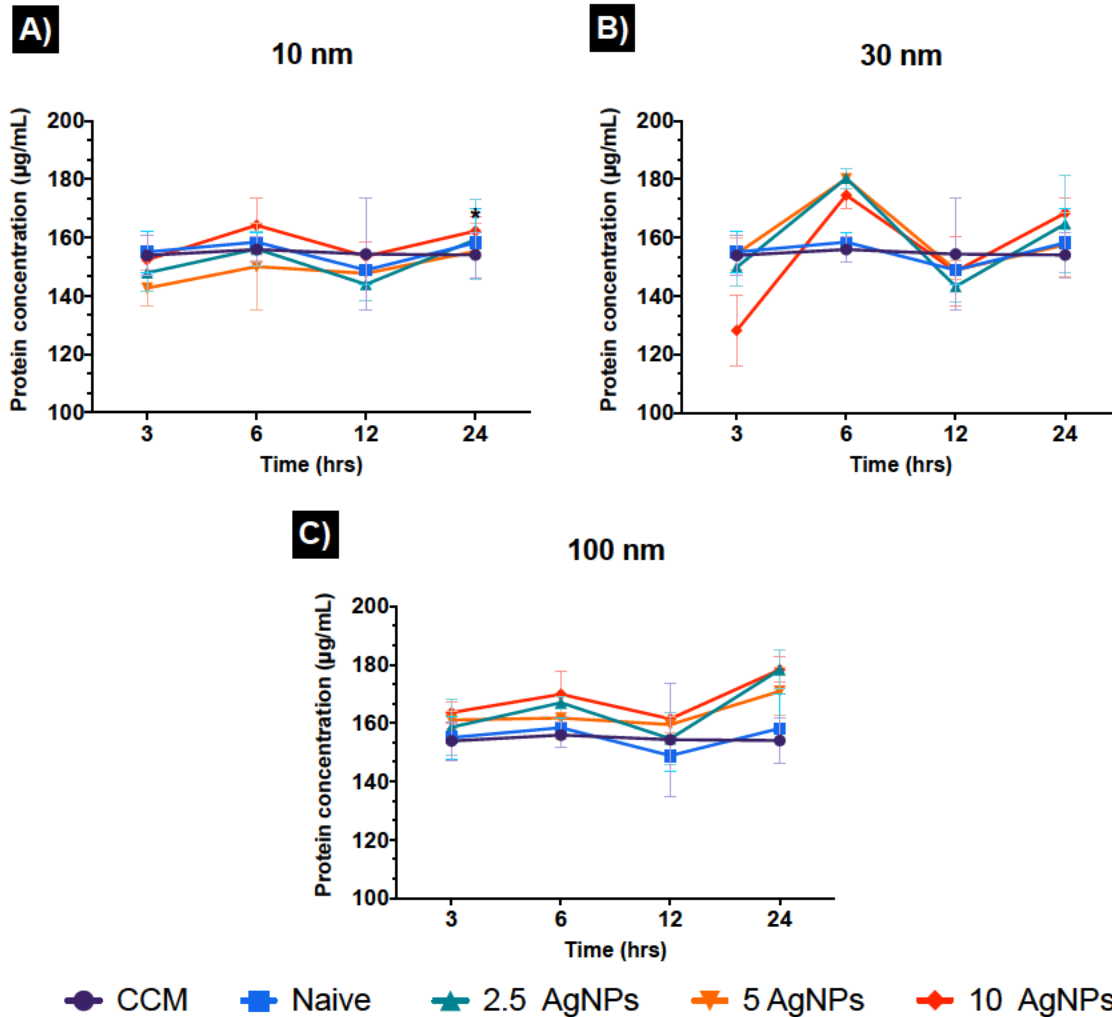


Figure 4.9. Proteins secreted during AgNPs exposure in medium supplemented with 10% FBS. ZF4 cells were exposed to 2.5, 5, and 10 µg/mL of AgNPs prepared in CCM (10% FBS), and the protein content in the medium was measured by BCA assay at 3, 6, 12, and 24 hours, as a means to assess the cellular response to NP exposure and to quantify the number of proteins secreted by the ZF4 cells in response to increasing exposure time. A control of cells (without NP treatment) in CCM only was included to compare with the NPs treatments. Data with asterisks (*) indicate a statistically significant difference (* $p < 0.05$) between the treatment compared to the untreated control (naive).

4.5 Discussion

The physicochemical properties of NPs can strongly influence their toxicity in biological systems leading to different outcomes [81, 108, 248]. In this study, we demonstrated that the addition of proteins strongly affected the NPs characteristics, creating a new biological identity (protein corona) that was reflected in the hydrodynamic size, polydispersity index (PDI), zeta potential, and absorption spectra in CCM [248, 334, 364].

The intracellular uptake and fate of the NPs can be influenced by their physicochemical properties, cell type, and constituents in the complex medium, such as proteins that can modulate the cellular uptake, for example by enabling the NPs to engage cellular receptors following formation of the protein corona [80, 365, 366]. The SDS-PAGE gel also revealed that after 24 hours (Figure 4.8), the smaller AgNPs (10 nm) presented a number of highly visible protein lines along the length of the band for the medium and high AgNP concentrations, showing a clear separation of the protein sizes, ranging between 250-8KDa, which can be related to other serum related proteins such as Apolipoprotein A-I (28 kDa) and Apolipoprotein A-II (17.4 kDa) [332]. ZF4 proteins (secreted by the cells) were also found in response to damage induced by the AgNPs, including p65 transcription factor (51.1 kDa), retinoic acid receptor RXR-gamma-A, and max-interacting protein 1 (27.6 kDa). These proteins are found in the nucleus and are related to DNA regulation and binding transcription activity, such as ataxin-3 Fragment (34.5 kDa), involved in protein de-ubiquitination and located in the nucleus as well as swelling dependent chloride channel protein (27.4 KDa), which is located in the cytoplasm, nucleus, and plasma membrane [363]. A full list of the identified proteins can be found in Table 4.1.

The differences between the NPs sizes and their protein composition may be related to the curvature of the NPs, and to the fact that the 10 nm solution contains a much larger number of particles (NPs/mL) and a much larger surface area for protein adsorption compared to the larger AgNPs at constant mass [342]. Hence, smaller NPs may have a higher likelihood to bind proteins due to their large SA as suggested by other authors [332, 339, 367]. Another aspect to consider is the type of proteins in the complex environment; for example, albumin and fibrinogen are proteins that will bind and dominate the particle surface due to higher abundance, especially at short exposure times. These proteins may eventually be displaced by proteins with higher affinity and slower kinetics, increasing the protein diversity of the protein corona [366]. Similarly, certain proteins secreted by ZF4 cells could have a higher affinity for the AgNPs compared to the serum proteins, potentially increasing the competition of proteins and displacement of weakly bound proteins [364, 366]. Measurements of the total protein concentration (in suspension) revealed an approximate 5-10% increment of the total secreted proteins after 24 hours compared the untreated control. This suggests that the secreted proteins might have a higher affinity compared to the serum proteins, increasing the competition of proteins and displacing weakly bound proteins by forming stronger bindings onto the NP surface area in the biological environment; however further studies are necessary to fully understand the role of the secreted proteins [364, 366].

Metal NPs, such as AgNPs are likely to partially dissolve in complex environments, such as CCM, leading to release of Ag ions (Ag^+) and Ag complexation, to form species such as AgCl [83, 342]. The quantification of the total Ag in cells presented here suggested a close link between exposure time and total Ag concentration. For example,

the total Ag uptake for all AgNP sizes was greatly increased (higher $\mu\text{g/mL}$ concentrations) after 24 hours for all the treatments, compared to 2 hours. In addition, a size and concentration effect were observed, displaying higher Ag concentrations for the 10 and 100 nm size, compared to the 30 nm size. In this regard, certain metal NPs, such as AgNPs may act as a “delivery vehicle” for the metal ions; when the NPs interact with cells, some NPs may stick onto the cell surface, and high concentrations of metal ions could be locally released, providing a continuous slow release of metal ions in the cell [12]. In addition, another important aspect to consider in the uptake of Ag ions is the ability of metals to mimic other ions in various carrier-mediated processes, a process widely described for trace metals [64, 119]. For example, Ag^+ has been demonstrated to enter freshwater rainbow trout via the Na^+ channel situated on the branchial apical membrane, including via P-type ATPase, and Cu^+ transporters [83, 368]. In this regard, the high total Ag^+ intracellular concentrations detected for the 10 nm could be linked to a major abundance of ions in the media due to dissolution (as demonstrated in Chapter 2), including the possible uptake of ionic Ag via ion channels and/or transporters. Conversely, the 100 nm results can be potentially related to a combination of dissolution and sedimentation, which may increase their contact with the cells and therefore their Ag^+ uptake. However, further studies are necessary to confirm these suggestions.

In contrast to uptake of Ag^+ , NPs are too big to be moved into the cells via ion transporters, or paracellular diffusion pathways; hence the most likely route of uptake is via endocytosis [369]. Once the NPs are engulfed by the cell membrane, the formation of EE is rapidly activated to sort the internalized cargo to different intracellular destinations [369]. The internalised cargo remains for only a few minutes in EE (between 5 to 10

minutes), then, the EE progressively acidify and mature to late endosomes [369]. In this regard, results for the EE induction (EEI) revealed higher amounts of NP trafficking during the first 2 hours for all NP concentrations and sizes, compared to longer exposure times (24 hours).

The internalisation of external matter via endocytic compartments is likely to occur in ZF4 cells. TEM images of cells treated with the highest AgNP concentration (10 µg/mL) demonstrated the presence of “particles” inside vesicles in the cells. However, it is important to highlight those particles are of an unknown composition, as the elemental composition of the material (silver) has not been confirmed. Despite this, it is hypothesized that particles shown in the TEM images correspond to “AgNPs”; however, studies such as energy-dispersive X-ray analysis (EDX) are necessary to confirm these findings, and to exclude artifacts [83, 185].

Assuming that the particles in the images are AgNPs and compared to their core size recorded in their initial characterisation (using TEM); the analysis of the internalised particles indicated a reduction in their initial size as well as visible loss of density or fragmentation once inside the vesicles for all the AgNPs, which was most evident for the 10 nm AgNPs (see figure 2C), consistent with the dissolution results. The magnification of the TEM images from cells treated with small and medium AgNPs (10 and 30 nm) showed NPs in the cytoplasm as well as in close proximity to the nuclear area (see Figure 2 A and D), whereas TEM images for cells treated with 100 nm showed a larger number of NPs surrounding the cell membrane, with no visible signs of agglomeration. The reduction in diameter of the NPs perhaps can be attributed to the fact they are not AgNPs and/or dissolution (if AgNPs), as well as size reductions due to lysosomal degradation by

hydrolases, which can digest proteins, nucleic acids, lipids, and extracellular agents, as described by other studies [370, 371]. In addition, it has been suggested that NPs may be able to escape from the intracellular vesicles [372, 373]. This process has been described as the Enhanced Trojan Horse effect, which refers to the cellular internalization of metal NPs via an active processes, resulting in an enhanced release of the toxic ions such as Ag^+ (increasing the intracellular Ag^+ concentrations) as a result of cation-induced lysosomal damage or dysfunction [370].

On the other hand, the size of the NPs may also play a role in the cellular uptake, as an optimal particle size for active uptake in mammal and fish cells has been suggested [86, 101, 374]. For example, Qiang et al., 2020 suggested the smaller sizes up to 20 nm are more likely to be internalised than larger sizes, providing evidence for enhanced uptake and toxicity for smaller sizes (4 nm) in zebrafish [60]. Similarly, the size and mass concentration also proved to affect the uptake pathway during the assessment with pharmaceutical inhibitors (Figure 4.4). Results for the inhibition of the endocytosis pathways showed that treatment with chlorpromazine has no effect on the uptake of 10 and 30 nm AgNPs, therefore the clathrin pathway was not activated for most of the concentrations, except at the 10 $\mu\text{g}/\text{mL}$ for the 10 nm size. Here, the caveolae-mediated and macropinocytosis pathways were mainly responsible for the uptake of the 10 nm AgNPs, showing similar percentages of uptake by both pathways. Likewise, NPs could also be internalised due to their small size during the engulfment of large volumes of the extracellular medium, which allows the internalisation of fluid-phase nutrients such as proteins and ATP, and sampling of the environment for foreign agents [106].

Conversely, the 30 nm AgNPs displayed inhibition of the caveolae pathway at all AgNPs concentrations tested; similar results were displayed by the 100 nm size for this pathway, which also showed inhibition of the other evaluated pathways. These results suggest that the 30 and 100 nm uptake are linked to the strong participation of lipid raft-associated receptors during their internalisation [89, 92]. It is important to mention that the NP uptake was measured only at short exposure times (2 hours), as it has been reported that the inhibition of one uptake pathway can result in the activation of other endocytic uptake pathways [88, 92]. When selecting a specific inhibitor for the desired endocytosis pathway it is important to take into account the effective inhibition as well as cytotoxicity of the pharmacological inhibitors, before their co-incubation with the NPs, as severe disruption (in terms of toxicity) may inactivate or activate other molecular processes as part of the cell's defence mechanism, which may lead to different outcomes [92].

Autophagy as is involved in the formation of membrane vesicles for degradation and recycling of intracellular and extracellular components; thus, it could be considered as another (non-endocytotic) pathway that cells may use to cope with NP exposure [270, 375, 376]. Autophagy has been demonstrated during the early development of zebrafish embryos. The expression and transformation of LC3-I to LC3-II (proteins that indicate autophagosome development and maturation) play a key role in early zebrafish development and normal biogenesis and function. Furthermore, autophagy has been described as a self-protective mechanism, whereby excessive levels of autophagy could be considered as a lethal mechanism[373]. In this regard, results for the induction of autophagy in the ZF4 cells showed highest percentages (%) for the 10 nm AgNPs,

especially at the lowest AgNP concentration (2.5 µg/mL), whereas the medium and large AgNPs showed lower values compared to the smallest AgNPs and the untreated cells. This suggests that autophagy levels could potentially be related to either the level of stress the cells are experiencing due to the NP-size effect and/or as part of a natural process. Henceforth, studies should provide insights about the autophagy mechanisms in embryonic fish cells.

The induction of autophagy under stress conditions and as part of the cytotoxic response has also been identified in fish species [107, 377, 378]. For example, in fish embryos, increased levels of the autophagy-related genes Atg3, Atg5, beclin1, and the cleavage of LC3, can strongly induce autophagy, affecting embryonic development and proper fusion of lysosomes (or endosomes) and autophagosomes [270]. As mentioned above, the increased autophagy response in our study could potentially be linked to the selective removal of damaged proteins and/or organelles, leading to cytotoxic responses. However, studies that explore the proteins involved the autophagy response in ZF4 cells are needed to tease out these pathways.

4.6 Conclusions

The present study illustrated the uptake mechanisms of three representative AgNP sizes (10, 30 and 100 nm) in embryonic zebrafish cells (ZF4). Quantification of the total Ag in ZF4 cells was higher for the 10 and 100 nm NPs compared to the 30 nm after 24 hours of exposure. The inhibition of the caveolae, clathrin, and macropinocytosis endocytic pathways by pharmaceutical inhibitors (genistein, chlorpromazine, and wortmannin respectively) demonstrated that internalisation of AgNPs by ZF4 cells may include

multiple uptake routes, depending on the particle size. Results revealed that uptake of AgNPs was mainly via macropinocytosis, whereas the uptake of the 30 and 100 nm sized particles was mediated via the caveolae-mediated pathway.

In addition, the AgNP mass concentration, size, and time of exposure were closely linked to their intracellular fate, potentially disrupting the formation of early endosomes, as well as activating autophagy as a non-endocytic uptake process. Further studies are necessary to identify the elemental composition of the materials in the TEM images; however, particles of an unknown composition were visualised surrounding the plasma membrane in the cytoplasm and close to the nucleus, and confocal microscopy reflectance indicates the presence of AgNPs. In addition, changes in their diameter were recorded, suggesting that particles underwent some dissolution following internalisation.

4.7 Acknowledgements

ACQ, IL and EVJ acknowledge support from the European Union Horizon 2020 Programme (H2020) projects as stated in section 2.7.2, Acknowledgements in Chapter 2. ACQ would like to thank the Advanced Mass Spectrometry facility from the University of Birmingham for the protein analysis and Theresa Morris for their kind assistance with the TEM samples.

Chapter 5: Discussion, future work, and conclusions

5.1 Discussion

There is limited information about the cytotoxic effects of AgNPs in embryonic zebrafish cells (ZF4) compared to other fish cell models, such as rainbow trout gill (and liver) cells, which have been widely exploited in many fields. Despite the valuable scientific advances provided by the use of fish cells in toxicology, the assessment of the negative outcomes of NPs in the aquatic environment and biological systems highlights a continuous need for new alternative and representative models that elucidate complex biological responses [228, 379]. Towards this goal, we implemented commercially available ZF4 cells to explore its suitability as an alternative toxicological model, evaluating cytotoxic and uptake responses triggered after exposure to AgNPs and ionic Ag (AgNO_3). The overall aim of this thesis was to provide an initial assessment of the biological responses using an early-stage model, potentially supporting the implementation of zebrafish cells as an essential part of a 21st-century nanotoxicological assessment strategy [58, 99, 294]. In addition, the thesis successfully examined a few key areas relevant to NP toxicity (Figure 5.1) that were initially hypothesised, including:

- I. Providing significant information on the importance of the dynamic behaviour of AgNPs in different biological suspensions and its influence on the physiochemical properties of the AgNPs.
- II. Examining the internalisation mechanism of AgNPs in ZF4 cells, including the endocytic and non-endocytic responses.

III. Evaluating several biological mechanisms of toxicity imposed by AgNPs, including the activation of cytotoxic responses, and the interplay between these mechanisms.

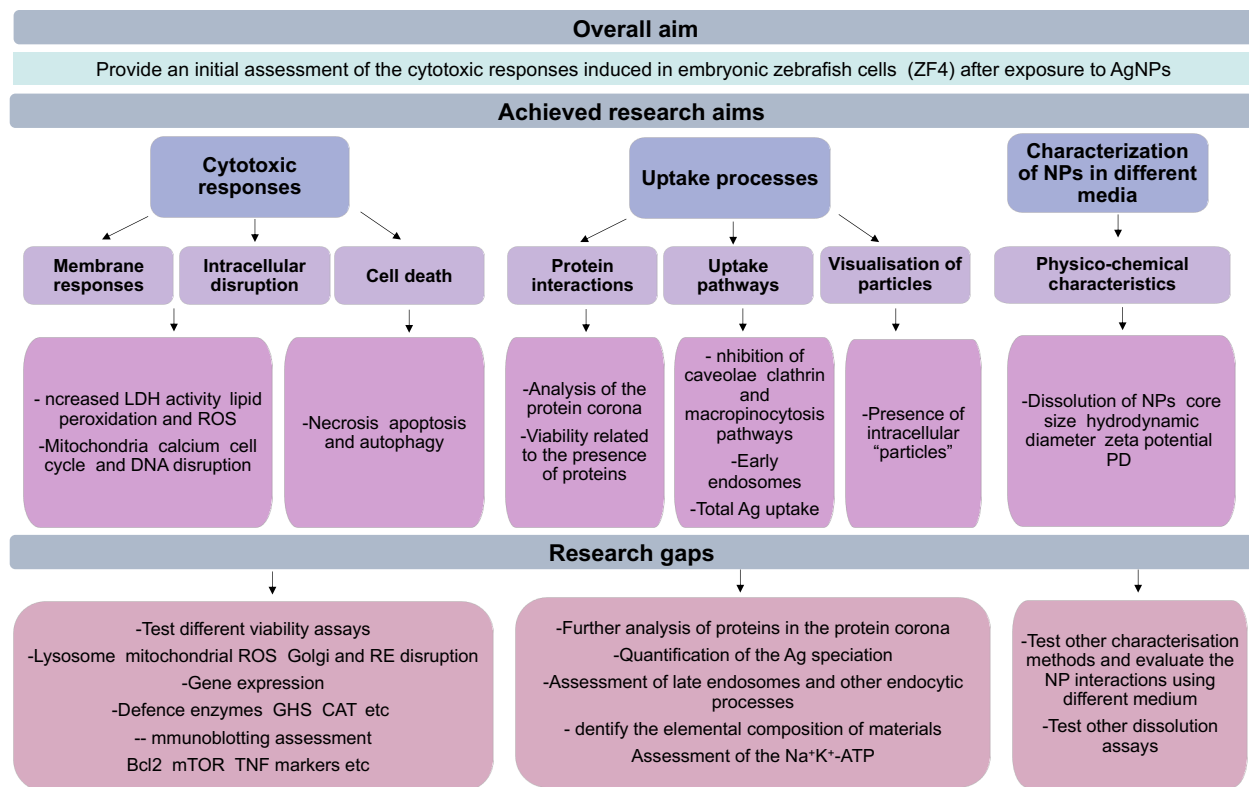


Figure 5.1. Aims and gaps addressed by the research presented in this thesis. The figure shows the research aims accomplished during the study. Below this, the research gaps that still need to be addressed and that arose from the research undertaken are presented, including recommendations on techniques and assays that will support filling of the remaining research gaps.

5.1.1 Characterisation of the NPs

Changes in the physicochemical characteristics of the AgNPs were evaluated over a 24-hour timescale and under relevant exposure conditions, including dissolution, polydispersity index, and charge of the NPs, using different biological fluids, such as UPW

and cell medium supplemented (or not) with serum. This step is highly important in order to understand the possible outcomes in biological systems, as the dispersal of AgNPs in simple suspensions such as UPW does not reflect the complex interactions between NPs and biomolecules that occurs in the environment, leading to difficulties when interpreting the data, and if the dispersion details are not adequately reported, resulting in studies that cannot be reproduced by others [333-335]. In addition, it has been demonstrated that the constituents of the cell culture medium, such as proteins, ligands, inorganic salts, and other biomolecules can induce physicochemical changes as soon as they interact with AgNPs, exposing the cells to a new complex mixture of NPs, Ag ions, and other ion-ligand complexes, and altering the particle surfaces and associated particle–cell interactions [52, 57, 334, 380].

As discussed in chapters 2, 3 and 4, the behaviour of AgNPs in simple (ultra-pure water) and complex medium (cell culture) demonstrated that the surrounding environment plays a key role in modifying the pristine characteristics of AgNPs (as shown in DLS results). In addition, the dissolution of the AgNPs was strongly linked to the initial particle size, displaying higher dissolutions rates for the 10 nm, followed by the 30 nm and lastly the 100 nm AgNPs in both tested media, demonstrating a strong correlation between the size of the NPs and their dissolution concentrations, and with the nature and composition of the testing media [55, 56, 294, 381]. In this regard, and as discussed in chapter 1, the use of different experimental methods to evaluate the dissolution of the AgNPs in complex environments is necessary, as the centrifugation method used for the dissolution experiments was costly and time-consuming and is an *ex-situ* approach rather than assessing the behaviour *in situ* in the cells in real time. Several steps were performed to

standardise a protocol to improve the recovery of Ag from the cells, and modifications were made to ensure quality control was achieved (e.g., good analytical recovery) in CCM. Conversely, the recovery of Ag was easy for UPW, whereas samples in CCM required longer and additional centrifugation steps. Different approaches are encouraged to improve the analysis. For example, dialysis is an inexpensive and reliable method, as well as single cell ICP-MS. However, acid digestion protocols for ICP-MS are considered as destructive methods, they can provide insights into the total ionic silver in the cells over time. Besides, silver speciation could be potentially assessed, leading to new insights into the behaviour of AgNP in biological fluids [382, 383]. Additionally, the use of single particle and single cells variants of ICP-MS would allow analysis of *in situ* dissolution and cell-by-cell analysis of the AgNP loading [384].

5.1.2 Uptake mechanisms in ZF4 cells

The work in Chapter 3, initially provides qualitative information about the potential fate of AgNPs in cells, whereas work in Chapter 4 quantitatively assess the total Ag in ZF4 cells. Both methods showed similar trends for the 10 nm size, with higher intensities using confocal microscopy (Chapter 2) and higher total Ag concentrations, as discussed in Chapter 4, which suggests the role of the NP size and dissolution. Ag and other transition metals (e.g., Cu) can enter the cells via channels or other transporters, having affinity to bind avidly to the –SH groups of the Na⁺/K⁺-ATPase [368]. A limitation in this study is that the uptake of Ag ions in ZF4 cells was not included. Hence, assessment of the uptake of Ag needs to be further investigated, including whether AgNO₃ (as controls) and AgNPs (dissolved Ag) inhibit the Na⁺/K⁺-ATPase activity in ZF4 cells. This important evaluation

can reveal whether the inhibition of enzyme activity is attributable primarily to a particle-specific and/or a dissolved silver ion effect.

The evaluation of the total Ag in ZF4 cells as the dissolution experiment were set after a range of published methods for extracting NMs from fish tissues and cells were tried. However, it seemed that these were inapplicable to Ag-based materials and/or for this kind of cells. Hence, the protocol described in Chapter 2 and 4 was optimized for Ag and may be metal-specific, so if the method is intended to be applied to other materials, the process of validation will need to be repeated. The total uptake of Ag (Chapter 4) was higher for the smaller size NPs, followed by the 100 nm and lastly the 30 nm. Showing a different trend than the one recorded for most of biological responses, which in order of magnitude was size related 10 nm ~ 30 nm ~ 100 nm. The response for the internalisation pathways revealed that the preferred endocytic pathway for uptake in cells was based on the NPs size, as suggested by other authors in rainbow trout cell studies [86, 99].

Sensitivity to pharmacological agents suggests that diffusion alone cannot be responsible for the AgNPs accumulation in cells (Chapter 4). The experimental design was developed by testing different concentrations based on literature. Chlorpromazine was arguably a selective inhibitor of clathrin-mediated endocytosis, obtaining a noticeable inhibition of transferrin uptake at the concentration of 10 µg/mL. Genisten, a tyrosine kinase inhibitor broadly reduces actin cytoskeletal movement, hence it was used as a calveolae-mediated endocytosis inhibitor. Cells treated with this agent demonstrated higher toxicity and noticeable changes in their morphology; besides, several concentrations were tested to obtain a satisfactory inhibition of cholera toxin b. Wortmannin is a PI 3-kinase inhibitor 3-methyladenine, which does not prevent

macropinosome formation, but inhibits macropinosome maturation, also show reduced cell viability. In addition, several concentrations were tested for this inhibitor, showing a satisfactory inhibition of dextran after 10 minutes, as longer incubation times reduced the cell viability beyond 70%. In this regard, the use of different pharmaceutical inhibitors to shut-down specific uptake pathways and correlation of this with the amount of total Ag may be explored, due to their relative importance as routes of AgNP internalisation [91]. Another important aspect to consider is the potential interaction of the pharmaceutical inhibitor with metal transporting ATPases, which are known to be involved in loading metal ions into the cells.

The evidence presented in the TEM images (Chapter 4) implies that AgNP uptake may occur through vesicular processes. However, as also discussed in Chapter 4, studies including application of correlated reflectance and electron microscopy and EDX are necessary to fully validate these findings. Similarly, synchrotron approaches such as XANES will be helpful to understand how the cells processes the NPs in endosomes, lysosomes and following lysosomal escape [385]. On the other hand, it has been suggested that the internalised cargo remains for only a few minutes in EE (between 5 to 10 minutes), then, the EE mature to late endosomes [369]. Based on this, assessment of the early endosomes complemented with late endosomes will provide further insights about the internalisation of NPs by ZF4 cells. Moreover, the incorporation of AgNO₃ as an ionic control would be helpful to understand whether the Ag ions affect the biological response of the cells.

5.1.3 Mechanistic insights from protein binding

The presence of proteins in the cell culture medium produced a modulatory effect in the toxicity towards ZF4 cells as shown in Chapter 3. The corona formation reduced the binding of the NPs to the cellular membrane and instead drove the NPs to interact with the cells via receptor mediated processes. Evaluation of the cytotoxic responses in both tested media were assessed using LDH activity. As discussed in Chapter 2, this protocol was selected due to the lack of NP interferences with the assay [262, 386]. Many colourimetric assays are incompatible with the intrinsic properties of the NPs, such as having overlapping emission/absorption or binding of assay molecules to the particle surface. In this regard, complementary assays including label-free methods, can be implemented to assess the cell viability, including assessment of the possible interferences of the NPs with the assay.

The evaluated cytotoxicity for AgNPs and AgNO₃ was much lower in CCM treatments compared to SFM treatments. These differences were related to protein corona formed on the NPs in the CCM, which reduced the direct interaction of the NPs with the cells, as well as inducing less agglomeration and reduced dissolution of the NPs, whereas, for the SFM treatments, the enhanced toxicity could be associated with the strong adhesion of the bare NPs to the cell membrane, disrupting the membrane as well as pulling out intracellular proteins.

In addition, as demonstrated in Chapter 4, mass spectrometry analysis of the protein corona revealed the presence of stress related proteins. The experimental design of these studies needs to be further improved. For example, the assessment of the protein corona

from subcellular compartments can reveal protein binding and a larger number of intracellular proteins [83]. In addition, a different approach to reveal the protein corona can be used. In Chapter 4, the proteins were isolated by a protocol that has been widely implemented and validated. However, processing the samples using gel-based separation and fractionation technique can be destructive and fractions of proteins can be lost in the processing. Hence, gel-free fractionation methods can be a feasible option, improving the sample recovery, and reproducibility, making the proteomic profiling more efficient, sensitive, and enhancing the number of identified proteins [387].

5.1.4 Potential cytotoxicity- Is there a nano effect?

An initial hypothesis evaluated in the thesis was that the AgNPs would reveal different physiological effects in comparison to the ionic version of the material (AgNO_3). In the present studies, ZF4 cells successfully tolerated exposures to Ag and AgNPs over different timepoints (24 hours maximum). Chapters 2 and 3 demonstrated that the cell responded to the stimulus with the activation of different mechanisms, as reflected in either the induction and/or inhibition of the evaluated biological endpoints. The first evaluated cytotoxic responses induced by the AgNPs were at cell membrane level, which is considered the first barrier to be encountered by the NPs [109]. Based on the integrity of the cell membranes, a size-dependent response to the AgNPs was found, with high percentages of cytotoxicity for the ionic Ag, and small NPs (10 nm). Interestingly these results agree with the dissolution experiments, which displayed higher dissolution rates for the smaller AgNPs compared to the larger NPs, suggesting the potential role of the Ag ions in the toxicity. In addition to dissolved Ag toxicity, it is important to consider the

fact that small NPs may have a faster and easier internalisation across the plasma membrane, and have higher particle numbers at constant mass concentration, as well as a higher rate of release of silver ions.

Other biological responses were also assessed, including the generation of oxidative stress and lipid peroxidation. Chapters 2 and 3 displayed clear differences between the particulate and ionic forms, as Ag^+ showed higher total ROS compared to NPs, which also demonstrated a size-dependent response. In this regard, different endpoints and lower exposure concentrations can be further considered to evaluate cytotoxicity through different experimental approaches. For example, the use of fluorescent probes was widely implemented through this thesis, as fluorescent dyes are sensitive indicators for many biological processes. Hence, fluorescent-based techniques can be further used to explore the antioxidant responses activated to mitigate ROS generation, which may include: GSH, superoxide dismutase (SOD), catalase (CAT), glutathione peroxidase (GPx) [388]. Aside from the cytotoxic responses, the possible interferences of fluorescent/colorimetric assays with NPs should be explored, as suggested in Chapter 2 with the implementation of the modified LDH assay.

The evaluation of the mitochondrial permeability (MP) (Chapter 2) revealed ZF4 cell sensitivity to changes in the Ag ions and AgNPs concentrations. These results suggest the potential role of the NP itself in the toxicity to mitochondria; however, assays that determine mitochondrial disturbances, such as mitochondrial ROS, mitophagy and acidic organelle disruption are necessary. For example, protein expression of such pathways by immunoblotting assessment could be interesting to verify the reliability of the results [389]. Similarly, lower exposure concentrations could be tested to determine

whether the intensity drop with some biological assays (e.g., autophagy) is due to the damage in the evaluated pathway, a result of lower cell numbers due to cytotoxicity or due to natural inactivation of the pathway and triggering of other pathways.

The autophagy response was higher for the smaller sized NPs, as assessed using two different approaches, which included flow cytometry (Chapter 2), and confocal microscopy (Chapter 4), thus demonstrating the reliability of assessing responses using fluoresce probes). Based on this, it would be beneficial to assess whether the autophagy markers (e.g., mTOR, LC3, and p62) are responsible for the activation of the autophagy flux in ZF4 cells after exposure to treatment and/or if the response is higher as part of the normal activity during the development of embryonic zebrafish cells, as discussed in Chapter 4.

An interesting approach to verify the results above is through the assessment of caspases, such as caspase 9, Smac/DIABLO and endonucleases, preferably by immunoblotting techniques. The assessment of the intracellular Ca^{2+} mobilisation, in Chapter 3, demonstrated that the flux was increased by exposure to AgNPs, whereas for AgNO_3 this was reduced. It is important to highlight that the work presented in this chapter was discussed in terms of mechanisms of Ag toxicity and Ca^{2+} overload. Therefore, further studies to explore the potential inhibition of the Na^+/K^+ -ATPase channel by Ag^+ leading to elevated intracellular Na^+ and influence on the intracellular Ca^{2+} would be a key next step, including assessment of the decline of Ca^{2+} by AgNO_3 .

The occurrence of DNA double strand breaks as discussed in chapter 3, also displayed clear differences between the particulate and ionic form. When comparing by NP size, the smaller AgNPs displayed the highest percentages of DNA breaks, most likely

due to its faster dissolution and concomitant release of ions, confirming that ultimately it is the presence of ionic Ag that causes more toxicity than the nanoparticulate form. This may suggest that the DNA damage resulting from AgNP exposure led to an attempt by the cells to overcome the impairment. However, there was no statistical difference between the AgNPs and AgNO₃ treatments, although some disruption of the cell cycle and lengthening of the duration the cells spent in certain phases was recorded, perhaps due to the activation of cell death mechanisms. Hence, it would be interesting to investigate whether this trend would have continued if the exposure treatments had been changed, including longer durations and lower concentrations, increasing from n = 3 to a higher number of replicates, etc. The ability of Ag⁺ ions to bind to DNA base pairs, and interaction with the thiol groups of different enzymes and phosphorus-containing bases, should not be neglected, and further studies such as mismatching DNA duplexes, DNA compaction, and DNA damage assays would be beneficial to explore, as demonstrated in fish and mammal cell models [224, 390, 391].

When the cellular damage is irreparable, the cell triggers cell death to preserve the genomic stability, which is considered the final biological outcome as a response to cellular damage. Interestingly, the cell death mechanisms strongly correlated with the size and (ionic) form of the AgNPs, as discussed in chapter 2. Based on the insights gained from a number of fluorescent methods, the results demonstrated differences between AgNPs and AgNO₃ treatments, showing cellular responses linked to the initiation of apoptosis via the mitochondrial pathway for the medium and large AgNPs sizes and via necrosis for the smaller NP size and ionic Ag. However, molecular responses can be further incorporated, along with molecular biology and immunoblotting techniques (e.g.,

western blot) to detect the specific proteins expressed during the activation of cell death pathways, such as p53 and caspases 8, 7 and 9, to improve the accuracy of the findings.

Based on the above findings, one can determine that there is a neglectable size effect for the PVP-AgNPs used in this study. However, most of the analysed biological responses were enhanced by exposure to metal ions, confirming that the ions could be considered more toxic than the NPs, at least for ZF4 cells. Besides, small sized NPs and AgNO₃ showed similar toxicity effects, confirming the role of dissolved Ag ions in toxicity as smaller NMs undergo faster dissolution than larger ones due to their larger surface area.

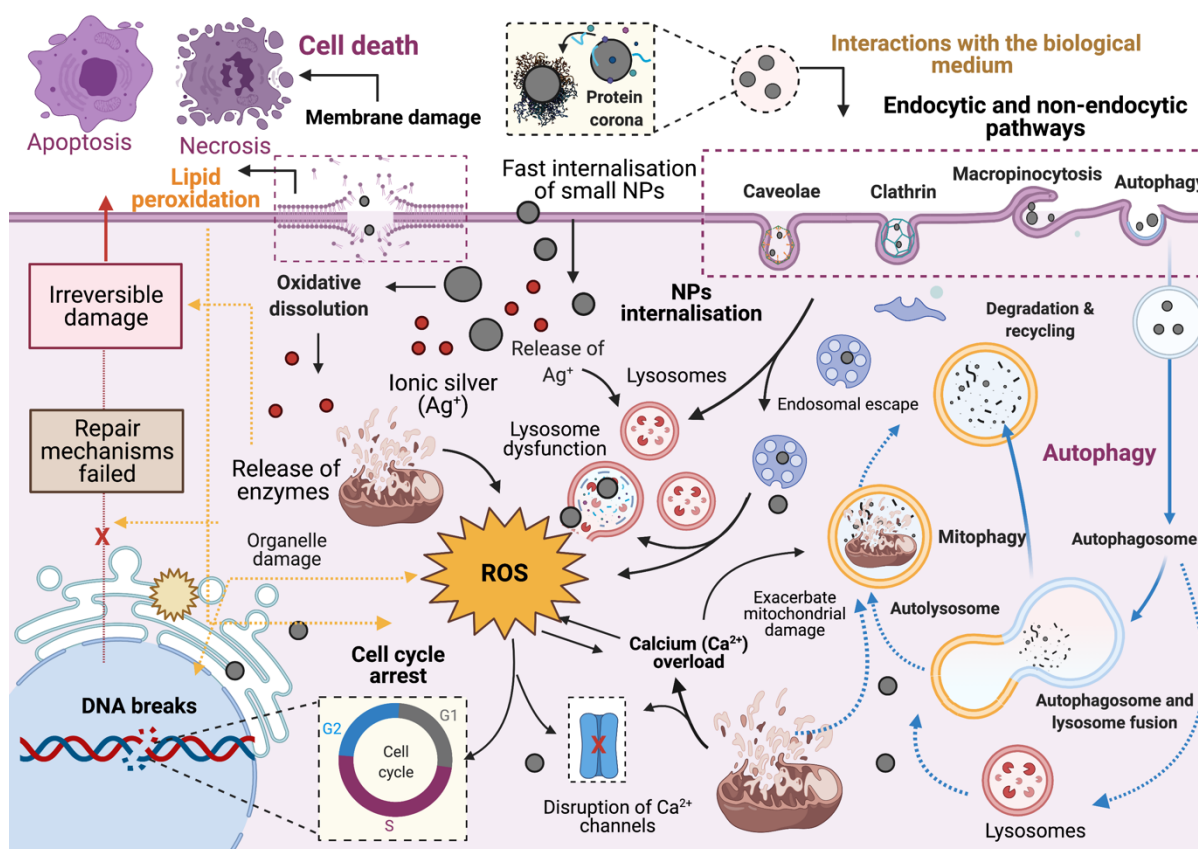


Figure 5.2. Biological responses triggered in ZF4 cells after exposure to AgNPs and ionic Ag. The image represents the hypothetical mechanisms triggered in ZF4 cells, including the NP interactions with constituents of the cell media, internalisation of the AgNPs by the various receptor-mediated or diffusion / damage processes, and the cytotoxic mechanisms induced such as generation of reactive oxygen species (ROS),

disturbances to calcium flux, lysosomal and mitochondrial activity, cell cycle arrest and DNA breaks, resulting in cell repair or cell death via autophagy, apoptosis or necrosis depending on the severity of the damage. Image created with BioRender software.

5.1.5 Regulatory context

Nanotechnology is an area with large potential benefits for consumers, workers and patients. However, like a double edge sword, AgNPs have given rise to concerns regarding their potential risks associated with their release, transformation, and fate in the environment.

The production (and import) of new NMs and their sale on the EU market is subject to the European Registration, Evaluation, Authorization and Restrictions of Chemicals (REACH) legislation. The growing concerns to include new physical forms of existing chemicals into REACH regulations led to the publishing of an Annex to REACH and the introduction of the concepts of nanoforms and sets of nanoforms to explicitly describe and assess NMs. These are covered under the “substance” definition in REACH, and the revised Annex also addresses one of the previous major concerns regarding the data requirements being triggered above 1 tonne of production, including for existing chemical substances that already have a CAS number [392].

While production volumes of NMs are often used as a proxy for potential exposures, the predicted environmental concentrations of Ag^+ in surface waters are expected to be between ng L^{-1} and mg kg^{-1} in sediments containing silver from NMs, although this will depend on the modelling approach used and the quality of the input data utilised. Commercial products often contain pristine AgNPs, however, this may not be the most relevant form in the environment, as biogeochemical processes may transform and

complex Ag^+ , with potential effects in organisms and in the food web such as fishes [393]. Based on this, the characterisation of the tested NMs in relevant medium is vital to account for behaviours such as aggregation and agglomeration in testing strategies (Chapter 2, 3 and 4).

On the other hand, evaluation of the risks posed by NMs and NPs is necessary in order to continue taking advantage of the benefits of this technology. Fish testing has been widely implemented and validated by use in regulatory toxicology (e.g., OECD TG No. 236 - Fish Embryo Acute Toxicity (FET) Test). However, given the growing need to reduce animal testing, the scientific community has developed a number of *in vitro* approaches that promote to the reduction, replacement, and refinement (3Rs framework) of vertebrates used in toxicology. Moreover, this is required to be considered under the REACH legislation for new substances, including NMs and in modified OECD test procedures, with justification for NMs. For example, the use of rainbow trout gill cells has been widely implemented in toxicity tests, as the gills are the first tissue that encounter chemicals due to their large surface area in the fish. In addition, rainbow trout cell culture-based methods have been recently approved by the OECD as the latest guideline in the field of environmental toxicology due to their relevance [219].

Throughout this thesis, metal and/or metal NP exposures were performed in ZF4 cells for a maximum of 24 hours to provide an initial toxicity assessment. However, it is important to consider that after 2-3 weeks of continuous exposure, the cell viability may dramatically decrease. Therefore, the risk for mortality of fish in the environment would be likely high. Here, predictions of chronic effects are unclear, but changes in the viability, and trace element disturbances over a long time of exposure are likely to occur.

The AgNPs concentrations tested on ZF4 cells throughout this thesis (Chapters 2, 3, and 4) may not fully represent real environmental concentrations. However, the analysis of the negative impacts may represent a likely future environmental scenario that fish may encounter, if the uncontrolled production and discharge of AgNPs continues to rise. For example, Chapter 4 present highlights of the uptake of Ag in cells, where improvements to the described methodologies could be used to partially inform policy makers on risk assessments. Furthermore, legislations need take into account the particle size. For example, the data presented in Chapter 2 and 4 demonstrated the uptake hazard of Ag and AgNPs is greater in smaller sized NPs compared to than larger NPs. Observations regarding the potential toxicity of smaller sized NPs and the bulk material (Ag⁺) were evident in most of the assessed responses (Chapter 2, 3 and 4). Furthermore, the hazard potential of the NP and Ag ions on organelle integrity was recorded on the mitochondria potential (Chapter 2), including ROS overgeneration and disruption of the genomic stability (Chapter 3), as well as activation of cell death modalities (Chapter 2). Therefore, the size of the NPs should be considered in risk assessments, including the potential hazard resulting from metal accumulations in cells, and their effects on wildlife and to human health.

One of the aims of this thesis was to initially assess to potential toxicity of AgNPs to the ZF4 cells. The provided materials and data presented in this thesis may support the acquisition of new biological data in a different fish species. There are also clear differences between fish cells in terms of their sensitivity to NPs and NMs that need to be considered in a future regulatory context. For example, during the embryonic development, the embryo is more sensitive and vulnerable to lower concentrations of

metals than adults. Here, for accuracy and complete understanding, the same methods should be conducted in different fish stages. For this, side-by-side studies with cells, embryo, and fish may highlight if the current framework for material testing covers a sufficient breadth of life stages, and if further standardization of test guidelines for NMs is needed.

Certainly, ZF4 cells studies are not intended (or even feasible) to replace fish cell tests utilising rainbow trout gill cells, which is a validated *in vitro* approach for toxicity testing. Conversely, ZF4 cells may provide another model for biological comparison, supporting insights into the toxicity, internalization, and effects of NPs in the embryonic stage (early-stage) of fish, rather than in fish adult cells, and without the interference of the embryo's chorion. For NMs testing, the chorion has been demonstrated to influence the quantification and visualisation of internalized NPs.

While AgNPs based products continue to improve various aspects of human life, it remains vital to evaluate their risks to the natural environment, preferably through the implementation of *in vitro* testing strategies. As chronic exposure to AgNPs and Ag complexes is likely to impact multiple generations, influencing significant toxic effects in populations and ecosystems; where new methodologies to assess adaption and resistance mechanisms are also needed. In this regard, a publication (not directly part of thesis), looked at bacterial adaption of Ag ions and AgNPs over multiple generations, demonstrating the existence of AgNP-specific effects. For example, the expression of cytoplasmic proteins, metal ion transporter (TauB), and those with metal-binding domains (ThiL and PP 2397) were linked only for Ag ions [394]. Conversely, cell surface proteins, including cytoskeletal membrane protein (FtsZ), membrane sensor and regulator (EnvZ

and GacS) and periplasmic protein (PP 2758) were associated for AgNP exposures [394].

5.2 Preliminary work towards ZF4 3D cell models

As mentioned in the previous sections of this Chapter, it is important to consider what future work would be useful to improve the significance of the findings as well as to fully support the use of ZF4 cells as an alternative aquatic model approach for *in vitro* toxicology.

All of the cytotoxic responses evaluated in chapters 2, 3 and 4 were accomplished in 2D cell culture models. However, to enhance the significance of these biological responses, other complex experimental methods and technologies that allow the implementation of more physiologically relevant cell cultures that take into account the complexity of tissue structure (for example), a next level of *in vitro* techniques should be tested. For example, through the use of three-dimensional (3D) models, which differ in functional states and tissue structures compared to 2D models, simulating barrier functions to mimic absorption and distribution of nanomaterials (NMs), as well as mimicking the cellular heterogeneity typical *in vivo* become possible [395].

Some very preliminary work towards this goal was undertaken (Figure 5.3); however, the university closure due to the pandemic prevented further work in this direction. In this regard, the preliminary results demonstrated that ZF4 cells have the potential to be used as part of 3D model toxicity approaches.

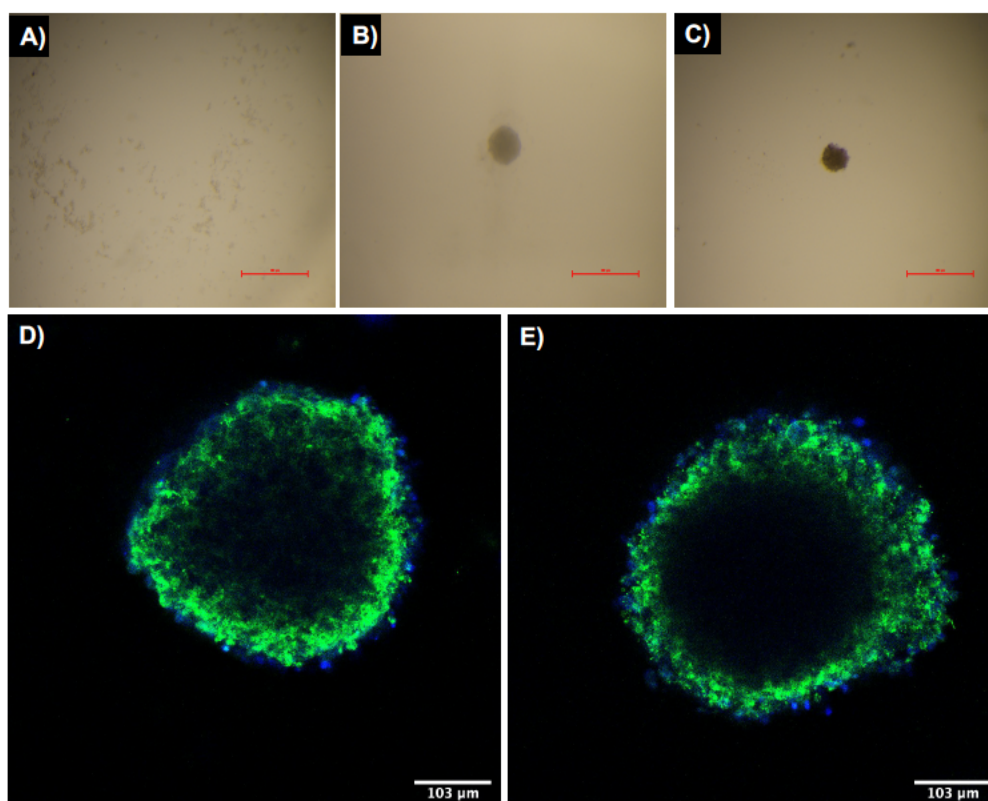


Figure 5.3. Preliminary experimental results to develop 3D models using ZF4 cells. Figures A-C) show the growth and development of ZF4 spheroids over 1, 3 and 6 days. Figure D) show the fluorescent staining of the ZF4 spheroids with blue for nucleus and green for membrane at days 3 and 6 respectively.

On the other hand, the use of microfluidic platforms is another experimental method that can reveal further interactions between NPs and biological fluids and tissues. This kind of bioengineered approach can potentially provide further insights about the toxicity, efficacy, and effects of NPs compared to static assays in conventional 2D cultures [396]. Providing new insights about the NPs' behaviour in a more realistic environmental approach.

5.3 Conclusions

In this thesis, important and novel information regarding the characterisation and toxicity of AgNPs and AgNO₃ in continuously cultured fish cells has been discussed. Here, the biological responses of ZF4 cells exposed to different AgNP sizes, form, and exposure concentrations was investigated, which demonstrated that this fibroblast-like embryonic fish can activate different biological mechanisms as a toxicological response. Moreover, cytotoxic effects were also linked to the amount of ionic silver released by the NPs, since the Ag⁺ and the AgNPs displayed similar responses for all the tested concentrations. Certainly, further experiments are needed to completely unravel the signalling pathways behind each evaluated mechanism. However, the results evaluated and discussed in this thesis provide relevant findings that encourage the potential use of ZF4 cells as a versatile tool to assess molecular and cytotoxic outcomes (Figure 5.1). Furthermore, this cell line offered comparable results to relevant biological models (fish and mammalian cell studies), as previously discussed throughout Chapters 2, 3, 4 and 5).

Conclusively, and based on the experimental data and literature discussed, it is feasible that ZF4 cells can be used to provide an initial evaluation of the cytotoxicity of different NMs, and well as to provide mechanistic insights into the signalling pathways affected by NM exposure. In addition, novel *in vitro* techniques along with non-experimental approaches, such as *in silico* computational assessment and In Vitro to In Vivo Extrapolation (IVIVE) software, can potentially increase the reliability of biological assays and generated data, reducing animal methods, contributing to building of the AOPs induced by NMs and NPs in cells, assisting the use of alternative toxicological

models for animal-free research studies, as well as enhancing the development of safety of new chemicals and nanomaterials. However, confirmation of the applicability and sensitivity of ZF4 cells, compared to embryos and whole fish, will be an important and essential next step towards validation of this cell model to support *in vitro* testing.

6. References

1. Buzea, C., I.I. Pacheco, and K. Robbie, *Nanomaterials and nanoparticles: Sources and toxicity*. Biointerphases, 2007. **2**(4): p. MR17-MR71.
2. Kolahalam, L.A., et al., *Review on nanomaterials: Synthesis and applications*. Materials Today: Proceedings, 2019. **18**: p. 2182-2190.
3. REACH, *Second Regulatory Review on Nanomaterials, COM(2012) 572 final*. 2012: European Commission, Brussels. p. 2.
4. Gottschalk, F., T. Sun, and B. Nowack, *Environmental concentrations of engineered nanomaterials: review of modeling and analytical studies*. Environ Pollut, 2013. **181**: p. 287-300.
5. Smita, S., et al., *Nanoparticles in the environment: assessment using the causal diagram approach*. Environmental Health, 2012. **11**(1): p. S13.
6. Sudha, P.N., et al., *Chapter 12 - Nanomaterials history, classification, unique properties, production and market*, in *Emerging Applications of Nanoparticles and Architecture Nanostructures*, A. Barhoum and A.S.H. Makhoulf, Editors. 2018, Elsevier. p. 341-384.
7. Mishra, R., et al., *The production, characterization and applications of nanoparticles in the textile industry*. Textile Progress, 2014. **46**(2): p. 133-226.
8. Guisbiers, G., S. Mejía-Rosales, and F. Leonard Deepak, *Nanomaterial Properties: Size and Shape Dependencies*. Journal of Nanomaterials, 2012. **2012**: p. 180976.
9. Elena Inshakova and Oleg Inshakov, *World market for nanomaterials: structure and trends*. MATEC Web of Conferences 129, 02013, 2017.
10. Davidovits, P., *Chapter 18 - Nanotechnology in Biology and Medicine*, in *Physics in Biology and Medicine (Fifth Edition)*, P. Davidovits, Editor. 2019, Academic Press. p. 293-305.
11. Hochella, M.F., Jr., et al., *Natural, incidental, and engineered nanomaterials and their impacts on the Earth system*. Science, 2019. **363**(6434).
12. Shaw, B.J. and R.D. Handy, *Physiological effects of nanoparticles on fish: a comparison of nanometals versus metal ions*. Environ Int, 2011. **37**(6): p. 1083-97.
13. Rauscher, H., K. Rasmussen, and B. Sokull-Klüttgen, *Regulatory Aspects of Nanomaterials in the EU*. 2017. **89**(3): p. 224-231.
14. Yang, Y. and P. Westerhoff, *Presence in, and Release of, Nanomaterials from Consumer Products*, in *Advances in Experimental Medicine and Biology*. 2014, Springer Netherlands. p. 1-17.
15. Zhang, X.-F., et al., *Silver Nanoparticles: Synthesis, Characterization, Properties, Applications, and Therapeutic Approaches*. International journal of molecular sciences, 2016. **17**(9): p. 1534.
16. Shafiq, M., et al., *An Overview of the Applications of Nanomaterials and Nanodevices in the Food Industry*. Foods, 2020. **9**(2).
17. Haider, A. and I.-K. Kang, *Preparation of Silver Nanoparticles and Their Industrial and Biomedical Applications: A Comprehensive Review*. Advances in Materials Science and Engineering, 2015. **2015**: p. 165257.
18. *Advanced Silver nano solutions applications*. 2019; Available from: <https://www.advanced.com.tr/en/application-colloidal-silver-nanoparticles/>.

19. Zhang, C., Z. Hu, and B. Deng, *Silver nanoparticles in aquatic environments: Physicochemical behavior and antimicrobial mechanisms*. Water Research, 2016. **88**: p. 403-427.
20. Rai, M., A. Yadav, and A. Gade, *Silver nanoparticles as a new generation of antimicrobials*. Biotechnology Advances, 2009. **27**(1): p. 76-83.
21. Khalandi, B., et al., *A Review on Potential Role of Silver Nanoparticles and Possible Mechanisms of their Actions on Bacteria*. Drug Res (Stuttg), 2017. **67**(2): p. 70-76.
22. Qing, Y.a., et al., *Potential antibacterial mechanism of silver nanoparticles and the optimization of orthopedic implants by advanced modification technologies*. International journal of nanomedicine, 2018. **13**: p. 3311-3327.
23. Kim, S.-H., et al., *Antibacterial activity of silver-nanoparticles against Staphylococcus aureus and Escherichia coli*. Microbiology and Biotechnology Letters, 2011. **39**(1): p. 77-85.
24. González-Fernández, S., et al., *Antibacterial effect of silver nanorings*. BMC Microbiology, 2020. **20**(1): p. 172.
25. Reidy, B., et al., *Mechanisms of Silver Nanoparticle Release, Transformation and Toxicity: A Critical Review of Current Knowledge and Recommendations for Future Studies and Applications*. Materials, 2013. **6**(6): p. 2295-2350.
26. Fabrega, J., et al., *Silver nanoparticles: Behaviour and effects in the aquatic environment*. Environment International, 2011. **37**(2): p. 517-531.
27. Ray, P.C., H. Yu, and P.P. Fu, *Toxicity and Environmental Risks of Nanomaterials: Challenges and Future Needs*. Journal of Environmental Science and Health, Part C, 2009. **27**(1): p. 1-35.
28. Pulit-Prociak, J. and M. Banach, *Silver nanoparticles – a material of the future...? Open Chemistry*, 2016. **14**.
29. Hedberg, J., et al., *Sequential Studies of Silver Released from Silver Nanoparticles in Aqueous Media Simulating Sweat, Laundry Detergent Solutions and Surface Water*. Environmental Science & Technology, 2014. **48**(13): p. 7314-7322.
30. Geranio, L., M. Heuberger, and B. Nowack, *The Behavior of Silver Nanotextiles during Washing*. Environmental Science & Technology, 2009. **43**(21): p. 8113-8118.
31. Ratola, N., et al., *Occurrence of organic microcontaminants in the wastewater treatment process. A mini review*. Journal of Hazardous Materials, 2012. **239-240**: p. 1-18.
32. Brown, J., *Impact of Silver Nanoparticles on Wastewater Treatment*. 2017. p. 255-267.
33. Ratte, H.T., *Bioaccumulation and toxicity of silver compounds: A review*. Environmental Toxicology and Chemistry, 1999. **18**(1): p. 89-108.
34. Thorslund, J., et al., *Speciation and hydrological transport of metals in non-acidic river systems of the Lake Baikal basin: Field data and model predictions*. Regional Environmental Change, 2017. **17**(7): p. 2007-2021.
35. Benn, T.M. and P. Westerhoff, *Nanoparticle Silver Released into Water from Commercially Available Sock Fabrics*. Environmental Science & Technology, 2008. **42**(11): p. 4133-4139.
36. Rearick, D.C., et al., *Spatial and temporal trends in the fate of silver nanoparticles in a whole-lake addition study*. PloS one, 2018. **13**(8): p. e0201412-e0201412.
37. Syafiuddin, A., et al., *Silver Nanoparticles in the Water Environment in Malaysia: Inspection, characterization, removal, modeling, and future perspective*. Scientific Reports, 2018. **8**(1): p. 986.

38. Kaegi, R., et al., *Behavior of metallic silver nanoparticles in a pilot wastewater treatment plant*. Environ Sci Technol, 2011. **45**(9): p. 3902-8.
39. Behra, R., et al., *Bioavailability of silver nanoparticles and ions: from a chemical and biochemical perspective*. Journal of The Royal Society Interface, 2013. **10**(87): p. 20130396.
40. Wilkinson, K.J. and J. Buffle, *Critical Evaluation of Physicochemical Parameters and Processes for Modelling the Biological Uptake of Trace Metals in Environmental (Aquatic) Systems*, in *Physicochemical Kinetics and Transport at Biointerfaces*. 2004. p. 445-533.
41. Misra, S.K., et al., *The complexity of nanoparticle dissolution and its importance in nanotoxicological studies*. Science of The Total Environment, 2012. **438**: p. 225-232.
42. Liu, J. and R.H. Hurt, *Ion Release Kinetics and Particle Persistence in Aqueous Nano-Silver Colloids*. Environmental Science & Technology, 2010. **44**(6): p. 2169-2175.
43. Lowry, G.V., et al., *Transformations of Nanomaterials in the Environment*. Environmental Science & Technology, 2012. **46**(13): p. 6893-6899.
44. Navarro, E., et al., *Toxicity of silver nanoparticles to Chlamydomonas reinhardtii*. Environ Sci Technol, 2008. **42**(23): p. 8959-64.
45. Hartland, A., et al., *The environmental significance of natural nanoparticles*. Nat Educ Knowl, 2013. **4**.
46. Zhang, W., *Nanoparticle Aggregation: Principles and Modeling*, in *Advances in Experimental Medicine and Biology*. 2014, Springer Netherlands. p. 19-43.
47. Handy, R.D., R. Owen, and E. Valsami-Jones, *The ecotoxicology of nanoparticles and nanomaterials: current status, knowledge gaps, challenges, and future needs*. Ecotoxicology, 2008. **17**(5): p. 315-25.
48. Dukhin, A.S. and P.J. Goetz, *Chapter 2 - Fundamentals of Interface and Colloid Science*, in *Characterization of Liquids, Dispersions, Emulsions, and Porous Materials Using Ultrasound (Third Edition)*, A.S. Dukhin and P.J. Goetz, Editors. 2017, Elsevier. p. 19-83.
49. Wang, H., et al., *Stability and aggregation of silver and titanium dioxide nanoparticles in seawater: role of salinity and dissolved organic carbon*. Environ Toxicol Chem, 2014. **33**(5): p. 1023-9.
50. Gondikas, A., et al., *Nanomaterial Fate in Seawater: A Rapid Sink or Intermittent Stabilization?* Frontiers in Environmental Science, 2020. **8**(151).
51. Li, X. and J.J. Lenhart, *Aggregation and Dissolution of Silver Nanoparticles in Natural Surface Water*. Environmental Science & Technology, 2012. **46**(10): p. 5378-5386.
52. Smith, J.N., et al., *All that is silver is not toxic: silver ion and particle kinetics reveals the role of silver ion aging and dosimetry on the toxicity of silver nanoparticles*. Particle and Fibre Toxicology, 2018. **15**(1): p. 47.
53. Loza, K., et al., *The dissolution and biological effects of silver nanoparticles in biological media*. Journal of Materials Chemistry B, 2014. **2**(12): p. 1634.
54. Adamczyk, Z., et al., *Oxidative dissolution of silver nanoparticles: A new theoretical approach*. Journal of Colloid and Interface Science, 2016. **469**: p. 355-364.
55. Zhang, W., et al., *Modeling the Primary Size Effects of Citrate-Coated Silver Nanoparticles on Their Ion Release Kinetics*. Environmental Science & Technology, 2011. **45**(10): p. 4422-4428.
56. Peretyazhko, T.S., Q. Zhang, and V.L. Colvin, *Size-Controlled Dissolution of Silver Nanoparticles at Neutral and Acidic pH Conditions: Kinetics and Size Changes*. Environmental Science & Technology, 2014. **48**(20): p. 11954-11961.

57. Moore, T.L., et al., *Nanoparticle colloidal stability in cell culture media and impact on cellular interactions*. Chemical Society Reviews, 2015. **44**(17): p. 6287-6305.
58. Minghetti, M. and K. Schirmer, *Effect of media composition on bioavailability and toxicity of silver and silver nanoparticles in fish intestinal cells (RTgutGC)*. Nanotoxicology, 2016. **10**(10): p. 1526-1534.
59. Groh, K.J., et al., *Critical influence of chloride ions on silver ion-mediated acute toxicity of silver nanoparticles to zebrafish embryos*. Nanotoxicology, 2015. **9**(1): p. 81-91.
60. Qiang, L., et al., *Silver Nanoparticles in Zebrafish (Danio rerio) Embryos: Uptake, Growth and Molecular Responses*. International journal of molecular sciences, 2020. **21**(5): p. 1876.
61. Handy, R.D., et al., *The ecotoxicology and chemistry of manufactured nanoparticles*. Ecotoxicology, 2008. **17**(4): p. 287-314.
62. Yue, Y., et al., *Toxicity of silver nanoparticles to a fish gill cell line: Role of medium composition*. Nanotoxicology, 2014. **9**(1): p. 54-63.
63. Scown, T.M., et al., *Effects of aqueous exposure to silver nanoparticles of different sizes in rainbow trout*. Toxicol Sci, 2010. **115**(2): p. 521-34.
64. Handy, R.D. and F.B. Eddy, *Transport of Solutes Across Biological Membranes in Eukaryotes: An Environmental Perspective*, in *Physicochemical Kinetics and Transport at Biointerfaces*. 2004. p. 337-356.
65. Hogstrand, C. and C.M. Wood, *Toward a better understanding of the bioavailability, physiology, and toxicity of silver in fish: Implications for water quality criteria*. Environmental Toxicology and Chemistry, 1998. **17**(4): p. 547-561.
66. Osborne, O.J., et al., *Organ-Specific and Size-Dependent Ag Nanoparticle Toxicity in Gills and Intestines of Adult Zebrafish*. ACS Nano, 2015. **9**(10): p. 9573-9584.
67. Handy, R.D., F.B. Eddy, and H. Baines, *Sodium-dependent copper uptake across epithelia: a review of rationale with experimental evidence from gill and intestine*. Biochim Biophys Acta, 2002. **1566**(1-2): p. 104-15.
68. Morgan, T.P., et al., *Time course analysis of the mechanism by which silver inhibits active Na⁺ and Cl⁻ uptake in gills of rainbow trout*. American Journal of Physiology-Regulatory, Integrative and Comparative Physiology, 2004. **287**(1): p. R234-R242.
69. Brix, K.V., et al., *Characterization of the effects of binary metal mixtures on short-term uptake of Ag, Cu, and Ni by rainbow trout (Oncorhynchus mykiss)*. Aquat Toxicol, 2016. **180**: p. 236-246.
70. Zhao, F., et al., *Cellular Uptake, Intracellular Trafficking, and Cytotoxicity of Nanomaterials*. Small, 2011. **7**(10): p. 1322-1337.
71. Griffitt, R.J., et al., *Effects of particle composition and species on toxicity of metallic nanomaterials in aquatic organisms*. Environmental toxicology and chemistry, 2008. **2008 v.27 no.9**(no. 9): p. pp. 1972-1978.
72. Sathya, V., et al., *Acute and sublethal effects in an Indian major carp Cirrhinus mrigala exposed to silver nitrate: Gill Na⁺/K⁺-ATPase, plasma electrolytes and biochemical alterations*. Fish Shellfish Immunol, 2012. **32**(5): p. 862-8.
73. Katuli, K.K., et al., *Silver nanoparticles inhibit the gill Na⁺/K⁺-ATPase and erythrocyte AChE activities and induce the stress response in adult zebrafish (Danio rerio)*. Ecotoxicology and environmental safety, 2014. **106**: p. 173-80.

74. Kwok, K.W.H., et al., *Uptake of silver nanoparticles and toxicity to early life stages of Japanese medaka (Oryzias latipes): Effect of coating materials*. Aquatic Toxicology, 2012. **120-121**: p. 59-66.
75. Sohn, E.K., et al., *Aquatic Toxicity Comparison of Silver Nanoparticles and Silver Nanowires*. BioMed Research International, 2015. **2015**: p. 893049.
76. Valerio-García, R.C., et al., *Exposure to silver nanoparticles produces oxidative stress and affects macromolecular and metabolic biomarkers in the goodeid fish Chapalichthys pardalis*. Science of The Total Environment, 2017. **583**: p. 308-318.
77. Huk, A., et al., *Is the toxic potential of nanosilver dependent on its size?* Particle and fibre toxicology, 2014. **11**: p. 65-65.
78. Saptarshi, S.R., A. Duschl, and A.L. Lopata, *Interaction of nanoparticles with proteins: relation to bio-reactivity of the nanoparticle*. Journal of Nanobiotechnology, 2013. **11**(1): p. 26.
79. Cedervall, T., et al., *Understanding the nanoparticle–protein corona using methods to quantify exchange rates and affinities of proteins for nanoparticles*. Proceedings of the National Academy of Sciences, 2007. **104**(7): p. 2050.
80. Lundqvist, M., et al., *The Evolution of the Protein Corona around Nanoparticles: A Test Study*. ACS Nano, 2011. **5**(9): p. 7503-7509.
81. Monopoli, M.P., et al., *Physical–Chemical Aspects of Protein Corona: Relevance to in Vitro and in Vivo Biological Impacts of Nanoparticles*. Journal of the American Chemical Society, 2011. **133**(8): p. 2525-2534.
82. Wheeler, K.E., et al., *Environmental dimensions of the protein corona*. Nature Nanotechnology, 2021. **16**(6): p. 617-629.
83. Yue, Y., et al., *Silver nanoparticle–protein interactions in intact rainbow trout gill cells*. Environmental Science: Nano, 2016. **3**(5): p. 1174-1185.
84. Hayashi, Y., et al., *Female versus male biological identities of nanoparticles determine the interaction with immune cells in fish*. Environmental Science: Nano, 2017. **4**(4): p. 895-906.
85. Gao, J., et al., *Protein Corona Analysis of Silver Nanoparticles Exposed to Fish Plasma*. Environmental science & technology letters, 2017. **4**(5): p. 174-179.
86. Yue, Y., et al., *Interaction of silver nanoparticles with algae and fish cells: a side by side comparison*. Journal of Nanobiotechnology, 2017. **15**(1): p. 16.
87. Gustafson, H.H., et al., *Nanoparticle Uptake: The Phagocyte Problem*. Nano today, 2015. **10**(4): p. 487-510.
88. Vercauteren, D., et al., *The use of inhibitors to study endocytic pathways of gene carriers: optimization and pitfalls*. Molecular therapy : the journal of the American Society of Gene Therapy, 2010. **18**(3): p. 561-569.
89. Rejman, J., et al., *Size-dependent internalization of particles via the pathways of clathrin- and caveolae-mediated endocytosis*. The Biochemical journal, 2004. **377**(Pt 1): p. 159-169.
90. Ng, C.T., et al., *Clathrin-Mediated Endocytosis of Gold Nanoparticles In Vitro*. The Anatomical Record, 2015. **298**(2): p. 418-427.
91. Guggenheim, E.J., J.Z. Rappoport, and I. Lynch, *Mechanisms for cellular uptake of nanosized clinical MRI contrast agents*. Nanotoxicology, 2020. **14**(4): p. 504-532.
92. dos Santos, T., et al., *Effects of Transport Inhibitors on the Cellular Uptake of Carboxylated Polystyrene Nanoparticles in Different Cell Lines*. PLOS ONE, 2011. **6**(9): p. e24438.

93. Glick, D., S. Barth, and K.F. Macleod, *Autophagy: cellular and molecular mechanisms*. The Journal of pathology, 2010. **221**(1): p. 3-12.
94. Handy, R.D., et al., *Manufactured nanoparticles: their uptake and effects on fish--a mechanistic analysis*. Ecotoxicology, 2008. **17**(5): p. 396-409.
95. Smith, C.J., B.J. Shaw, and R.D. Handy, *Toxicity of single walled carbon nanotubes to rainbow trout, (Oncorhynchus mykiss): respiratory toxicity, organ pathologies, and other physiological effects*. Aquat Toxicol, 2007. **82**(2): p. 94-109.
96. Milić, M., et al., *Cellular uptake and toxicity effects of silver nanoparticles in mammalian kidney cells*. J Appl Toxicol, 2015. **35**(6): p. 581-92.
97. Zhao, J. and M.H. Stenzel, *Entry of nanoparticles into cells: the importance of nanoparticle properties*. Polymer Chemistry, 2018. **9**(3): p. 259-272.
98. Foroozandeh, P. and A.A. Aziz, *Insight into Cellular Uptake and Intracellular Trafficking of Nanoparticles*. Nanoscale research letters, 2018. **13**(1): p. 339-339.
99. Felix, L.C., V.A. Ortega, and G.G. Goss, *Cellular uptake and intracellular localization of poly (acrylic acid) nanoparticles in a rainbow trout (Oncorhynchus mykiss) gill epithelial cell line, RTgill-W1*. Aquatic Toxicology, 2017. **192**: p. 58-68.
100. Lammel, T., et al., *Endocytosis, intracellular fate, accumulation, and agglomeration of titanium dioxide (TiO₂) nanoparticles in the rainbow trout liver cell line RTL-W1*. Environmental Science and Pollution Research, 2019. **26**(15): p. 15354-15372.
101. Sendra, M., et al., *Size matters: Zebrafish (Danio rerio) as a model to study toxicity of nanoplastics from cells to the whole organism*. Environmental Pollution, 2021. **268**: p. 115769.
102. Bury, N.R. and C.M. Wood, *Mechanism of branchial apical silver uptake by rainbow trout is via the proton-coupled Na(+) channel*. Am J Physiol, 1999. **277**(5): p. R1385-91.
103. Cooper, G.M., *The Cell: A Molecular Approach*, S.M.S.A. 2000, Editor. 2000.
104. Mosquera, J., I. García, and L.M. Liz-Marzán, *Cellular Uptake of Nanoparticles versus Small Molecules: A Matter of Size*. Accounts of Chemical Research, 2018. **51**(9): p. 2305-2313.
105. Kou, L., et al., *The endocytosis and intracellular fate of nanomedicines: Implication for rational design*. Asian Journal of Pharmaceutical Sciences, 2013. **8**(1): p. 1-10.
106. Recouvreur, M.V. and C. Commisso, *Macropinocytosis: A Metabolic Adaptation to Nutrient Stress in Cancer*. 2017. **8**(261).
107. Ostaszewska, T., et al., *Cytotoxicity of silver and copper nanoparticles on rainbow trout (Oncorhynchus mykiss) hepatocytes*. Environmental Science and Pollution Research, 2018. **25**(1): p. 908-915.
108. Sukhanova, A., et al., *Dependence of Nanoparticle Toxicity on Their Physical and Chemical Properties*. Nanoscale research letters, 2018. **13**(1): p. 44-44.
109. Nazemidashtarjandi, S. and A.M. Farnoud, *Membrane outer leaflet is the primary regulator of membrane damage induced by silica nanoparticles in vesicles and erythrocytes*. Environmental Science: Nano, 2019. **6**(4): p. 1219-1232.
110. Contini, C., et al., *Nanoparticle–membrane interactions*. Journal of Experimental Nanoscience, 2018. **13**(1): p. 62-81.
111. Monopoli, M.P., et al., *Formation and characterization of the nanoparticle-protein corona*. Methods Mol Biol, 2013. **1025**: p. 137-55.
112. Connolly, M., et al., *Comparative Cytotoxicity Study of Silver Nanoparticles (AgNPs) in a Variety of Rainbow Trout Cell Lines (RTL-W1, RTH-149, RTG-2) and Primary*

- Hepatocytes*. International Journal of Environmental Research and Public Health, 2015. **12**(5): p. 5386-5405.
113. Bermejo-Nogales, A., et al., *Effects of a silver nanomaterial on cellular organelles and time course of oxidative stress in a fish cell line (PLHC-1)*. Comp Biochem Physiol C Toxicol Pharmacol, 2016. **190**: p. 54-65.
 114. Yan, N., B.Z. Tang, and W.-X. Wang, *Intracellular trafficking of silver nanoparticles and silver ions determined their specific mitotoxicity to the zebrafish cell line*. Environmental Science: Nano, 2021.
 115. Gliga, A.R., et al., *Size-dependent cytotoxicity of silver nanoparticles in human lung cells: the role of cellular uptake, agglomeration and Ag release*. Particle and fibre toxicology, 2014. **11**: p. 11-11.
 116. Farkas, J., et al., *Effects of silver and gold nanoparticles on rainbow trout (Oncorhynchus mykiss) hepatocytes*. Aquat Toxicol, 2010. **96**(1): p. 44-52.
 117. dos Santos, N.M., et al., *Fish and apoptosis: molecules and pathways*. Curr Pharm Des, 2008. **14**(2): p. 148-69.
 118. Comhaire, S., et al., *Cobalt uptake across the gills of the common carp, Cyprinus carpio, as a function of calcium concentration in the water of acclimation and exposure*. Comparative Biochemistry and Physiology Part C: Pharmacology, Toxicology and Endocrinology, 1994. **109**(1): p. 63-76.
 119. Wood, C.M., R.C. Playle, and C. Hogstrand, *Physiology and modeling of mechanisms of silver uptake and toxicity in fish*. Environmental Toxicology and Chemistry, 1999. **18**(1): p. 71-83.
 120. Flik, G., et al., *Cellular Calcium Transport in Fish: Unique and Universal Mechanisms*. Physiological Zoology, 1996. **69**(2): p. 403-417.
 121. Flik, G. and P.M. Verboost, *Chapter 13 Cellular mechanisms in calcium transport and homeostasis in fish*, in *Biochemistry and Molecular Biology of Fishes*, P.W. Hochachka and T.P. Mommsen, Editors. 1995, Elsevier. p. 251-263.
 122. Calamari, D., R. Marchetti, and G. Vailati, *Influence of water hardness on cadmium toxicity to Salmo gairdneri Rich*. Water Research, 1980. **14**(10): p. 1421-1426.
 123. Hogstrand, C., et al., *Mechanisms of zinc uptake in gills of freshwater rainbow trout: interplay with calcium transport*. American Journal of Physiology-Regulatory, Integrative and Comparative Physiology, 1996. **270**(5): p. R1141-R1147.
 124. Perry, S.F., *The chloride cell: structure and function in the gills of freshwater fishes*. Annual review of physiology, 1997. **59**(1): p. 325-347.
 125. Bury, N.R., F. Galvez, and C.M. Wood, *Effects of chloride, calcium, and dissolved organic carbon on silver toxicity: Comparison between rainbow trout and fathead minnows*. Environmental Toxicology and Chemistry: An International Journal, 1999. **18**(1): p. 56-62.
 126. Bury, N.R., J.C. McGeer, and C.M. Wood, *Effects of altering freshwater chemistry on physiological responses of rainbow trout to silver exposure*. Environmental Toxicology and Chemistry: An International Journal, 1999. **18**(1): p. 49-55.
 127. Morgan, I.J., R.P. Henry, and C.M. Wood, *The mechanism of acute silver nitrate toxicity in freshwater rainbow trout (Oncorhynchus mykiss) is inhibition of gill Na⁺ and Cl⁻ transport*. Aquatic Toxicology, 1997. **38**(1-3): p. 145-163.
 128. Li, L.H., et al., *The Golgi Apparatus: Panel Point of Cytosolic Ca²⁺ Regulation*. Neurosignals, 2013. **21**(3-4): p. 272-284.

129. Stutzmann, G.E. and M.P. Mattson, *Endoplasmic reticulum Ca(2+) handling in excitable cells in health and disease*. Pharmacological reviews, 2011. **63**(3): p. 700-727.
130. Das, C., et al., *Cortisol modulates calcium release-activated calcium channel gating in fish hepatocytes*. Scientific Reports, 2021. **11**(1): p. 9621.
131. Meindl, C., et al., *Intracellular calcium levels as screening tool for nanoparticle toxicity*. Journal of applied toxicology : JAT, 2015. **35**(10): p. 1150-1159.
132. Togo, T., *Chapter Five - Signaling pathways involved in adaptive responses to cell membrane disruption*, in *Current Topics in Membranes*, L.O. Andrade, Editor. 2019, Academic Press. p. 99-127.
133. Dong, Z., et al., *Calcium in cell injury and death*. Annual review of pathology, 2006. **1**: p. 405-34.
134. Miller, M.A. and J.F. Zachary, *Mechanisms and Morphology of Cellular Injury, Adaptation, and Death*. Pathologic Basis of Veterinary Disease, 2017: p. 2-43.e19.
135. Henry-Mowatt, J., et al., *Role of mitochondrial membrane permeabilization in apoptosis and cancer*. Oncogene, 2004. **23**(16): p. 2850-2860.
136. Guo, C., et al., *Oxidative stress, mitochondrial damage and neurodegenerative diseases*. Neural regeneration research, 2013. **8**(21): p. 2003-2014.
137. Piao, M.J., et al., *Silver nanoparticles induce oxidative cell damage in human liver cells through inhibition of reduced glutathione and induction of mitochondria-involved apoptosis*. Toxicology Letters, 2011. **201**(1): p. 92-100.
138. Ma, W., et al., *Silver nanoparticle exposure induced mitochondrial stress, caspase-3 activation and cell death: amelioration by sodium selenite*. International journal of biological sciences, 2015. **11**(8): p. 860-867.
139. Li, X., et al., *Targeting mitochondrial reactive oxygen species as novel therapy for inflammatory diseases and cancers*. Journal of hematology & oncology, 2013. **6**: p. 19-19.
140. Pizzino, G., et al., *Oxidative Stress: Harms and Benefits for Human Health*. Oxidative medicine and cellular longevity, 2017. **2017**: p. 8416763-8416763.
141. Fu, P.P., et al., *Mechanisms of nanotoxicity: Generation of reactive oxygen species*. Journal of Food and Drug Analysis, 2014. **22**(1): p. 64-75.
142. Covarrubias, L., et al., *Function of reactive oxygen species during animal development: Passive or active?* Developmental Biology, 2008. **320**(1): p. 1-11.
143. Lungu-Mitea, S., A. Oskarsson, and J. Lundqvist, *Development of an oxidative stress in vitro assay in zebrafish (Danio rerio) cell lines*. Scientific reports, 2018. **8**(1): p. 12380-12380.
144. Martin, M.T., et al., *Impact of environmental chemicals on key transcription regulators and correlation to toxicity end points within EPA's ToxCast program*. Chem Res Toxicol, 2010. **23**(3): p. 578-90.
145. Choi, J.E., et al., *Induction of oxidative stress and apoptosis by silver nanoparticles in the liver of adult zebrafish*. Aquatic Toxicology, 2010. **100**(2): p. 151-159.
146. Garcia-Reyero, N., et al., *Differential Effects and Potential Adverse Outcomes of Ionic Silver and Silver Nanoparticles in Vivo and in Vitro*. Environmental Science & Technology, 2014. **48**(8): p. 4546-4555.
147. Akter, M., et al., *A systematic review on silver nanoparticles-induced cytotoxicity: Physicochemical properties and perspectives*. Journal of Advanced Research, 2018. **9**: p. 1-16.

148. Higgs, E., et al., *Induction of apoptosis in Ogg1-null mouse embryonic fibroblasts by GSH depletion is independent of DNA damage*. Toxicology Letters, 2020. **332**.
149. Anastassopoulou, J., *Metal–DNA interactions*. Journal of Molecular Structure, 2003. **651-653**: p. 19-26.
150. Chatterjee, N. and G.C. Walker, *Mechanisms of DNA damage, repair, and mutagenesis*. Environmental and molecular mutagenesis, 2017. **58(5)**: p. 235-263.
151. Sancar, A., et al., *Molecular mechanisms of mammalian DNA repair and the DNA damage checkpoints*. Annu Rev Biochem, 2004. **73**: p. 39-85.
152. Morris, D.L., *DNA-bound metal ions: recent developments*. Biomolecular Concepts, 2014. **5(5)**: p. 397-407.
153. Campos, A. and A. Clemente-Blanco, *Cell Cycle and DNA Repair Regulation in the Damage Response: Protein Phosphatases Take Over the Reins*. International journal of molecular sciences, 2020. **21(2)**: p. 446.
154. Perde-Schrepler, M., et al., *Size-Dependent Cytotoxicity and Genotoxicity of Silver Nanoparticles in Cochlear Cells <i>In Vitro</i>*. Journal of Nanomaterials, 2019. **2019**: p. 6090259.
155. Mao, B.-H., et al., *Silver nanoparticles have lethal and sublethal adverse effects on development and longevity by inducing ROS-mediated stress responses*. Scientific Reports, 2018. **8(1)**: p. 2445.
156. Wan, R., et al., *DNA damage caused by metal nanoparticles: involvement of oxidative stress and activation of ATM*. Chemical research in toxicology, 2012. **25(7)**: p. 1402-1411.
157. de Lapuente, J., et al., *The Comet Assay and its applications in the field of ecotoxicology: a mature tool that continues to expand its perspectives*. Frontiers in genetics, 2015. **6**: p. 180-180.
158. Akcha, F., G. Leday, and A. Pfohl-Leszkowicz, *Measurement of DNA adducts and strand breaks in dab (Limanda limanda) collected in the field: effects of biotic (age, sex) and abiotic (sampling site and period) factors on the extent of DNA damage*. Mutation Research/Fundamental and Molecular Mechanisms of Mutagenesis, 2004. **552(1-2)**: p. 197-207.
159. George, S., et al., *Differential Effect of Solar Light in Increasing the Toxicity of Silver and Titanium Dioxide Nanoparticles to a Fish Cell Line and Zebrafish Embryos*. Environmental Science & Technology, 2014. **48(11)**: p. 6374-6382.
160. Silva, E. and T. Ideker, *Transcriptional responses to DNA damage*. DNA repair, 2019. **79**: p. 40-49.
161. Canedo, A. and T.L. Rocha, *Zebrafish (Danio rerio) using as model for genotoxicity and DNA repair assessments: Historical review, current status and trends*. Science of The Total Environment, 2021. **762**: p. 144084.
162. Uniprot. 2022; Available from: <https://www.uniprot.org>.
163. O'Rourke, J. and A. Deans, *The FANCA to FANCD3 of DNA interstrand crosslink repair: Lessons from Fanconi anemia*, in *DNA Repair in Cancer Therapy*. 2016, Elsevier. p. 353-381.
164. Teles, M., et al., *Toxicogenomics of Gold Nanoparticles in a Marine Fish: Linkage to Classical Biomarkers*. Frontiers in Marine Science, 2019. **6(147)**.
165. Fulda, S., et al., *Cellular Stress Responses: Cell Survival and Cell Death J International Journal of Cell Biology*. 2010. **2010**: p. 23.

166. Galluzzi, L., et al., *Molecular mechanisms of cell death: recommendations of the Nomenclature Committee on Cell Death 2018*. Cell Death & Differentiation, 2018. **25**(3): p. 486-541.
167. Green, D.R. and F. Llambi, *Cell Death Signaling*. Cold Spring Harbor perspectives in biology, 2015. **7**(12): p. a006080.
168. Sun, H., et al., *Gold Nanoparticle-Induced Cell Death and Potential Applications in Nanomedicine*. International journal of molecular sciences, 2018. **19**(3): p. 754.
169. Chipuk, J.E., L. Bouchier-Hayes, and D.R. Green, *Mitochondrial outer membrane permeabilization during apoptosis: the innocent bystander scenario*. Cell Death & Differentiation, 2006. **13**(8): p. 1396-1402.
170. AnvariFar, H., et al., *Apoptosis in fish: environmental factors and programmed cell death*. Cell and Tissue Research, 2017. **368**(3): p. 425-439.
171. Okada, Y. and E. Maeno, *Apoptosis, cell volume regulation and volume-regulatory chloride channels*. Comparative Biochemistry and Physiology Part A: Molecular & Integrative Physiology, 2001. **130**(3): p. 377-383.
172. Wise, J.P., Sr., et al., *Silver nanospheres are cytotoxic and genotoxic to fish cells*. Aquatic toxicology (Amsterdam, Netherlands), 2010. **97**(1): p. 34-41.
173. Takahashi, H., et al., *Prolactin receptor and proliferating/apoptotic cells in esophagus of the Mozambique tilapia (Oreochromis mossambicus) in fresh water and in seawater*. Gen Comp Endocrinol, 2007. **152**(2-3): p. 326-31.
174. Yonekawa, T. and A. Thorburn, *Autophagy and cell death*. Essays in biochemistry, 2013. **55**: p. 105-117.
175. Levine, B., N. Mizushima, and H.W. Virgin, *Autophagy in immunity and inflammation*. Nature, 2011. **469**(7330): p. 323-35.
176. Dunlop, E.A. and A.R. Tee, *mTOR and autophagy: A dynamic relationship governed by nutrients and energy*. Seminars in Cell & Developmental Biology, 2014. **36**: p. 121-129.
177. Denton, D. and S. Kumar, *Autophagy-dependent cell death*. Cell Death & Differentiation, 2019. **26**(4): p. 605-616.
178. Su, L.-J., et al., *Reactive Oxygen Species-Induced Lipid Peroxidation in Apoptosis, Autophagy, and Ferroptosis* J Oxidative Medicine and Cellular Longevity. 2019. **2019**: p. 13.
179. Yabu, T., et al., *Induction of Autophagy by Amino Acid Starvation in Fish Cells*. Marine Biotechnology, 2012. **14**(4): p. 491-501.
180. Lescat, L., et al., *Chaperone-Mediated Autophagy in the Light of Evolution: Insight from Fish*. Molecular Biology and Evolution, 2020. **37**(10): p. 2887-2899.
181. Jung, S., H. Jeong, and S.-W. Yu, *Autophagy as a decisive process for cell death*. Experimental & Molecular Medicine, 2020. **52**(6): p. 921-930.
182. Karch, J., et al., *Autophagic cell death is dependent on lysosomal membrane permeability through Bax and Bak*. Elife, 2017. **6**: p. e30543.
183. Yu, L., et al., *Autophagic programmed cell death by selective catalase degradation*. Proceedings of the National Academy of Sciences, 2006. **103**(13): p. 4952-4957.
184. Dasari, S.K., et al., *Signalome-wide RNAi screen identifies GBA1 as a positive mediator of autophagic cell death*. Cell Death & Differentiation, 2017. **24**(7): p. 1288-1302.
185. Farkas, J., et al., *Uptake and effects of manufactured silver nanoparticles in rainbow trout (Oncorhynchus mykiss) gill cells*. Aquatic Toxicology, 2011. **101**(1): p. 117-125.

186. Sayed, A.E.-D.H., et al., *Histopathological and histochemical effects of silver nanoparticles on the gills and muscles of African catfish (Clarias gariepinus)*. Scientific African, 2020. **7**: p. e00230.
187. D'Arcy, M.S., *Cell death: a review of the major forms of apoptosis, necrosis and autophagy*. Cell Biol Int, 2019. **43**(6): p. 582-592.
188. Linhua, H., W. Zhenyu, and X. Baoshan, *Effect of sub-acute exposure to TiO₂ nanoparticles on oxidative stress and histopathological changes in Juvenile Carp (Cyprinus carpio)*. Journal of Environmental Sciences, 2009. **21**(10): p. 1459-1466.
189. Braunbeck, T., et al., *The fish embryo test (FET): origin, applications, and future*. Environmental Science and Pollution Research, 2015. **22**(21): p. 16247-16261.
190. Strähle, U., et al., *Zebrafish embryos as an alternative to animal experiments—A commentary on the definition of the onset of protected life stages in animal welfare regulations*. Reproductive Toxicology, 2012. **33**(2): p. 128-132.
191. Zhang, C., C. Willett, and T. Fremgen, *Zebrafish: an animal model for toxicological studies*. Current Protocols in Toxicology, 2003. **17**(1): p. 1.7. 1-1.7. 18.
192. McGrath, P. and C.-Q. Li, *Zebrafish: a predictive model for assessing drug-induced toxicity*. Drug discovery today, 2008. **13**(9-10): p. 394-401.
193. He, J.-H., et al., *Zebrafish models for assessing developmental and reproductive toxicity*. Neurotoxicology and teratology, 2014. **42**: p. 35-42.
194. OECD, *Fish Toxicity Testing Framework*. 2014.
195. OECD, *Test No. 203: Fish, Acute Toxicity Test*. 2019.
196. Handy, R.D. and B.J. Shaw, *Ecotoxicity of nanomaterials to fish: challenges for ecotoxicity testing*. Integr Environ Assess Manag, 2007. **3**(3): p. 458-60.
197. Shaw, B.J., et al., *A critical evaluation of the fish early-life stage toxicity test for engineered nanomaterials: experimental modifications and recommendations*. Arch Toxicol, 2016. **90**(9): p. 2077-2107.
198. Haque, E. and A.C. Ward, *Zebrafish as a Model to Evaluate Nanoparticle Toxicity*. Nanomaterials (Basel), 2018. **8**(7).
199. Lawrence, C., et al., *Regulatory compliance and the zebrafish*. Zebrafish, 2009. **6**(4): p. 453-456.
200. OECD. *OECD Guidance for testing of chemicals, Draft revised version Fish, Acute Toxicity Test*. 2018; Available from: <https://www.oecd.org/chemicalsafety/testing/draft-revised-test-guideline-203-fish-acute-toxicity-test.pdf>.
201. OECD, *Fish, Early-life Stage Toxicity Test. OECD Guidelines for the Testing of Chemicals, Section 2*. . 1992.
202. Lungu-Mitea, S., et al., *Modeling Bioavailable Concentrations in Zebrafish Cell Lines and Embryos Increases the Correlation of Toxicity Potencies across Test Systems*. Environmental Science & Technology, 2021. **55**(1): p. 447-457.
203. OECD, *Test No. 236: Fish Embryo Acute Toxicity (FET) Test*. 2013.
204. Lee, K.J., et al., *In vivo imaging of transport and biocompatibility of single silver nanoparticles in early development of zebrafish embryos*. ACS Nano, 2007. **1**(2): p. 133-43.
205. Kim, K.-T. and R.L. Tanguay, *The role of chorion on toxicity of silver nanoparticles in the embryonic zebrafish assay*. Environmental health and toxicology, 2014. **29**: p. e2014021-e2014021.

206. Duan, J., et al., *Toxic effects of silica nanoparticles on zebrafish embryos and larvae*. PLoS one, 2013. **8**(9): p. e74606.
207. Mandrell, D., et al., *Automated zebrafish chorion removal and single embryo placement: optimizing throughput of zebrafish developmental toxicity screens*. Journal of laboratory automation, 2012. **17**(1): p. 66-74.
208. Panzica-Kelly, J.M., C.X. Zhang, and K.A. Augustine-Rauch, *Optimization and Performance Assessment of the Chorion-Off [Dechorinated] Zebrafish Developmental Toxicity Assay*. Toxicological Sciences, 2015. **146**(1): p. 127-134.
209. Zielińska, A., et al., *Nanotoxicology and Nanosafety: Safety-By-Design and Testing at a Glance*. International journal of environmental research and public health, 2020. **17**(13): p. 4657.
210. Glyn, S., D. Alan, and F. Margherita, *Cell Culture Methods for In Vitro Toxicology*. 1 ed. 2001: Springer Netherlands. IX, 153.
211. Allen, D.D., et al., *Cell Lines as In Vitro Models for Drug Screening and Toxicity Studies*. Drug Development and Industrial Pharmacy, 2005. **31**(8): p. 757-768.
212. Burden, N., et al., *The 3Rs as a framework to support a 21st century approach for nanosafety assessment*. Nano Today, 2017. **12**: p. 10-13.
213. Wolf, K. and M. Quimby, *Established eurythermic line of fish cells in vitro*. Science, 1962. **135**(3508): p. 1065-1066.
214. Fent, K., *Fish cell lines as versatile tools in ecotoxicology: assessment of cytotoxicity, cytochrome P4501A induction potential and estrogenic activity of chemicals and environmental samples*. Toxicology in Vitro, 2001. **15**(4): p. 477-488.
215. Castaño, A., et al., *The use of fish cells in ecotoxicology. The report and recommendations of ECVAM Workshop 47*. Altern Lab Anim, 2003. **31**(3): p. 317-51.
216. Minghetti, M. and K. Schirmer, *Interference of silver nanoparticles with essential metal homeostasis in a novel enterohepatic fish in vitro system*. Environmental Science: Nano, 2019. **6**(6): p. 1777-1790.
217. Bermejo-Nogales, A., et al., *Negligible cytotoxicity induced by different titanium dioxide nanoparticles in fish cell lines*. Ecotoxicology and Environmental Safety, 2017. **138**: p. 309-319.
218. Vo, N.T., et al., *Cytotoxicity evaluation of silica nanoparticles using fish cell lines*. In Vitro Cell Dev Biol Anim, 2014. **50**(5): p. 427-38.
219. OECD, *Test No. 249: Fish Cell Line Acute Toxicity - The RTgill-W1 cell line assay*. 2021.
220. Katsumiti, A., et al., *Mechanisms of Toxicity of Ag Nanoparticles in Comparison to Bulk and Ionic Ag on Mussel Hemocytes and Gill Cells*. PLoS ONE, 2015. **10**(6): p. e0129039.
221. Fernández-Cruz, M.L., et al., *Comparative cytotoxicity induced by bulk and nanoparticulated ZnO in the fish and human hepatoma cell lines PLHC-1 and Hep G2*. Nanotoxicology, 2013. **7**(5): p. 935-52.
222. Lammel, T. and J. Sturve, *Assessment of titanium dioxide nanoparticle toxicity in the rainbow trout (*Onchorynchus mykiss*) liver and gill cell lines RTL-W1 and RTgill-W1 under particular consideration of nanoparticle stability and interference with fluorometric assays*. NanoImpact, 2018. **11**: p. 1-19.
223. Sharma, N., et al., *Assessment of DNA damage and molecular responses in *Labeo rohita* (Hamilton, 1822) following short-term exposure to silver nanoparticles*. Food and Chemical Toxicology, 2016. **96**: p. 122-132.

224. Taju, G., et al., *In vitro* assay for the toxicity of silver nanoparticles using heart and gill cell lines of *Catla catla* and gill cell line of *Labeo rohita*. *Comparative Biochemistry and Physiology Part C: Toxicology & Pharmacology*, 2014. **161**: p. 41-52.
225. Chen, L.Q., B. Kang, and J. Ling, *Cytotoxicity of cuprous oxide nanoparticles to fish blood cells: hemolysis and internalization*. *Journal of Nanoparticle Research*, 2013. **15**(3): p. 1507.
226. Melby, E.S., et al., *Impact of lithiated cobalt oxide and phosphate nanoparticles on rainbow trout gill epithelial cells*. *Nanotoxicology*, 2018. **12**(10): p. 1166-1181.
227. Ciarlo, C.A. and L.I. Zon, *Embryonic cell culture in zebrafish*. *Methods Cell Biol*, 2016. **133**: p. 1-10.
228. Bols, N.C., et al., *Chapter 2 Use of fish cell lines in the toxicology and ecotoxicology of fish. Piscine cell lines in environmental toxicology*, in *Biochemistry and Molecular Biology of Fishes*, T.P. Mommsen and T.W. Moon, Editors. 2005, Elsevier. p. 43-84.
229. Lungu-Mitea, S., A. Oskarsson, and J. Lundqvist, *Development of an oxidative stress in vitro assay in zebrafish (*Danio rerio*) cell lines*. *Scientific Reports*, 2018. **8**(1): p. 12380.
230. Li, Z., et al., *RNA sequencing provides insights into the toxicogenomic response of ZF4 cells to methyl methanesulfonate*. *Journal of Applied Toxicology*, 2015. **36**(1): p. 94-104.
231. Ji, X., et al., *Identification and characterization of miRNAs involved in cold acclimation of zebrafish ZF4 cells*. *PLOS ONE*, 2020. **15**(1): p. e0226905.
232. Ding, C., et al., *Exploration of the bacterial invasion capacity of *Listeria monocytogenes* in ZF4 cells*. *Microbial Pathogenesis*, 2018. **124**: p. 238-243.
233. Driever, W. and Z. Rangini, *Characterization of a cell line derived from zebrafish (*Brachydanio rerio*) embryos*. *In Vitro Cell Dev Biol Anim*, 1993. **29a**(9): p. 749-54.
234. Segner, H., *Cytotoxicity Assays with Fish Cells as an Alternative to the Acute Lethality Test with Fish*. *Alternatives to Laboratory Animals*, 2004. **32**(4): p. 375-382.
235. Gülden, M., S. Mörchel, and H. Seibert, *Comparison of mammalian and fish cell line cytotoxicity: impact of endpoint and exposure duration*. *Aquatic Toxicology*, 2005. **71**(3): p. 229-236.
236. Castaño, A. and M.a.J. Gómez-Lechón, *Comparison of basal cytotoxicity data between mammalian and fish cell lines: A literature survey*. *Toxicology in Vitro*, 2005. **19**(5): p. 695-705.
237. Ishimatsu, A., et al., *Physiological effects on fishes in a high-CO₂ world*. *Journal of Geophysical Research: Oceans*, 2005. **110**(C9).
238. Smith, P.J., et al., *Cellular entry of nanoparticles via serum sensitive clathrin-mediated endocytosis, and plasma membrane permeabilization*. *International journal of nanomedicine*, 2012. **7**: p. 2045-2055.
239. Lungu-Mitea, S. and J. Lundqvist, *Potentials and pitfalls of transient in vitro reporter bioassays: interference by vector geometry and cytotoxicity in recombinant zebrafish cell lines*. *Archives of Toxicology*, 2020. **94**(8): p. 2769-2784.
240. Fabian, E., et al., *In vitro-to-in vivo extrapolation (IVIVE) by PBTK modeling for animal-free risk assessment approaches of potential endocrine-disrupting compounds*. *Archives of Toxicology*, 2019. **93**(2): p. 401-416.
241. Zhang, Q., et al., *Bridging the Data Gap From in vitro Toxicity Testing to Chemical Safety Assessment Through Computational Modeling*. *Frontiers in Public Health*, 2018. **6**(261).
242. Wang, X. and W.-X. Wang, *Cu-based nanoparticle toxicity to zebrafish cells regulated by cellular discharges*. *Environmental Pollution*, 2021. **292**: p. 118296.

243. Sun, A., et al., *Unique interplay between Zn²⁺ and nZnO determined the dynamic cellular stress in zebrafish cells*. *Environmental Science: Nano*, 2021. **8**(8): p. 2324-2335.
244. Garcia-Calvo, E., P. Cabezas-Sanchez, and J.L. Luque-Garcia, *In-vitro and in-vivo evaluation of the molecular mechanisms involved in the toxicity associated to CdSe/ZnS quantum dots exposure*. *Chemosphere*, 2021. **263**: p. 128170.
245. Yat, L.C., *Investigating dissolution kinetics and cytotoxicity of zinc oxide nanomaterials*. 2019, The Hong Kong University of Science and Technology: <https://lbezone.ust.hk/bib/991012753262303412#>.
246. Yang, Y. and P. Westerhoff, *Presence and Release of Nanomaterials from Consumer Products*, in *Advances in Experimental Medicine and Biology*. 2014, Springer Netherlands. p. 1-17.
247. Pourzahedi, L. and M.J. Eckelman, *Environmental Life Cycle Assessment of Nanosilver-Enabled Bandages*. *Environmental Science & Technology*, 2015. **49**(1): p. 361-368.
248. Donahue, N.D., H. Acar, and S. Wilhelm, *Concepts of nanoparticle cellular uptake, intracellular trafficking, and kinetics in nanomedicine*. *Advanced Drug Delivery Reviews*, 2019. **143**: p. 68-96.
249. Lee, W.S., et al., *The Relationship between Dissolution Behavior and the Toxicity of Silver Nanoparticles on Zebrafish Embryos in Different Ionic Environments*. *Nanomaterials (Basel, Switzerland)*, 2018. **8**(9): p. 652.
250. Levard, C., et al., *Environmental Transformations of Silver Nanoparticles: Impact on Stability and Toxicity*. *Environmental Science & Technology*, 2012. **46**(13): p. 6900-6914.
251. Marano, F., et al., *Cellular Mechanisms of Nanoparticle's Toxicity*, in *Encyclopedia of Nanotechnology*, B. Bhushan, Editor. 2012, Springer Netherlands: Dordrecht. p. 404-411.
252. Ayala, A., M.F. Muñoz, and S. Argüelles, *Lipid Peroxidation: Production, Metabolism, and Signaling Mechanisms of Malondialdehyde and 4-Hydroxy-2-Nonenal*. *Oxidative Medicine and Cellular Longevity*, 2014. **2014**: p. 360438.
253. Törnqvist, E., et al., *Strategic focus on 3R principles reveals major reductions in the use of animals in pharmaceutical toxicity testing*. *PloS one*, 2014. **9**(7): p. e101638-e101638.
254. Stadnicka-Michalak, J., et al., *Measured and Modeled Toxicokinetics in Cultured Fish Cells and Application to In Vitro - In Vivo Toxicity Extrapolation*. *PLOS ONE*, 2014. **9**(3): p. e92303.
255. Bury, N.R., S. Schnell, and C. Hogstrand, *Gill cell culture systems as models for aquatic environmental monitoring*. *The Journal of Experimental Biology*, 2014. **217**(5): p. 639.
256. Gerloff, K., et al., *The Adverse Outcome Pathway approach in nanotoxicology*. *Computational Toxicology*, 2017. **1**: p. 3-11.
257. Nel, A., et al., *Nanomaterial toxicity testing in the 21st century: use of a predictive toxicological approach and high-throughput screening*. *Accounts of chemical research*, 2013. **46**(3): p. 607-621.
258. Drasler, B., et al., *In vitro approaches to assess the hazard of nanomaterials*. *NanoImpact*, 2017. **8**: p. 99-116.
259. Loza, K. and M. Epple, *Silver nanoparticles in complex media: an easy procedure to discriminate between metallic silver nanoparticles, reprecipitated silver chloride, and dissolved silver species*. *RSC Advances*, 2018. **8**(43): p. 24386-24391.
260. Mwilu, S.K., et al., *Separation and measurement of silver nanoparticles and silver ions using magnetic particles*. *Science of The Total Environment*, 2014. **472**: p. 316-323.

261. Thio, B.J., et al., *Mobility of capped silver nanoparticles under environmentally relevant conditions*. Environ Sci Technol, 2012. **46**(13): p. 6985-91.
262. Ali-Boucetta, H., et al., *Cellular uptake and cytotoxic impact of chemically functionalized and polymer-coated carbon nanotubes*. Small, 2011. **7**(22): p. 3230-8.
263. Larsson, P., et al., *Optimization of cell viability assays to improve replicability and reproducibility of cancer drug sensitivity screens*. Scientific Reports, 2020. **10**(1): p. 5798.
264. Bilberg, K., et al., *In Vivo Toxicity of Silver Nanoparticles and Silver Ions in Zebrafish (Danio rerio)* J Journal of Toxicology. 2012. **2012**: p. 9.
265. Kim, K.-T., et al., *Silver nanoparticle toxicity in the embryonic zebrafish is governed by particle dispersion and ionic environment*. Nanotechnology, 2013. **24**(11): p. 115101-115101.
266. Holder, A.L., et al., *Particle-Induced Artifacts in the MTT and LDH Viability Assays*. Chemical Research in Toxicology, 2012. **25**(9): p. 1885-1892.
267. Kumar, G., et al., *Flow cytometry evaluation of in vitro cellular necrosis and apoptosis induced by silver nanoparticles*. Food Chem Toxicol, 2015. **85**: p. 45-51.
268. Promega. *Technical bulletin, CytoTox 96® Non-Radioactive Cytotoxicity Assay*. 2016; Available from: <https://www.promega.com/-/media/files/resources/protocols/technical-bulletins/0/cytotox-96-nonradioactive-cytotoxicity-assay-protocol.pdf>.
269. Kumar, P., A. Nagarajan, and P.D. Uchil, *Analysis of Cell Viability by the Lactate Dehydrogenase Assay*. Cold Spring Harb Protoc, 2018. **2018**(6).
270. Xia, X., et al., *Emerging regulatory mechanisms and functions of autophagy in fish*. Aquaculture, 2019. **511**: p. 734212.
271. Séité, S., et al., *The Autophagic Flux Inhibitor Bafilomycine A1 Affects the Expression of Intermediary Metabolism-Related Genes in Trout Hepatocytes*. Frontiers in Physiology, 2019. **10**(263).
272. Dymowska, A.K., et al., *Acid-sensing ion channels are involved in epithelial Na⁺ uptake in the rainbow trout *Oncorhynchus mykiss**. American journal of physiology. Cell physiology, 2014. **307**(3): p. C255-C265.
273. Modrzyński, J.J., J.H. Christensen, and K.K. Brandt, *Evaluation of dimethyl sulfoxide (DMSO) as a co-solvent for toxicity testing of hydrophobic organic compounds*. Ecotoxicology, 2019. **28**(9): p. 1136-1141.
274. Palchadhuri, R., et al., *A Small Molecule that Induces Intrinsic Pathway Apoptosis with Unparalleled Speed*. Cell Reports, 2015. **13**(9): p. 2027-2036.
275. Belmokhtar, C.A., J. Hillion, and E. Ségal-Bendirdjian, *Staurosporine induces apoptosis through both caspase-dependent and caspase-independent mechanisms*. Oncogene, 2001. **20**(26): p. 3354-62.
276. Krumschnabel, G., et al., *Staurosporine-induced cell death in salmonid cells: the role of apoptotic volume decrease, ion fluxes and MAP kinase signaling*. Apoptosis, 2007. **12**(10): p. 1755-1768.
277. Kaszuba, M., et al., *Measuring sub nanometre sizes using dynamic light scattering*. Journal of Nanoparticle Research, 2008. **10**(5): p. 823-829.
278. Berrecoso, G., J. Crecente-Campo, and M.J. Alonso, *Unveiling the pitfalls of the protein corona of polymeric drug nanocarriers*. Drug Delivery and Translational Research, 2020. **10**(3): p. 730-750.
279. Pallavicini, P., et al., *Fast dissolution of silver nanoparticles at physiological pH*. Journal of Colloid and Interface Science, 2020. **563**: p. 177-188.

280. Zorova, L.D., et al., *Mitochondrial membrane potential*. Analytical biochemistry, 2018. **552**: p. 50-59.
281. Wang, F., et al., *Time resolved study of cell death mechanisms induced by amine-modified polystyrene nanoparticles*. Nanoscale, 2013. **5**(22): p. 10868-10876.
282. Li, M., et al., *Effects of molecular weight-fractionated natural organic matter on the phytoavailability of silver nanoparticles*. Environmental Science: Nano, 2018. **5**(4): p. 969-979.
283. Arora, S., et al., *Cellular responses induced by silver nanoparticles: In vitro studies*. Toxicology Letters, 2008. **179**(2): p. 93-100.
284. Turan, N.B., et al., *Nanoparticles in the aquatic environment: Usage, properties, transformation and toxicity—A review*. Process Safety and Environmental Protection, 2019. **130**: p. 238-249.
285. Walczyk, D., et al., *What the Cell “Sees” in Bionanoscience*. Journal of the American Chemical Society, 2010. **132**(16): p. 5761-5768.
286. Deng, Z.J., et al., *Molecular interaction of poly(acrylic acid) gold nanoparticles with human fibrinogen*. ACS Nano, 2012. **6**(10): p. 8962-9.
287. Ellis, L.-J.A., et al., *Seasonal variability of natural water chemistry affects the fate and behaviour of silver nanoparticles*. Chemosphere, 2018. **191**: p. 616-625.
288. Ellis, L.-J.A., E. Valsami-Jones, and I. Lynch, *Exposure medium and particle ageing moderate the toxicological effects of nanomaterials to Daphnia magna over multiple generations: a case for standard test review?* Environmental Science: Nano, 2020. **7**(4): p. 1136-1149.
289. Borm, P., et al., *Research Strategies for Safety Evaluation of Nanomaterials, Part V: Role of Dissolution in Biological Fate and Effects of Nanoscale Particles*. Toxicological Sciences, 2006. **90**(1): p. 23-32.
290. Yue, Y., et al., *Toxicity of silver nanoparticles to a fish gill cell line: Role of medium composition*. Nanotoxicology, 2015. **9**(1): p. 54-63.
291. Shi, J., et al., *Amino acid-dependent transformations of citrate-coated silver nanoparticles: Impact on morphology, stability and toxicity*. Toxicology Letters, 2014. **229**(1): p. 17-24.
292. Yue, Y., et al., *Silver nanoparticles inhibit fish gill cell proliferation in protein-free culture medium*. Nanotoxicology, 2016. **10**(8): p. 1075-1083.
293. Briffa, S.M., et al., *Uptake and impacts of polyvinylpyrrolidone (PVP) capped metal oxide nanoparticles on Daphnia magna: role of core composition and acquired corona*. Environmental Science: Nano, 2018. **5**(7): p. 1745-1756.
294. George, S., et al., *Surface defects on plate-shaped silver nanoparticles contribute to its hazard potential in a fish gill cell line and zebrafish embryos*. ACS nano, 2012. **6**(5): p. 3745-3759.
295. Degger, N., A.C.K. Tse, and R.S.S. Wu, *Silver nanoparticles disrupt regulation of steroidogenesis in fish ovarian cells*. Aquatic Toxicology, 2015. **169**: p. 143-151.
296. Yang, Y., et al., *Mechanism of cell death induced by silica nanoparticles in hepatocyte cells is by apoptosis*. International journal of molecular medicine, 2019. **44**(3): p. 903-912.
297. Book, F., et al., *Ecotoxicity screening of seven different types of commercial silica nanoparticles using cellular and organismic assays: Importance of surface and size*. NanoImpact, 2019. **13**: p. 100-111.

298. MacCuspie, R.I., *Chapter 4 - Characterization of Nanomaterials for NanoEHS Studies*, in *Nanotechnology Environmental Health and Safety (Third Edition)*, M.S. Hull and D.M. Bowman, Editors. 2018, William Andrew Publishing: Boston. p. 59-82.
299. Li, Z., et al., *Effect of size on dissolution thermodynamics of nanoparticles: A theoretical and experimental research*. Materials Chemistry and Physics, 2018. **214**: p. 499-506.
300. Gaiser, B.K., et al., *Interspecies comparisons on the uptake and toxicity of silver and cerium dioxide nanoparticles*. Environmental Toxicology and Chemistry, 2012. **31**(1): p. 144-154.
301. Teeguarden, J.G., et al., *Particokinetics in vitro: dosimetry considerations for in vitro nanoparticle toxicity assessments*. Toxicol Sci, 2007. **95**(2): p. 300-12.
302. Fehaid, A. and A. Taniguchi, *Size-Dependent Effect of Silver Nanoparticles on the Tumor Necrosis Factor α -Induced DNA Damage Response*. International journal of molecular sciences, 2019. **20**(5): p. 1038.
303. Krohne, T.U., et al., *Lipid peroxidation products reduce lysosomal protease activities in human retinal pigment epithelial cells via two different mechanisms of action*. Experimental Eye Research, 2010. **90**(2): p. 261-266.
304. Fehaid, A. and A. Taniguchi, *Silver nanoparticles reduce the apoptosis induced by tumor necrosis factor- α* . Sci Technol Adv Mater, 2018. **19**(1): p. 526-534.
305. Stern, S.T., P.P. Adisheshaiah, and R.M. Crist, *Autophagy and lysosomal dysfunction as emerging mechanisms of nanomaterial toxicity*. Particle and Fibre Toxicology, 2012. **9**(1): p. 20.
306. Khan, M.I., et al., *Induction of ROS, mitochondrial damage and autophagy in lung epithelial cancer cells by iron oxide nanoparticles*. Biomaterials, 2012. **33**(5): p. 1477-1488.
307. Kroemer, G. and M. Jäättelä, *Lysosomes and autophagy in cell death control*. Nat Rev Cancer, 2005. **5**(11): p. 886-97.
308. Van Houten, B., S.E. Hunter, and J.N. Meyer, *Mitochondrial DNA damage induced autophagy, cell death, and disease*. Frontiers in bioscience (Landmark edition), 2016. **21**: p. 42-54.
309. Zhao, H., et al., *Titanium Dioxide Nanoparticles Induce Mitochondrial Dynamic Imbalance and Damage in HT22 Cells J Journal of Nanomaterials*. 2019. **2019**: p. 16.
310. Repnik, U., M.H. Cesen, and B. Turk, *The endolysosomal system in cell death and survival*. Cold Spring Harb Perspect Biol, 2013. **5**(1): p. a008755.
311. Pereira, A.C., et al., *The zebrafish embryotoxicity test (ZET) for nanotoxicity assessment: from morphological to molecular approach*. Environmental Pollution, 2019. **252**: p. 1841-1853.
312. Chakraborty, C., et al., *Zebrafish: A complete animal model to enumerate the nanoparticle toxicity*. Journal of nanobiotechnology, 2016. **14**(1): p. 65-65.
313. Schaeck, M., et al., *Fish as research tools: alternatives to in vivo experiments*. Altern Lab Anim, 2013. **41**(3): p. 219-29.
314. Tanneberger, K., et al., *Predicting fish acute toxicity using a fish gill cell line-based toxicity assay*. Environ Sci Technol, 2013. **47**(2): p. 1110-9.
315. Handy, R.D., et al., *Proposal for a tiered dietary bioaccumulation testing strategy for engineered nanomaterials using fish*. Environmental Science: Nano, 2018. **5**(9): p. 2030-2046.

316. Lewinski, N.A., *Nanoparticle Cytotoxicity*, in *Encyclopedia of Nanotechnology*, B. Bhushan, Editor. 2012, Springer Netherlands: Dordrecht. p. 1644-1651.
317. Görlach, A., et al., *Calcium and ROS: A mutual interplay*. Redox biology, 2015. **6**: p. 260-271.
318. Cheng, X., et al., *Calcium signaling in membrane repair*. Seminars in cell & developmental biology, 2015. **45**: p. 24-31.
319. Rizzuto, R., et al., *Ca²⁺ signaling, mitochondria and cell death*. Current molecular medicine, 2008. **8**(2): p. 119-130.
320. Adiele, R.C., D. Stevens, and C. Kamunde, *Cadmium- and calcium-mediated toxicity in rainbow trout (*Oncorhynchus mykiss*) in vivo: Interactions on fitness and mitochondrial endpoints*. Chemosphere, 2011. **85**(10): p. 1604-1613.
321. Cooke, M.S., et al., *Oxidative DNA damage: mechanisms, mutation, and disease*. The FASEB Journal, 2003. **17**(10): p. 1195-1214.
322. Singh, N., et al., *Exposure to Engineered Nanomaterials: Impact on DNA Repair Pathways*. International journal of molecular sciences, 2017. **18**(7): p. 1515.
323. Hsiao, I.L. and Y.-J. Huang, *Effects of serum on cytotoxicity of nano- and micro-sized ZnO particles*. Journal of nanoparticle research : an interdisciplinary forum for nanoscale science and technology, 2013. **15**(9): p. 1829-1829.
324. Nel, A.E., et al., *Understanding biophysicochemical interactions at the nano-bio interface*. Nat Mater, 2009. **8**(7): p. 543-57.
325. Monopoli, M.P., et al., *Biomolecular coronas provide the biological identity of nanosized materials*. Nat Nanotechnol, 2012. **7**(12): p. 779-86.
326. Christine Labno. *Basic Intensity Quantification with ImageJ*. 2018; Available from: <https://www.unige.ch/medecine/bioimaging/files/1914/1208/6000/Quantification.pdf>.
327. AAT Bioquest. *Screen Quest™ Fluo-8 Medium Removal Calcium Assay Kit*. 2008; Available from: <https://www.aatbio.com/products/screen-quest-fluo-8-medium-removal-calcium-assay-kit-optimized-for-difficult-cell-lines>.
328. Kusakabe, H. and H. Tateno, *Shortening of alkaline DNA unwinding time does not interfere with detecting DNA damage to mouse and human spermatozoa in the comet assay*. Asian journal of andrology, 2011. **13**(1): p. 172-174.
329. Kim, J.A., et al., *Role of cell cycle on the cellular uptake and dilution of nanoparticles in a cell population*. Nature Nanotechnology, 2012. **7**(1): p. 62-68.
330. Suvarna, M., et al., *Understanding the Stability of Nanoparticle–Protein Interactions: Effect of Particle Size on Adsorption, Conformation and Thermodynamic Properties of Serum Albumin Proteins*. ACS Applied Nano Materials, 2018. **1**(10): p. 5524-5535.
331. Murdock, R.C., et al., *Characterization of Nanomaterial Dispersion in Solution Prior to In Vitro Exposure Using Dynamic Light Scattering Technique*. Toxicological Sciences, 2007. **101**(2): p. 239-253.
332. Shannahan, J.H., et al., *Silver Nanoparticle Protein Corona Composition in Cell Culture Media*. PLOS ONE, 2013. **8**(9): p. e74001.
333. Halamoda-Kenzaoui, B., et al., *Dispersion Behaviour of Silica Nanoparticles in Biological Media and Its Influence on Cellular Uptake*. PLOS ONE, 2015. **10**(10): p. e0141593.
334. Montes-Burgos, I., et al., *Characterisation of nanoparticle size and state prior to nanotoxicological studies*. Journal of Nanoparticle Research, 2010. **12**(1): p. 47-53.
335. Moore, T.L., et al., *Nanoparticle administration method in cell culture alters particle-cell interaction*. Scientific Reports, 2019. **9**(1): p. 900.

336. Jiang, H.S., et al., *Interaction between Silver Nanoparticles and Two Dehydrogenases: Role of Thiol Groups*. *Small*, 2019. **15**: p. 1900860.
337. Foldbjerg, R., et al., *Silver nanoparticles – wolves in sheep's clothing?* *Toxicology Research*, 2015. **4**(3): p. 563-575.
338. Lesniak, A., et al., *Effects of the Presence or Absence of a Protein Corona on Silica Nanoparticle Uptake and Impact on Cells*. *ACS Nano*, 2012. **6**(7): p. 5845-5857.
339. Guggenheim, E.J., et al., *Refining in vitro models for nanomaterial exposure to cells and tissues*. *NanoImpact*, 2018. **10**: p. 121-142.
340. Tekie, F.S.M., et al., *Controlling evolution of protein corona: a prosperous approach to improve chitosan-based nanoparticle biodistribution and half-life*. *Scientific Reports*, 2020. **10**(1): p. 9664.
341. Abdelkhalik, A., et al., *Impact of nanoparticle surface functionalization on the protein corona and cellular adhesion, uptake and transport*. *Journal of Nanobiotechnology*, 2018. **16**(1): p. 70.
342. Quevedo, A.C., I. Lynch, and E. Valsami-Jones, *Silver nanoparticle induced toxicity and cell death mechanisms in embryonic zebrafish cells*. *Nanoscale*, 2021. **13**(12): p. 6142-6161.
343. Fröhlich, E., *Cellular elimination of nanoparticles*. *Environmental Toxicology and Pharmacology*, 2016. **46**: p. 90-94.
344. Panariti, A., G. Misericchi, and I. Rivolta, *The effect of nanoparticle uptake on cellular behavior: disrupting or enabling functions?* *Nanotechnology, science and applications*, 2012. **5**: p. 87-100.
345. Huang, C.-C., et al., *Oxidative stress, calcium homeostasis, and altered gene expression in human lung epithelial cells exposed to ZnO nanoparticles*. *Toxicology in Vitro*, 2010. **24**(1): p. 45-55.
346. Manke, A., L. Wang, and Y. Rojanasakul, *Mechanisms of nanoparticle-induced oxidative stress and toxicity*. *Biomed Res Int*, 2013. **2013**: p. 942916.
347. Kiselyov, K. and S. Muallem, *ROS and intracellular ion channels*. *Cell calcium*, 2016. **60**(2): p. 108-114.
348. Lin, C.-H. and P.-P. Hwang, *The Control of Calcium Metabolism in Zebrafish (Danio rerio)*. *International journal of molecular sciences*, 2016. **17**(11): p. 1783.
349. Wyrsh, P., et al., *Cytosolic Ca²⁺ shifts as early markers of cytotoxicity*. *Cell Communication and Signaling*, 2013. **11**(1): p. 11.
350. Orrenius, S., B. Zhivotovsky, and P. Nicotera, *Regulation of cell death: the calcium–apoptosis link*. *Nature Reviews Molecular Cell Biology*, 2003. **4**(7): p. 552-565.
351. Li, L., et al., *Silver nanoparticles and silver ions cause inflammatory response through induction of cell necrosis and the release of mitochondria in vivo and in vitro*. *Cell Biol Toxicol*, 2020.
352. Torigoe, H., et al., *Thermodynamic Properties of the Specific Binding Between Ag⁺ Ions and C:C Mismatched Base Pairs in Duplex DNA*. *Nucleosides, Nucleotides & Nucleic Acids*, 2011. **30**(2): p. 149-167.
353. Bastos, V., et al., *A study of the effects of citrate-coated silver nanoparticles on RAW 264.7 cells using a toolbox of cytotoxic endpoints*. *Journal of Nanoparticle Research*, 2017. **19**(5): p. 163.

354. Eom, H.-J. and J. Choi, *p38 MAPK Activation, DNA Damage, Cell Cycle Arrest and Apoptosis As Mechanisms of Toxicity of Silver Nanoparticles in Jurkat T Cells*. Environmental Science & Technology, 2010. **44**(21): p. 8337-8342.
355. Foldbjerg, R., et al., *Global Gene Expression Profiling of Human Lung Epithelial Cells After Exposure to Nanosilver*. Toxicological Sciences, 2012. **130**(1): p. 145-157.
356. Wang, X.W., et al., *GADD45 induction of a G2/M cell cycle checkpoint*. Proc Natl Acad Sci U S A, 1999. **96**(7): p. 3706-11.
357. Martinez-Finley, E.J., et al., *Cellular transport and homeostasis of essential and nonessential metals*. Metallomics, 2012. **4**(7): p. 593-605.
358. Kettler, K., et al., *Exploring the effect of silver nanoparticle size and medium composition on uptake into pulmonary epithelial 16HBE14o-cells*. Journal of Nanoparticle Research, 2016. **18**(7): p. 182.
359. Fabricius, A.-L., et al., *ICP-MS-based characterization of inorganic nanoparticles--sample preparation and off-line fractionation strategies*. Analytical and bioanalytical chemistry, 2014. **406**(2): p. 467-479.
360. Ellis, L.-J.A., et al., *Multigenerational Exposures of Daphnia Magna to Pristine and Aged Silver Nanoparticles: Epigenetic Changes and Phenotypical Ageing Related Effects*. Small (Weinheim an der Bergstrasse, Germany), 2020. **16**(21): p. e2000301.
361. Docter, D., et al., *Quantitative profiling of the protein coronas that form around nanoparticles*. Nature Protocols, 2014. **9**(9): p. 2030-2044.
362. Dutta, D. and J.G. Donaldson, *Search for inhibitors of endocytosis: Intended specificity and unintended consequences*. Cellular logistics, 2012. **2**(4): p. 203-208.
363. ZFIN. *The Zebrafish Information Network*. 2021; Available from: <https://zfin.org>.
364. Nasser, F. and I. Lynch, *Secreted protein eco-corona mediates uptake and impacts of polystyrene nanoparticles on Daphnia magna*. Journal of Proteomics, 2016. **137**: p. 45-51.
365. Maiorano, G., et al., *Effects of cell culture media on the dynamic formation of protein-nanoparticle complexes and influence on the cellular response*. ACS Nano, 2010. **4**(12): p. 7481-91.
366. Cedervall, T., et al., *Understanding the nanoparticle-protein corona using methods to quantify exchange rates and affinities of proteins for nanoparticles*. Proceedings of the National Academy of Sciences, 2007. **104**(7): p. 2050-2055.
367. Durán, N., et al., *Silver nanoparticle protein corona and toxicity: a mini-review*. Journal of Nanobiotechnology, 2015. **13**(1): p. 55.
368. Bury, N.R., et al., *ATP-Dependent Silver Transport across the Basolateral Membrane of Rainbow Trout Gills*. Toxicology and Applied Pharmacology, 1999. **159**(1): p. 1-8.
369. Jovic, M., et al., *The early endosome: a busy sorting station for proteins at the crossroads*. Histology and histopathology, 2010. **25**(1): p. 99-112.
370. Sabella, S., et al., *A general mechanism for intracellular toxicity of metal-containing nanoparticles*. Nanoscale, 2014. **6**(12): p. 7052-7061.
371. Balfourier, A., et al., *Unexpected intracellular biodegradation and recrystallization of gold nanoparticles*. 2020. **117**(1): p. 103-113.
372. Xia, L., et al., *Endocytosed nanoparticles hold endosomes and stimulate binucleated cells formation*. Particle and Fibre Toxicology, 2016. **13**(1): p. 63.
373. Manshian, B.B., et al., *The impact of nanoparticle-driven lysosomal alkalization on cellular functionality*. Journal of nanobiotechnology, 2018. **16**(1): p. 85-85.

374. Wang, Z., et al., *Size and dynamics of caveolae studied using nanoparticles in living endothelial cells*. ACS nano, 2009. **3**(12): p. 4110-4116.
375. Birgisdottir Å, B. and T. Johansen, *Autophagy and endocytosis - interconnections and interdependencies*. J Cell Sci, 2020. **133**(10).
376. Anozie, U.C. and P. Dalhaimer, *Molecular links among non-biodegradable nanoparticles, reactive oxygen species, and autophagy*. Advanced Drug Delivery Reviews, 2017. **122**: p. 65-73.
377. Auclair, J., et al., *The influence of surface coatings on the toxicity of silver nanoparticle in rainbow trout*. Comparative Biochemistry and Physiology Part C: Toxicology & Pharmacology, 2019. **226**: p. 108623.
378. Vevers, W.F. and A.N. Jha, *Genotoxic and cytotoxic potential of titanium dioxide (TiO₂) nanoparticles on fish cells in vitro*. Ecotoxicology, 2008. **17**(5): p. 410-20.
379. Kniewald, J., et al., *Alternative models for toxicity testing of xenobiotics*. Arh Hig Rada Toksikol, 2005. **56**(2): p. 195-204.
380. Hansen, U. and A.F. Thünemann, *Characterization of Silver Nanoparticles in Cell Culture Medium Containing Fetal Bovine Serum*. Langmuir, 2015. **31**(24): p. 6842-6852.
381. Sun, J., et al., *Effect of particle size on solubility, dissolution rate, and oral bioavailability: evaluation using coenzyme Q₁₀ as naked nanocrystals*. International journal of nanomedicine, 2012. **7**: p. 5733-5744.
382. Odzak, N., et al., *Dissolution of metal and metal oxide nanoparticles in aqueous media*. Environmental Pollution, 2014. **191**: p. 132-138.
383. Steinmetz, L., et al., *A comparative study of silver nanoparticle dissolution under physiological conditions*. Nanoscale Advances, 2020. **2**(12): p. 5760-5768.
384. Clark, N.J., et al., *Development of a suitable detection method for silver nanoparticles in fish tissue using single particle ICP-MS*. Environmental Science: Nano, 2019. **6**(11): p. 3388-3400.
385. Jiang, X., et al., *Fast intracellular dissolution and persistent cellular uptake of silver nanoparticles in CHO-K1 cells: implication for cytotoxicity*. Nanotoxicology, 2015. **9**(2): p. 181-189.
386. Han, X., et al., *Validation of an LDH assay for assessing nanoparticle toxicity*. Toxicology, 2011. **287**(1-3): p. 99-104.
387. Jafari, M., et al., *Comparison of in-gel protein separation techniques commonly used for fractionation in mass spectrometry-based proteomic profiling*. Electrophoresis, 2012. **33**(16): p. 2516-2526.
388. Haida, Z. and M. Hakimian, *A comprehensive review on the determination of enzymatic assay and nonenzymatic antioxidant activities*. Food science & nutrition, 2019. **7**(5): p. 1555-1563.
389. Redmann, M., et al., *Methods for assessing mitochondrial quality control mechanisms and cellular consequences in cell culture*. Redox Biology, 2018. **17**: p. 59-69.
390. Bin-Jumah, M., et al., *Effects of Green Silver Nanoparticles on Apoptosis and Oxidative Stress in Normal and Cancerous Human Hepatic Cells in vitro*. International Journal of Nanomedicine, 2020. **Volume 15**.
391. Awasthi, K.K., et al., *Silver nanoparticle induced cytotoxicity, oxidative stress, and DNA damage in CHO cells*. Journal of Nanoparticle Research, 2013. **15**(9): p. 1898.
392. REACH. *Updated guidance for registering substances in nanoform*. 2020; Available from: <https://echa.europa.eu/-/updated-guidance-for-registering-substances-in-nanoform>.


393. Clark, N.J., D. Boyle, and R.D. Handy, *An assessment of the dietary bioavailability of silver nanomaterials in rainbow trout using an ex vivo gut sac technique*. *Environmental Science: Nano*, 2019. **6**(2): p. 646-660.
394. Dong, F., et al., *Experimental evolution of Pseudomonas putida under silver ion versus nanoparticle stress*. *Environ Microbiol*, 2021.
395. Chen, L., et al., *Skin Toxicity Assessment of Silver Nanoparticles in a 3D Epidermal Model Compared to 2D Keratinocytes*. *International journal of nanomedicine*, 2019. **14**: p. 9707-9719.
396. McCormick, S.C., et al., *The Use of Microfluidics in Cytotoxicity and Nanotoxicity Experiments*. *Micromachines*, 2017. **8**(4): p. 124.
397. Gerritzen, M.J.H., et al., *High throughput nanoparticle tracking analysis for monitoring outer membrane vesicle production*. *Journal of extracellular vesicles*, 2017. **6**(1): p. 1333883-1333883.

7. SI Chapter 2

Silver nanoparticle induced toxicity and cell death mechanisms in embryonic zebrafish cells

Ana C. Quevedo, Iseult Lynch*, Eugenia Valsami-Jones

School of Geography, Earth and Environmental Sciences, University of Birmingham, Edgbaston, Birmingham, B15 2TT, UK.

Corresponding author: * 

7.1 Methodology

7.1.1 Characterisation of AgNPs: detailed methodology

Samples for Transmission Electron Microscopy (TEM) were prepared by diluting the stock suspension (1000 $\mu\text{g}/\text{mL}$) with ultrapure water to a final concentration of 100 $\mu\text{g}/\text{mL}$. The diluted suspension (15 μL) was immediately loaded onto a 200 mesh Formvar coated copper grid (Agar Scientific, AGS138). After 2 hours the sample was gently washed with ultrapure water and left to dry for 24 hours inside a plastic tray to avoid dust.

Samples for Nanoparticle Tracking Analysis (NTA) (NS300, Malvern) were prepared by diluting 5 μL of the AgNP stock suspension (1000 $\mu\text{g}/\text{mL}$) in 20 mL of ultrapure water for a final concentration of 0.25 $\mu\text{g}/\text{mL}$. Then 1 mL of the diluted suspension was added to 19 mL of ultrapure water, to achieve a final working solution concentration of 0.012 $\mu\text{g}/\text{mL}$. Afterwards, 1 mL of the diluted NP suspension was loaded into the syringe pump and flushed into the NTA chamber at a 1000 seconds injection time. As soon as the NPs were visualized the flow interval was changed to 50 seconds (circa 5.2 $\mu\text{L}/\text{min}$ [397]). The video was recorded and then analysed using the automatic settings of the NTA. The auto setup sets the camera level for standard measurement runs, including the autofocus and optimum camera level as follows: screen gain 1.0 and camera level 7. It is important to mention that these setting may vary depending on the brightness and concentration of

the analysed sample, it is recommended to use a minimum concentration of 10^9 particles per mL to ensure the detection of the sample as suggested in the NTA user manual. The equipment's temperature was set to room temperature (22 °C). For further information the reader is directed to the manual for the NanoSight NS300 instrument.

Samples for Dynamic Light Scattering (DLS) (Zetasizer Nano ZS, Malvern) were prepared at a final concentration of 10 µg/mL in 1 mL of either ultrapure water (UPW) or complete cell medium (CCM) containing 10% foetal bovine serum (FBS). The hydrodynamic diameter was analysed as soon as the samples were prepared (7 runs per sample), afterwards the samples in the DLS cuvettes were incubated at 28°C for 24 hours, then the hydrodynamic diameter was recorded again. Results are representative of the average of three independent experiments, each measurement includes the average of 7 DLS runs. The instrument software was v3.30 and the measurements were recorded by selecting parameters according to the type of measurement (size or zeta potential) and the physical properties of the AgNPs, i.e., refractive index 0.135 and absorption index (k) 3.99. The equipment's temperature was set to 22 °C.

7.2 Results

7.2.1 Characterisation of the AgNPs

Table S7.1. Characterisation of AgNPs by TEM and NTA. The table shows the summary of the results obtained in the assessment of the core size by TEM and hydrodynamic diameter by NTA. The AgNPs were only prepared in ultrapure water (UPW) (n=1). See detailed methodology in section 2.3.1 for further details about the sample preparation and working concentrations for each sample.

	Water		
AgNPs size	10 nm	30 nm	100 nm
TEM	13 ± 2.4	34 ± 2.8	101.6 ± 9.2
Hydrodynamic diameter (NTA)	35.9 ± 11.7	37.8 ± 7.4	107 ± 10.4

Abbreviations: Nanoparticle tracking Analysis (NTA), Transmission electron microscopy (TEM).

Table S7.2. Characterisation of the NPs and cell medium by DLS. The cell medium was supplemented with 10% FBS and measured after 0 and 24 hours of incubation. The table shows the mean and standard deviation (SD) of three individual samples (mean \pm SD). No statistical differences between timepoints were found for the cell medium alone. The characterisation of the AgNPs in cell medium shows the size, zeta potential and PDI at 0 and 24 hours using three different AgNPs concentrations (2.5, 5 and 10 $\mu\text{g/mL}$) in cell medium supplemented with 10% Foetal Bovine Serum (FBS). Data with similar letters (upper and lowercase) indicate a statistically significant difference ($p < 0.05$) between time points (0 and 24 hours) for each NP size at the same concentration. Identical symbols denote a statistically significant difference ($p < 0.05$) in the hydrodynamic size between the selected NP sizes.

Cell medium (CCM)							
Time	Hydrodynamic diameter (nm)		Zeta potential (mV)		Polydispersity index (PDI)		
	Result	SD	Result	SD	Result	SD	
0 hours	13.61	2.29	14.72	0.52	0.51	0.05	
24 hours	13.85	1.49	14.13	0.33	0.41	0.00	
AgNPs							
AgNPs size	Time	AgNPs concentration $\mu\text{g/mL}$					
		2.5		5		10	
Hydrodynamic diameter (nm)							
		Result	SD	Result	SD	Result	SD
10 nm	0 hours	87.94	11.26	88.98	15.26	113.70	3.40*E
	24 hours	107.4	3.22\$	105.67	2.12	99.20	1.02 e@
30 nm	0 hours	92.87	3.71	98.68	3.64	106.06	4.85
	24 hours	90.29	3.65 %	92.66	7.33 \$	92.21	0.13 @
100 nm	0 hours	143.97	2.51F	144.43	1.07 G	140.93	0.92
	24 hours	152.63	4.97 f %	155.07	0.12 g\$	156.66	3.97 @
Zeta potential (mV)							
10 nm	0 hours	-10.11	1.44	-7.31	0.59	-8.13	1.19
	24 hours	-10.55	1.23	-10.14	0.84	-10.20	0.56
30 nm	0 hours	-6.99	0.55	-6.47	1.44	-8.03	1.05
	24 hours	-12.13	1.20	-11.73	1.10	-12.30	1.57
100 nm	0 hours	-6.70	1.10	-6.25	0.90	-7.01	1.36
	24 hours	-11.00	0.46	-12.33	1.44	-11.77	1.05

Polydispersity index							
10 nm	0 hours	0.57	0.02	0.54	0.03	0.43	0.02
	24 hours	0.57	0.01	0.52	0.01	0.40	0.01
30 nm	0 hours	0.5	0.01	0.46	0.04	0.32	0.02
	24 hours	0.54	0.03	0.43	0.03	0.37	0.01
100 nm	0 hours	0.07	0.02	0.07	0.01	0.04	0.01
	24 hours	0.14	0.02	0.12	0.01	0.08	0.00

Table S7.3. Characterisation of the AgNPs in ultrapure water by DLS. The table shows the characterisation of the size, zeta potential and PDI at 0 and 24 hours using three different AgNPs concentrations (2.5, 5 and 10 µg/mL) in ultra-pure water. Data represents the mean ± SD) three individual replicates. Data with similar letters (upper and lowercase) indicate a statistically significant difference ($p < 0.05$) between time points (0 and 24 hours) for each NP size at the same concentration. Identical symbols after the values denote statistical difference ($p < 0.05$) in the hydrodynamic size between the selected NP sizes.

AgNPs size	Time	AgNPs concentration µg/mL					
		2.5		5		10	
Hydrodynamic diameter (nm)							
		Result	STDV	Result	STDV	Result	STDV
10 nm	0 hours	64.05	9.36	64.18	1.71 A	69.58	8.37
	24 hours	76.3	5.95	75.06	3.6 ja	67.58	8.71 ñ
30 nm	0 hours	56.18	3.13	71.9	0.14	72.02	0.50 ñb
	24 hours	60.06	7.00	70.22	6.07	59.73	2.03 B
100 nm	0 hours	102.27	0.75 C	105.38	0.11	139.47	3.89
	24 hours	107.26	0.04 c	105.08	1.78 j	137.63	1.07
Zeta potential (mV)							
10 nm	0 hours	-8.16	0.79	-6.99	0.25	-8.70	0.95
	24 hours	-7.48	2.52	-9.40	0.42	-10.15	0.78
30 nm	0 hours	-6.77	0.56	-6.86	1.80	-7.42	2.55
	24 hours	-7.75	0.78	-8.30	1.13	-9.95	0.78
100 nm	0 hours	-5.64	0.04	-6.34	1.26	-7.75	0.69
	24 hours	-9.95	0.78	-8.30	2.26	-10.80	1.41
Polydispersity index							
10 nm	0 hours	0.13	0.02	0.14	0	0.12	0.03
	24 hours	0.32	0	0.15	0.01	0.29	0.04
30 nm	0 hours	0.15	0.03	0.25	0.03	0.2	0.00
	24 hours	0.26	0.01	0.21	0.01	0.3	0.05
100 nm	0 hours	0.2	0.00	0.25	0.04	0.4	0.01
	24 hours	0.32	0.02	0.35	0.05	0.36	0.01

7.2.2 Dissolution of the AgNPs in water and CCM.

The possible interactions of the filters with ionic Ag in water and in cell culture medium (CCM, DMEM-F12, supplemented with 10% FBS) was evaluated by preparing a stock suspension of 2 µg/mL of Ag as AgNO₃ (highest exposure concentration used in the biological assays) in both testing media. The samples were centrifugated at 20,817 x g for 5 and 30 minutes respectively. This procedure was repeated twice for samples in CCM, including 2 additional washes (500 µL) between centrifugations. The total Ag concentrations after centrifugation were diluted 20-fold and then analysed by ICP-MS. Results after dilution demonstrated a recovery of Ag >95% compared to the initial concentration; therefore, corrections were not applied for these results.

Sample	Total Ag µg/mL
CCM	1.90 ± 0.03
Water	1.93 ± 0.01

Table S7.4. Dissolution of the AgNPs. Dissolved fraction of the AgNPs was determined after centrifugation of the AgNPs in either UPW or CCM (DMEM-F12 supplemented with 10% FBS) at different time points. Results show the mean of three individual replicates (n = 3) and their standard deviation (mean ± SD). Data for the total Ag measured by ICP-MS are expressed in µg/mL. The percentage (%) of dissolved silver (or % of free silver ions) was obtained after dividing the final concentration values by the initial concentration and multiplying by 100%. The maximum dissolution rate (Max. Diss. rate) was obtained from the initial slopes of the raw data. This is presented as µg mL⁻¹ h⁻¹.

Time in hours	UPW samples											
	10 nm				30 nm				100 nm			
	Ag mean µg/mL	STDV	Dissolved Ag %	Max. Diss rate (MDR) µg mL ⁻¹ h ⁻¹	Ag mean µg/mL	STDV	Dissolved Ag %	Max. Diss rate (MDR) µg mL ⁻¹ h ⁻¹	Ag mean µg/mL	STDV	Dissolved Ag %	Max. Diss rate (MDR) µg mL ⁻¹ h ⁻¹
0.25	0.53	0.01	5.3	0.827	0.163	0.18	1.6	0.583	0.0025	0.002	0.03	0.021
0.5	0.927	0.07	9.3	0.749	0.591	0.06	5.9	0.515	0.0126	0.003	0.13	0.018
1	1.259	0.06	12.6	0.603	0.694	0.01	6.9	0.390	0.0207	0.004	0.21	0.013
1.5	1.43	0.01	14.3	0.472	0.828	0.04	8.3	0.281	0.0233	0.004	0.23	0.008
2	1.559	0.03	15.6	0.357	0.87	0.03	8.7	0.186	0.0238	0.001	0.24	0.005
4	2.034	0.01	20.3	0.049	1.068	0.25	10.7	0.045	0.025	0.001	0.25	0.004
8	2.124	0.2	21.2	0.167	1.074	0.02	10.7	0.2061	0.025	0.001	0.25	0.017
	CCM samples											
	10 nm				30 nm				100 nm			

Time in hours	Ag mean $\mu\text{g/mL}$	SD	Dissolved Ag %	Max. Diss rate $\mu\text{g mL}^{-1} \text{h}^{-1}$	Ag mean $\mu\text{g/mL}$	SD	Dissolved Ag %	Max. Diss rate $\mu\text{g mL}^{-1} \text{h}^{-1}$	Ag mean $\mu\text{g/mL}$	SD	Dissolved Ag %	Max. Diss rate $\mu\text{g mL}^{-1} \text{h}^{-1}$
0.25	0.104	0.01	1.0	0.090	0.096	0.041	1.0	0.038	0.0303	0.011	0.30	0.103
0.5	0.173	0.02	1.7	0.078	0.135	0.015	1.4	0.030	0.0398	0.005	0.40	0.061
1	0.207	0.06	2.1	0.056	0.114	0.024	1.1	0.016	0.0441	0.03	0.44	0.013
1.5	0.195	0.04	1.9	0.038	0.132	0.009	1.3	0.005	0.0426	0.035	0.43	0.076
2	0.209	0.02	2.1	0.021	0.134	0.01	1.3	0.005	0.0622	0.012	0.62	0.126
4	0.224	0.01	2.2	0.016	0.1	0.022	1.0	0.022	0.438	0.11	4.38	0.208
8	0.202	0.01	2.0	0.038	0.109	0.013	1.1	0.044	0.514	0.291	5.14	0.205

7.2.2.1 Maximum dissolution rate

The maximum dissolution rate of the AgNPs was obtained by assuming a first order kinetic equation. For this, a curve was plotted using the measured ionic Ag concentrations versus time in hours (*hrs*) (see example):

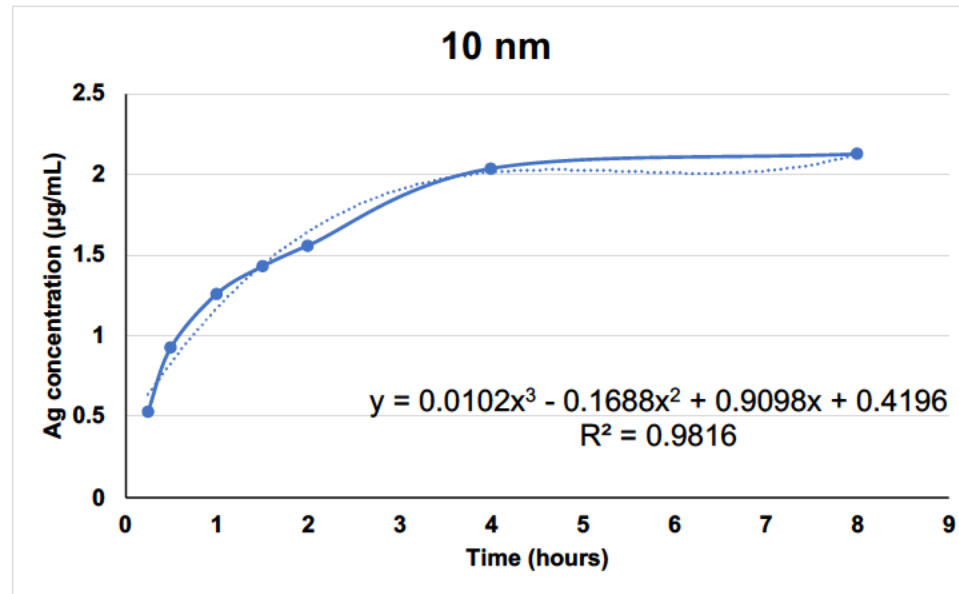


Figure S7.1. Curve and equation to obtain the maximum dissolution rate. A trendline was added, then the R^2 and equation were displayed on the plot. Finally, the equation was derived as shown below and the maximum dissolution rate (MDR) was calculated. See the example for the 10 nm sized AgNP at 0.25 hours.

- a) $y = 0.0102t^3 - 0.1688t^2 + 0.9098 + 0.4196$
- b) *derived equation* = $0.0306 * hrs^2 - 0.3376 * hrs + 0.9098$
- c) $MDR = 0.0306 * 0.25 - 0.3376 * 0.25 + 0.9098$
- d) $MDR = 0.82 \mu\text{g mL}^{-1} \text{ h}^{-1}$

7.2.3 Cell viability: LDH assay

Table S7.5. LDH raw data for ZF4 cells exposed to AgNPs of different sizes. The table shows the raw data in arbitrary units (A.U) for the LDH experiments. Cells were exposed to several concentrations (2.5, 5 and 10 µg/mL) and sizes 10, 30 and 100 nm of AgNPs. No statistical analyses were performed for the raw data.

		AgNPs								
Time	Conc. µg/mL	10 nm			30 nm			100 nm		
		R1	R2	R3	R1	R2	R3	R1	R2	R3
3 hours	Naive	0.099	0.106	0.101	0.151	0.144	0.162	0.265	0.265	0.273
	5	0.107	0.107	0.107	0.147	0.142	0.151	0.252	0.261	0.261
	10	0.103	0.103	0.103	0.134	0.139	0.162	0.261	0.26	0.258
	20	0.101	0.101	0.101	0.13	0.123	0.131	0.261	0.269	0.263
	30	0.103	0.103	0.103	0.132	0.117	0.121	0.19	0.222	0.227
	40	0.101	0.101	0.101	0.111	0.112	0.107	0.211	0.201	0.197
	60	0.102	0.102	0.102	0.093	0.086	0.109	0.181	0.192	0.186
24 hours	Naive	0.474	0.474	0.474	0.245	0.225	0.23	0.386	0.42	0.383
	5	0.308	0.308	0.308	0.176	0.176	0.176	0.346	0.379	0.325
	10	0.212	0.212	0.212	0.158	0.158	0.158	0.242	0.242	0.242
	20	0.159	0.141	0.153	0.102	0.102	0.102	0.209	0.238	0.168
	30	0.134	0.155	0.136	0.107	0.107	0.107	0.151	0.153	0.142
	40	0.123	0.098	0.105	0.098	0.098	0.098	0.126	0.117	0.102
	60	0.083	0.087	0.074	0.096	0.096	0.096	0.097	0.109	0.083
48 hours	Naive	0.38	0.408	0.417	0.355	0.398	0.453	0.36	0.359	0.355
	5	0.146	0.171	0.159	0.157	0.179	0.159	0.229	0.188	0.194
	10	0.145	0.145	0.145	0.195	0.143	0.157	0.124	0.113	0.095
	20	0.141	0.141	0.141	0.117	0.124	0.126	0.087	0.088	0.074

	30	0.122	0.124	0.12	0.09	0.112	0.116	0.072	0.074	0.063
	40	0.114	0.115	0.115	0.093	0.117	0.098	0.068	0.068	0.07
	60	0.085	0.082	0.083	0.088	0.078	0.089	0.072	0.06	0.073
72 hours	Naive	0.305	0.463	0.413	0.398	0.345	0.426	0.529	0.419	0.482
	5	0.057	0.075	0.075	0.084	0.157	0.076	0.286	0.265	0.1
	10	0.072	0.058	0.068	0.09	0.096	0.11	0.125	0.123	0.37
	20	0.062	0.059	0.06	0.083	0.089	0.082	0.067	0.071	0.065
	30	0.066	0.05	0.082	0.086	0.093	0.079	0.062	0.06	0.065
	40	0.059	0.06	0.057	0.078	0.079	0.105	0.063	0.064	0.091
	60	0.055	0.056	0.057	0.058	0.078	0.057	0.058	0.057	0.061

Table S7.6. Raw data for AgNO₃ treatments. The table shows the raw data from the LDH experiments in arbitrary units (A.U) for the LDH. Cells were exposed to several concentrations of AgNO₃ (1, 1.5 and 2 µg/mL) for 3, 6, 12, 24 and 72 hours. R: means replicate. No statistical analyses were performed for the raw data.

AgNO₃									
Time	Conc. µg/mL	R1	R2	R3	Time	Conc. µg/mL	R1	R2	R3
3 hours	Naive	0.116	0.112	0.108	24 hours	Naive	0.405	0.405	0.405
	0.5	0.111	0.109	0.113		0.5	0.403	0.403	0.403
	1	0.113	0.106	0.116		1	0.35	0.35	0.35
	2	0.116	0.109	0.107		2	0.198	0.198	0.198
	3	0.081	0.085	0.108		3	0.09	0.09	0.09
	5	0.07	0.063	0.053		5	0.067	0.067	0.067
	8	0.064	0.063	0.055		8	0.057	0.057	0.057
48 hours	Naive	0.444	0.444	0.444	72 hours	Naive	0.454	0.335	0.347
	0.5	0.168	0.159	0.174		0.5	0.128	0.092	0.138
	1	0.167	0.14	0.179		1	0.078	0.085	0.095

2	0.098	0.131	0.145		2	0.073	0.072	0.074
3	0.081	0.082	0.108		3	0.054	0.058	0.058
5	0.075	0.074	0.071		5	0.053	0.042	0.043
8	0.056	0.058	0.059		8	0.036	0.04	0.045

Table S7.7. Viability of ZF4 cells after treatment with AgNPs or AgNO₃. Cell viability was measured using Lactate dehydrogenase (LDH) assay at different time points and concentrations. Treatments were prepared fresh in CCM supplemented with 10% FBS. The table shows the mean of three individual replicates \pm standard deviation. Results are presented as percentage cell viability (%) and their standard deviation. Data with asterisks (*) indicate a statistically significant difference of the AgNPs treatments (*p < 0.05, **p < 0.01, and ***p < 0.001) compared with naive cells. A statistical analysis was performed between treatments to show any NM-size and/or ionic effect. Similar letters (upper and lower case) and/or equivalent symbols denote statistically significant differences (p < 0.05) between the selected AgNP sizes and/or Ag ion concentrations at the same timepoint.

10 nm							
Time (hours)	Naive	5 AgNPs	10 AgNPs	20 AgNPs	30 AgNPs	40 AgNPs	60 AgNPs
3	100 \pm 0	100 \pm 0	100 \pm 0	100 \pm 0 _A	100 \pm 0 _{CD}	99.01 \pm 4.97	99.57 \pm 0.83
24	100 \pm 0	69.19 \pm 1.53	50.52 \pm 4.59* _{KN}	34.98 \pm 2.12* _V	32.81 \pm 2.68* _{LO}	25.17 \pm 28.54* _{QR} EFG	18.46 \pm 1.54* _{HJI}
48	100 \pm 0	39.50 \pm 3.11**	33.47 \pm 2.28	31.70 \pm 3.77* _V	30.37 \pm 0.49** _Y	28.54 \pm 0.14** _{WZ}	20.74 \pm 0.38** _{Z φ æ}
72	100 \pm 0	19.22 \pm 2.89*	18.38 \pm 2.01*	16.80 \pm 0.42*	18.38 \pm 4.45*	16.34 \pm 0.42*	15.59 \pm 0.27*
30 nm							

3	100 ± 0	96.28 ± 2.96	95.19 ± 6.22	84.02 ± 2.86*** _{ab}	80.96 ± 5.09	71.88 ± 1.73 _E	63.02 ± 7.73 _h
24	100 ± 0	80.14 ± 4.35	56.47 ± 2.31**	48.85 ± 1.86*	47.57 ± 4.50*	46.57 ± 2.11* _{qS}	43.86 ± 5.29* _U
48	100 ± 0	41.04 ± 3.02*	37.04 ± 6.69	30.43 ± 1.17*	26.36 ± 3.48* _v	25.53 ± 3.15* _w	21.14 ± 1.51* _ϕ
72	100 ± 0	22.45 ± 3.02*	23.32 ± 2.63*	21.72 ± 0.97*	22.07 ± 2.12*	22.41 ± 3.98*	16.51 ± 3.04*
100 nm							
3	100 ± 0	96.75 ± 1.76	97.96 ± 1.84	98.58 ± 1.27	79.91 ± 1.91*	75.84 ± 2.69* _f	69.61 ± 2.05**
24	100 ± 0	88.31 ± 6.86	56.34 ± 2.57* _M	51.72 ± 8.87	37.51 ± 1.47*** _P	29.01 ± 3.05** _{sT}	24.30 ± 3.28**
48	100 ± 0	56.89 ± 6.18*	30.91 ± 4.08**	23.18 ± 2.18*** _v	19.46 ± 1.63***	19.18 ± 0.32***	19.08 ± 2.02** _{zæ}
72	95.96 ± 6.98	45.52 ± 4.51	26.55 ± 0.95	14.19 ± 0.64*	13.07 ± 0.52*	13.24 ± 0.70*	12.30 ± 0.43*
AgNO₃							
Time (hours)	Naive	0.5 AgNO₃	1 AgNO₃	2 AgNO₃	3 AgNO₃	5 AgNO₃	8 AgNO₃
3	100 ± 0	99.10 ± 1.54	99.70 ± 0.89	98.81 ± 3.09 _b	84.88 ± 2.23* _{cd}	55.35 ± 7.62* _g	54.16 ± 4.40**
24	100 ± 0	95.45 ± 7.45	82.96 ± 3.55 _{kmn}	51.37 ± 2.36**	20.76 ± 1.92*** _{op}	16.71 ± 1.03*** _{rt}	13.77 ± 1.27*** _u
48	100 ± 0	39.50 ± 1.72***	33.44 ± 4.55**	28.38 ± 5.50**	20.25 ± 3.49**	16.76 ± 0.47 _z	13.94 ± 0.34***
72	100 ± 0	31.51 ± 6.38**	22.71 ± 2.25*	19.27 ± 0.02**	14.96 ± 0.61**	12.14 ± 1.60**	10.65 ± 1.91**

7.2.4 Autophagy results

Table S7.8. Primary data for autophagy results following AgNP exposure. The table shows the intensity of FITC obtained after the analysis with FlowJo software. R: means replicate. Results are expressed in arbitrary units (A.U) unless otherwise stated. No statistical analyses were performed for the raw data.

Treatments	Naive			Rapamycin			Bafilomycin		
	R1	R2	R3	R1	R2	R3	R1	R2	R3
Controls	1524	1591	1593	1619	1635	1639	1483	1502	1504
	1524	1591	1593	1619	1635	1639	1477	1502	1504
	1524	1591	1593	1619	1635	1639	1683	1502	1504
Nanoparticles concentrations									
	2.5 µg/mL			5 µg/mL			10 µg/mL		
10 nm	1607	1603	1645	1592	1690	1656	1591	1557	1644
30 nm	1575	1569	1569	1614	1630	1635	1649	1659	1636
100 nm	1607	1662	1567	1592	1699	1509	1691	1574	1513
AgNO₃ concentrations									
	1 µg/mL			1.5 µg/mL			2 µg/mL		
Ionic Ag	1635	1204	1205	1619	1395	1336	1610	1523	1473

Table S7.9. Autophagy percentage (%) induced in ZF4 cells exposed to AgNPs and AgNO₃. FITC intensities were first normalised to percentage (%) against naïve cells. The table shows the % of induction (mean ± SD) of three individual replicates. Data with asterisks (*) indicate a statistically significant difference of the AgNPs treatments (*p < 0.05) compared to naïve cells. Data with similar letters (upper and lower case) represent statistically significant differences (p < 0.05) between the selected concentrations. No differences were found between the AgNP sizes and/or between NMs and AgNO₃.

Size AgNPs	Naive	2.5 AgNPs µg/mL	5 AgNPs µg/mL	10 AgNPs µg/mL
10 nm	100 ± 2.50	103.12 ± 1.47	104.88 ± 3.17*	101.78 ± 2.79
30 nm	100 ± 2.50	100.10 ± 0.22	103.63 ± 0.69	105.01 ± 0.73
			A	a

100nm	100 ± 2.50	102.71 ± 3.03	101.95 ± 6.70	101.48 ± 5.76
	Naive	1 AgNO₃ μg/mL	1.5 AgNO₃ μg/mL	2 AgNO₃ μg/mL
Mean Intensity	0 ± 0	85.90 ± 15.84	92.40 ± 4.41	97.83 ± 2.55

7.2.4.1 Figures autophagy

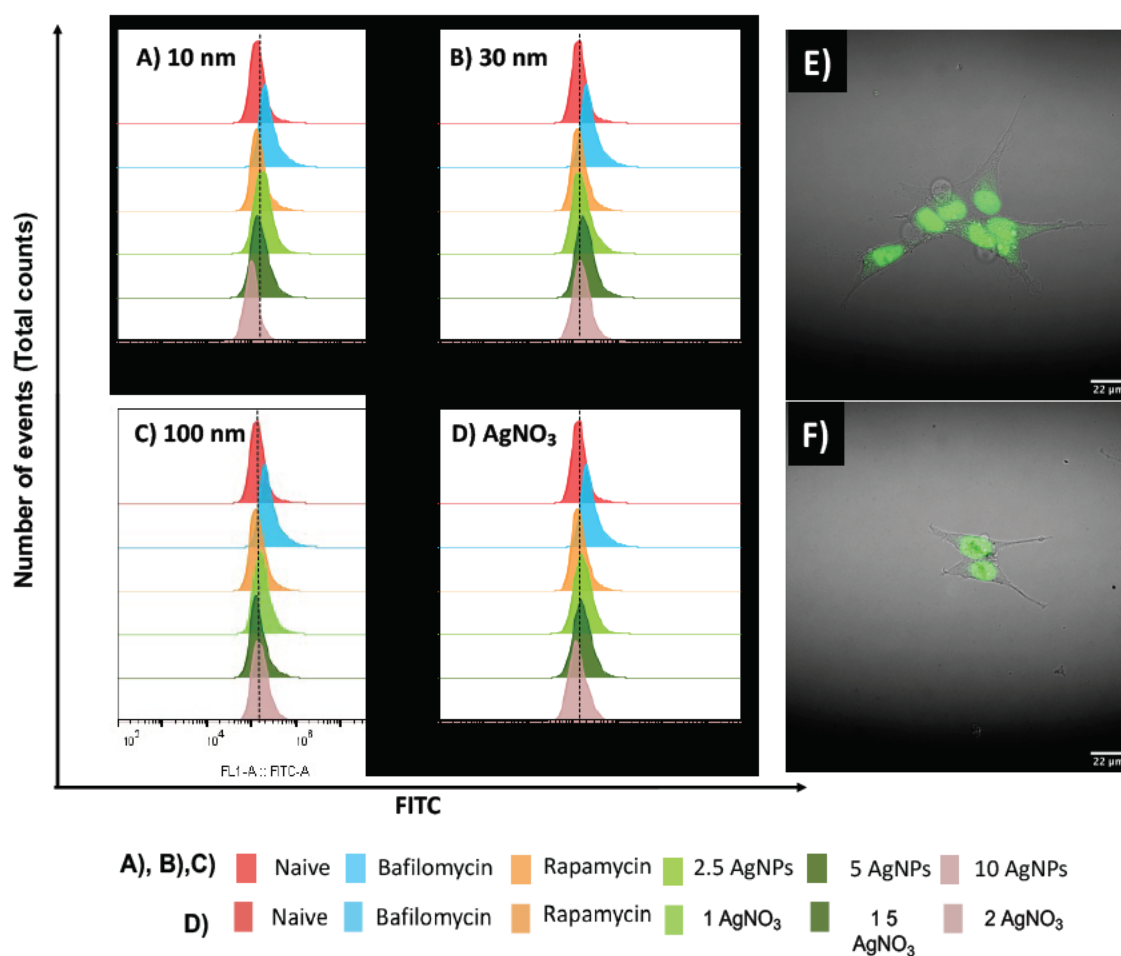


Figure S7.2. Autophagy results. The A-D shows representative FlowJo histograms for the treatments. Cells were treated with 2.5, 5 and 10 μg/mL of 10, 30 nm and 100 nm AgNP sizes and AgNO₃ 1, 1.5, 2 μg/mL for 24 hours. Controls are shown as naïve (untreated cells), 100 μM Bafilomycin (to reduce autophagy) and 10 μM Rapamycin (to induce autophagy). E-F images show cells stained with the autophagosome marker (green) to confirm the viability of the assay. Images were recorded with NIKON air

microscopes at 60X objective and using the Fluorescein isothiocyanate (FITC) filter, which has a fluorescence Excitation/Emission of 499/521 nm. Figure E shows naïve and F cells treated with 10 µg/mL of 10 nm AgNPs for 24 hours.

7.2.5 Data analysis for the apoptosis versus necrosis assay

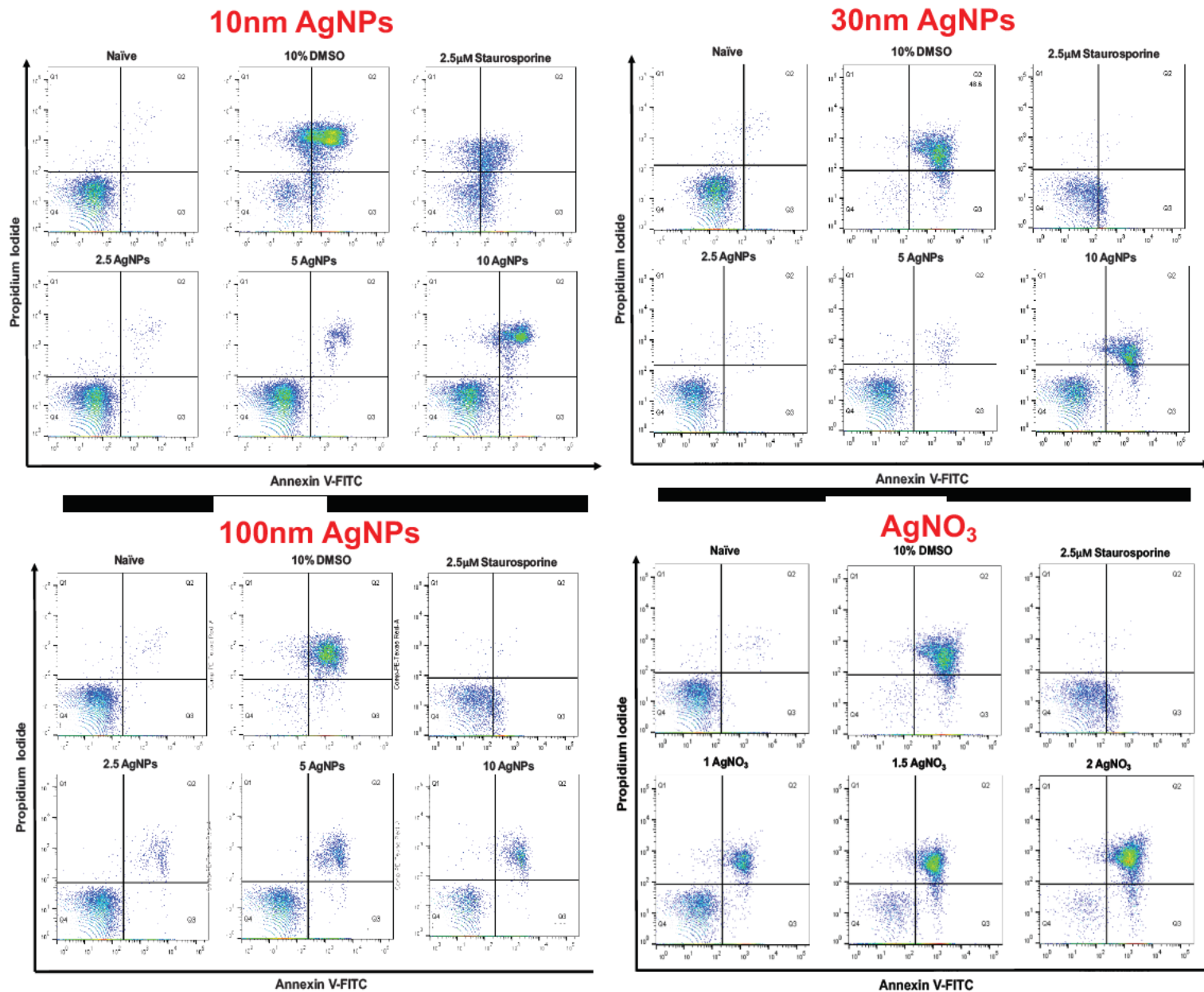


Figure S7.3. Representative scatter plots of the AgNPs treatments and controls. The figures represent one of the three replicates obtained after analysis with FlowJo software. The AgNPs represent treatments with 2.5, 5 and 10 $\mu\text{g}/\text{mL}$ of 10, 30n and 100 nm AgNP sizes and AgNO_3 1, 1.5, 2 $\mu\text{g}/\text{mL}$ for 24 hours. Controls are shown as naive (untreated cells), 10% DMSO (necrosis) and 2.5 μM Staurosporine (apoptosis).

Table S7.10. Analysis of the mechanisms of cell death - % of the cell population undergoing apoptosis and necrosis. Cells were treated with 2.5, 5 and 10 µ/mL of three different AgNPs sizes and 1, 1.5 and 2 µg/mL of AgNO₃ for 24 hours. Data are presented as the mean percentage (%) for apoptosis and necrosis staining of the cells at the different exposure concentrations. Values represent the average of three individual replicates and their standard deviation. Data with asterisks (*) indicate a statistically significant difference (*p < 0.05, **p < 0.01, and ***p < 0.001) of AgNPs and AgNO₃ treatments compared to the untreated control. Similar letters (upper and lower case) next to the value denotes statistically significant difference (p < 0.05) between the selected NP sizes and/or concentrations.

% Cell population	Naive	2.5 AgNPs µg/mL	5 AgNPs µg/mL	10 AgNPs µg/mL
10 nm				
Live cells	95.43 ± 2.28	72.30 ± 17.5	65.53 ± 21.53	53.27 ± 7.12*
Apoptotic cells	3.220 ± 1.85	11.92 ± 4.03	17.95 ± 9.58	21.30 ± 1.65**
Necrotic cells	1.357 ± 0.44	15.77 ± 13.11	16.57 ± 12.31	25.46 ± 5.52*
30 nm				
Live cells	96 ± 1.40	94.80 ± 3.34	88.20 ± 7.97	60.97 ± 1.68***
Apoptotic cells	2.137 ± 2.38	1.750 ± 0.62 A	4.457 ± 0.28 C	12.16 ± 8.95
Necrotic cells	1.543 ± 0.17	2.123 ± 1.37	4.483 ± 2.92	25.91 ± 5.59
100 nm				
Live cells	95 ± 1.60	95.13 ± 2.10	91.40 ± 5.58	87.57 ± 14.61
Apoptotic cells	2.68 ± 2.16	2.913 ± 0.89B	3.847 ± 0.69	4.833 ± 3.60
Necrotic cells	1.23 ± 0.49	1.95 ± 1.25	4.47 ± 5.01	7.57 ± 10.99
AgNO₃				
	Naive	1 AgNO ₃ µg/mL	1.5 AgNO ₃ µg/mL	2 AgNO ₃ µg/mL
Live cells	94.20 ± 1.13	55.35 ± 0.35	20.40 ± 1.13*	9.385 ± 0.46*
Apoptotic cells	4.22 ± 0.93	24.85 ± 0.21ab	24.40 ± 0.70 c	18.60 ± 0.56
Necrotic cells	1.595 ± 0.21	19.81 ± 0.07*	55.15 ± 0.45*	70.54 ± 2.28*

7.2. 6 Mitochondrial permeability

Table S11. Primary data for the mitochondrial potential assay. The table shows the fluorescence intensity for FITC. Cells were treated with 2.5, 5 and 10 μmL of three different AgNPs sizes and 1, 1.5 and 2 $\mu\text{g/mL}$ of AgNO_3 for 24 hours. A positive control of hydrogen peroxide (100 μM) was included for 30 minutes. R: means replicate. All results are presented in A.U. No statistical analyses were performed for the raw data.

Treatment	Naive			H_2O_2 100 μM					
	R1	R2	R3	R1	R2	R3			
Controls	7523	7279	7886	5812	5892	5871			
Nanoparticles									
	2.5 $\mu\text{g/mL}$			5 $\mu\text{g/mL}$			10 $\mu\text{g/mL}$		
	R1	R2	R3	R1	R2	R3	R1	R2	R3
10 nm	6940	6094	6784	6346	7012	6831	7186	7117	6240
30 nm	6650	6169	6605	6457	7093	7037	6457	6180	7156
100 nm	6771	7338	7383	6986	6593	6899	6644	8029	6604
AgNO_3									
	1 $\mu\text{g/mL}$			1.5 $\mu\text{g/mL}$			2 $\mu\text{g/mL}$		
Ionic Ag	7295	7419	6889	6904	5884	6936	6535	6872	6307

Table S7.12. Normalized % values for mitochondrial permeability. The table shows the normalized mean intensities and SD for FITC against the untreated control of three individual replicates (mean \pm SD) . Naive cells were used as 100% to represent healthy mitochondrial membranes. Compromised membranes resulted in lower fluorescence intensities values. Cells were treated with 2.5, 5 and 10 μmL of three different AgNPs sizes and 1, 1.5 and 2 $\mu\text{g/mL}$ of AgNO_3 for 24 hours. Results are presented in $\mu\text{g/mL}$ unless otherwise stated. Data with asterisks (*) indicate a statistically significant difference of the AgNPs treatments (* $p < 0.05$) compared to naïve. No statistically significant differences were found, suggesting that there is no NM size effect.

AgNPs Size	Naive	H_2O_2 100 μM	2.5 AgNPs	5 AgNPs	10 AgNPs
10nm	100 \pm 4.03	77.46 \pm 0.54	87.35 \pm 5.95	88.98 \pm 4.55	90.54 \pm 6.97
30nm	100 \pm 4.03	77.46 \pm 0.54	85.61 \pm 3.51*	90.74 \pm 4.65	87.24 \pm 6.65*
100nm	100 \pm 4.03	77.46 \pm 0.54	94.72 \pm 4.51	90.25 \pm 2.72	87.58 \pm 0.37

	Naive	1.0 AgNO ₃	1.5 AgNO ₃	2.0 AgNO ₃
Mean Intensity	100 ± 4.03	95.22 ± 3.66	86.94 ± 7.91*	86.89 ± 3.75*

7.2.7 Lipid peroxidation results

Table S7.13. Fluorescence ratios of Texas red to FITC. The ratios represent the mean of three individual replicates analysed using flow cytometry. Ratios were automatically calculated by FlowJo Software. No statistical analyses were performed for the raw data.

Treatment	Naive			H ₂ O ₂ 100 µM					
	R1	R2	R3	R1	R2	R3			
Controls	0.666	1.033	0.665	0.603	0.532	0.591			
AgNPs sizes	Nanoparticles								
	2.5 µg/mL			5 µg/mL			10 µg/mL		
	R1	R2	R3	R1	R2	R3	R1	R2	R3
10 nm	0.478	0.792	0.591	0.316	0.563	0.430	0.284	0.388	0.348
30 nm	0.536	0.779	6605	0.449	0.797	0.588	0.401	0.692	0.500
100 nm	0.604	0.635	0.452	0.598	0.755	0.789	0.592	0.806	0.785
	AgNO₃								
	1 µg/mL			1.5 µg/mL			2 µg/mL		
Ionic Ag	0.386	0.438	0.321	0.320	0.474	0.307	0.308	0.364	0.173

Table S7.14. Lipid peroxidation of ZF4 cells after AgNPs and AgNO₃ treatments. Results are presented as the ratio of the fluorescence of Texas red to FITC. Treatments are presented in µg/mL unless otherwise stated. The ratios represent the mean and standard deviation of three individual replicates calculated by FlowJo Software. Data with asterisks (*) indicate a statistically significant difference (*p < 0.05, **p < 0.01, and ***p < 0.001) of AgNPs and AgNO₃ treatments compared to the untreated control. Similar letters next to the values (upper and lower case) denote statistically significant difference (p < 0.05) between the selected NP sizes and concentrations.

AgNPs Size	Naive	100 μ M Cumene hydroperoxide	2.5 AgNPs	5 AgNPs	10 AgNPs
10nm	0.78 \pm 0.21	0.58 \pm 0.38	0.62 \pm 0.15	0.43 \pm 0.12	0.33 \pm 0.05 A
30nm	0.78 \pm 0.21	0.58 \pm 0.38	0.62 \pm 0.13	0.61 \pm 0.17	0.53 \pm 0.14
100nm	0.78 \pm 0.21	0.58 \pm 0.38	0.56 \pm 0.09	0.71 \pm 0.10	0.72 \pm 0.11 a
	Naive	100 μ M Cumene hydroperoxid e	1 AgNO ₃	1.5 AgNO ₃	2 AgNO ₃
Mean	0.78 \pm 0.21	0.58 \pm 0.11	0.38 \pm 0.05*	0.36 \pm 0.09**	0.28 \pm 0.09***

7.2.8 Particle number concentration

The particle number calculations (PNC) were performed as described by Huk et al. (2014) and Book et al. [77, 297]. Particle concentration (NPs/mL) and the mass (Ag) concentration (mg/mL) were located in the technical specification of the NPs provided by the manufacturer, and the mass concentration of the AgNPs was presented in mg/mL (n = 1).

$$PNC = NPs \text{ mass concentration} * \frac{NPs/mL}{Mass Ag}$$

Calculation of the percentage (%) of cell viability was estimated based on the 50% viable cells obtained in the LDH assay. For example, if 8,000 cells were initially treated with 10 μ g/mL of 10 nm AgNPs, the recorded viability after 24 hours was 50.52%. Based on this, an estimated number of cells was calculated to be 4042 cells (50.52*8000 based on the decrease in the cell population). Then, the number of NPs needed to decrease cell viability by 50% was calculated in an equal number of cells (i.e., 4000 cells), although

some treatments showed slight variation after 24 hours exposed to the EC₅₀ concentration (n = 1). The following calculation was implemented:

$$NPs \text{ in cells} = 4000(\text{equal no. of cells}) * \frac{NPs/mL}{\text{no. cells after 24 hrs}}$$

Table S7.15. Values for the replotting mass to NPs/mL. The table shows the particle numbers per volume (NPs/mL) for the mass concentrations used in the study (2.5, 5 and 10 µg/mL) as well as the % of the mean of viable cells (that remained after 24 hours) treatment with AgNPs using different sizes, estimated number of particles (NPs/mL), and mass concentration (n = 1).

AgNPs size	Mass concentrations (µg/mL)					
	2.5		5		10	
	NPs/mL	% viability	NPs/mL	% viability	NPs/mL	% viability
10 nm	4.40E+11	80	8.80E+11	69.67	1.76E+12	50.52767
30 nm	1.46E+10	90	2.92E+10	80.14	5.85E+10	53.1428571
100 nm	4.17E+08	92	8.33E+08	82.31	1.67E+09	56.34595

7.2.9 Surface area (SA) calculations

Calculations of AgNP total surface area were performed using the density of silver (10.49 g/cm³), the NP radius in the test medium as determined by DLS measurements and assuming a spherical shape of the NPs, as described in by Teeguarden et al., (2007) and Book et al., (2019) [297, 301]. For this the equation to calculate the volume of a sphere was used:

$$V = 4/3(\pi*r^3)$$

For example, for the lowest AgNPs concentration (2.5 µg/mL) of the 10 nm size, the formula was implemented as followed:

Value	Results	Calculation
Mass (gm)	0.0025	Not applicable
Diameter (nm)	107	r^2
Radius (r)	53.5	Diameter/2
Density (g/cm ³)	10.49	Not applicable
Volume (V)	0.00023832	Mass/Density
Vol per particle (v)	641431.015	$4/3 \cdot \pi \cdot r^3$
N	3.7155E-10	V/v
SA per particle (m ²)	35968.0943	$4 \cdot \pi \cdot r^2$
Total SA m ² /g	1.34E-05	$N \cdot sa (m^2)$

8. SI Chapter 3

Cellular repair mechanisms triggered by exposure to Silver Nanoparticles (AgNPs) and ionic silver (AgNO₃) in embryonic zebrafish cells (ZF4)

8.1 Methodology

8.1.1 Comet assay: buffer preparation

Lysis stock solution (1 L)

Preparation: Dissolve 146.4 g of NaCl (2.5 M), 37.2 g of ethylenedinitrilotetraacetic acid disodium salt dihydrate (Na₂EDTA - 2H₂O) (0.1 M), and 1.21 g of Tris HCl (8 mM) in 800 mL of dH₂O and adjust pH to 10 using approximately 8 g of solid NaOH pellets, bring up to 1 L of UPW, autoclave and store at 4 °C.

On the day of the assay, add to the lysis solution 10% DMSO and 1% Triton X-100, and set to chill at 4°C.

NaOH 10M solution (500 mL)

Preparation: Dissolve 195 g of NaOH pellets and bring solution up to 500 mL. Keep the solution at 4 °C. Note: This produces a dangerous exothermic reaction so use the appropriate measures during its preparation.

Na₂EDTA 200mM solution (500 mL)

Preparation: Dissolve 37.2 g of EDTA pellets to water and bring up 500 mL. Adjust the pH to 8.

Electrophoretic Buffer solution (2.5 L)

Preparation: Mix 75 mL of NaOH (10M) with 12.5 mL of Na₂EDTA (0.2M) in a glass bottle for a concentration of 300 mM and 1 mM respectively, bring up to a final volume of 2.5 L with cold water (4 °C). The individual solutions can be prepared in advance and kept at 4°C for 1 month. However, on the day of the assay, the electrophoretic buffer needs to be prepared fresh.

Neutralization solution (500 mL)

Preparation: Dissolve 31.5 g of Tris HCL (0.4 M) in 500 mL H₂O and adjust to pH 7.5 with Hydrochloric acid (HCl). Store the solution at 4 °C.

Preparation of the precoated slides (1 %)

Glass slides were boiled in water for 5 minutes and then set to dry overnight. Then, Normal Melting point Agarose (NMA) (1g) was dissolved in 99 mL of PBS for a total volume of 100 mL by microwave. Then, 50 mL of the diluted NMA suspension was kept warm by placing 45 mL into a falcon tube and set at 50 °C in a heat block. The rest of the NMA solution was stored at 4 °C.

Slides were dipped into the NMA for 10 seconds, the back was wiped, and the slides were set to dry onto a flat surface overnight.

Preparation of the low melting point agarose (0.7 %)

Low melting point agarose was diluted in PBS for a final concentration of 0.7 % in total volume of 50 mL.

8.2 Results

8.2.1 Characterisation of the NPs

Table S8.1. Characterisation by dynamic light scattering (DLS) of PVP-capped silver nanoparticles (AgNPs) in DMEM F/12 serum free medium (SFM) and/or complete culture medium (CCM) containing 10 % foetal bovine serum at 0 and 24 hours. The Table shows the characterisation of the AgNPs in different media and at different time points. Data with similar letters (upper and lowercase letters) indicate a statistically significant difference ($p < 0.05$) between the selected concentrations and time points (0 and 24 hours). Similar symbols represent significant differences ($p < 0.05$) in the hydrodynamic size of the NPs between SFM and CCM treatments.

AgNPs size	Hydrodynamic diameter (nm)			
	SFM		CCM	
Sample	Time (hours)			
	0	24	0	24
Medium	1.20 ± 0.11	1.36 ± 0.20	12.95 ± 0.64	12.85 ± 0.69
10 nm	47.86 ± 0.01	617.21 ± 0.1	94.49 ± 0.03 C	105.66 ± 0.3 c
30 nm	94.82 ± 0.01 A	690 ± 0.1 a#	95.10 ± 2.85	102.65 ± 0.02 #
100 nm	135.9 ± 0.05 B	540.93 ± 0.03 b\$	160.60 ± 0.52 D	175.06 ± 0.5 d\$
	PDI			
	SFM		CCM	
Medium	0.10 ± 0.01	0.09 ± 0.00	0.50 ± 0.05	0.51 ± 0.00
10 nm	0.23 ± 0.01	1 ± 0	0.53 ± 0.03	0.52 ± 0.07
30 nm	0.24 ± 0.01	1 ± 0	0.45 ± 0.03	0.43 ± 0.02
100 nm	0.03 ± 0.01	0.52 ± 0.03	0.06 ± 0.07	0.12 ± 0.08
	Zeta potential (mV)			
	SFM		CCM	
10 nm	-7.44 ± 0.74	-7.31 ± 0.58	-10.55 ± 1.22	-10.47 ± 0.83
30 nm	-6.98 ± 0.55	-5.80 ± 0.28	-12.13 ± 1.20	-11.73 ± 1.09
100 nm	-6.69 ± 1.10	-6.25 ± 0.90	-11.0 ± 0.45	-12.33 ± 1.43

Abbreviations: Dynamic Light Scattering (DLS), Serum Free Media (SFM), Complete Culture Media (CCM), nanometer (nm), and Polydispersity index (PDI).

8.2.2 Lactate dehydrogenase (LDH) assay

Note: Primary data for LDH in serum free medium is not available due to issues with the storage device used to keep this data. The file was corrupted, and it was not possible to recover the raw data.

Data for LDH assay performed in cell culture medium (DMEM F/12) supplemented with 10% FBS can be found in the supplementary information of chapter 2.

Table S8.2. Viability of ZF4 cells after treatment with AgNPs or AgNO₃ in SFM. Cell viability was measured using the LDH assay at different times post exposure. The table shows the mean and \pm SD of three individual replicates, and results are presented in percentages (%). Data with asterisks (*) indicate statistically significant differences between AgNPs treatments compared with the naïve control at each time point (* $p < 0.05$, ** $p < 0.01$, and *** $p < 0.001$). A statistical analysis was performed between treatments to show NM-size effect and/or metal salt versus NM effects. Similar letters (upper and lower case) and/or equal symbols denote statistically significant differences ($p < 0.05$) between the selected AgNP and AgNO₃ treatments.

10 nm AgNPs								
Concentrations in $\mu\text{g/mL}$								
Time (hours)	Naive	0.25	0.5	1	1.5	2	2.5	
3	99.33 \pm 0.57	92.11 _{ABC} \pm 0.85	89.55 \pm 2.25	86.99 \pm 7.58	84.15 \pm 4.92	83.29 \pm 4.97	80.73 \pm 3.55	
6	99 \pm 1.03	90.12 \pm 2.46	85.71 \pm 3.01	79.74 \pm 1.80	63.11 \pm 3.71* G	55.72 \pm 3.44** J	51.17 \pm 6.43* M	
12	99 \pm 1.01	84.79 \pm 2.68* P	76.74 \pm 4.25 S	67.08 \pm 5.97 V	59.09 \pm 3.82* YB	53.83 \pm 5.43* UO	41.40 \pm 7.45* OO	
24	98.33 \pm 1.15	73.76 \pm 6.28	65.81 \pm 8.86 Ø	49.23 \pm 1.52** \$&	31.68 \pm 2.11**	31.07 \pm 1.55* ¢	31.68 \pm 0.42*** †	
30 nm AgNPs								
3	99.33 \pm 0.57	92.39 \pm 0.98* D	90.12 \pm 4.20	88.13 \pm 3.55	86.14 \pm 2.25	84.43 \pm 0.85**	73.91 \pm 0.98***	

6	99 ± 1.03	90.12 ± 2.99	92.39 ± 1.30**	± 86.14 ± 3.07 _F	± 82.16 ± 4.20	79.88 ± 4.85	62.54 ± 5.48*
12	99 ± 1.01	88.89 ± 1.72	85.71 ± 4.09	77.01 ± 1.65** _w	± 82.85 ± 2.12* _{YaS}	± 70.11 ± 6.74	58.79 ± 5.03*
24	98.33 ± 1.15	91.57 ± 6.09	84.33 ± 7.88	70.53 ± 7.15	51.18 ± 5.80*	43.14 ± 1.46***	33.39 ± 0.84*** _‡
100 nm AgNPs							
3	99.33 ± 0.57	90.68 ± 2.60	87.56 ± 3.44	86.70 ± 1.30*	± 81.59 ± 4.20	72.77 ± 2.74*	67.94 ± 2.60**
6	99 ± 1.03	85.85 ± 0.98**	84.71 ± 0.98**	± 82.44 ± 7.15	70.22 ± 5.67	62.26 ± 5.59	59.41 ± 9.51*
12	99 ± 1.01	87.27 ± 3.31	83.26 ± 1.88* _u	± 80.60 ± 5.32	70.05 ± 2.66** _{âSÉ}	± 60.05 ± 4.15*	58.12 ± 4.16*
24	98.33 ± 1.15	87.81 ± 2.77	83.78 ± 4.74	69.95 ± 8.15	53.87 ± 0.42***	± 47.53 ± 1.26** _A	41.92 ± 4.97*
AgNO₃ (ionic control)							
Concentrations in µg/mL							
Time (hours)	Naïve	0.5 AgNO₃	1 AgNO₃	2 AgNO₃	3 AgNO₃	5 AgNO₃	8 AgNO₃
3	98.81 ± 2.06	99.10 ± 1.54	99.10 ± 0.89	98.21 ± 3.09	74.88 ± 2.23	55.35 ± 7.62*	54.16 ± 4.40**
6	100 ± 0.49	95.45 ± 7.45	82.96 ± 3.55	50.37 ± 2.36**	± 20.76 ± 1.92*** _{hl}	± 15.71 ± 1.03*** _{jk}	± 13.06 ± 1.27***
12	99.26 ± 1.27	38.07 ± 1.72*** _{pqr}	36.93 ± 4.55** _{stu}	± 28.41 ± 5.50* _{vwz}	± 20.59 ± 3.49** _{ßÉ}	± 16.71 ± 0.47***	± 13.14 ± 0.34*** _{Öx}
24	93.36 ± 5.98	31.51 ± 6.38*	22.71 ± 2.25* _{øÛ_i}	± 19.27 ± 0.02* _%	± 14.96 ± 0.61*	12.14 ± 1.60** _{φA}	10.65 ± 1.91* _{‡‡æ}

8.2.3 AgNP internalisation by ZF4 cells

The analysis was performed by manually drawing a region of interest (ROI) in the acquired image by FIJI. First, the image was separated into the various channels (green, red and blue) (Fig. 1 A), then FIJI was set to record the mean grey value for the NPs (Fig. 1 B), the ROI was carefully selected and added to the ROI toolbar (Fig. 1 C), then the intensity was measured and the total intensity of fluorescence per NP (visible intracellular accumulations of NPs) was calculated by taking the intensity values for the selected area and subtracting the intracellular background fluorescence from an adjacent area without cells of equal size as the selected area as described by Smith *et al.*, (2012) and Guggenheim *et al.*, (2020). Three individual samples per AgNP treatment were prepared; then, three cells per replicate were analysed, for a total of nine cells per treatment (n=9). The intensities were plotted using GraphPad software.



Figure S8.4. Example of the manual analysis of the AgNP reflectance intensity following exposure of the ZF4 cells to 10 nm AgNPs for 2 hours at 2.5 $\mu\text{g}/\text{mL}$. **A)** Composite image of a group of cells. Green shows the cell membrane, blue/light green the nucleus, red are the lysosomes and white are the NPs. Due to interference between the reflectance channel and the dye for cell membrane (A), the green channel was removed to visualize better the presence of the NPs for images B and C. **B)** Reflected intensity of the AgNPs – comparison with A indicates that the NPs are broadly associated with the cellular membranes. **C)** Zoomed image of a cell in figure B to show the manual drawing of the region of interest (ROI) by FIJI. The scale bar for all the images is 22 μm . Images were taken with a NIKON A1R 808 series microscope at 60X objective.

Table S8.3. NP reflectance Intensities of the AgNPs following uptake into cells. The table shows the raw intensities obtained in the reflectance channel (488) after 2 and 24 hours of exposure to 2.5, 5 and 10 µg/mL of 10, 30 and 100 nm AgNPs. Final represents intensity after subtraction of the background. Results are expressed in arbitrary units (A.U.) unless otherwise stated. R means replicate. No statistical analyses were performed on the raw data.

NPs size	2 hours									
	Concentration	2.5 µg/mL			5 µg/mL			10 µg/mL		
10 nm		R1	R2	R3	R1	R2	R3	R1	R2	R3
	Raw Intensity	219169	323068	161692	308149	97394	190019	119260	230363	254053
		179767	276699	315422	282555	162455	244281	157451	312932	144111
		139189	362580	180810	279572	128488	251461	130246	259706	127855
	Background	3838	90267	895	30553	21204	16928	30900	89738	3638
		3521	82723	34112	27667	18292	18780	16053	51309	3292
		3047	122440	35306	33124	24082	17450	23544	24073	2847
	Final	175906	222306	195870	259644	108253	210868	112153	212627	172081
	30 nm									
Raw Intensity		127472	216079	104721	138008	263291	138692	91629	133893	129123
		149059	447344	196606	245189	186340	104361	85067	226499	109673
		164485	156582	68099	77238	100683	59780	62109	68250	106299
Background		12807	19090	369	1508	3124	817	122	3262	716
		16944	59963	612	1472	2123	693	232	2471	30
		28886	26757	541	6519	1302	620	104	3185	626
Final		127459	238065	122635	150312	181255	100234	79449	139908	114574
100 nm										
	Raw Intensity	168881	256233	105430	17667	126476	132545	114040	146446	82975
		175486	185892	43194	231381	93770	228979	79707	200853	77021
		83254	177616	130324	124147	81489	67707	137935	111604	116595
	Background	21165	11284	2386	237	4715	1019	2230	2777	1942
		30314	2315	16255	5239	1156	883	2763	4089	1400
		16219	2565	1942	3165	1136	1355	3791	5642	1345
	Final	119975	201193	86121	121518	98243	141992	107633	148799	90635

NPs size	24 hours									
	Concentration	2.5 µg/mL			5 µg/mL			10 µg/mL		
10 nm		R1	R2	R3	R1	R2	R3	R1	R2	R3
	Raw Intensity		56063	62060	27399	161400	39034	48613	52207	52516
		47801	59532	78697	42243	56662	49652	42988	45451	37716
		55044	27202	42210	36029	25477	42597	41602	159143	41195
Background		461	44	40	785	1175	168	117	71	137
		165	80	5299	370	5064	94	140	133	65
		636	61	851	281	571	142	44	128	67
Final		52549	49537	47372	79412	38121	46819	45499	85593	57400
30 nm										
	Raw Intensity	66900	97700	37113	71714	76594	41287	114870	69392	23087
Background		89024	139492	21743	178221	123685	70783	38943	94194	81265
		40334	85282	46463	65526	57618	44483	47953	99488	55018
		99	323	197	485	137	27	33	355	156
Final		47	439	174	239	95	83	89	371	2922
		67	416	373	200	335	195	98	488	227
		65348	107099	34858	104846	85777	52082	67182	87287	52021
100 nm										
	Raw Intensity	82977	63388	139244	67809	74914	107507	107608	77726	116403
Background		71366	142827	125100	133392	55729	29317	78435	159994	103235
		59473	57872	75568	58494	49436	57146	44744	96901	86041
		153	208	1957	359	122	450	154	429	34
Final		274	265	818	74	2734	56	101	257	40
		412	1435	416	54	55	27	152	475	30
		70992	87393	112240	86403	59056	64479	76793	111153	101858

Table S8.4. Mean of the AgNP cellular intensities from 9 cells over three independent replicates. The table shows the mean and SD (n =3) of the reflected intensities (X1000) analysed by FIJI after their incubation for either 2 or 24 hours. Similar letters (upper and lower case) beside the values denote statistically significant difference ($p < 0.05$) between the selected NM sizes and/or concentrations.

Size	2.5 AgNPs (µg/mL)	5 AgNPs (µg/mL)	10 AgNPs (µg/mL)
2 hours			
10 nm	199.51 ± 21.2 AB	172.92 ± 56.28	165.62 ± 50.54
30 nm	162.72 ± 8.58	143.93 ± 40.88	111.31 ± 30.36 a
100 nm	135.76 ± 65.29	120.11 ± 30.93	115.68 ± 29.90 b
24 hours			
10 nm	48.81 ± 2.60	54.78 ± 21.76	62.83 ± 20.59 C
30 nm	69.10 ± 36.26	80.93 ± 16.75	68.83 ± 17.69
100 nm	90.28 ± 20.76	69.97 ± 14.47	96.60 ± 17.73 c

8.2.4 Calculation of mass concentration and NPs/mL.

The mass concentration (10 µg/mL) was calculated to obtain the number of particles per millilitre (NPs/mL). The calculation steps are found in the section “Particle number concentration” in the supplementary information of Chapter 2.

AgNPs size	NPs/mL
10 nm	1.76E+12
30 nm	5.85E+10
100 nm	1.67E+09

Table S8.5. Number of NP spots per cell area. Intensities recorded for the visible intracellular accumulations of NPs after 2 and 24 hours at different AgNP concentrations. Results are expressed in arbitrary units (A.U.) unless otherwise stated. R means replicate. No statistical analyses were performed for the raw data.

NP size	2 hours								
	2.5 µg/mL			5 AgNPs µg/mL			10 AgNPs µg/mL		
Conc	R1	R2	R3	R1	R2	R3	R1	R2	R3
.									

10 nm	0.0047	0.0061	0.0073	0.0014	0.0042	0.0047	0.0023	0.0018	0.0042
30 nm	0.0019	0.0020	0.0012	0.0017	0.0029	0.0009	0.0031	0.0035	0.0016
100 nm	0.0022	0.0004	0.0003	0.0029	0.0031	0.0028	0.0028	0.0030	0.0054
	24 hours								
	2.5 AgNPs			5 AgNPs			10 AgNPs		
10 nm	0.0045	0.0031	0.0144	0.0212	0.0141	0.0071	0.0203	0.0278	0.0129
30 nm	0.0047	0.0070	0.0043	0.0039	0.0057	0.0050	0.0092	0.0113	0.0154
100 nm	0.0081	0.0080	0.0193	0.0087	0.0107	0.0039	0.0033	0.0029	0.0156

Table S8.6. Number of NP spots per cell area after 2 or 24 hours of exposure to different concentrations of the AgNPs. Results represent the average of three individual samples (mean \pm SD) per AgNP concentration and size. Similar letters (upper and lower case) beside the values denote statistically significant difference ($p < 0.05$) between the selected NP sizes and/or concentrations.

Size	2.5 AgNPs ($\mu\text{g/mL}$)	5 AgNPs ($\mu\text{g/mL}$)	10 AgNPs ($\mu\text{g/mL}$)
2 hours			
10 nm	0.006 \pm 0.001 D	0.003 \pm 0.002	0.003 \pm 0.001
30 nm	0.002 \pm 0.004	0.002 \pm 0.001	0.003 \pm 0.001
100 nm	0.001 \pm 0.001 dE	0.003 \pm 0.001	0.004 \pm 0.001 e
24 hours			
10 nm	0.007 \pm 0.006	0.014 \pm 0.007	0.020 \pm 0.007
30 nm	0.005 \pm 0.001	0.005 \pm 0.001	0.012 \pm 0.003
100 nm	0.012 \pm 0.007	0.008 \pm 0.004	0.07 \pm 0.007

8.2.5 Calcium homeostasis

Table S8.7. Primary data of intercellular calcium following exposure to AgNPs. The table shows the intensities of Fluo-8 NW dye. Cells were treated with 2.5, 5 and 10 µg/mL of 10, 30 and 100 nm AgNPs respectively, as well as 1, 1.5 and 2 µg/mL of AgNO₃. Results are expressed in arbitrary units (A.U.) unless otherwise stated. R means replicate. No statistical analyses were performed for the raw data.

	Controls								
	R1			R2			R3		
Naive	14395			14897			14997		
DMSO	53887			52051			47495		
	AgNPs								
NP size	2.5 µg/mL			5 µg/mL			10 µg/mL		
	R1	R2	R3	R1	R2	R3	R1	R2	R3
10 nm	46272	57305	33225	35667	34627	27703	27092	25188	27832
30 nm	21904	17968	18951	25731	23571	35268	36165	32133	34661
100 nm	27221	26709	27496	15243	21735	21791	44357	29422	26760
	AgNO ₃								
	1 µg/mL			1.5 µg/mL			2 µg/mL		
N/A	23460	24476	23902	13789	12456	12508	12881	14185	14215

Table S8.8. Normalised intercellular calcium data. The table shows the Fluo-8 NW intensity values after subtraction of the mean of the naïve cells in order to normalise the data. R means replicate. No statistical analyses were performed for the raw data.

	Controls								
	R1			R2			R3		
Naive	-368			134			234		
DMSO	39123.8			37287.8			32731.8		
	AgNPs								
NP size	2.5 µg/mL			5 µg/mL			10 µg/mL		
	R1	R2	R3	R1	R2	R3	R1	R2	R3
10 nm	31509	42542	18462	20904	19864	12940	12329	10425	13069
30 nm	7141	3205	4188	10968	8808	20505	21402	17370	19898

100 nm	12458	11946	12733	480	6972	7028	29594	14659	11997
	AgNO₃								
	1 µg/mL			1.5 µg/mL			2 µg/mL		
N/A	8697	9713	9139	-974	-2307	-2255	-1882	-578	-548

Table S8.9. Normalised calcium results after exposure to AgNPs or AgNO₃. Intensities of Fluo-8 NW expression are normalised relative to the naïve control. Results represent the mean ± standard deviation of three individual replicates. Data with asterisks (*) indicate statistically significant differences between AgNPs treatments compared with the naïve control at each time point (*p < 0.05, **p < 0.01, and ***p < 0.001). Similar letters (upper and lower case) beside the values denote statistically significant difference (p < 0.05) between the selected NM sizes and/or concentrations.

AgNPs size	Naive	2.5 AgNPs (µg/mL)	5 AgNPs (µg/mL)	10 AgNPs (µg/mL)
10 nm	0 ± 0	308.3 ± 120.12 B	179 ± 43.58	119.3 ± 13.86*
30 nm	0 ± 0	48.33 ± 20.25 A	134.3 ± 62.18	195.6 ± 20.27* a
100 nm	0 ± 0	123.6 ± 4.16** b	48.33 ± 37.52	187.66 ± 94.78
AgNO₃	Naive	1 AgNO₃ (µg/mL)	1.5 AgNO₃ (µg/mL)	2 AgNO₃ (µg/mL)
Ionic Ag	0 ± 0	91.67 ± 5.03***	-18.67 ± 7.5**	-10.00 ± 7.81*

8.2.6 Oxidative stress

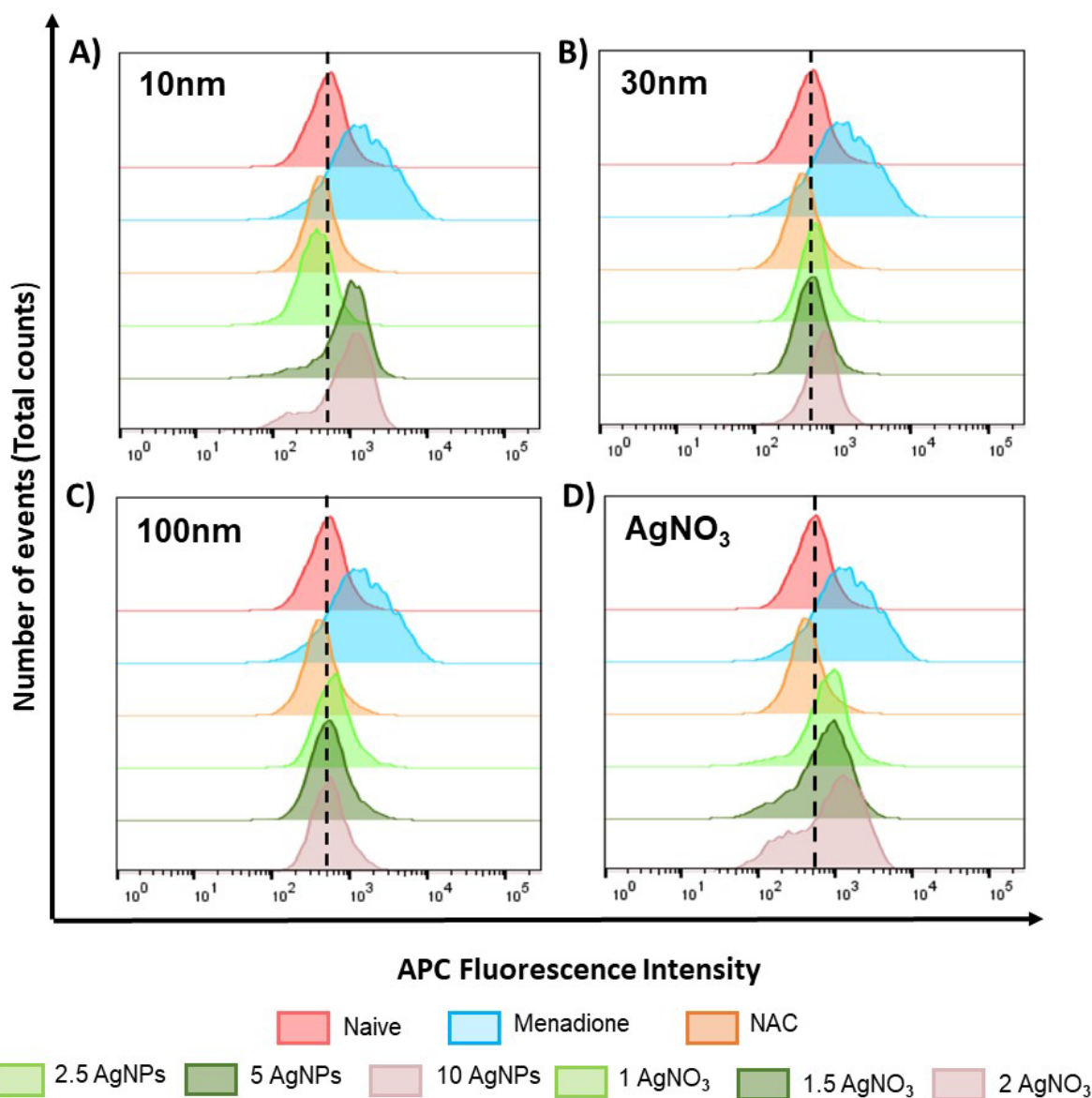


Figure S8.5. Oxidative stress histogram plots for ZF4 cells. Histograms representing the number of cell counts versus the Allophycocyanin (APC) dye fluorescence intensities obtained from the analysis by Flowjo software. A), B) and C) show the results for 2.5, 5 and 10 $\mu\text{g}/\text{mL}$ of 10, 30 and 100nm AgNPs respectively, while D) shows the histograms for the AgNO₃ treatments (1, 1.5 and 2 $\mu\text{g}/\text{mL}$). The dashed lines in the middle of the pictures represent the mean intensity of the naïve cells and can be used as a reference for the shifting of peaks induced by the various treatments.

Table S10. Intensities of ROS fluorescence in the oxidative stress experiments. The table shows allophycocyanin (APC) dye fluorescence intensities of cells treated with 2.5, 5 and 10 µg/mL of 10, 30 and 100 nm AgNPs respectively, as well as 1, 1.5 and 2 µg/mL of AgNO₃. 100 µM menadione and 5 mM of N-acetyl-L-cysteine (NAC) were included as positive controls to induce and inhibit ROS production, respectively. Results are expressed in arbitrary units (A.U.) unless otherwise stated. R means replicate. No statistical analyses were performed for the raw data.

	Naive			Menadione			NAC		
Controls	R1	R2	R3	R1	R2	R3	R1	R2	R3
	338	483	374	804	1281	1473	177	269	260
NPs size	Nanoparticles								
	2.5 µg/mL			5 µg/mL			10 µg/mL		
10 nm	570	346	351	740	913	878	796	930	870
30 nm	521	558	547	452	507	498	725	690	661
100 nm	517	582	587	464	514	495	593	525	503
	AgNO ₃								
Ionic Ag	Naive			Menadione			NAC		
	414	483	374	1350	1281	1473	1340	1281	1273
	1 µg/mL			1.5 µg/mL			2 µg/mL		
	1635	1204	1205	1619	1395	1336	1610	1523	1473

Table S8.11. Raw data for ROS intensities following exposure to AgNPs. The table shows the three replicates for all the controls, AgNPs and AgNO₃. Results are expressed in arbitrary units (A.U.) unless otherwise stated. R means replicate. No statistical analyses were performed for the raw data.

Size NPs	Naive			Menadione			NAC		
	R1	R2	R3	R1	R2	R3	R1	R2	R3
Control s	84.85	121.2	93.89	201.8	321.5	369.7	44.44	67.53	65.27
	6			4	9	9			

	Nanoparticles								
	2.5 µg/mL			5 µg/mL			10 µg/mL		
10 nm	143.1			185.7 229.2 220.4			199.8 233.4 218.4		
	0	86.86	88.12	7	1	2	3	7	1
30 nm	130.7 140.0 137.3			113.4 127.2 125.0			182.0 173.2 165.9		
	9	8	2	7	8	2	1	2	4
100 nm	129.7 146.1 147.3			116.4 129.0 124.2			148.8 131.8 126.2		
	9	1	6	9	4	7	7	0	8
Control and ionic Ag	AgNO ₃								
	Naive			Menadione			NAC		
	114.0			316.2 302.3 300.4					
	97.72	0	88.28	9	6	7	50.98	53.11	73.64
	1 µg/mL			1.5 µg/mL			2 µg/mL		
130.2 181.2 174.6			166.4 171.6 161.4			218.3 198.5 207.7			
	9	7	7	0	0	5	3	1	1

Table S8.12. Normalised intensities for the oxidative stress results. The mean APC intensities were normalised to percentages (%) relative to the naïve. Data with asterisks (*) indicate statistically significant differences between AgNPs treatments (*p < 0.05, **p < 0.01, and ***p < 0.001) and the naïve cells. Similar letters (upper and lower case) next to the results denote statistically significant difference (p < 0.05) between the selected concentrations.

AgNPs size	Naive	2.5 AgNPs (µg/mL)	5 AgNPs (µg/mL)	10 AgNPs (µg/mL)
10 nm	100 ± 18.95	106.2 ± 32.11AB	211.8 ± 22.96***	217.2 ± 16.85***ab
30 nm	100 ± 18.95	136.1 ± 4.77***CD	121.9 ± 7.9**	173.7 ± 8.0***cd
100 nm	100 ± 18.95	141.1 ± 9.80*	123.3 ± 6.33**	135.6 ± 11.78*
AgNO ₃	Naive	1 AgNO ₃ (µg/mL)	1.5 AgNO ₃ (µg/mL)	2 AgNO ₃ (µg/mL)
	100 ± 13.02	162.01 ± 27.89**	166.5 ± 5.07**	208.2 ± 9.92***

8.2.7 Cell cycle

Table S8.13. Raw data from replicates, cell cycle analysis following exposure to AgNPs. Cells were exposed to 2.5, 5 and 10 µg/mL of 10, 30 and 100 nm AgNPs respectively, as well as 1, 1.5 and 2 µg/mL of AgNO₃. 3 µM Topotecan and 10 µM of were included as positive controls to induce arrest in specific cell cycle phases. R means replicate. No statistical analyses were performed for this data.

Treatment	Cell cycle phase	Naive			Topotecan 3µM			Etoposide 10µM		
		R1	R2	R3	R1	R2	R3	R1	R2	R3
Control s	G1	64	64.4	68	65.9	65.5	65.5	45.9	41	56.4
	S	17.4	16.3	18.8	15.5	19.9	18.5	48.3	47.9	34.8
	G2	10.8	8.19	11.1	6.05	8.48	6.62	0	5.46	4.41
AgNPs										
		2.5 µg/mL			5 µg/mL			10 µg/mL		
10 nm	G1	63.8	64.9	58.1	61.1	60.8	53.4	61.8	62.3	59.7
	S	16	16.5	17.3	18.1	11.9	10.7	18.1	12.8	10.7
	G2	11	11.6	11.3	8.11	5.85	3.53	8.78	9.68	7.52
30 nm	G1	63.2	66	65.2	64.7	70.2	68.2	63.7	70.2	61.3
	S	14.7	14	13.3	14.5	12.2	15.4	15.8	12.2	12
	G2	10.4	10.7	16	12.04	12.8	14.7	12.1	12.8	12.7
100 nm	G1	63.6	60.3	65.8	65.7	63.2	65.7	63.4	68.3	65.5
	S	8.03	18.3	17.4	15.7	18.5	16.7	15.4	15.6	17
	G2	6.28	14.2	12.6	10.3	14.6	12.5	9.47	10.2	13.2
AgNO₃										
Ionic Ag		1 µg/mL			1.5 µg/mL			2 µg/mL		
	G1	65.3	59.9	67.6	69.1	69.3	69.3	72.7	62.6	67.6
	S	17.3	16.9	15.2	15.6	8.36	13.8	13.4	9.09	15.2
	G2	12.5	12.1	7.99	8.66	6.83	5.87	7.02	7.38	7.99

Table S8.14. Cell cycle percentages for each phase. Results were automatically calculated by FlowJo software, using the cell cycle tool. Data with asterisks (*) indicate statistically significant differences between AgNPs treatments (*p < 0.05) compared to naive cells. Similar letters (upper and lower case) next to the values represent statistically significant difference (p < 0.05) between the selected concentrations.

10 nm				
Cell cycle phase	Naive	2.5 AgNPs (µg/mL)	5 AgNPs (µg/mL)	10 AgNPs (µg/mL)
G1	65.46 ± 2.2	62.26 ± 3.65 A	58.43 ± 4.36 a	61.26 ± 1.38
S	17.50 ± 1.25	16.60 ± 0.65	13.56 ± 3.97	13.86 ± 3.81
G2	10.03 ± 1.6	11.30 ± 0.3	5.83 ± 2.29	8.66 ± 1.08
30 nm				
G1	65.46 ± 2.2	64.8 ± 1.44	67.70 ± 2.78	65.06 ± 4.6
S	17.50 ± 1.25	14.0 ± 0.7	14.03 ± 1.65*	13.33 ± 2.13
G2	10.03 ± 1.6	12.36 ± 3.15	13.18 ± 1.37	12.53 ± 0.37
100 nm				
G1	65.46 ± 2.2	63.0 ± 3.88	64.86 ± 1.44	65.73 ± 2.45
S	17.50 ± 1.25	14.57 ± 5.68	16.96 ± 1.41	16.01 ± 0.87
G2	10.03 ± 1.6	11.02 ± 4.18	12.46 ± 2.15	10.95 ± 1.97
AgNO ₃				
Cell cycle phase	Naive	1 AgNO ₃ (µg/mL)	1.5 AgNO ₃ (µg/mL)	2 AgNO ₃ (µg/mL)
G1	65.46 ± 2.2	62.13 ± 2.81	68.35 ± 1.06	71.0 ± 2.40
S	17.50 ± 1.25	17.8 ± 1.22	13.05 ± 4.06	12.09 ± 2.61
G2	10.03 ± 1.6	11.76 ± 0.94 B	7.87 ± 0.92	6.75 ± 0.78 b

8.2.8 Cell cycle histograms

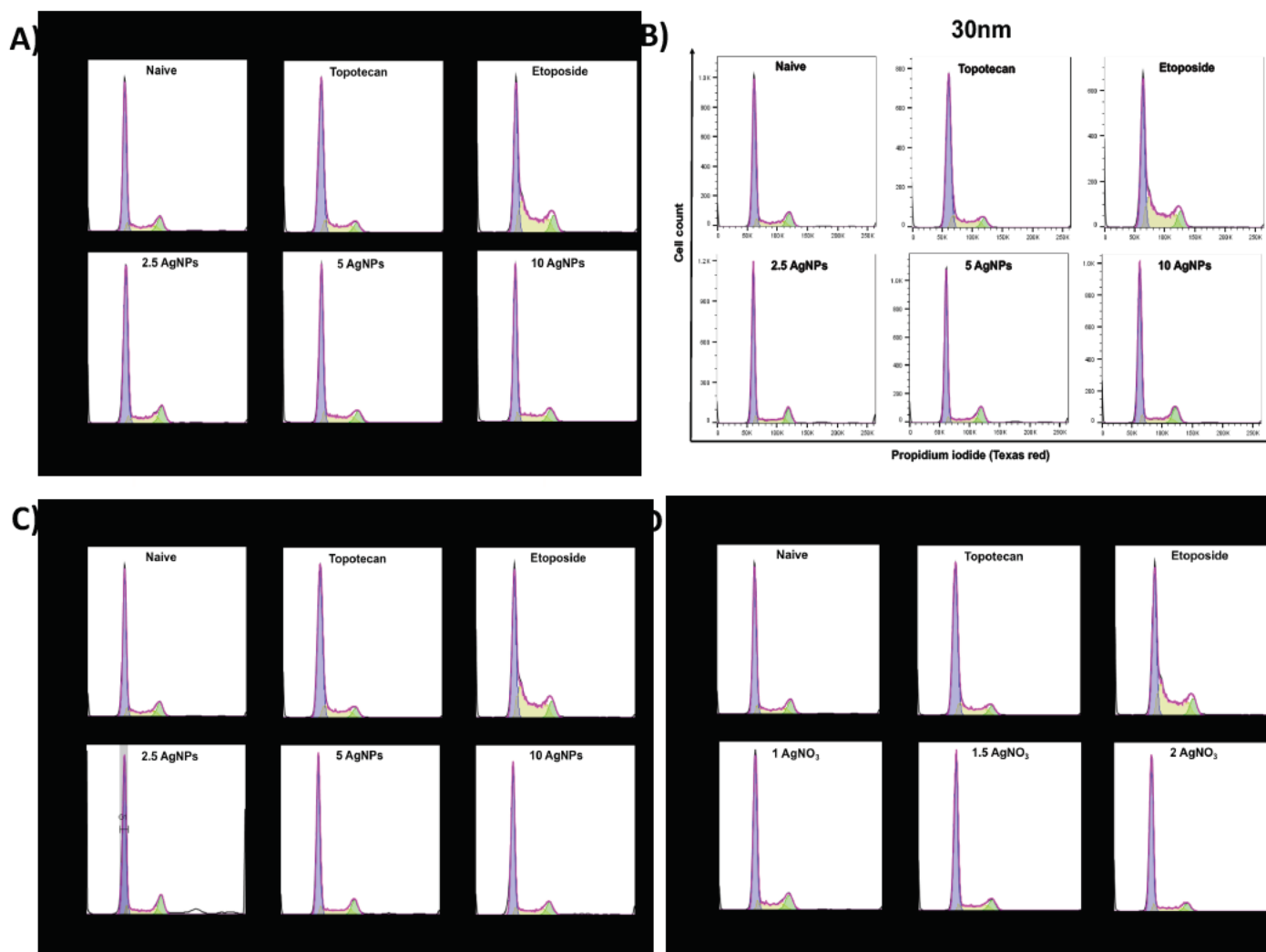


Figure S8.6. Propidium iodide intensities versus the total cell counts (10,000) were analysed by FlowJo V10 software using the cell cycle tool. A) shows data for 10 nm, B) for 30 nm, C) for 100nm AgNPs, and D) for the ionic control (AgNO₃). Cell cycle images represent one of three individual replicates used for the analysis

8.2.9 Comet assay to determine NM-induced DNA breaks

Table S8.15. Full results of DNA tail percentage of three individual replicates from Comet assay. The table shows the results obtained by scoring 50 comets per replicate, for a total of 150 comets per treatment. No statistical analyses were performed for this data.

Controls									
	R1			R2			R3		
Naive	0.915			1.177			3.566		
DMSO	78.076			51.049			42.562		
AgNPs									
NP size	2.5 µg/mL			5 µg/mL			10 µg/mL		
	R1	R2	R3	R1	R2	R3	R1	R2	R3
10 nm	6.045	10.57 9	6.045	6.090	13.93 1	6.090	13.48 9	7.372	13.48 9
30 nm	4.838	15.29 2	4.838	3.293	20.08 3	3.293	5.188	11.00 2	15.18 8
100 nm	5.862	7.361	5.862	5.108	9.670	5.108	7.495	15.40 4	7.495
AgNO ₃									
	1 µg/mL			1.5 µg/mL			2 µg/mL		
N/A	79.04 6	74.40 2	78.99 3	80.98 4	83.60 8	83.40 9	83.59 3	81.86 0	83.25 7

Table S8.16. Summary of the DNA percentage strand breaks (%). Results represent the mean DNA tail percentage of three individual replicates, obtained by scoring 50 comets per replicate, for a total of 150 comets per treatment. Comets were analysed and scored using IV comet macro software. H₂O₂ was used as the positive control. Data with asterisks (*) indicate statistically significant differences between AgNPs treatments (*p < 0.05, ***p < 0.001) and the naïve cells. Similar letters (upper and lower case) next to the values represent statistically significant difference (p < 0.05) between the selected NM concentrations.

AgNPs					
AgNPs Size (nm)	Naive	H ₂ O ₂ 200µM	2.5 AgNPs	5 AgNPs	10 AgNPs
10nm	1.88 ± 1.45	46.81 ± 6.02	7.55 ± 2.61	8.70 ± 4.52	11.45 ± 3.53*

30nm	1.88 ± 1.45	46.81 ± 6.02	8.32 ± 6.03	8.88 ± 9.69	10.46 ± 5.02
100nm	1.88 ± 1.45	46.81 ± 6.02	6.36 ± 0.86	6.62 ± 2.63	10.13 ± 4.56*
AgNO₃					
AgNO₃	Naive	H₂O₂	1 AgNO₃	1.5 AgNO₃	2 AgNO₃
		200µM	(µg/mL)	(µg/mL)	(µg/mL)
	1.88 ± 1.45	46.81 ± 6.02	79.48 ± 2.67***AB	82.67 ± 1.46***b	82.90 ± 0.91***a

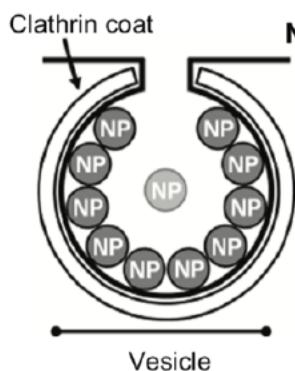
8.2.10 Estimation of the uptake mechanism via membrane bound or fluid phase internalization.

A calculation was used to quantitatively estimate the likelihood of NPs entering cells through either direct membrane bound interactions or through fluid encapsulation, based upon the properties of the vesicles and the NPs (e.g., NP size) as described in [91] and [238].

First, the number of NPs/mL present (for the highest AgNPs concentration, 10 µg/mL) was calculated as described in the section “particle number concentration” in the supplementary information of Chapter 2. Then, the NPs/mL was calculated for the three AgNP sizes and was substituted into the following equations (shown also in Table S17).

Notation:

- Vesicle diameter $D = 150$ nm,
- Clathrin coat thickness $C = 22$ nm,
- Lipid bilayer thickness $L = 5$ nm,
- NP concentration in fluid $c = 4.54 \times 10^{13}$ NPs/mL,
- NP radius $P = 10$ nm,
- Inner lumen radius of a vesicle $r = D/2 - C - L$,
- Internal volume of a vesicle $V = 4\pi r^3/3$.



Number of NP entering through different mechanisms:

- Fluid phase: An average volume V of NP laden fluid contains $N_f = V_c$ nanoparticles
- Receptor mediated: NPs will pack like circles on an inner radius $\rho = r - p$. We neglect the curvature of the vesicle and calculate the number of NPs which can bind simultaneously to a flat region with equivalent surface area giving $N_R = 0.91 (4\pi\rho^2)/(\pi P^2)$ nanoparticles (where 0.91 is the circle close packing density). Note this will be an over estimate

Figure S7. Number of particles entering through different mechanisms.

The calculations are based on the hypothesis that the membrane surface has the ability to be coated in NPs as described in Guggenheim *et al.*, (2020) and Smith *et al.*, (2012). Three possible diameters of the vesicles (150, 300 and 500 nm) were used to further understand the likelihood of the NPs entering the cells via the different routes, as suggested by [91, 238]. In each case, the calculations are likely to be an over-estimation, partly due to neglecting the membrane surface curvature in the NP attachment at the surface; however, they provide insights about the likelihood of uptake via the different possible NP uptake routes. Table S17 exemplifies the calculations used, and the input data based on the 10 nm AgNPs. The remaining concentrations are shown in Figure S7.

Table S8.17. Calculations to obtain the estimated number of particles that can enter a cell through fluid-phase endocytosis compared to via receptor mediated endocytosis. Equations adapted from [91, 238]. The equations can be used to determine the most likely means of NP entry: fluid phase or receptor mediated. The close circle packing density (where all NPs are touching and attached to a flat surface) is 0.91. The curvature of the membrane is neglected and therefore the estimated uptake rate is likely to be an overestimation. Formulas are represented as shown in an Excel sheet.

Notation	Value	Details/unit
Vesicle diameter (D)	150	nm
Coat thickness (C)	22	nm
Lipid bilayer thickness (L)	5	nm
NP concentration (c)	1.76E+12	NP/mL (10µg/mL only)
NP radius (P)	10	nm
Fluid phase (passive) clathrin		
r	$(D/2)-C-L$	Inner radius
Internal volume vesicle (V)	$(4*PI*r^3)/3$	Lumen volume
p	r-P	Packing radius lumen
NP on surface (N ₁)	$0.91*(4*PI*p^2)/(PI*P^2)$	NPs on surface
N _f	V*c	NP in lumen
Receptor mediated No clathrin		

r	$(D/2)-L$	Inner radius
Internal volume vesicle (V)	$(4*PI*r^3)/3$	Lumen volume
p	r-P	Packing radius lumen
NP on surface (N_1)	$0.91*(4*PI*p^2)/(PI*P^2)$	NPs on surface
N_f	$V*c$	NP in lumen

Table S8.18. Summary of the calculations of the likelihood of NPs entry into the ZF4 cells via fluid phase of membrane bound mechanisms. The table shows the results obtained using the calculations previously described (Table S8.17) for three vesicle diameters and the three different AgNP sizes (10, 30 and 100 nm).

AgNPs size (10 nm)				
Vesicle diameter	Fluid phase (clathrin-coated)		Membrane bound / receptor mediated (non clathrin coated)	
	NPs on surface	NPs in lumen	NPs on surface	NPs in lumen
150 nm	52.56	8.15E+17	131.04	2.53E+18
300 nm	464.79	1.37E+19	663.39	2.25E+19
500 nm	1651.43	8.18E+19	2010.19	1.08E+20
AgNPs size (30 nm)				
Vesicle diameter	Fluid phase (clathrin assumption)		Membrane bound (receptor mediated) no Clathrin coat	
	NPs on surface	NPs in lumen	NPs on surface	NPs in lumen
150 nm	1.31	2.71E+16	6.47	8.41E+16
300 nm	34.98	4.56E+17	53.49	7.47E+17
500 nm	150.65	2.72E+18	186.95	3.60E+18
AgNPs size (100 nm)				
Vesicle diameter	Fluid phase (Clathrin assumption)		Membrane bound (receptor mediated) no Clathrin coat	
	NPs on surface	NPs in lumen	NPs on surface	NPs in lumen
150 nm	0.98	7.74E+14	0.33	2.40E+15
300 nm	0.19	1.30E+16	0.74	2.13E+16
500 nm	5.51	7.76E+16	7.65	1.03E+17

30 nm Size			30 nm Size			30 nm Size		
Vesicle diameter D)	150	nm	Vesicle diameter D)	300	nm	Vesicle diameter D)	500	nm
Coat thickness C)	22	nm	Coat thickness C)	22	nm	Coat thickness C)	22	nm
Lipid bilayer thickness L)	5	nm	Lipid bilayer thickness L)	5	nm	Lipid bilayer thickness L)	5	nm
NP concentration c)	5.85E+10	NP/mL (10µg/mL only)	NP concentration c)	5.85E+10	NP/mL	NP concentration c)	5.85E+10	NP/mL
NP radius P)	30	nm	NP radius P)	30	nm	NP radius P)	30	nm
Fluid phase (passive) clathrin			Fluid phase (passive) clathrin			Fluid phase (passive) clathrin		
r	48	Inner radius	r	123	Inner radius	r	223	Inner radius
Internal volume vesicle V)	463247	Lumen volume	Internal volume vesicle V)	7794781	Lumen volume	Internal volume vesicle V)	46451870	Lumen volume
p	18	Packing radius lumen	p	93	Packing radius lumen	p	193	Packing radius lumen
NP on surface N ₁)	1.31	Np on surface	NP on surface N ₁)	34.98	Np on surface	NP on surface N ₁)	150.65	Np on surface
N _f	2.71E+16	NP in lumen	N _f	4.56E+17	NP in lumen	N _f	2.72E+18	NP in lumen
Receptor mediated No clathrin			Receptor mediated No clathrin			Receptor mediated No clathrin		
r	70		r	145		r	245	
Internal volume vesicle V)	1436755		Internal volume vesicle V)	12770051		Internal volume vesicle V)	61600872	
p	40		p	115		p	215	
NP on surface N ₁)	6.47		NP on surface N ₁)	53.49		NP on surface N ₁)	186.95	
N _f	8.41E+16		N _f	7.47E+17		N _f	3.60E+18	
10 nm Size			10 nm Size			10 nm Size		
Vesicle diameter D)	150	nm	Vesicle diameter D)	300	nm	Vesicle diameter D)	500	nm
Coat thickness C)	22	nm	Coat thickness C)	22	nm	Coat thickness C)	22	nm
Lipid bilayer thickness L)	5	nm	Lipid bilayer thickness L)	5	nm	Lipid bilayer thickness L)	5	nm
NP concentration c)	1.76E+12	NP/mL (10µg/mL only)	NP concentration c)	1.76E+12	NP/mL	NP concentration c)	1.76E+12	NP/mL
NP radius P)	10	nm	NP radius P)	10	nm	NP radius P)	10	nm
Fluid phase (passive) clathrin			Fluid phase (passive) clathrin			Fluid phase (passive) clathrin		
r	48	Inner radius	r	123	Inner radius	r	223	Inner radius
Internal volume vesicle V)	463247	Lumen volume	Internal volume vesicle V)	7794781	Lumen volume	Internal volume vesicle V)	46451870	Lumen volume
p	38	Packing radius lumen	p	113	Packing radius lumen	p	213	Packing radius lumen
NP on surface N ₁)	52.56	Np on surface	NP on surface N ₁)	464.79	Np on surface	NP on surface N ₁)	1651.43	Np on surface
N _f	8.15E+17	NP in lumen	N _f	1.37E+19	NP in lumen	N _f	8.18E+19	NP in lumen
Receptor mediated No clathrin			Receptor mediated No clathrin			Receptor mediated No clathrin		
r	70		r	145		r	245	
Internal volume vesicle V)	1436755		Internal volume vesicle V)	12770051		Internal volume vesicle V)	61600872	
p	60		p	135		p	235	
NP on surface N ₁)	131.04		NP on surface N ₁)	663.39		NP on surface N ₁)	2010.19	
N _f	2.53E+18		N _f	2.25E+19		N _f	1.08E+20	

100 nm Size			100 nm Size			100 nm Size		
Vesicle diameter D)	150	nm	Vesicle diameter D)	300	nm	Vesicle diameter D)	500	nm
Coat thickness C)	22	nm	Coat thickness C)	22	nm	Coat thickness C)	22	nm
Lipid bilayer thickness L)	5	nm	Lipid bilayer thickness L)	5	nm	Lipid bilayer thickness L)	5	nm
NP concentration c)	1.67E+09	NP/mL (10µg/mL only)	NP concentration c)	1.67E+09	NP/mL	NP concentration c)	1.67E+09	NP/mL
NP radius P)	100	nm	NP radius P)	100	nm	NP radius P)	100	nm
Fluid phase (passive) clathrin			Fluid phase (passive) clathrin			Fluid phase (passive) clathrin		
r	48	Inner radius	r	123	Inner radius	r	223	Inner radius
Internal volume vesicle V)	463247	Lumen volume	Internal volume vesicle V)	7794781	Lumen volume	Internal volume vesicle V)	46451870	Lumen volume
p	-52	Packing radius lumen	p	23	Packing radius lumen	p	123	Packing radius lumen
NP on surface N ₁)	0.98	N _p on surface	NP on surface N ₁)	0.19	N _p on surface	NP on surface N ₁)	5.51	N _p on surface
N _r	7.74E+14	N _p in lumen	N _r	1.30E+16	N _p in lumen	N _r	7.76E+16	N _p in lumen
Receptor mediated No clathrin			Receptor mediated No clathrin			Receptor mediated No clathrin		
r	70		r	145		r	245	
Internal volume vesicle V)	1436755		Internal volume vesicle V)	12770051		Internal volume vesicle V)	61600872	
p	-30		p	45		p	145	
NP on surface N ₁)	0.33		NP on surface N ₁)	0.74		NP on surface N ₁)	7.65	
N _r	2.40E+15		N _r	2.13E+16		N _r	1.03E+17	

Figure S8.8. Calculations to obtain the number of particles that can enter a cell through fluid-phase endocytosis compared to entry via receptor mediated endocytosis for all AgNP concentrations and sizes. Formulas for each step can be found above as Table S17.

9. SI Chapter 4

Cellular uptake mechanisms of silver nanoparticles (AgNPs) in embryonic zebrafish cells (ZF4)

9.1 Results

9.1.1 Characterisation of the AgNPs.

Table S9.1. Full results for the characterisation of the AgNPs. R means replicate. The characterisation of the AgNPs was performed by different methods including Dynamic Light scattering (DLS), and Ultraviolet–visible spectroscopy (UV-vis). Polydispersity index and zeta potential were evaluated by DLS. No statistical analyses were performed on this data.

		Complete Culture Media (CCM)								
NP size		10 nm			30 nm			100 nm		
Time (hours)		Hydrodynamic diameter (nm)								
		R1	R2	R3	R1	R2	R3	R1	R2	R3
0		73.83	69.92	63.97	75.28	73.48	75.67	138.7	138.8	136.9
24		131.13	126	128.5	136.5	178.4	167.2	177.7	182.3	186.2
		Polydispersity index (PDI)								
0		0.482	0.476	0.483	0.298	0.298	0.303	0.053	0.069	0.041
24		0.517	0.497	0.5	0.358	0.438	0.479	0.129	0.145	0.158
		Zeta potential (mV)								
0		-7.48	-7.44	-8.38	-8.64	-8.61	-8.78	-8.42	-7.9	-7.97
24		-11.4	-12.2	-13.1	-10.7	-9.48	-11.2	-8.4	-10.9	-10.8
		Ultra-pure water (UPW)								
Time (hours)		Hydrodynamic diameter (nm)								
0		66.83	66.77	65.49	76.8	75.8	78.45	130	131.1	127.9
24		66.67	68.27	69.23	80.95	80.79	82.72	128.9	125.8	126.6
		Polydispersity index (PDI)								
0		0.434	0.421	0.426	0.146	0.143	0.146	0.071	0.071	0.051
24		0.43	0.415	0.432	0.133	0.148	0.153	0.047	0.027	0.031
		Zeta potential (mV)								
0		-18.4	-17.2	-17.6	-27.9	-29.2	-28.7	-52.6	-51.7	-50
24		-18	-21.4	-21.6	-28.5	-29	-33	-24.1	-23.3	-23

Table S9.2. Characterisation of the AgNPs in Ultrapure Water (UPW) and Complete Culture Media (CCM) (DMEM-F12 supplemented with 10% FBS) at 0 and 24 hours. Results represent the mean of three individual replicates and their standard deviation. Data with asterisks (*) indicate statistical differences (* $p < 0.05$ and ** $p < 0.01$) between timepoints (0 and 24 hours) for the selected NP size. Similar letters (upper and lowercase letters) beside the values represent statistically significant differences ($p < 0.05$) between the selected sizes for the same testing fluid. Identical symbols denote statistical difference ($p < 0.05$) between water and CCM for the same NM size.

10 nm				
	Water 0 hours	Water 24 hours	CCM 0 hours	CCM 24 hours
Hydrodynamic diameter (DLS)	66.36 ± 0.7 C	68.05 ± 1.29 \$cd	69.24 ± 4.96** A	128.54 ± 2.56 ** \$ab
PDI	0.42 ± 0.007	0.42 ± 0.009	0.48 ± 0.004	0.505 ± 0.001
Zeta potential (mV)	-17.73 ± 0.61	-20.33 ± 2.02*	-7.48 ± 0.53	-12.23 ± 0.85
UV-Vis (abs)	1.283 ± 0.000	0.745 ± 0.000	0.952 ± 0.000	0.552 ± 0.000
30 nm				
	Water 0 hours	Water 24 hours	CCM 0 hours	CCM 24 hours
Hydrodynamic diameter (DLS)	77.01 ± 1.33 D	81.48 ± 1.07*	74.81 ± 1.61 B	160.70 ± 21.69
PDI	0.14 ± 0.002	0.14 ± 0.01	0.30 ± 0.003	0.42 ± 0.06
Zeta potential (mV)	-28.60 ± 0.65	-30.16 ± 2.46	-8.67 ± 0.09	-10.46 ± 0.88
UV-Vis (abs)	0.698 ± 0.010	0.403 ± 0.011	1.093 ± 0.003	1.072 ± 0.000
100 nm				
	Water 0 hours	Water 24 hours	CCM 0 hours	CCM 24 hours
Hydrodynamic diameter (DLS)	129.66 ± 1.62	127.1 ± 1.60 %	138.13 ± 1.06	182.06 ± 4.25* %
PDI	0.06 ± 0.01	0.03 ± 0.011	0.05 ± 0.01	0.14 ± 0.01
Zeta potential (mV)	-51.43 ± 1.32	-23.46 ± 0.56	-8.09 ± 0.28*	-10.03 ± 1.41
UV-Vis (abs)	0.318 ± 0.037	0.293 ± 0.001	0.617 ± 0.002	1.195 ± 0.003

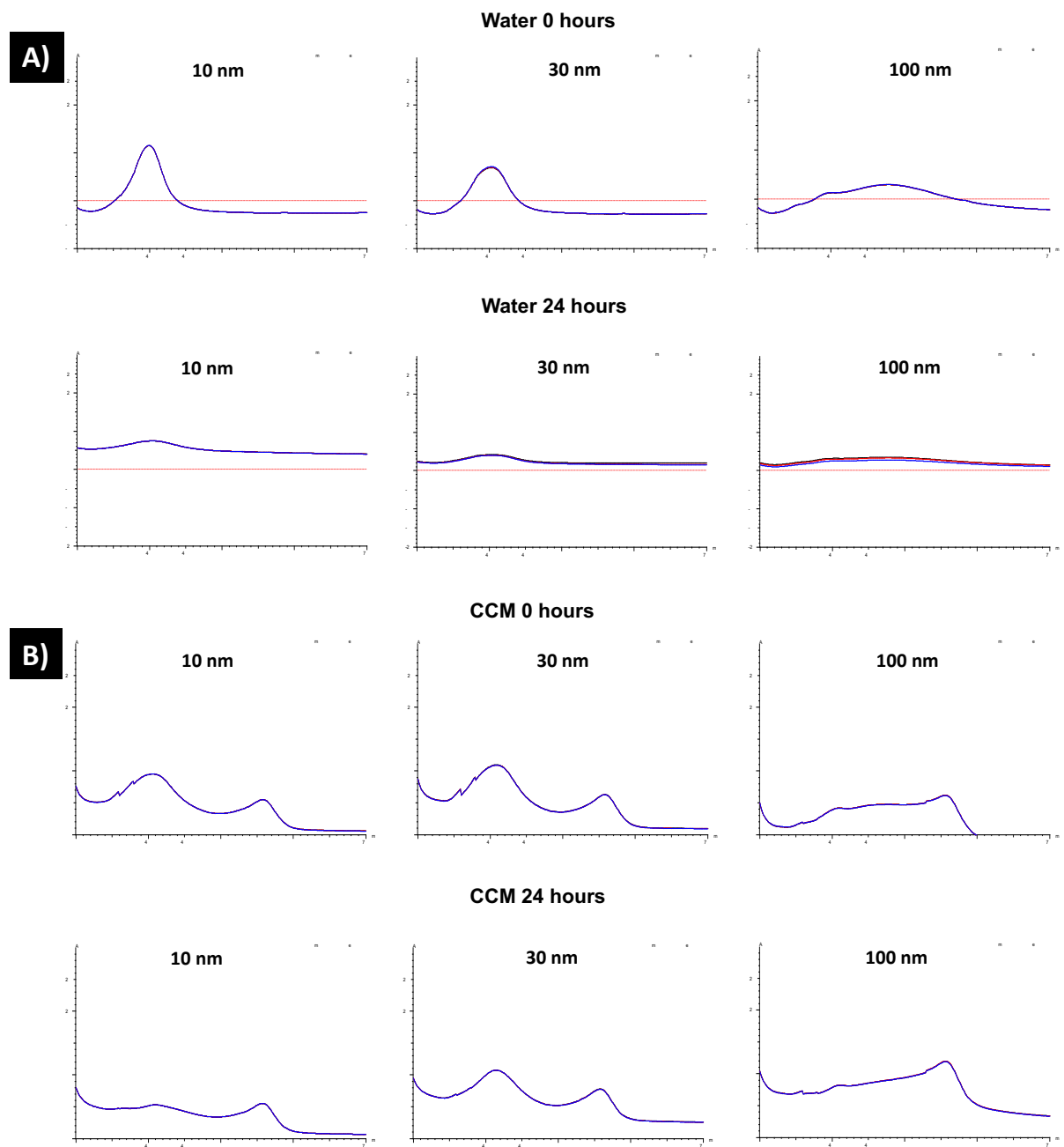


Figure S1. UV-vis images of the 10, 30 and 100 nm AgNPs at 0 and 24 hours in (A) UPW and (B) CCM.

9.1.2 Cellular uptake determined by Inductively Coupled Plasma Mass Spectrometry (ICP-MS)

The total intracellular concentration of Ag⁺ (µg/mL) was measured using ICP-MS after different exposure times. All concentrations were above the ICP-MS detection limit (0.000005 µg/mL).

Table S9.3. Results of the intracellular total Ag. Results were obtained after analysis of the total Ag concentration in ZF4 cells using ICP-MS. Data is presented in µg/mL and was obtained after multiplication by the dilution factor used when preparing the samples for analysis. R means replicate. No statistical analyses were performed for this data.

NPs size	2.5 µg/mL			5 µg/mL			10 µg/mL		
	R1	R2	R3	R1	R2	R3	R1	R2	R3
2 hours									
10 nm	1.46	0.41	0.54	0.83	0.49	0.47	0.36	0.22	0.19
30 nm	0.13	0.02	0.02	0.01	0.01	0.03	0.03	0.03	0.03
100 nm	0.051	0.06	0.09	0.03	0.04	0.04	0.04	0.02	0.03
24 hours									
10 nm	0.73	1.023	0.836	2.891	3.016	2.829	2.721	6.486	5.97
30 nm	0.718	0.417	0.506	0.828	0.859	0.914	2.721	2.726	2.365
100 nm	1.322	1.388	1.554	2.684	2.73	3.282	6.001	4.82	4.587

Table S9.4. Results for the total Ag⁺ concentration determined by ICP-MS. Cells were treated with different concentrations and sizes of AgNPs for 2 and 24 hours. Results (µg/mL) represent the mean of three independent replicates and their standard deviation (mean ± SD). Data with asterisks (*) indicate a statistically significant difference (*p < 0.05 and ***p < 0.001) between cells treated with AgNPs and naive cells (non-treated cells) (0.003 ± 0.006) for each time point and concentration. Similar letters (upper and lowercase letters) next to the values represent statistically significant differences (p < 0.05) between the selected concentrations and sizes.

AgNP size	AgNP concentration		
	2.5 µg/mL	5 µg/mL	10 µg/mL
2 hours			
10 nm	0.80 ± 0.57	0.59 ± 0.20	0.25 ± 0.09 j
30 nm	0.05 ± 0.06	0.01 ± 0.01	0.03 ± 0.01
100 nm	0.07 ± 0.02 J	0.03 ± 0.006	0.03 ± 0.01
24 hours			
10 nm	0.86 ± 0.14 AB	2.91 ± 0.09*** bcD	5.05 ± 2.20 EG

30 nm	0.54 ± 0.15 ef	0.86 ± 0.04*** HI	2.60 ± 0.20* g
100 nm	1.42 ± 0.12* cdi	2.88 ± 0.33* h	5.13 ± 0.75* af

9.1.3 Inhibition of the cellular uptake pathways

Table S9.5. Inhibition of the cellular uptake pathways by their respective positive controls. The pharmaceutical inhibitor concentrations were confirmed by inhibition of the respective specific pathway using confocal microscopy. R means replicate. Results are expressed in arbitrary units (A.U.) unless otherwise stated. Intensity results were normalised to % with respect to naive (non- inhibited cells). Data with asterisks (*) indicate a statistically significant difference (**p < 0.01) compared to the naive cells. No statistical analysis was performed for this data.

Genistein			
	R1	R2	R3
Control	95.742	113.776	140.576
Inhibitor	89.197	94.164	92.17
Normalised %	76.43	80.69	78.98
Average (%) ± SD	78.70 ± 2.14***		
Chlorpromazine			
Control	111.581	138.419	165.829
Inhibitor	101.612	104.204	107.912
Normalised %	73.31	75.18	77.85
Average ± SD	75.44 ± 2.28***		
Wortmannin			
Control	137.573	136.746	137.544
Inhibitor	111.283	107.87	107.293
Normalised %	81.06	78.57	78.15
Average ± SD	79.26 ± 1.57***		

Table S9.6. Cell viability after application of the various receptor inhibitors. The results were obtained using LDH activity (Absorbance at 440 nm). Normalised (%) results were obtained by normalising absorbance against the naïve cells. Average represents the mean ± SD of three replicates. Data with asterisks (*) indicate a statistically significant difference (**p < 0.01) compared to the naive cells.

Absorbance (A.U)			
	R1	R2	R3
Control	0.2756	0.2729	0.2644
Gen	0.2571	0.2463	0.246

CLZ	0.2059	0.2143	0.2521
Wort	0.2527	0.2273	0.2375
Normalised (%)			
Control	100.8969	99.90848	96.79663
CLZ	94.12411	90.17024	90.06041
wort	75.37983	78.45506	92.29361
Gen	92.51327	83.21435	86.94856
Average (%)			
Control	100 ± 0		
CLZ	87.55 ± 4.67		
wort	91.45 ± 2.31**		
Gen	82.04 ± 9.00		

After confirming the effective receptor inhibition using confocal microscopy, the selected inhibitor concentrations were used to inhibit the desired pathways, and the total amount of Ag⁺ was assessed by ICP-MS and compared to that in the untreated control. Any difference is due to a reduction of the specific internalisation pathway. Chlorpromazine is an inhibitor of the clathrin-mediated uptake pathway, while genistein interferes with caveolae-mediated endocytosis and wortmannin also inhibits macropinocytosis.

Table S9.7. Primary ICP-MS data for Ag content in cells treated with the different inhibitors. Results represent the raw data (after correction for the dilution factor) obtained using ICP-MS. Results are expressed in $\mu\text{g/mL}$. No statistical analyses were performed for this data.

NPs size	Concentration and replicate	Control (no inhibitor)			Chlorpromazine			Genistein			Wortmannin		
		R1	R2	R3	R1	R2	R3	R1	R2	R3	R1	R2	R3
10 nm	2.5 AgNPs	0.375	0.370	0.391	0.364	0.388	0.380	0.260	0.257	0.276	0.267	0.125	0.207
	5 AgNPs	1.191	1.202	1.012	1.038	1.159	0.973	0.302	0.329	0.414	0.286	0.332	0.323
	10 AgNPs	4.624	4.497	4.998	1.669	2.101	1.813	0.317	0.370	0.264	0.380	0.310	0.750
30 nm	2.5 AgNPs	0.429	0.388	0.439	0.256	0.409	0.313	0.070	0.061	0.094	0.193	0.322	0.283
	5 AgNPs	0.686	0.693	0.758	0.678	0.607	0.560	0.213	0.232	0.199	0.571	0.264	0.717
	10 AgNPs	1.325	1.314	1.286	1.320	1.325	1.311	0.523	0.349	0.376	0.390	0.486	0.443
100 nm	2.5 AgNPs	0.720	0.686	0.961	0.256	0.409	0.313	0.125	0.116	0.164	0.345	0.589	0.533
	5 AgNPs	1.141	1.116	1.067	0.678	0.607	0.560	0.314	0.363	0.297	0.878	0.402	0.439
	10 AgNPs	1.483	1.434	1.535	1.590	1.325	1.311	0.582	0.392	0.421	0.435	0.554	0.494

Table S9.8. Normalised results of internalised Ag determined by ICP-MS following treatment of the cells with the inhibitors. Table shows results normalised to percentage (%) against naïve. R means replicate. No statistical analyses were performed for this data.

NPs size	Concentration and replicate	Control (no inhibitor)			Chlorpromazine			Genistein			Wortmannin		
		R1	R2	R3	R1	R2	R3	R1	R2	R3	R1	R2	R3
10 nm	2.5 AgNPs	99.09	97.80	103.11	96.11	102.47	100.43	68.64	67.79	72.98	70.45	33.03	54.72
	5 AgNPs	104.94	105.89	89.18	91.45	102.15	85.71	26.64	29.02	36.48	25.20	29.22	28.43
	10 AgNPs	98.25	95.55	106.20	35.46	44.64	38.53	6.74	7.86	5.62	8.07	6.59	15.94
30 nm	2.5 AgNPs	102.45	92.74	104.81	61.24	97.77	74.79	16.75	14.57	22.39	45.98	76.99	67.58
	5 AgNPs	96.37	97.23	106.40	95.24	85.28	78.65	29.91	32.64	27.95	80.16	37.04	100.72
	10 AgNPs	101.28	100.41	98.31	100.87	101.24	100.19	39.94	26.68	28.70	29.83	37.17	33.90
100 nm	2.5 AgNPs	93.20	88.69	124.36	33.18	52.98	40.52	16.16	14.97	21.18	44.62	76.25	68.93
	5 AgNPs	103.00	100.68	96.32	61.23	54.83	50.57	28.32	32.76	26.77	79.22	36.28	39.62
	10 AgNPs	99.96	96.66	103.42	107.12	89.26	88.33	39.23	26.40	28.34	29.31	37.32	33.31

Table S9.9. Inhibition of uptake pathways and resulting changes in AgNP uptake and internalisation. After the inhibition of the desired pathway, cells were treated with the different concentrations and sizes of AgNP for 2 hours. Then, the total Ag⁺ was quantified using ICP-MS. The results are normalized to percentage against their control (no inhibitor). The results represent the mean of three individual replicates ± standard deviation. Data with asterisks (*) indicate statistically significant differences between AgNPs treatments compared with the naïve control (*p < 0.05, **p < 0.01, and ***p < 0.001). Similar letters (upper and lowercase letters) next to the values represent statistically significant difference (p < 0.05) between the selected concentrations and inhibitors.

AgNP concentration	Control (no inhibitor)	Chlorpromazine (clathrin-mediated)	Genistein (caveolae-mediated)	Wortmannin (macro pinocytosis)
10 nm				
2.5 µg/mL	100 ± 2.76	98.70 ± 2.24 A	70.38 ± 3.67*** a	54.48 ± 19.30
5 µg/mL	100 ± 6.38	93.10 ± 8.34 BC	30.71 ± 5.13* b	27.61 ± 2.12* c
10 µg/mL	100 ± 5.53	39.54 ± 4.67* DE	6.74 ± 1.12** d	7.27 ± 1.05*** e
30 nm				
2.5 µg/mL	100 ± 2.76	77.38 ± 17.57	17.90 ± 4.03**	63.16 ± 16.47
5 µg/mL	100 ± 6.38	86.53 ± 8.32	30.16 ± 2.35* F	72.64 ± 32.44 f
10 µg/mL	100 ± 5.53	100.7 ± 0.75 GH	31.68 ± 7.24** g	33.67 ± 3.60** h
100 nm				
2.5 µg/mL	100 ± 2.76	42.22 ± 10.24	17.43 ± 3.91*	63.26 ± 16.55
5 µg/mL	100 ± 6.38	55.54 ± 5.36** I	29.28 ± 3.10** i	51.70 ± 23.88
10 µg/mL	100 ± 5.53	94.04 ± 10.59 JK	31.32 ± 6.91* j	33.31 ± 4.00** k

9.1.4 Visualisation of the intracellular AgNPs

Cells were treated with the highest concentration of 10, 30 and 100 nm AgNPs (10 µg/mL) for 24 hours, then cells were processed (for transmission electron microscopy (TEM) analysis to assess the size of the internalised AgNPs. Images of the ultramicrotome sections were recorded using JEOL 1200EX 80kV and JEOL 1400EX 80kV microscopes. The intracellular size of the AgNPs in the vacuoles was

calculated using Image J software. A total of 20 NPs were counted for each AgNPs size to calculate their average size and standard deviation. Similarly, the diameter of 3 vacuoles (with AgNPs inside) was used to calculate their average size and standard deviation following internalisation of particles of each size.

To calculate the percentage of reduction of the AgNP size following internalisation by the cells, the following calculations were implemented. First, the NP diameter was normalised to percentage (%) based on the NP core size obtained using TEM. The TEM samples for core size were prepared in UPW as described in the supplementary information of Chapter 2.

- 1)
$$\text{Diameter in \%} = \frac{(\text{Mean NPs diameter} * 100)}{\text{NPs TEM size}}$$
- 2)
$$\% \text{ of reduction} = \text{Diameter in \%} - 100$$

Table S9.10. Intracellular AgNP size determined by TEM. Cells were treated with 10 µg/mL of different AgNPs sizes for 24 hours and processed for TEM analysis. The NPs inside the vesicles were counted to calculate their average and standard deviation. The diameter of 3 vacuoles (with AgNPs inside) were used to calculate their average and standard deviation for each AgNP size.

AgNPs size	TEM size (nm)	Intracellular NPs		Vacuole diameter nm
		Size (nm)	Reduction (%)	
10 nm	13 ± 2.4	5.50 ± 3.56	57.62	717.46 ± 78.57
30 nm	34 ± 2.8	27.52 ± 4.20	19.04	678.87 ± 2.17
100 nm	101 ± 9.2	96.78 ± 8.36	4.12	697.86 ± 53.76

9.1.5 Early endosomes induction (EEI).

Table S9.11. Data for early endosomes induction (EEI) in response to AgNP exposure. The table shows the raw intensity values determined by fluorescence. R means replicate. Results are expressed in arbitrary units (A.U.) unless otherwise stated. No statistical analyses were performed for the raw data.

	2 hours								
Naive	31353			34564			34087		
	2.5 µg/mL			5 µg/mL			10 µg/mL		
	R1	R2	R3	R1	R2	R3	R1	R2	R3
10 nm	40080	40771	47191	40591	41545	42989	41415	43404	46918
30 nm	40343	40508	47499	41002	44067	45073	41877	43613	50134
100 nm	45008	40502	47900	45820	46390	40326	45831	42524	42491
	24 hours								
10 nm	40019	40957	45630	40228	40202	41681	41148	43002	45724
30 nm	41340	42054	46143	41433	44850	44434	40999	44318	49785
100 nm	44348	43460	47500	44147	45004	47320	46568	45048	44244

Table S9.12. Normalised results of EEI in response to AgNP exposure. Table shows results normalised to percentage (%) against naïve. R means replicate. No statistical analyses were performed for this data.

	2 hours								
	2.5 µg/mL			5 µg/mL			10 µg/mL		
	R1	R2	R3	R1	R2	R3	R1	R2	R3
10 nm	120.24	122.31	141.57	121.77	124.63	128.96	124.24	130.21	140.75
30 nm	121.02	121.52	142.49	123.00	132.20	135.21	125.63	130.83	150.40
100 nm	135.02	121.50	143.69	137.45	139.16	120.97	137.49	127.57	127.47
	24 hours								

10 nm	105.39	107.86	120.16	105.94	105.87	109.76	108.36	113.24	120.41
30 nm	108.86	110.75	121.51	109.11	118.11	117.01	107.97	116.71	131.10
100 nm	116.79	114.45	125.09	116.26	118.51	124.61	122.63	118.63	116.51

Table S9.13. Early endosome induction (EEI) in response to AgNP exposure. Cells were exposed to different concentrations and sizes of AgNPs for 2 and 24 hours, then the intensity of red fluorescent protein was recorded using a fluorescence plate reader and results normalised to percentage (%) against naïve. Results show the average of three individual replicates and their standard deviation. Data with asterisks (*) indicate statistically significant differences between AgNPs treatments compared with the naïve control at each time point (*p < 0.05, **p < 0.01). Data with upper and lowercase letters next to the values indicate statistical differences (p < 0.05) between the selected NP sizes and concentrations.

AgNPs size	Naive	2.5 µg/mL	5 µg/mL	10 µg/mL
2 hours				
10 nm	100 ± 0.0	128.62 ± 11.76	125.1 ± 3.62**	131.73 ± 8.35
30 nm	100 ± 0.0	128.34 ± 12.25	130.1 ± 6.36*	135.61 ± 13.06
100 nm	100 ± 0.0	133.40 ± 11.18	132.5 ± 10.05	130.84 ± 5.75*
24 hours				
10 nm	100 ± 0.0	111.13 ± 7.91	107.18 ± 2.22 A	114.0 ± 6.06
30 nm	100 ± 0.0	131.70 ± 6.82	114.74 ± 4.91	118.59 ± 11.68*
100 nm	100 ± 0.0	118.77 ± 5.59	119.79 ± 4.32 a	119.25 ± 3.10*

9.1.6 Autophagy response

Table S9.14. Autophagy induction following AgNP exposure. The autophagy response was assessed by confocal microscopy. Images were taken and the intensity of the fluorescein isothiocyanate (FITC) filter, which has a fluorescence excitation/emission of 499/521 nm (autophagosome marker, Cell Meter™ assay kit) in cells after the exposure of AgNPs was recorded. R means replicate. No statistical analyses were performed for this data.

	R1			R2			R3		
Naive	1012.508			1012.508			1012.508		
	AgNPs concentrations								
	2.5 µg/mL			5 µg/mL			10 µg/mL		
NP size	R1	R2	R3	R1	R2	R3	R1	R2	R3
10 nm	2196.162	1682.631	2214.944	1798.908	1252.542	1949.523	2010.764	2120.382	1329.783
30 nm	1433.964	1054.893	1354.358	983.305	979.783	1064.82	910.679	1158.456	988.932
100 nm	945.928	966.004	1023.956	960.935	1058.524	863.213	911.031	909.337	966.223

Table S9.15. Normalised autophagy results. Table shows normalised results to percentage (%) against naïve. R means replicate. No statistical analyses were performed for this data.

	AgNPs concentrations								
	2.5 µg/mL			5 µg/mL			10 µg/mL		
NP size	R1	R2	R3	R1	R2	R3	R1	R2	R3
10 nm	247.19	189.39	249.30	202.48	140.98	219.43	226.32	238.66	149.67
30 nm	161.40	118.74	152.44	110.68	110.28	119.85	102.50	130.39	111.31
100 nm	106.47	108.73	115.25	108.16	119.14	97.16	102.54	102.35	108.76

Table S9.16. Autophagy results. Cells were treated with different concentrations and sizes of AgNPs for 24 hours. Then, the mean intensity of the autophagosome marker was recorded by image J. The intensity results after 24 hours exposure was normalized to percentage (%) against naïve. The results represent the mean of three individual replicates and their standard deviation. Data with asterisks (*) indicate a statistically significant difference (* $p < 0.05$) compared to the naïve cells. Data with upper and lowercase letters next to the values indicate statistically significant differences ($p < 0.05$) between the selected NP sizes at the same concentration.

AgNPs size	Naive	2.5 $\mu\text{g/mL}$	5 $\mu\text{g/mL}$	10 $\mu\text{g/mL}$
10 nm	100 \pm 0.0	228.6 \pm 33.9* A	187.6 \pm 41.27	204.8 \pm 48.2
30 nm	100 \pm 0.0	144.1 \pm 22.4 a	113.6 \pm 5.41	114.7 \pm 14.2
100 nm	100 \pm 0.0	110.1 \pm 4.56	108.1 \pm 10.9	104.5 \pm 3.64

9.1.7 Images autophagy

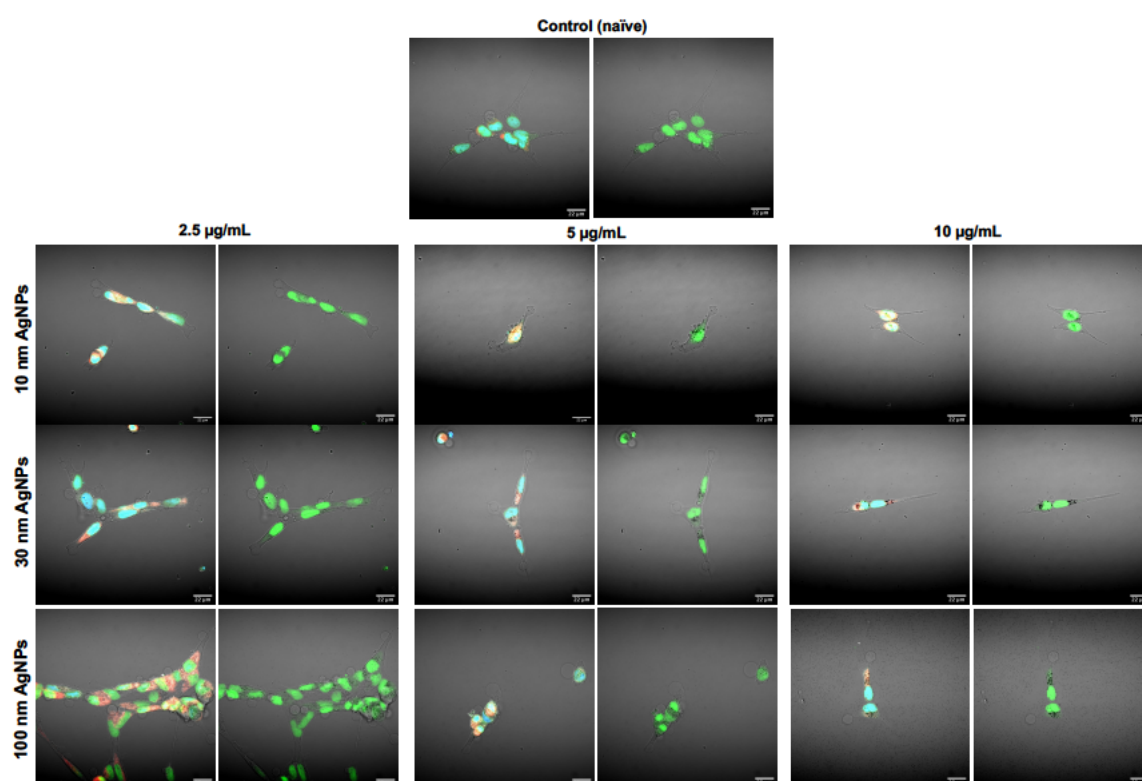


Figure S9.2. Images of autophagy induction. Cells were exposed for 24 hours to AgNPs at different concentrations and sizes. Then, images were taken with a 60X objective lens and optical zoom using a NIKON A1R 808 microscope. The

images (left) show the overlay of three different staining used for cell localisation, blue for nucleus, red for lysosomes and green the autophagy dye. All the images (except control) have also an overlay of the 488-channel intensity for the nanoparticles (white dots).

9.1.8 Secreted proteins: protocol.

To further understand the role of the ZF4 cell secreted proteins in the formation of the protein corona, the total protein content of AgNPs treatments in CCM and SFM was quantified. The experiment was designed to mimic the real conditions in which most of the experiments in this study were performed (NPs and proteins in free solution). Here, cells were seeded in 6 well plates and at a density of 5×10^5 cells/mL using DMEM/F12 supplemented with 10% FBS and 1% penicillin and streptomycin at 28 °C and 5% CO₂. After 24 hrs, cells were treated with 2.5, 5 and 10 µg/mL of 10, 30 and 100 nm AgNPs in CCM. Afterwards, (at 3, 6, 12 and 24 hours) the volume in the wells (1mL) with the NP treatments was gently resuspended, then a sample of 20 µL (under sterile conditions) was taken and placed in 96 well plates. The protein quantification was immediately performed by Pierce™ BCA Protein Assay Kit following the supplier protocol. A control with naive cells in CCM was also included to demonstrate changes in the protein concentrations across the time points.

Table S9.17. Results for secreted proteins. R means replicate, CCM: Complete culture medium containing 10% foetal bovine serum. AgNP concentrations are expressed in µg/mL. Protein results are in percentage (%). No statistical analyses were performed for this data.

10 nm															
Time (hours)	CCM			Naive			2.5 AgNPs			5 AgNPs			10 AgNPs		
	R1	R2	R3	R1	R2	R3	R1	R2	R3	R1	R2	R3	R1	R2	R3
3	161.1 11	152.6 77	147.8 59	162.9 09	148.5 45	153.7 37	151.6 67	151.3 33	140.6 46	135.9 19	144.1 01	147.9 49	150.6 87	154.0 61	152.3 43
6	178.6 16	152.8 69	158.9 49	160.6 36	156.2 12	167.4 14	150.3 74	155.6 67	162.2 22	158.3 94	159.0 71	132.6 97	154.4 34	165.5 25	172.7 07
12	140.4 24	146.1 92	176.3 64	143.9 09	154.3 23	148.3 94	145.9 39	147.9 6	137.8 69	146.3 03	149.3 23	147.5 76	151.6 06	149.8 69	159.1 82
24	160	157	145.1 11	166.5 86	163.4 04	144.5 25	143.5 76	167.6 97	166.5 86	163.4 04	144.5 25	157.7 98	161.7 78	157.4 55	167.4 44
30 nm															
Time (hours)	CCM			Naive			2.5 AgNPs			5 AgNPs			10 AgNPs		
	R1	R2	R3	R1	R2	R3	R1	R2	R3	R1	R2	R3	R1	R2	R3
3	161.1 11	152.6 77	147.8 59	162.9 09	148.5 45	153.7 37	150.8 38	155.4 75	143.1 31	160.1 52	153.9 8	149.1 41	136.8 38	119.5 15	160.1 01
6	178.6 16	152.8 69	158.9 49	160.6 36	156.2 12	167.4 14	181.0 81	183.2 02	176.6 16	180.7 07	178.4 44	181.2 63	169.2 83	177.7 68	176.5 45
12	140.4 24	146.1 92	176.3 64	143.9 09	154.3 23	148.3 94	145.3 23	147.1 62	137.2 63	146.8 18	147.4 95	152.3 94	135.4 65	151.4 85	158.3 64
24	160	157	145.1 11	166.5 86	163.4 04	144.5 25	173.8 59	145.3 43	174.7 88	167.4 75	145.8 99	159.0 71	164.2 22	166.9 29	173.9 9
100 nm															
Time (hours)	CCM			Naive			2.5 AgNPs			5 AgNPs			10 AgNPs		
	R1	R2	R3	R1	R2	R3	R1	R2	R3	R1	R2	R3	R1	R2	R3
3	161.1 11	152.6 77	147.8 59	162.9 09	148.5 45	153.7 37	162.1 01	166.1 11	147.5 96	164.4 04	159.6 77	159.1 11	161.1 52	161.8 99	167.7 58
6	178.6 16	152.8 69	158.9 49	160.6 36	156.2 12	167.4 14	166.5 25	165.2 42	169.1 52	153.1 52	166.5 45	165.5 45	160.9 49	175.3 03	173.4 14

12	140.4 24	146.1 92	176.3 64	143.9 09	154.3 23	148.3 94	150.8 89	164.6 87	148.3 94	156.5 15	162.2 83	159.6 46	163.4 95	159.6 36	161.2 12
24	160	157	145.1 11	166.5 86	163.4 04	144.5 25	171.1 92	179.2 42	184.5 05	178.8 99	162.3 33	171.4 04	173.3 54	179.9 19	181.6 97

